

Anti-Proton to Proton Ratio in Au+Au Collisions at STAR

Dissertation
zur Erlangung des Doktorgrades
der Naturwissenschaften

vorgelegt beim Fachbereich Physik
der Johann Wolfgang Goethe-Universität
in Frankfurt am Main

von
Jens Berger
aus Frankfurt am Main

Frankfurt am Main, 2003
(D F 1)

Vom Fachbereich Physik der Johann Wolfgang Goethe-Universität
als Dissertation angenommen.

Dekan: Prof. Dr. Horst Schmidt-Böcking

Gutachter: Prof. Dr. Reinhard Stock
Prof. Dr. Dieter Röhrich

Datum der Disputation:

Zusammenfassung

In dieser Arbeit wird das Antiproton zu Proton Verhältnis in Gold+Gold Kollisionen ($^{197}\text{Au} + ^{197}\text{Au}$) bei einer Schwerpunktsenergie von $\sqrt{s_{NN}} = 200$ GeV, bei mittlerer Rapidität und bei einem Transversalimpuls von bis zu 4.5 GeV/ c , vermessen und mit Modellrechnungen verglichen. Die Messung wurde am STAR Experiment am *Relativistic Heavy Ion Collider* (RHIC) in Brookhaven, NY, USA durchgeführt.

Die elementaren Bausteine der Kernmaterie sind Quarks die über Gluonen stark wechselwirken und in Hadronen (Baryonen und Mesonen) gebunden sind (Kapitel 1). Die mathematische Beschreibung der starken Wechselwirkung ist durch die Quanten Chromo Dynamic (QCD) gegeben. QCD ist eine nicht abelsche Eichtheorie, die die Wechselwirkung der fermionischen Quarks über den Austausch von bosonischen Gluonen beschreibt. In der QCD tragen Quarks sowie Gluonen Farbladungen (r, g, b). Baryonen bestehen aus 3 Quarks unterschiedlicher Farbe und Meson aus Quarks, die jeweils Farbe und anti-Farbe tragen

In der QCD trägt das Austauscheteilchen (das Gluon) auch Farbladung und stellt somit eine Quelle des Feldes dar. Dies spiegelt sich in dem nicht abelschen Charakter der QCD wieder. Für Kernmaterie im Grundzustand ($\rho_0 \sim 0.15$ GeV/fm³) resultiert daher: 1) Bei kleinen Quark Abständen, oder starken Impulsübertragen, q , fällt die Kopplungskonstante der starken Wechselwirkung (α_s) logarithmisch ab und Quarks und Gluonen sind schwach gebunden (*asymptotic freedom*). Bei hohem q , typischerweise $q^2 > 2$ GeV, ist die Kopplung durch α_s schwach genug, so daß eine störungstheoretische Behandlung der QCD möglich ist (pQCD). 2) Bei weiten Distanzen, oder kleinen q , ist α_s gross. Durch die Zunahme der Kopplungsstärke wird daher beim Versuch ein Quark aus dem Verbund eines Hadrons herauszulösen, mit wachsendem Abstand immer mehr Energie benötigt, so daß es schliesslich günstiger ist ein neues Quark-Antiquark Paar zu bilden. Quarks sind deshalb immer in Hadronen (Mesonen und Baryonen) gebunden (*confinement*). Wenn Kernmaterie stark komprimiert wird ($5\rho_0$ bis $10\rho_0$), steigen Energiedichte und Temperatur und möglicherweise erfährt die Kernmaterie einen Phasenübergang zu einem Zustand der als Quark-Gluon-Plasma (QGP) bezeichnet wird. Quarks wären dann nicht mehr in Hadronen gebunden und bewegen sich frei, zusammen mit Gluonen.

QCD Gitter Rechnungen sagen einen Phasenübergang der hadronischen Kernmaterie in ein QGP, bei einer Temperatur vom $T_c = 173 \pm 8$ MeV und verschwindender Nettobaryonendichte voraus (Nettbaryonendichte = Dichte der Baryonen – Antibaryonen). Die Energiedichte bei dieser Temperatur wird mit $\epsilon_c \simeq 0.75 \pm 0.25$ GeV/fm³ abgeschätzt, dies entspricht etwa $6\rho_0$. Dies hat auch Konsequenzen für andere Gebiete der Physik, beispielsweise nach dem Standard Kosmologischen Modell hat sich Kernmaterie zum Zeitpunkt des frühen Universums, kurze Zeit nach dem Urknall, in einem ähnlichen Zustand befunden.

Schwerionenkollisionen bei ultrarelativistischen Energien, wie z.B. Gold+Gold Kollisionen bei $\sqrt{s_{NN}} = 200$ GeV, bieten die Möglichkeit, Kernmaterie unter extremen Bedingungen zu studieren. In einer solchen Kollision wird für sehr kurze Zeit (einige fermi/c), ein Bereich aus dichter und heißer Kernmaterie erzeugt, der als „Feuerball“ bezeichnet wird. Wenn Energiedichte und Temperatur hinreichend hoch sind, erwartet man, daß die Kernmaterie in einer QGP-Phase vorliegt. Der Übergang von dieser Phase in hadronische Materie sollte zu Signaturen in den gemessenen Teilchenmultiplizitäten und Impulsspektren führen.

Bevor RHIC im Jahre 2000 startete, wurden Blei+Blei Kollisionen am CERN SPS bei Schwerpunktsenergien von bis zu $\sqrt{s_{NN}} = 17.3$ GeV studiert. Die Interpretation des Feuerballes als ein Hadrongas im Rahmen einer statistischen Modell Analyse, deuten darauf hin, daß in Kollisionen bei dieser Energie eine Temperatur von $T \sim 160$ MeV erreicht wird. Diese Temperatur liegt in der Nähe der kritischen Temperatur. Aus der hohen Dominanz der Baryonen gegenüber der Anti-Baryonen bei dieser Schwerpunktsenergie resultiert das baryonchemischen Potential von $\mu_B \sim 245$ MeV.

Die Messung des Antiproton zu Proton Verhältnis bei einer mehr als 10 fach höheren Schwerpunktsenergie am RHIC Collider, erlaubt zusammen mit weiteren Hadron-Verhältnissen die Bestimmung der Temperatur und des baryonchemischen Potentials zum Zeitpunkt des chemischen Ausfrieren der Hadron. Andererseits sind bei RHIC Energien die Wirkungsquerschnitte für harte Prozesse erhöht gegenüber SPS Energien. Auch wenn diese Ereignisse immer noch relativ selten sind (1 pro 100 bis 1000 Ereignisse), so sind sie bei RHIC, entweder durch sehr hohe Statistik, oder durch die verwendung spezieller Trigger zugänglich. Dies eröffnet die Möglichkeit, harte Prozesse zu vermessen, und die Resultate mit pQCD Rechnungen zu vergleichen. In dieser Arbeit wurde daher ein besonderer Schwerpunkt auf die Messung von Protonen mit einem hohem Transversalimpuls gelegt.

Der RHIC Collider (Kapitel 2) besteht aus 2 konzentrischen Ringen mit einem Umfang vom 3,8 km, und stellt an 6 Interaktionspunkten Kollisionen von Ionen zur Verfügung. In $^{197}\text{Au} + ^{197}\text{Au}$ Kollisionen wird eine Schwerpunktsenergie von bis zu $\sqrt{s_{NN}} = 200$ GeV erreicht. Das STAR Experiment (Kapitel 3) am RHIC Collider ist ein Hadronen-Detektor, der sich durch eine hohe

Präzision in der Impulsmessung auszeichnet. Der Hauptdetector ist eine grossvolumige *Time Projection Chamber* (TPC) die in einem Magnetfeld von maximal $B = 0.5$ T betrieben wird. Die TPC dient einerseits zur Impulsmessung der Hadronen, andererseits können durch Messung des spezifischen Energieverlustes der Hadronen im Gas der TPC, dE/dx , Teilchen identifiziert werden. Bei mittlerer Rapidität, können Protonen mit einem Impuls vom $0.3 < p_{\perp} < 1.0$ GeV/ c bei $B = 0.5$ T in der TPC identifiziert werden. Für die Protonen Identifikation bei höheren Impulsen von bis zu $p_{\perp} \leq 4.5$ GeV/ c wurde ein *Ring Imaging Čerenkov*-Detektor (RICH-Detektor) benutzt. Hierbei wird ausgenutzt, daß Teilchen, die durch ein dielektrisches Medium gehen, Čerenkov-Strahlung emittieren. Die Čerenkov-Photonen werden in einem Kegel um die Teilchentrajektorie emittiert. Der Öffnungswinkel des Kegels ist abhängig von der Geschwindigkeit des Teilchens. Diese Korrelation ermöglicht bei gegebenen Impuls die Teilchenidentifikation. Der RICH-Detektor ist bei mittlerer Rapidität plaziert, und deckt $\sim 2\%$ der TPC-Akzeptanz in einem Bereich von $|\eta| < 0.3$, $\Delta = 20^{\circ}$ ab. Dadurch durchqueren nur eine kleine Anzahl von Teilchen mit einem hohen Impuls den Detektor. Pro Ereignis einer zentralen $^{197}\text{Au} + ^{197}\text{Au}$ Kollision wurde im Schnitt ein Teilchen mit einem Impuls $p > 1$ GeV/ c gemessen, wobei die Anzahl der Teilchen pro weiteren GeV/ c um etwa eine Zehnerpotenz abfällt. In jedem ~ 100 sten Ereignis wurde daher ein Teilchen mit einem Impuls $p > 3$ GeV/ c in der Akzeptanz des RICH-Detektors detektiert.

Dieser Sachverhalt macht den Einsatz des Level-3 Triggers (Sektion 3.8) notwendig, um im gespeicherten Datensatz, Ereignisse die ein Teilchen mit hohem Impuls in der Akzeptanz des RICH-Detektors enthalten, anzureichern. Der Level-3 Trigger erlaubt die Echtzeit (*on-line*) Rekonstruktion von zentralen $^{197}\text{Au} + ^{197}\text{Au}$ Ereignissen bei einer Ausleserate der Detektoren von 50 Hz, wobei die Rate mit der Ereignisse gespeichert werden können etwa eine Zehnerpotenz niedriger ist. Somit ist er Trigger in der Lage, seltene Ereignisse um maximal den Faktor ~ 10 anzureichern. Das Trigger System rekonstruiert hierbei etwa 6 MB an nullterdrückten TPC Rohdaten per Ereignis und führt eine Ja-Nein Entscheidung, ob ein gegebenes Ereignis selektiert werden soll oder nicht, in etwa 100 ms durch. Der RICH-Algorithmus (Sektion 4.3.4) lief während der Strahlzeit in 2001 zusammen mit 3 weiteren Trigger Algorithmen auf dem Level-3 Trigger System und selektierte Ereignisse, die ein Teilchen mit einem Impuls $p > 3$ GeV/ c , in der Akzeptanz des RICH-Detektors haben (RICH-Kandidaten). Zur effizienten Selektion der Ereignissen, mit dem Level-3 Trigger, ist die Kenntnis der Rekonstruktionseffizienz und Impulsauflösung des Systems notwendig. Die *off-line* Event Rekonstruktion, nach der Datennahme, und die *on-line* Rekonstruktion auf dem Level-3 Trigger, werden in Kapitel 4 beschrieben und miteinander verglichen. Die Rekonstruktionseffizienz der *on-line* Rekonstruktion beträgt $\sim 80\%$ verglichen mit der *off-line* Rekonstruktion. Die Impulsauflösung der *on-line* rekonstruktion ist sehr ähnlich der Impulsauflösung der *off-line* Rekonstruktion. Die Triggeref-

fizienz des RICH-Algorithmusses betrug $\sim 80\%$ während der Datennahme.

Die Datenanalyse (Kapitel 5) unterteilt sich in die Analyse von Protonen und Antiproton, die in der TPC identifiziert (Sektion 5.1) wurden, und der Protonen und Antiproton, die im RICH-Detektor identifiziert wurden (Sektion 5.2). Bei der Messung des Antiproton zu Proton Verhältnisses in der TPC, wurde ein *minimum bias* Datensatz, der Ereignisse aller Zentralitäten und ein Datensatz, der mit einem zentralem Trigger die 5% zentralsten Ereignisse selektiert, analysiert. Jeder Datensatz bestand aus jeweils einer Million Ereignissen. Die identifizierten Protonen stammen nicht ausschließlich aus der Reaktion, sondern auch aus sekundären Interaktionen von primären Teilchen mit dem Detektormaterial. Andererseits werden Anti-Protonen in Detektor Material absorbiert. Die identifizierten Protonen und Antiprotonen Multiplizitäten wurden auf diese Effekte korrigiert. Ausserdem wurde eine Korrektur des Energieverlustes des rekonstruierten Protonen Impulses durchgeführt.

Für die 5% zentralsten $^{197}\text{Au} + ^{197}\text{Au}$ Kollisionen wurde ein mittleres Antiproton zu Proton Verhältnis von $\langle \bar{p}/p \rangle|_{0.4 < p_{\perp} < 1.0 \text{ GeV}/c} = 0.81 \pm 0.002_{\text{stat.}} \pm 0.05_{\text{syst.}}$ im gemessenen Transversalimpulsbereich und im gemessenen Rapiditätsbereich ein mittleres Verhältnis von $\langle \bar{p}/p \rangle|_{-0.5 < y < 0.5} = 0.82 \pm 0.002_{\text{stat.}} \pm 0.05_{\text{syst.}}$ ermittelt. Das Verhältnis ist unabhängig von Transversalimpuls und Rapidität innerhalb des gemessenen Bereiches. Eine leichte Zentralitätsabhängigkeit von $\bar{p}/p = 0.83 \pm 0.002_{\text{stat.}} \pm 0.05_{\text{syst.}}$ für periphere Kollisionen (weniger als 80% zentral) and ein Abfall des Verhältnisses auf $\bar{p}/p = 0.78 \pm 0.002_{\text{stat.}} \pm 0.05_{\text{syst.}}$ für die 5% zentralsten Kollisionen (Figur 5.13, 5.14) wurde gemessen. Diese Analyse, die auf *off-line* rekonstruierten Daten basiert, wurde mit der *on-line* Rekonstruktion des Level-3 Trigger Systems verglichen und hohe Übereinstimmung wurde festgestellt (Sektion 5.1.11).

Bei der Analyse des Antiproton zu Proton Verhältnisses im RICH-Detektor, stand ein Datensatz vom 2.5 Millionen zentralen $^{197}\text{Au} + ^{197}\text{Au}$ Ereignissen zur Verfügung. Aufgrund der geringen Luminosität des RHIC Colliders wurde nur ein Teil des Datensatzes mit Ereignissen, die mit dem RICH-Algorithmus selektiert wurden, angereichert. Die Kapazität des Level-3 Trigger Systems konnte daher bei weitem nicht ausgenutzt werden.

Die RICH identifizierten Protonen und Antiprotonen wurden auf Absorption im Detektormaterial korrigiert. Der Absorptionseffekt ist aufgrund des zusätzlichen Detektormaterials, das Teilchen im Vergleich zur TPC traversieren müssen, erhöht. Unter Berücksichtigung des zusätzlichen Detektormaterials wurde der wesentlich geringe Proton Untergrund bei hohen Impulsen abgeschätzt. Das gemessene Anti-Protonen zu Protonen Verhältnis fügt sich ab einem transversalen Impuls vom $p_{\perp} = 1.3 \text{ GeV}/c$ an das Resultat der TPC-Messung an. Ein leichter Abfall des Verhältnisses auf $\bar{p}/p = 0.645 \pm 0.005_{\text{stat.}} \pm 0.10_{\text{syst.}}$ bei einem Impuls von $p_{\perp} = 4.25 \text{ GeV}/c$ wurde gemessen (Figur 5.34). Bei der Interpretation dieses Ergebnisses ist

zu beachten, daß der systematische Fehler der Messung bei hohem transversalen Impuls ansteigt.

Die Ergebnisse der Messung werden in Kapitel 6 diskutiert und in Kapitel 7 zusammengefasst. Das gemessene Antiproton zu Proton Verhältnis im transversalen Impulsbereich von $0.4 < p_{\perp} < 1.0$ GeV/ c ist ~ 12.5 höher, als in zentralen Kollisionen bei der höchsten Schwerpunktsenergie am SPS. Die hohe Symmetrie zwischen Protonen und Antiprotonen bedeutet, daß die zentrale Rapiditätsregion bei RHIC fast frei vom Nettoprotonen ist. Die leichte Assymmetrie könnte sich aus dem Beitrag der Valenzquarks in einem Szenario, in dem der Kern abbricht, erklären. In einem solchen Szenario wird der absolute Wert des Verhältnisses sowie die Unabhängigkeit des Verhältnisses von der Rapidität gut reproduziert. Hierbei wird die Fragmentation von Quarks und Antiquarks in Protonen angenommen. Ein realistischeres Rekombinations Szenario würde erhebliche Quark Paar Erzeugung, beispielsweise durch Gluon-Fusion, verlangen.

Das gemessene Antiproton zu Proton Verhältnis stimmt gut mit der Vorhersage des statistischen Modelles bei einer Temperatur von $T = 177 \pm 7$ MeV und einem baryochemischen Potetial von $\mu_B = 29 \pm 8$ MeV überein, speziell wenn eine Korrektur der abgeschätzten Beiträge vom Zerfall seltsamer Baryonen vorgenommen wird. Diese Temperatur im Vergleich zur höchsten SPS Energie, ist nur geringfügig höher, während das baryochemische Potetial, entsprechend der höheren Symmetrie der Baryonen und Antibaryonen, um einen Faktor 10 geringer ist. Wie bei den SPS Energien sind diese Parameter nahe an der in Figur 1.6 gezeichneten Phasengrenze zu einem QGP.

Ein Vergleich des Antiproton zu Proton Verhältnisses bei höheren Transversalimpulsen von bis zu $p_{\perp} = 4.5$ GeV/ c , mit den Voraussagen einer pQCD Rechnung und einer nicht perturbativen *Soft+Quench* Modelles zeigt, daß die geringe Abhängigkeit des Verhältnisses vom transversen Impuls besser vom *Soft+Quench* Modell beschrieben wird (Figur 6.2). Dies deutet darauf hin, daß der höchste hier gemessene transversale Impuls von $p_{\perp} = 4.5$ GeV/ c zu gering ist, um das gemessene Antiproton zu Proton Verhältnis mit pQCD Rechnungen zu beschreiben.

Als Ausblick dieser Arbeit läßt sich zusammenfassen, daß hier zwei für die Schwerionen Physik neuartige Techniken mit Erfolg zur Anwendung kamen: Der RICH-Detektor und ein Level-3 Trigger System.

Korrigierte Hadronen Spektren, identifiziert im RICH, sind voraussichtlich bald verfügbar. Wobei unter anderem untersucht wird, ob eine Korrektur des Energieverlustes der Teilchen, sich in einer höheren Auflösung der Čerenkov Spektren niederschlägt.

Das ALICE Experiment am LHC ($\sqrt{s_{NN}} = 5,5$ TeV) wird mit sieben, 1/3 grösseren als dem hier verwendeten, RICH-Detektormodulen bei mittlerer Ra-

pidität ausgestattet sein. Ein Problem des hier verwendeten RICH-Detektors, der ein ALICE-Prototyp darstellt, war die geringe Anzahl der *cluster* die den projizierten Čerenkov Kegel auf der Ausleseebene definierten. Dies wird bei den ALICE-Detektormodulen durch einen etwas dickeren Radiator und eine höhere Effizienz der Umwandlung von Čerenkov Photonen in Elektronen verbessert sein. Dadurch wird die Effizienz und Auflösung des Detektors wesentlich erhöht.

Das Level-3 Trigger System wurde in dieser Arbeit erfolgreich zum Anreichern von RICH-Kandidaten verwendet. Es bestehen Pläne Trigger Level-2 and Level-3 in Kombination mit dem Elektromagnetischen Kalorimeter in der kommenden $^{197}\text{Au} + ^{197}\text{Au}$ Strahlzeit (2004) zur Selektion von Ereignissen mit Upsilon-Kandidaten ($\Upsilon \rightarrow e^+e^-$) zu verwenden.

Ein ähnliches System (der High Level Trigger, HLT) wird bei ALICE zur Anwendung kommen. Wobei die mit dem Level-3 Trigger gemachten Erfahrungen einfließen werden. Der Alice HLT wird bei einer höheren Rate betrieben werden. Ausserdem werden dem HLT die Detektorinformationen z.B. vom *Transition Radiation Detektor* (TRD) zur Verfügung stehen. Dies wird das effiziente Triggern auf seltene Ereignisse ermöglichen.

Contents

1. Introduction	1
1.1. Hadronic Matter	2
1.2. Heavy Ion Collisions	7
1.2.1. Impact Parameter and Centrality	7
1.3. Definition of Kinematic Variables	8
1.4. Space and Time Evolution of a Heavy Ion Collision	9
1.4.1. Initial Stage	11
1.4.2. Chemical Equilibrium	12
1.4.3. Thermal Freeze-Out	14
1.5. Anti-Proton to Proton Ratio	15
2. The RHIC Collider	17
2.1. A Brief Description	17
2.2. Injection into RHIC	18
2.3. Collider Design	20
2.4. Experiments at RHIC	22
2.5. Commissioning and Operation of RHIC	24
2.5.1. First Year of RHIC Operation	24
2.5.2. Second Year of RHIC Operation	27
3. The STAR Experiment	31
3.1. STAR Instrumentation Overview	31
3.2. The STAR Coordinate System	34
3.3. The STAR Magnet	34
3.4. Description of STAR Detectors	35

Contents

3.4.1.	The Time Projection Chamber	35
3.4.2.	Ring Imaging Čerenkov Detector	41
3.4.3.	Forward Time Projection Chamber	47
3.4.4.	Silicon Vertex Tracker	48
3.5.	Trigger Detectors	49
3.5.1.	Zero Degree Calorimeters	49
3.5.2.	Central Trigger Barrel	50
3.6.	Trigger	51
3.7.	Data Acquisition	52
3.8.	The Level-3 Trigger System	53
3.8.1.	Architecture	55
4.	Event Reconstruction	57
4.1.	Event Reconstruction in the TPC	57
4.1.1.	Cluster Reconstruction	57
4.1.2.	Coordinate Transforms and Distortion Corrections	59
4.1.3.	Track Reconstruction	61
4.1.4.	Particle Identification via dE/dx in the TPC	62
4.1.5.	Global Track Model	63
4.1.6.	Event Vertex Reconstruction	65
4.1.7.	Primary Track Model	65
4.2.	RICH Event Reconstruction	66
4.3.	On-line TPC Event Reconstruction	69
4.3.1.	Cluster Reconstruction	70
4.3.2.	Track Reconstruction	70
4.3.3.	Vertex Determination	73
4.3.4.	Level-3 RICH algorithm	75
4.3.5.	Online Event Visualization	76
5.	Analysis of Anti-Proton to Proton Ratio	79
5.1.	\bar{p}/p at Low Transverse Momentum	79
5.1.1.	Dataset	80
5.1.2.	Trigger Operation	80

5.1.3.	Vertex Position Determination	82
5.1.4.	Centrality Considerations	82
5.1.5.	Detector Acceptance	84
5.1.6.	Proton Identification	85
5.1.7.	Corrections	87
5.1.8.	Corrected \bar{p}/p Ratio in Minimum Bias Events	95
5.1.9.	Corrected \bar{p}/p Ratio in Central Events	95
5.1.10.	Systematic Errors	98
5.1.11.	Comparison to On-line Reconstructed Events	99
5.2.	\bar{p}/p Analysis at High Transverse Momentum	109
5.2.1.	Central Dataset Details	110
5.2.2.	Event Centrality and Vertex Distribution	110
5.2.3.	Track Quality Criteria	111
5.2.4.	Level-3 Trigger Enhancement	112
5.2.5.	Pseudorapidity Distribution of Particles in the Acceptance of the RICH Detector	116
5.2.6.	Particle Identification using the RICH Detector	118
5.2.7.	Raw \bar{p}/p Ratio from RICH Detector Data	122
5.2.8.	Corrections to Raw RICH Detector \bar{p}/p Ratio	124
5.3.	\bar{p}/p for Low & High Transverse Momentum	125
6.	Results and Discussion	129
6.1.	Feed-down of \bar{p} and p from Heavier Baryons	129
6.2.	Energy Dependence of \bar{p}/p	130
6.3.	Transverse Momentum Dependence of \bar{p}/p	132
6.4.	Fragmentation versus Recombination Picture	133
7.	Conclusion	137
7.1.	Outlook	138
A.	Tables with Detector Attributes	139
B.	Tables with Results	143

Contents

1. Introduction

The subject of this thesis is the ratio of anti-protons to protons (\bar{p}/p) produced in gold ($^{197}\text{Au} + ^{197}\text{Au}$) collisions at the highest relativistic heavy ion collider (RHIC¹) energy ($\sqrt{s_{NN}} = 200$ GeV). The ratio measurement was carried out at the STAR experiment. At RHIC energies, heavy ion collisions create hadronic matter under extreme conditions, i.e. at high temperatures and low net-baryon densities (net-baryons = baryons – anti-baryons).

Strongly interacting nuclear matter, consisting of confined quarks in the form of baryons and mesons, can be described within the framework of quantum chromo dynamics (QCD). Lattice QCD calculations predict a phase transition of nuclear matter to a deconfined state of free quarks and gluons at the extreme conditions present in central heavy ion collisions at RHIC. The temperature and energy density achieved in such a collision can be determined from produced particle yields within the framework of different models. Additionally, characteristic changes in particle yields and other signatures are predicted in the case of a phase transition [1] [2] [3] [4].

Particle ratios, such as the relative proton to anti-proton yield in heavy ion collisions, are well described by statistical models [5] [6]. Based on thermodynamical principles, these models yield parameters at chemical freeze-out, such as temperature and baryon chemical potential.

Cross sections for high momentum particles increase with collision energy. With the energies achieved at RHIC, hard processes become more and more important. This is of special interest, since at high momentum transfer, a branch of QCD known as perturbative quantum chromo dynamics (pQCD), becomes computationally valid and can be employed as a theory. Thus, anti-proton to proton ratio measurements at high momentum can be compared with such pQCD calculations.

In the present study, anti-protons and protons at low momentum were reconstructed and identified in the time projection chamber (TPC) of the STAR experiment. The identification of high momentum anti-protons and protons involved a ring imaging Čerenkov (RICH) detector, with a relative small acceptance. Due to the small number of high momentum hadrons in the acceptance of the RICH

¹Brookhaven National Laboratory, Upton, N.Y. USA

1. Introduction

detector, the STAR Level-3 trigger was employed. This trigger level allows an event sample to be selected based on properties of fully reconstructed events of $^{197}\text{Au} + ^{197}\text{Au}$ collisions. A Level-3 trigger algorithm was designed to enrich recorded events with high momentum hadrons in the acceptance of the RICH detector by up to a factor of 10, at the proposed RHIC collider luminosity in 2001.

This thesis is structured as follows: Chapter 1 gives an overview of the field of heavy ion physics. In Chapter 2, the RHIC collider is introduced and the performance of the collider within the first 2 years of operation is reported. Chapter 3 gives an overview of the STAR experiment, including a description of the Level-3 trigger system. The off-line event reconstruction as well as the on-line reconstruction used by the Level-3 trigger is explained in Chapter 4. In Chapter 5, the analysis of anti-proton to proton ratio measurements is presented. The measurement of the ratio at low transverse momentum, using the regular off-line reconstruction is first given. The result is compared with the fast on-line reconstruction results obtained using the Level-3 trigger. Finally, the analysis of the anti-proton to proton ratio at high transverse momenta is described. In Chapter 6, the experimental results are discussed, before concluding and giving an outlook in Chapter 7.

1.1. Hadronic Matter

Quarks, together with leptons, are the fundamental constituents of matter. Quarks participate in strong, weak and electromagnetic interactions, whereas leptons are only involved in weak and electromagnetic interactions.

Hadrons appear as a triplet (baryons) or a doublet (mesons) of quarks. Evidence was recently given for the observation of a state which consists of 5 quarks [7]. Quarks having spin $s = 1/2$ are fermions and carry a baryon number $B = 1/3$. They occur in various flavors: $u = \text{up}$, $d = \text{down}$, $s = \text{strange}$, $c = \text{charmed}$, $b = \text{bottom}$, $t = \text{top}$ and carry fractional electric charges of $u, c, t = +2/3|e|$ and $d, s, b = -1/3|e|$. For every quark, an anti-quark exists having opposite quantum numbers. u -quarks and d -quarks are the lightest flavors. They form protons (uud) and neutrons (ddu). Since the proton and neutron have nearly the same mass ($m \sim 939$ MeV), the up and $down$ quarks must also have similar masses. From high energy electron scattering experiments, it was found that every quark doublet or triplet (valence quarks) is surrounded by other quarks which are neutral to the outside. These quarks are called sea quarks. In the following treatment, only valence quarks will be considered. Strong interactions between quarks can be described using quantum chromo dynamics (QCD). QCD is a non-Abelian SU(3) gauge theory, based on fermionic quarks interacting by the exchange of

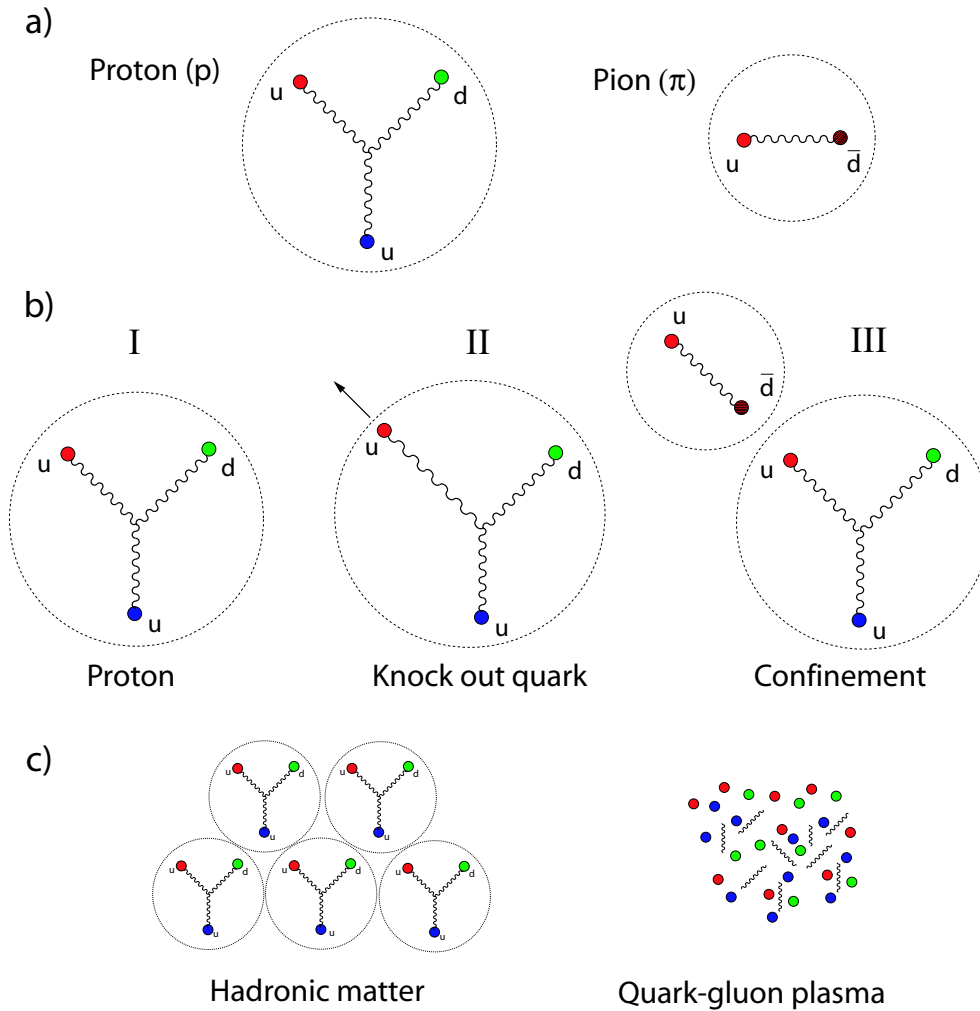


Figure 1.1.: a) Quark triplet, baryon (p) and quark doublet, meson (π). b) When an attempt is made to knock out a quark (II), the gluon is stretched and eventually the energy stored is sufficient to create a new quark/anti-quark pair (III). c) Quarks are confined in baryons in normal hadronic matter. In a quark-gluon plasma, quarks move freely in the absence of strong gluon coupling.

bosonic gluons (comparable to the photon in quantum electrodynamics). The gluon is a massless, flavorless vector particle with spin $s = 1$. In QCD, quarks and gluons carry strong colorcharges, such as $r = red$, $g = green$, $b = blue$ and $\bar{r} = anti-red$, $\bar{g} = anti-green$, $\bar{b} = anti-blue$, which are analogous to electric charges. Quarks carry color and anti-quarks carry anti-color, while gluons carry color and anti-color. As depicted in Figure 1.1a, baryons (e.g. a proton) consist of 3 different colored quarks. One of the quarks inside a meson (e.g. a pion)

1. Introduction

carries color, while the other carries anti-color (e.g. *red* and *anti-red*). Hence, baryons and mesons are confined objects which carry zero net color.

In QCD, the quanta which mediate the interaction, i.e. gluons, act as source of the field themselves. This reflects the non-Abelian character of the field. This feature of QCD is a crucial property which makes the coupling, α_s , decrease at small distances or large momentum transfer, since the gluon-gluon interaction dilutes the color charge [8]. The first order of perturbative expansion of α_s can be written as

$$\alpha_s(q^2) \approx \frac{4\pi}{b \ln(q^2/\Lambda_{QCD}^2)} \rightarrow 0, \quad q^2 \rightarrow \infty. \quad (1.1)$$

where q is the quark momentum transfer, Λ_{QCD} is a renormalization scale factor and b a constant [9] (Fig. 1.2a). This gives:

1. At short distances or large momentum transfer, q , the effective coupling constant $\alpha_s(q)$ in quark-quark couplings decreases logarithmically, i.e. quarks and gluons are weakly coupled, resulting in the phenomena of *asymptotic freedom*. At sufficiently high q (*hard processes*), the coupling strength is weak enough for pQCD to be computationally valid. Typically the lower limit favorable for pQCD is $q^2 \sim 2 \text{ GeV}$.
2. At large distances or small q , $\alpha_s(q)$ gets stronger thereby resulting in the phenomena of quark confinement.

In Figure 1.1b, quark confinement is depicted. The proton consists of 3 quarks held together by gluon exchanges, which can be imagined as being like elastic bands. If the gluons are not stretched, the coupling between the quarks in the proton is fairly weak (Figure 1.1b I). If there is an attempt to knock a quark out of the confined proton, (as might happen in a collision with a quark of another proton in a nucleus+nucleus collision), the gluon field gets stretched, and the force increases with separation (Figure 1.1b II). Eventually, the energy stored in the gluon becomes so large that a new quark/anti-quark pair (meson) is produced (Figure 1.1b III). Thus, the removal of a quark from the confined proton results in the production of another meson.

If nuclear matter gets compressed, resulting in an increase of temperature and pressure at densities ranging from $5\rho_0$ to $10\rho_0$ (where $\rho_0 \sim 0.15 \text{ GeV}/\text{fm}^3$ is the density of nuclear matter in the ground state), QCD predicts that interactions between quarks occur at short distances, governed by weak coupling. Meanwhile, long-range strong interactions become dynamically screened. This is illustrated by finite perturbation theory, which shows that the effective coupling constant, α_s , falls logarithmically (Fig. 1.2b) with increasing temperature:

$$\alpha_s(q^2) \propto \frac{1}{\ln T} \rightarrow 0, \quad T \rightarrow \infty. \quad (1.2)$$

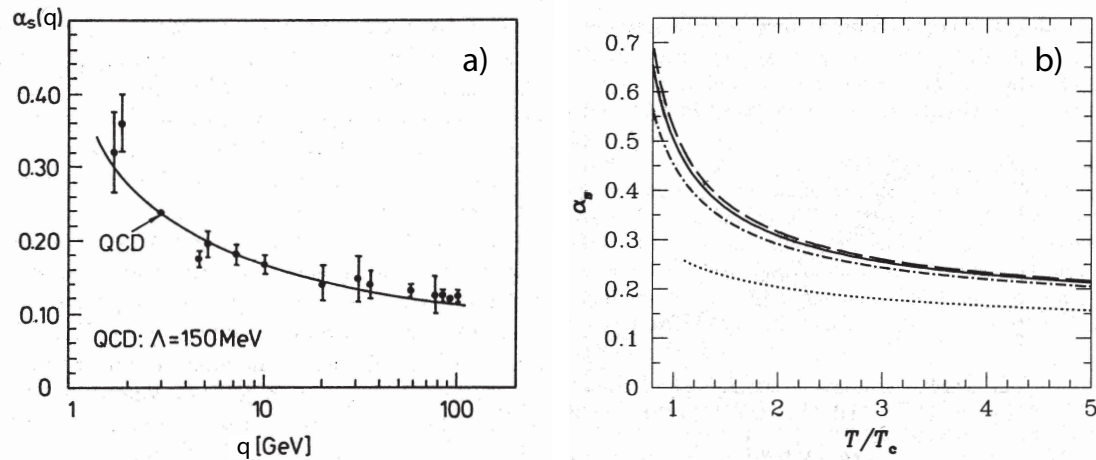


Figure 1.2.: a) Dependency of the effective coupling constant α_s on the momentum transfer q . b) Dependency of α_s and on the temperature T/T_c (b), where T_c is the critical temperature [8] [10].

Thus, for nuclear matter at very high temperatures, it is predicted that confined hadrons of nuclear matter undergo deconfinement (Fig. 1.1c) and that quarks move freely, i.e. they are not strongly bound in hadrons any more. This phase of quark matter is called the quark-gluon plasma (QGP) phase.

From the preceding argument, one would conclude that deconfinement sets in once q^2 ascends well into the perturbative domain, i.e. $q^2 \geq 100$ to 1000 GeV. This would correspond to temperatures of the order of $T = 10$ GeV. However, it turns out that the real deconfined QCD quark-gluon phase is not a consequence of asymptotic freedom, but of high energy density maintained over dimensions well in excess of the confinement scale, $1/\Lambda_{QCD} \approx 1$ fm. It is the phase transition from this state (to hadronic matter) which is the central topic of relativistic nucleus+nucleus collisions (which, in any case, could never reach $T \geq 10$ GeV).

From QCD numerical simulations on a discrete lattice [11], the phase boundary between a hadronic gas and a QGP is predicted to occur at a critical temperature of $T_c = 173 \pm 8$ MeV for a two flavor and $T_c = 154 \pm 8$ MeV for a 3 flavor calculation, at vanishing net-baryon density. The energy density, ϵ_c , of quark matter at T_c is estimated to be $\epsilon_c \simeq 0.75 \pm 0.25$ GeV/fm³ [11], which is up to $6\rho_0$.

A schematic view of the phase diagram of strongly interacting matter in the temperature versus baryon density plane is shown in Figure 1.3. A transition between the high temperature and high density phase is expected, giving rise to a phase boundary at the critical temperature $T_c(\rho)$, separating the hadron gas or liquid from the QGP phase. For $T < T_c(\rho)$, nuclear matter is composed of

1. Introduction

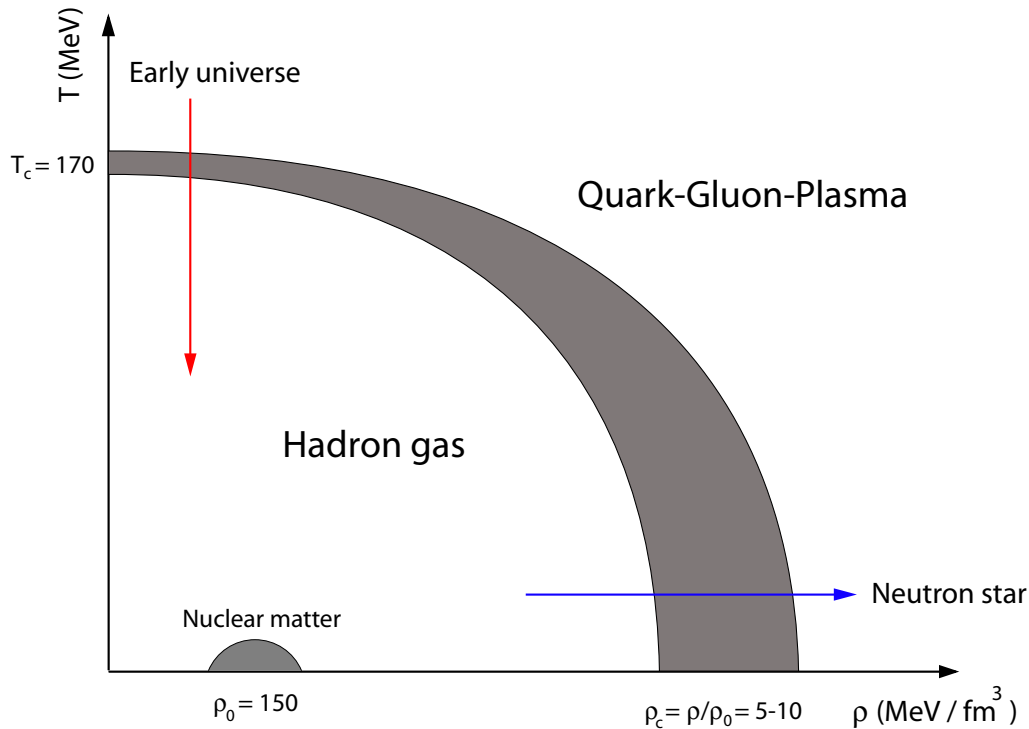


Figure 1.3.: Schematic phase diagram of strongly interacting hadronic matter. Temperature (T) versus density (ρ) values are obtained from lattice QCD calculations and from the standard cosmological model (see text). Arrows indicate a scenario where a phase transition between a hadron gas and a QGP or vice versa could occur.

baryons and mesons in a confined state (hadron phase). For $T \gg T_c(\rho)$, nuclear matter reaches a state with a larger degree of freedom, i.e. a QGP phase, where quarks move freely (Figure 1.1c). These considerations also have an impact on other physics disciplines. According to the standard cosmological model [12], the temperature of cosmic background radiation exceeded 200 MeV during the first 10 μs after the Big Bang. During the early universe, one would expect a low baryon density due to the symmetry of anti-baryons and baryons at that stage. Hence, the nuclear matter of the early universe was firstly in a QGP state, before crossing the phase boundary to become a hadron gas and later to form nuclear matter. The low temperature phase boundary is expected to occur during the collapse of a star, to a neutron star. Models predict that nuclear matter occurs at $5\rho_0$ to $8\rho_0$, in the center of such an object [13] [14]. The evolution of the early universe (high- T , low- ρ) and of neutron stars (low- T , high- ρ), are indicated by the solid red and blue lines in Figure 1.3, respectively.

1.2. Heavy Ion Collisions

Heavy ion collisions allow us to study the properties of strongly interacting matter under extreme conditions in the laboratory. The goal is to determine if hadronic matter reaches the critical temperature, $T_c(\rho)$, in such collisions, and if it subsequently undergoes a phase transition to a QGP. This can be attempted experimentally, by accelerating ions of heavy nuclei (e.g. gold) up to ultra-relativistic velocities and causing them to collide. In such a collision, a region of dense, hot, strongly interacting matter is created, which is typically referred to as a “fireball” [15]. When the fireball cools down, hadrons and leptons are created as remains of the collision. These remains are measured in huge particle detectors. The energy density, temperature and baryon densities which have occurred during the collision can be derived using model calculations. Characteristic changes in produced particle yields and other signatures are predicted in the case of a phase transition [1] [2] [3] [4].

1.2.1. Impact Parameter and Centrality

In a heavy ion collision, the impact parameter, b , determines the geometrical overlap of the colliding nuclei in a collision as shown in Figure 1.4 (where the nuclei are treated as spheres filled with nucleons). The smaller the impact parameter, the more central is the collision. The impact parameter is indicative of

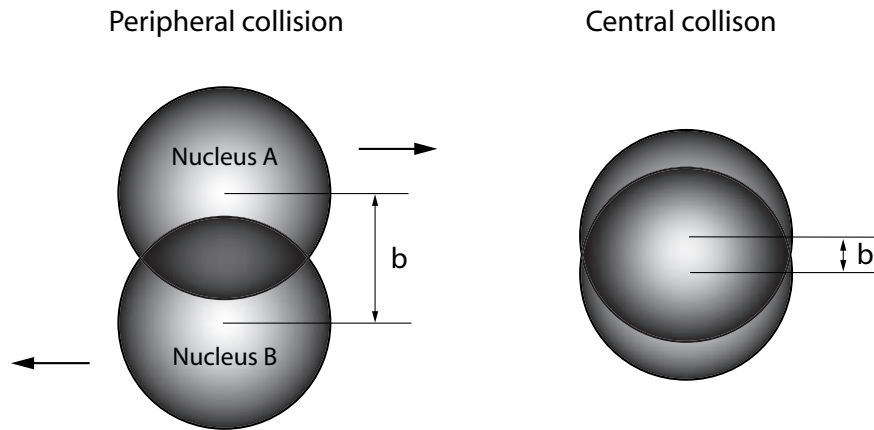


Figure 1.4.: Peripheral (central) collision of nucleus A and B with a large (small) impact parameter, b . The area of overlap is the region in the middle of the two spheres.

the energy density achieved, and the number of produced particles depends on the energy density (as will be shown in Section 1.4.1). The impact parameter

1. Introduction

can not be measured directly. However, the number of produced particles, which is correlated to the impact parameter, is a measurable quantity. The idea can be demonstrated within the framework of the *Glauber Model* [16]: A collision is treated on the baryon (nucleon) level, and the colliding nuclei are treated as spheres consisting of nucleons (Figure 1.4). In a geometrical model, the average number of nucleons which participate in a collision, N_{part} , at a given impact parameter, b , is calculated. For a given impact parameter, each of the participating nucleons produces a certain number of particles in multiple collisions with other nucleons. The number of nucleon collisions is given by the mean free path of a nucleon traversing the overlapping area. The total multiplicity can then be derived from the number of nucleon+nucleon collisions, and by the corresponding cross section. Thus, in the *Glauber Model*, the impact parameter, b , is the quantity relating the number of participating nucleons N_{part} , to the number of charged particles, N_{ch} , created in a collision.

1.3. Definition of Kinematic Variables

In this section, some common kinematic variables necessary to describe heavy ion collisions are introduced. In heavy ion physics, the variables are chosen such that they have simple properties when a change of the frame of reference occurs, i.e. under a Lorentz transformation along the beam axis. The produced particles are characterized by their momentum components, i.e. p_x , p_y and p_z , where the longitudinal component, p_z , is always along the beam axis. The total momentum, p , is the absolute value of the momentum components as follows:

$$|p| = \sqrt{p_x^2 + p_y^2 + p_z^2}. \quad (1.3)$$

The transverse momentum, p_{\perp} , i.e. the momentum perpendicular to the beam axis in the x - y -plane, is commonly used. It is given by

$$p_{\perp} = \sqrt{p_x^2 + p_y^2}. \quad (1.4)$$

In addition to the transverse momentum, the transverse mass of a particle with mass, m , is used:

$$m_{\perp} = \sqrt{p_x^2 + p_y^2 + m^2}. \quad (1.5)$$

The azimuthal angle, ϕ , is the angle in the x - y -plane given by

$$\phi = \arctan \frac{p_y}{p_x}. \quad (1.6)$$

The total energy of a particle with momentum, p , and mass, m , is given by

$$E = \sqrt{p_x^2 + p_y^2 + p_z^2 + m^2}. \quad (1.7)$$

1.4. Space and Time Evolution of a Heavy Ion Collision

Unlike p_{\perp} , the momentum component in the beam direction (p_z) is not invariant under a Lorentz transformation along the z -axis. Thus, the *rapidity variable*, y , is commonly used to describe the kinematic condition of a particle. The rapidity of the particle in one Lorentz reference frame is related to that in another, by an additive constant. The rapidity of a particle is defined in terms of its energy, E , and p_z :

$$y = \frac{1}{2} \ln \left(\frac{E + p_z}{E - p_z} \right). \quad (1.8)$$

It is a dimensionless quantity which is related to the ratio between the forward and backward light cone momentum, and can either be positive or negative. In the non-relativistic limit, the rapidity of a particle traveling in the longitudinal direction is equal to the velocity of the particle in units of the speed of light. To characterize the rapidity of a particle, it is necessary to measure the particle's energy, E , and its longitudinal momentum, p_z . In many experiments, it is only possible to measure the angle, θ , of the particle relative to the beam axis. Alternatively, the particle's longitudinal momentum can be measured, whereas its energy can not be (e.g. when the particle cannot be identified). In this case, it is useful to employ the *pseudorapidity variable*, η , defined as:

$$\eta = \ln[\tan(\theta/2)] = \frac{1}{2} \ln \left(\frac{|p| + p_z}{|p| - p_z} \right). \quad (1.9)$$

Comparing Equations 1.8 and 1.9, it can be seen that the *pseudorapidity variable* coincides with the *rapidity variable* for a particle with a small mass $|p| \sim E$.

The center of mass energy, per incident nucleon pair, $\sqrt{s_{NN}}$, of nucleon (a) with energy E_{N_a} and nucleon (b) with energy E_{N_b} in a collision ($a + b$), is given by

$$\sqrt{s_{NN}} = E_{N_a} + E_{N_b} = \sqrt{p_{z_a}^2 + m_{N_a}^2} + \sqrt{p_{z_b}^2 + m_{N_b}^2} \quad (1.10)$$

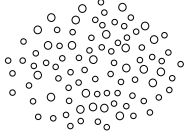
where p_{z_a} and p_{z_b} are the longitudinal momenta of nucleons a and b , measured in the same momentum frame, so that $p_{z_a} = -p_{z_b}$. This variable is commonly used in heavy ion physics and is easily calculated for a symmetric collision system.

1.4. Space and Time Evolution of a Heavy Ion Collision

In Figure 1.5, the current understanding of the time evolution in a heavy ion collision is illustrated [17] [16] [18]. The situation before the collision is depicted in (a). The nuclei are accelerated to relativistic speeds, which is why they appear as Lorentz-contracted disks. In (b), the initial conditions are illustrated. The nuclei collide and interactions at small distances between quarks (partons) of the

1. Introduction

e) Freeze out of Hadrons



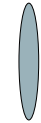
d) Hadronization



c) Chemical equilibrium



b) Initial stage



a) Before the collision

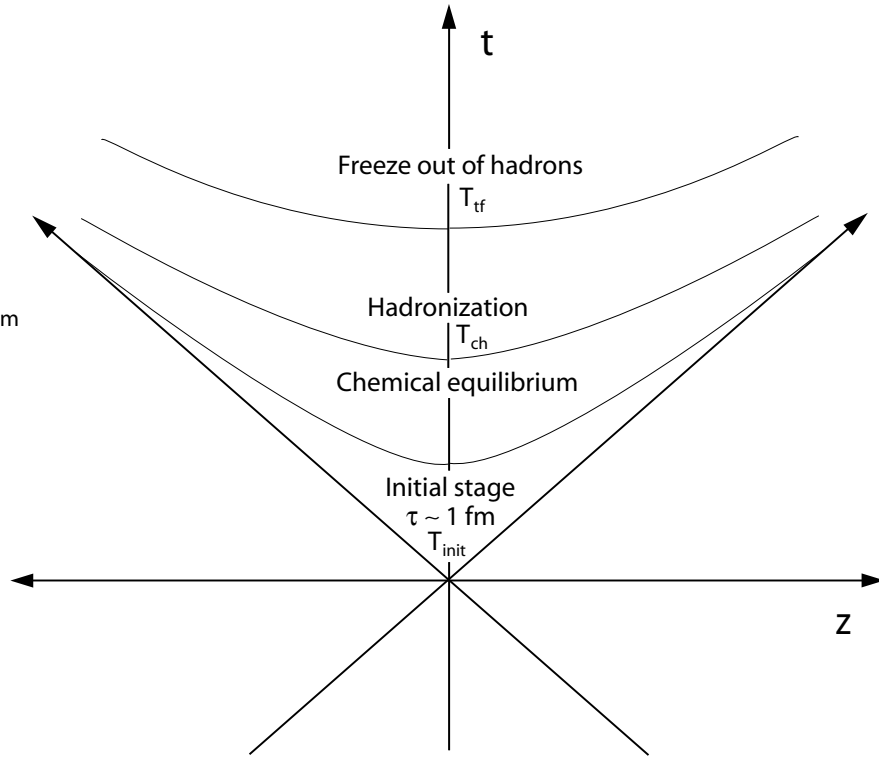
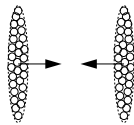


Figure 1.5.: Left: Lorentz-contracted nuclei collide and separate as a function of time. Right: Space-time evolution of a heavy ion collision (z is the beam axis).

participating nucleons take place in a small volume. The outcome of this primordial interaction is usually referred to as a fireball. At this stage, the energy density of the collision is expected to be at its highest. High energy densities, ϵ_{init} , and temperatures, T_{init} , during the initial stage, make conditions favorable for the creation of a state of deconfined hadrons in the fireball, i.e. a QGP. At this stage, hard processes with large momentum transfers occur, which fragment into hadrons having high momenta. In the following stage (c), the fireball, which consists of quark matter, cools down rapidly by expanding under pressure. Particle interactions become much “softer”, and processes at low transverse momentum play a dominant role. With the end of the production of new quarks, the system approaches chemical equilibrium. In (d), the hadronization phase is represented, when all quark matter hadronizes into mesons and baryons at chem-

ical freeze-out, at temperature T_{ch} . In principle, T_{ch} could also be substantially lower than the hadronization temperature, if chemical equilibrium could be maintained in the confined hadronic gas for a while. However, fits to the statistical model (see below and [5] [19]) indicate that this is probably not the case. The fits yield chemical freeze-out temperatures and densities close to the expected phase boundary shown in Figure 1.6. This hypothesis is further supported by dynamical rescattering studies of hadron gas emerging from the hadronization of a QGP, in which relative hadron multiplicities do not change much during the hadronic phase [20] [21]. The fireball in thermal equilibrium expands further and freezes out at temperature, T_{tf} . As the thermal freeze-out stage comes to an end (Figure 1.5 (e)), all hadronic interactions cease, and the emitted particles move freely toward the detectors, where they are measured.

1.4.1. Initial Stage

As already mentioned in Section 1.1, strongly interacting matter can be described using QCD. At sufficiently high momentum transfers, pQCD is applicable. At lower momentum transfers, lattice QCD calculations can be performed. However, it is not a trivial task to model all quark interactions which occur during a heavy ion collision.

Another approach is to employ phenomenological models to determine variables such as temperature and energy density, at different stages of a heavy ion collision. The initial conditions (at temperature T_{init} in Figure 1.5) can be estimated by a global observable, e.g. the number of particles produced in the collision, using the Bjorken formula. Bjorken [17] introduced this expression relating the energy density ϵ_0 at the initial state of a nucleus+nucleus collision, to the number of produced particles around mid-rapidity ($dn/dy|_{y=0}$), the overlapping area A of the two nuclei and the formation time, τ_0 , of the collision, by:

$$\epsilon_0 = \frac{m_t}{\tau_0 A} \frac{dN}{dy} \quad (1.11)$$

Applying this formula to the first results from $^{197}\text{Au} + ^{197}\text{Au}$ collisions at 130 GeV [22], and assuming a production time, $\tau_0 \sim 1 \text{ fm}/c$, the energy density can be estimated to be $3 < \epsilon_0 < 5 \text{ GeV}/\text{fm}^3$ [18]. This is higher than at the highest Super Proton Synchrotron (SPS²) energy of $\sqrt{s_{NN}} = 17.3 \text{ GeV}$, where an energy density of $\epsilon_0 \sim 3.2 \text{ GeV}/\text{fm}^3$ was achieved [23]. Considering the critical temperature, T_c , determined from lattice QCD calculations, these energy densities are high enough to create a QGP during the early stage of the collision.

²CERN, Geneva, Switzerland

1. Introduction

1.4.2. Chemical Equilibrium

Statistical methods can be used to describe interactions of strongly interacting matter in a heavy ion collision, if the system has reached chemical equilibrium. The concept is that the system freezes out from the fireball (with a high number of degrees of freedom) to a hadron gas consisting of statistically weighted components. It expands further - the chemical components remaining unchanged - and finally, it freezes out.

It was discovered [24] that such a system reaches thermodynamical, and subsequently chemical, equilibrium after a relaxation time, τ , (see Figure 1.5 $z = t = 0$) and can be understood in terms of the Gibbs grand canonical ensemble. Assuming chemical equilibrium, properties such as temperature T , pressure P , entropy S , particle number N , and energy E , can be determined (at temperature T_{ch} in Figure 1.5). The energy of such a hadron gas is

$$E(V, S, N) = -PV + TS + \mu_i Q_i \quad (1.12)$$

where V is the total reaction volume of the hadron gas and the chemical potential, μ_i , of species, i , with quantum number, Q_i , results from the conservation of quantum numbers throughout the evolution of the fireball. In the present case, the chemical potential is given by $\mu_i = \mu_B B_i + \mu_S S_i + \mu_I I_i$, where B is the baryon number and is given by the total number of participating nucleons. S is the strangeness number and is zero since nuclei have no initial strangeness and $I = (Z - N)/2$ is the isospin number (where Z is the atomic number and N is the number of neutrons).

The free energy, F , or the thermodynamic potential, of such a hadron gas is then

$$F(V, S, \mu) = E(V, S, Q) - ST - \mu_i Q_i \quad (1.13)$$

Introducing the canonical partition function, Z , F can be written as:

$$F(V, S, \mu) = -T \ln Z(V, T, \mu). \quad (1.14)$$

In the grand canonical ensemble analysis, Z specifies the relative weight Z_i , for each particle species i , in a multi-hadronic mixed gas at temperature T :

$$\ln Z_i(V, T, \mu) = \frac{g_i V}{6\pi^2 T} \int_0^\infty \frac{k^4 dk}{E_i(k) e^{(E_i(k) - \mu_i)/T} \pm 1} \quad (1.15)$$

where g_i is the statistical Landé factor, or degeneracy, of species i , V is the volume shared by all species, $E_i^2(k) = k^2 + m_i^2$ is the total energy of species i , at momentum k . The occurrence of the chemical potential μ_i , in Z_i is the result of adding Lagrange multipliers to the Lagrange density of the system, in order to enforce global conservation of net-baryon numbers that are specific to the total system within the volume V .

1.4. Space and Time Evolution of a Heavy Ion Collision

The pressure, P , conserved charge, Q , and entropy, S , can be derived from the free energy by

$$P = - \left(\frac{\partial F}{\partial V} \right)_{T, \mu} = T \frac{\partial \ln Z}{\partial V}, \quad (1.16)$$

$$S = - \left(\frac{\partial F}{\partial T} \right)_{V, \mu} = \frac{\partial (T \ln Z)}{\partial T}, \quad (1.17)$$

$$Q_i = - \left(\frac{\partial F}{\partial \mu_i} \right)_{V, T} = T \frac{\partial \ln Z}{\partial \mu_i}. \quad (1.18)$$

The particle density, ρ_i , of species i in the medium, is given by

$$\rho_i \equiv \frac{N_i}{V} = \frac{g_i}{2\pi^2} \int \frac{k^2 dk}{e^{(E_i(k) - \mu_i)/T} \pm 1}. \quad (1.19)$$

The density, ρ_i , depends only on the basic parameters V , T and $\mu_i = \mu_B, \mu_S, \mu_I$ where $\mu_S + \mu_I$ can be expressed in terms of μ_B by a set of coupled equations [6]. From ρ_i , the total multiplicity per event, n_i , is determined by multiplying by V . For an analysis of experimental data, a set of measured hadronic multiplicities ($N_i = \rho_i V$) are employed and Equation 1.19 is used to determine the remaining parameters - V , T and μ_B - in a fit. T and μ_B are usually determined in the first step, while maintaining V at a fixed value. V is then fit in a second step. Applying this formula to hadronic multiplicities from heavy ion collisions at different energies, the systematics of hadronic chemical freeze-out in the T - μ_B -plane, as shown in Figure 1.6, emerge.

The procedure to determine T, μ_i is less complex in the special case of anti-particle to particle multiplicity ratios (\bar{N}_i/N_i). Both Bose and Fermi statistics gives rise to the ± 1 term in Equation 1.19. For a simple approximation in the following example, Boltzmann classical statistics are employed so that the ± 1 term in Eq.1.19 can be neglected.

The measured ratio of anti-particle to particle mean multiplicity can be expressed as

$$\langle \bar{N}_i \rangle / \langle N_i \rangle = \bar{\rho}_i V / \rho_i V = \bar{\rho}_i / \rho_i \quad (1.20)$$

in which V drops out. Considering the ratio of the two integrals (Eq.1.19), shows that g_i, k and $E_i(k)$ drop out because statistics and phase space are identical for anti-particles and particles. This yields:

$$\langle \bar{N}_i \rangle / \langle N_i \rangle = \bar{\rho}_i / \rho_i = e^{(-\mu_i + \bar{\mu}_i)/T} = e^{-2\mu_i/T}. \quad (1.21)$$

If this is done for several ratios in combination (e.g. $\bar{p}/p, K^-/K^+, \bar{\Lambda}/\Lambda, \bar{\Omega}/\Omega$), a set of equations is found from which the maximum likelihood, T, μ_B , combination is derived. In a second step, V is determined by fitting Equation 1.19 to the pion multiplicity, $\langle N_\pi \rangle$, with known T and μ_B .

1. Introduction

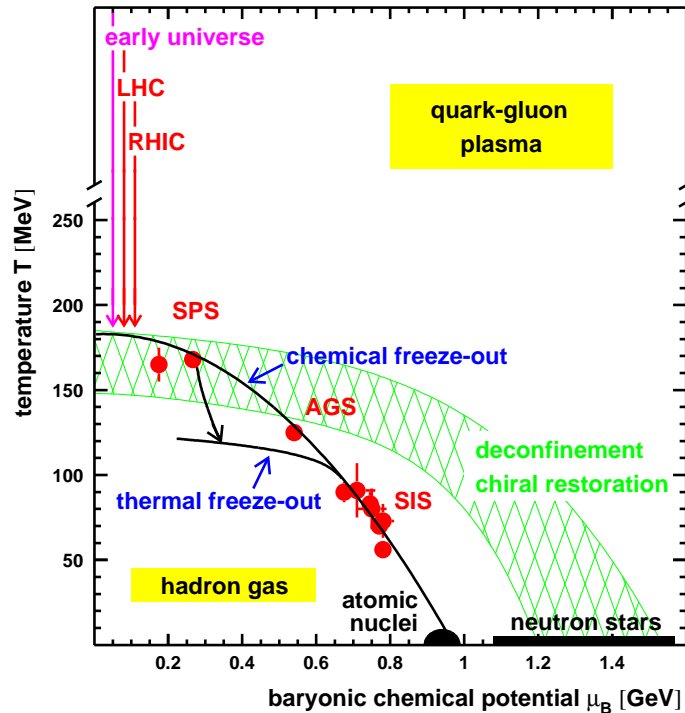


Figure 1.6.: Phase diagram of hadronic matter. Data points are obtained within the statistical model framework [19].

If only the anti-proton (\bar{p}) to proton (p) ratio is considered, and only baryon number B conservation is taken into account, the corresponding chemical potential, μ_B , Equation 1.21 becomes:

$$\bar{p}/p = \langle N_{\bar{p}} \rangle / \langle N_p \rangle = e^{-2\mu_B/T}. \quad (1.22)$$

This shows the direct dependence of the anti-proton to proton ratio on the temperature, T , and the baryon chemical potential, μ_B .

Figure 1.6 shows a summary of the T and μ_B values of a statistical analysis. The dependency of the temperature T , on the chemical potential μ_B , from various collision energies are shown. At SPS energies, chemical freeze-out occurs very close to the drawn phase transition boundary.

1.4.3. Thermal Freeze-Out

Looking at the particles coming from the fireball at thermal freeze-out, and assuming thermal equilibrium (at temperature T_{tf} in Figure 1.5), particle spectra taken within a narrow rapidity interval can be fit by a classical Boltzmann expo-

nential:

$$\frac{dN}{dm_{\perp}} \propto m_{\perp} e^{-m_{\perp}/T} \quad (1.23)$$

where the inverse slope parameter T is equal to the temperature T_{tf} in Figure 1.5. Thus, the temperature at thermal freeze-out is determined by fitting this formula to m_{\perp} spectra of a measured hadron species. This approach assumes a static fireball. However, it has been shown that the real situation is rather that of an expanding fireball, and thus the determined temperature, T , obtained from the fit, consists of two components $T = T_{tf} + m\beta_t^2$. T_{tf} is the real temperature of the fireball at freeze-out and an additional flow term consists of the mass, m , of the particle and the expansion velocity β_t .

In conclusion, the physical properties of the three different stages during the evolution of a heavy ion collision, as depicted in Figure 1.5, can be obtained using the approaches described in Sections 1.4.1, 1.4.2 and in the present section.

1.5. Anti-Proton to Proton Ratio

The production of anti-protons (\bar{p}) and protons (p) at mid-rapidity is customarily described by two processes: 1) Production of an anti-proton and a proton during the hadronization stage of the fireball 2) Transport of incident protons from beam rapidity $y_b = 5.36$, at the full RHIC energy, towards mid-rapidity. The ratio of anti-protons to protons is indicative of the number of net protons $p_{net} = p - \bar{p}$ in a heavy ion collision.

Measurements by NA49 [25] of the anti-proton to proton ratio from $^{208}\text{Pb}+^{208}\text{Pb}$ collisions at SPS beam energies of 40, 80, 160 GeV, resulting in center-of-mass energies of $\sqrt{s_{NN}} = 8.9, 10.4, 17.3$ GeV are shown in Figure 1.7. The ratios are found to be $\bar{p}/p = 7.51 \cdot 10^{-3}, 0.03, 0.065$ respectively. A strong dependency of the ratio on the center of mass energy is observed. However, even at the top SPS energy, proton multiplicities dominate by far (factor ~ 15).

The corresponding statistical model parameters where these ratios have been used, along with other particle ratios, are shown in Table 1.1.

Energy $\sqrt{s_{NN}}$	T (MeV)	μ_B (MeV)
8.9	148 ± 2	377 ± 7
10.4	155 ± 4	294 ± 15
17.3	158 ± 2	244.5 ± 4.7

Table 1.1.: Statistical model parameters from the analysis of hadron yields at various SPS energies [26] [27].

1. Introduction

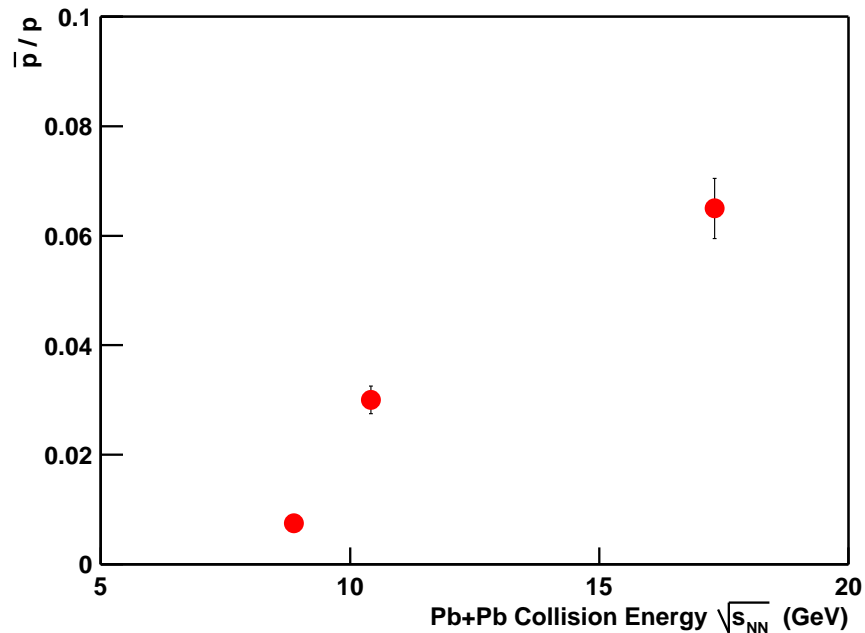


Figure 1.7.: Anti-proton to proton ratio at SPS energies [25].

The values for temperature, T , and baryon chemical potential, μ_B , are close to the phase boundary of Figure 1.6, especially at the top energy of $\sqrt{s_{NN}} = 17.3$ GeV. The interpretation of the statistical analysis of the fireball in terms of a hadron gas, combined with the observed strangeness enhancement, and J/ψ suppression, is the strongest argument for the creation of a “little big bang” in heavy ion collisions of the SPS program [28].

Thus, the motivation for the analysis of the anti-proton to proton ratio (\bar{p}/p) from $^{197}\text{Au} + ^{197}\text{Au}$ collisions at the top RHIC energy of $\sqrt{s_{NN}} = 200$ GeV is driven by two arguments: 1) To determine temperature and baryon-chemical potential in the framework of a statistical model. 2) To study the dependency of the anti-proton to proton ratio at high transverse momentum (p_{\perp}), since at the high momentum transfers experimentally accessible at RHIC energies, the data can be compared with pQCD calculations.

2. The RHIC Collider

2.1. A Brief Description

The relativistic heavy ion collider (RHIC) [30] [29] is a hadron accelerator and collider consisting of two independent, concentric storage rings with a circumference of 3.8 km each. The main research objective of RHIC is to study collisions of heavy ion beams of varying kinetic energies. RHIC's capability to provide a high collision rate for a wide range of nuclei at various energies is a must for the investigation of interesting physics phenomena. Heavy ion beams can be accelerated and stored in the two independent rings for up to 10 hours. The collider is designed to accelerate a range of nuclei, with the heaviest being gold and the lightest being hydrogen. Furthermore, RHIC is designed to allow asymmetric operation where, e.g. beams of deuterons collide with a gold beam. In the second year of RHIC operation (2001), the collider accelerated gold ($^{197}\text{Au}^{79+}$) up to a kinetic energy of 100 GeV/nucleon, leading to a center of mass energy of 40 TeV in a head-on $^{197}\text{Au} + ^{197}\text{Au}$ collision. This gives a center of mass energy per incident nucleon pair of $\sqrt{s_{NN}} = 200$ GeV. This is more than one order of magnitude higher than the head-on $^{208}\text{Pb} + ^{208}\text{Pb}$ fixed target collisions at the Super Proton Synchrotron (SPS) at CERN, where a center of mass energy of $\sqrt{s_{NN}} = 17.3$ GeV was achieved.

RHIC is also capable of accelerating lighter ions like oxygen, silicon, copper and iodine ($^{16}\text{O}^{8+}$, $^{28}\text{Si}^{14+}$, $^{63}\text{Cu}^{29+}$, $^{127}\text{I}^{53+}$). Due to their higher charge-to-mass ratio, these lighter ions can reach a higher momentum during acceleration, which results in a higher kinetic energy of up to 125 GeV/nucleon.

The collider is also designed to accelerate protons (p) up to kinetic energies of 250 GeV/nucleon resulting in p+p collisions with a center of mass energy of $\sqrt{s_{NN}} = 500$ GeV. Along with symmetric collision systems (p+p) and asymmetric collision systems ($^2\text{d} + ^{197}\text{Au}$) there is special interest in collisions of proton beams with different polarizations, with the goal to study the spin structure of the proton [31] [32]. Collisions of p+p with a center of mass energy of $\sqrt{s_{NN}} = 200$ GeV per incident nucleon pair took place during the second year of RHIC operation.

The ion beam consists of bunches of ionized nuclei which are accelerated around

2. The RHIC Collider

the collider until they reach their maximum energy. They are then stored, circulating at almost the speed of light, at 5 intersection regions the individual ion bunches collide. The collision rate R , is related to the luminosity L . The luminosity for symmetric operation of the collider is defined according to [33]:

$$L = \frac{3f_{rev} \gamma}{2} \frac{N_b N^2}{\epsilon \beta^*} \quad (2.1)$$

where $f_{rev} \sim 80$ kHz is the revolution frequency, γ the kinetic energy of the stored ions, N_b the number of ions per bunch and N the number of bunches. ϵ is the transverse emittance, β^* is the intersection region beta-functions at store. The product ($\epsilon\beta^*$) gives the cross sectional area, A , of the overlap between the two colliding beams of particles. RHIC was designed for an average luminosity of $L \sim 2 \times 10^{26} \text{ cm}^{-2} \text{ s}^{-1}$ operating in $^{197}\text{Au} + ^{197}\text{Au}$ mode at a kinetic energy of 100 GeV/nucleon. The luminosity increases for lighter species. In p+p mode the luminosity is expected to reach $L \sim 1 \times 10^{31} \text{ cm}^{-2}\text{s}^{-1}$. An important feature of RHIC operation is the utilization of short bunches of nuclei which are made to collide head-on. This enhances the luminosity L and keeps both the average current and the stored energy in the rings low.

2.2. Injection into RHIC

Figure 2.1 illustrates the RHIC layout. For RHIC operation, a chain of injector accelerators (TANDEM and LINAC), a fast cycling synchrotron (BOOSTER) and the alternating gradient synchrotron (AGS) are required. For heavy ion operation, atoms are gradually ionized as they are accelerated. By the time they reach the RHIC injection energy they are fully ionized.

The following accelerator chain is used for operating in symmetric $^{197}\text{Au} + ^{197}\text{Au}$ collision mode [34] [29]: A TANDEM Van de Graf accelerator is used for the initial acceleration. Singly ionized gold atoms (Au^-) from a sputter ion source are accelerated from ground to +15 MeV potential at the terminal of the TANDEM. The pulsed beam then passes through a $3 \mu\text{g}/\text{cm}^2$ carbon stripper foil, yielding stripped ions in a Au^{+12} state. The stripped Au^{+12} ions are then accelerated back to ground potential, where the 530 ms beam pulse is ionized to Au^{+32} by another carbon stripper foil at the end of the TANDEM. At this stage the beam has an energy of approximately 1 MeV/nucleon. This beam is transported for about 680 m in the heavy ion transfer line (HITL) to reach the BOOSTER. The BOOSTER is designed to inject high intensity beams of heavy ions and protons into the AGS. It requires short, highly charged beam pulses with approximately 1 GeV/nucleon. Without the BOOSTER, the AGS could accelerate ions up to silicon ($^{28}\text{Si}^{14+}$). Due to its superior vacuum, the BOOSTER makes it possible for the AGS to accelerate and deliver heavy ions up to gold ($^{197}\text{Au}^{77+}$). After the

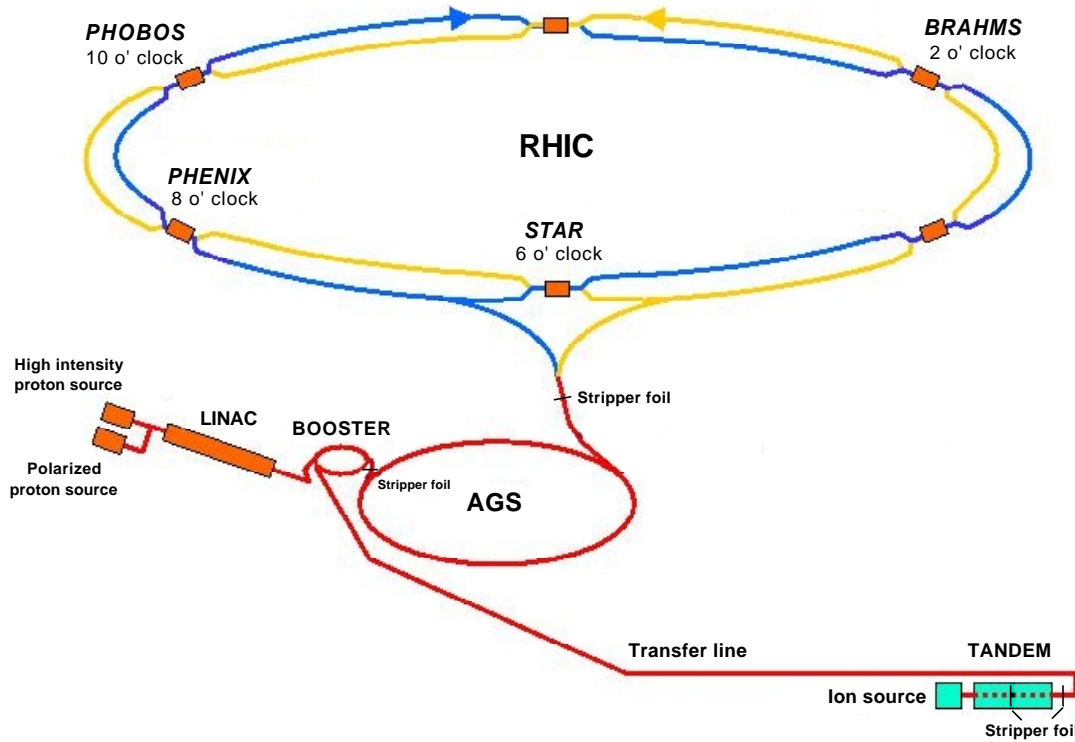


Figure 2.1.: Layout of the RHIC collider and its injector accelerators [33].

BOOSTER has accelerated the gold beam to about 100 MeV/nucleon, the beam passes through another stripper foil, which produces a beam of $^{197}\text{Au}^{77+}$ ions. This beam is then transferred to the AGS. During acceleration in the AGS, the beam bunches from the BOOSTER merge into one bunch, giving the required intensity of $\sim 1 \times 10^9$ gold ions per bunch. This bunch is accelerated to the RHIC injection kinetic energy of ~ 9 GeV/nucleon, when it is transferred to the RHIC rings using the AGS to RHIC transfer line. At the beginning of the transfer line, bunch ions are ionized to bare gold ions ($^{197}\text{Au}^{79+}$) by another stripper foil. The injection of the bunches into the RHIC rings is on a single-bunch basis.

In the case of symmetric proton operation, an ion source delivers protons or polarized protons, which are accelerated by the LINAC accelerator, and subsequently injected into the BOOSTER. The LINAC uses a radio-frequency electromagnetic field generated by a pre-injector, and nine accelerator cavities which accelerate the protons to a kinetic energy of 200 MeV at a maximum beam current of 35 mA. The protons are injected into the BOOSTER, and are pre-accelerated before they are transferred to the AGS. In the AGS, the protons are accelerated up to a kinetic energy of ~ 23 GeV. The injection into RHIC is similar to the heavy-ion procedure, except that stripper foils are not used.

2.3. Collider Design

The RHIC collider consists of two independent rings (i.e. blue and yellow) of superconducting magnets. The rings are enclosed in a tunnel which lies ~ 3.6 m underground. In the center of each ring is a beam pipe along which the ion beam travels. The ion beams travel in clockwise and counterclockwise directions in the blue and yellow rings, respectively. A vacuum of 10^{-11} bar is maintained in the beam pipes in order to eliminate interaction of the traversing ions with gas molecules. The collider consists of alternating straight and curved sections. In the curved sections, dipole magnets steer the ion beam along the curvature of the pipes. In the straight sections, quadrupole magnets guide the beam along the beam axis. All RHIC magnets are superconductive magnets. They are cooled by supercritical helium to maintain an operational temperature of < 4.6 K. Radio cavities located in the straight sections of the rings generate a high frequency electromagnetic field which is used either to accelerate or to store the bunches of particles at each pass around the ring. In the middle of each straight section is an intersection region where the beam pipes cross, allowing the particle beams to collide. At the six intersection regions, where the experimental areas are located, the trajectories of the incoming and outgoing beams merge. Dipole magnets are used to steer the beams so that they travel on the same trajectory for approximately 19 m. In the middle of this distance the bunches of nuclei collide, resulting in an interaction diamond of less than a meter (see below). After merging, another set of dipole magnets is used to separate the outgoing beams so that they return to their respective beam pipes. To fill the collider rings, ion bunches are transferred from the AGS and injected into the RHIC rings in a single-bunch mode, as described in Section 2.2. In acceleration mode the bunches are captured by the two radio cavities (Fig. 2.2b), which are operated at ~ 28 MHz. This frequency corresponds to a harmonic number of 360 e.g. the circumference of the collider rings is subdivided into 360 individual buckets with a length of 10.5 m, where bunches of ions can be placed. For the first 2 years of RHIC operation, the collider was run mainly in a mode where every 6th bucket was filled. This led to a total of 60 bunches in each ring. The 60 bunches are injected from the AGS into each collider ring in a bunch-to-bucket fashion, where the AGS extraction system transfers one single bunch made up of four AGS bunches into one of the collider rings. This cycle is repeated 2×15 times in order to fill each collider ring with 60 bunches. Filling both rings takes ~ 1 minute¹. After the bunches are injected into the rings, they are captured by the rising slope of the radio cavity electromagnetic field. Since the ions in the bunches are spread in velocity, the slow bunch-ions are accelerated by the rising slope of the radio frequency electromagnetic field while the faster bunch-ions are slowed down. The ions are accelerated to a speed

¹In reality, only 56 bunches were injected into the rings in order to leave a time window available for quality control purposes.



Figure 2.2.: a) The two RHIC rings, consisting of hundreds of magnets, inside the tunnel. b) One of the two radio frequency cavities [30].

that is close to the speed of light. After reaching that speed, only the energy of the ions is increased by the radio frequency electromagnetic field, so that ions with higher energy are less deflected by the dipole magnets. This makes them travel a longer path length, and introduces a delay relative to the ions with a lower energy. In this case an ion bucket must be on the falling slope of the radio frequency electromagnetic field, so that the more energetic (faster) ions are slowed down and the less energetic (slower) ions are accelerated. The energy at which this takes place is called the transition energy. At the transition energy, interaction between bunch ions can cause beam instabilities. Pulsed quadrupole magnets fed by fast power supplies are used to quickly increase the energy of the beam ions to a value above the transition energy. For gold ions the transition energy is 22.9 GeV/nucleon. All ions, except protons, are injected below the transition energy and have to be accelerated through the transition to reach the maximum energy. When the bunches are accelerated to maximum energy - a process which takes about another minute - the collider switches from the 28 MHz acceleration mode to the 200 MHz storage mode. The harmonic number of the storage mode is $h = 360 \times 7 = 2520$ resulting in a bucket length of 1.52 m. This high frequency enables the beam to be stored in short bunches having a length of ~ 25 cm [29]. Such a short bunch length results in a r.m.s longitudinal collision vertex distribution of ~ 18 cm at the six intersection regions where the counter-rotating beams collide. At each experiment, 2 zero degree calorimeters (ZDC) are installed. The ZDCs detect spectator neutrons emitted, within a cone along both beam directions, from the collision vertex. The coincidence signal of both ZDCs is used as a common trigger by the experiments (see Section 3.5.1).

2.4. Experiments at RHIC

In five of RHIC's six experimental areas (Figure 2.1), detectors are installed to measure the reaction products of the colliding ion beams:

The Broad Range Hadron Magnetic Spectrometer (BRAHMS) [35] is designed to measure charged hadrons over a wide range of rapidity and transverse momentum. The experiment consists of two spectrometer arms (see Figure 2.3a), with one arm located along the beam axis, and the other perpendicular to it. The fixed experiment is capable of covering only a small acceptance angle. However, the arms can be rotated with respect to the intersection region, thereby permitting a large acceptance angle to be scanned. Charged hadrons can be identified and the energy and momentum can be precisely determined.

PHOBOS [36], consists of a multiplicity array and a two arm spectrometer around the beam pipe (Figure 2.3b). Silicon pixel and silicon strip detectors are employed in this experiment. The multiplicity array covers a wide acceptance angle with a fine granularity in pseudorapidity and azimuth. Charged hadron identification and momentum determination are performed by the two arm spectrometer in a magnetic field.

The STAR [37] (Solenoidal Tracker at RHIC) experiment's main detector is a large volume time projection chamber (TPC) inside a $B = 0.5$ Tesla solenoid. With the TPC and the silicon vertex detector (SVT), high precision momentum reconstruction and particle identification can be performed. Energy of leptons can be determined by the electromagnetic calorimeter (EMC). Additional particle identification can be carried out with the ring imaging Čerenkov (RICH) detector and the time of flight (ToF) detectors. Due to the STAR's wide and continuous coverage, a large fraction of all produced hadrons created in one event of a heavy ion collision can be measured. This makes the experiment capable of analyzing events on an *event-by-event* basis. This experiment is described in greater detail in Chapter 3.

The main focus of the PHENIX experiment [38], is the detection of leptons and photons produced in a heavy ion collision. In this case, a drift chamber is placed inside a magnet at mid-rapidity in order to determine particle momenta. Additional detectors such as an EMC, ToF and a RICH detector are installed around the drift chamber in order to provide particle identification. With some of these detectors, hadron detection is also possible. Muon tracking chambers are installed in the forward direction for exclusive muon identification.

While BRAHMS, PHOBOS, STAR and PHENIX are designed with a view to studying collisions of heavy nuclei, as well as p+p collisions pp2pp is an experiment designed to study p+p elastic scattering using only polarized and unpolarized proton beams [39].

2.4. Experiments at RHIC

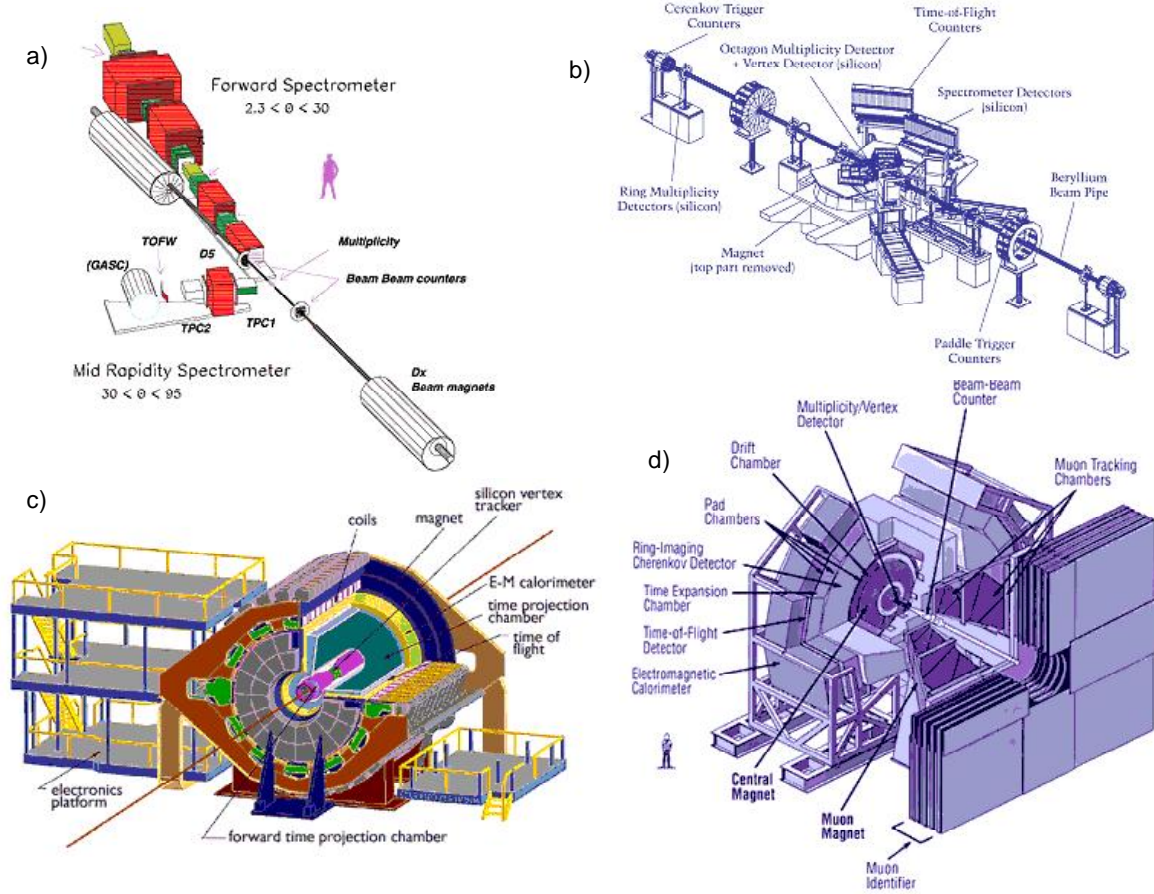


Figure 2.3.: Experiments at RHIC: a) BRAHMS. b) PHOBOS c) STAR
 d) PHENIX [30].

2.5. Commissioning and Operation of RHIC

The commissioning of the RHIC collider began in May 2000. This was followed by a short physics production run. In August of the following year, the second RHIC run started. In the next two sections, an account of the challenges encountered and surmounted during each of these runs is given.

2.5.1. First Year of RHIC Operation

The first time collisions were produced was during the RHIC commissioning run in 2000. After cooling down the superconducting collider magnets to < 4.6 K, what takes approximately 4 weeks, the objective was to accelerate and collide gold ions with an energy of up to 65 GeV/nucleon in both rings. During several attempts, the beam was lost and could not be steered. Another attempt was made at 30 GeV/nucleon, and it was possible to store the beams for about an hour, on several occasions. Steering of the beam was more successful, and on June 12th, 2000 at 9:12 p.m., the first RHIC collisions were detected by the STAR experiment. These collisions were displayed on an on-line event display (see Section 4.3.5) in the STAR control room. The on-line reconstruction of the Level-3 Trigger (see Section 3.8, 4.3) was used to display the measured clusters in the time projection chamber (TPC, see Chapter 3.4.1) along the reconstructed trajectories of the hadrons produced in the event of a $^{197}\text{Au} + ^{197}\text{Au}$ collision at $\sqrt{s_{NN}} = 60$ GeV (see Figure 2.4). In this figure, dots correspond to TPC clusters, lines illustrate the reconstructed trajectories of charged particles. All tracks appear as straight lines, since the STAR experiment was operated without a magnetic field at that time. The on-line reconstruction was also used to determine the vertex position of the events, and to estimate the number of particle trajectories coming from the primary vertex (Figure 2.5). The accelerator was operated in the 30 GeV/nucleon $^{197}\text{Au} + ^{197}\text{Au}$ beam mode until collisions at all six experiments were detected. A subsequent attempt to collide gold beams at 65 GeV/nucleon was successful, and collisions at 4 experiments were produced at a low rate.

At that stage, the collider commissioning phase ended and the physics production run started on August 24th and continued until September 4th. Figure 2.6a shows the ZDC coincidence rate evolution versus time at the STAR experiment during the 2000 run. The ZDC coincidence rate is indicative of the collision rate (as discussed in Section 3.5.1). The rate went up to ~ 180 Hz during the end of the production phase. Figure 2.6b shows the collision rate of a good store at the STAR experiment. The collision rate of ~ 40 Hz at the beginning of the run falls exponentially. After 7 hours the collision rate decreases to ~ 20 Hz. During the first RHIC run, the 200 MHz radio frequency system was not available. This

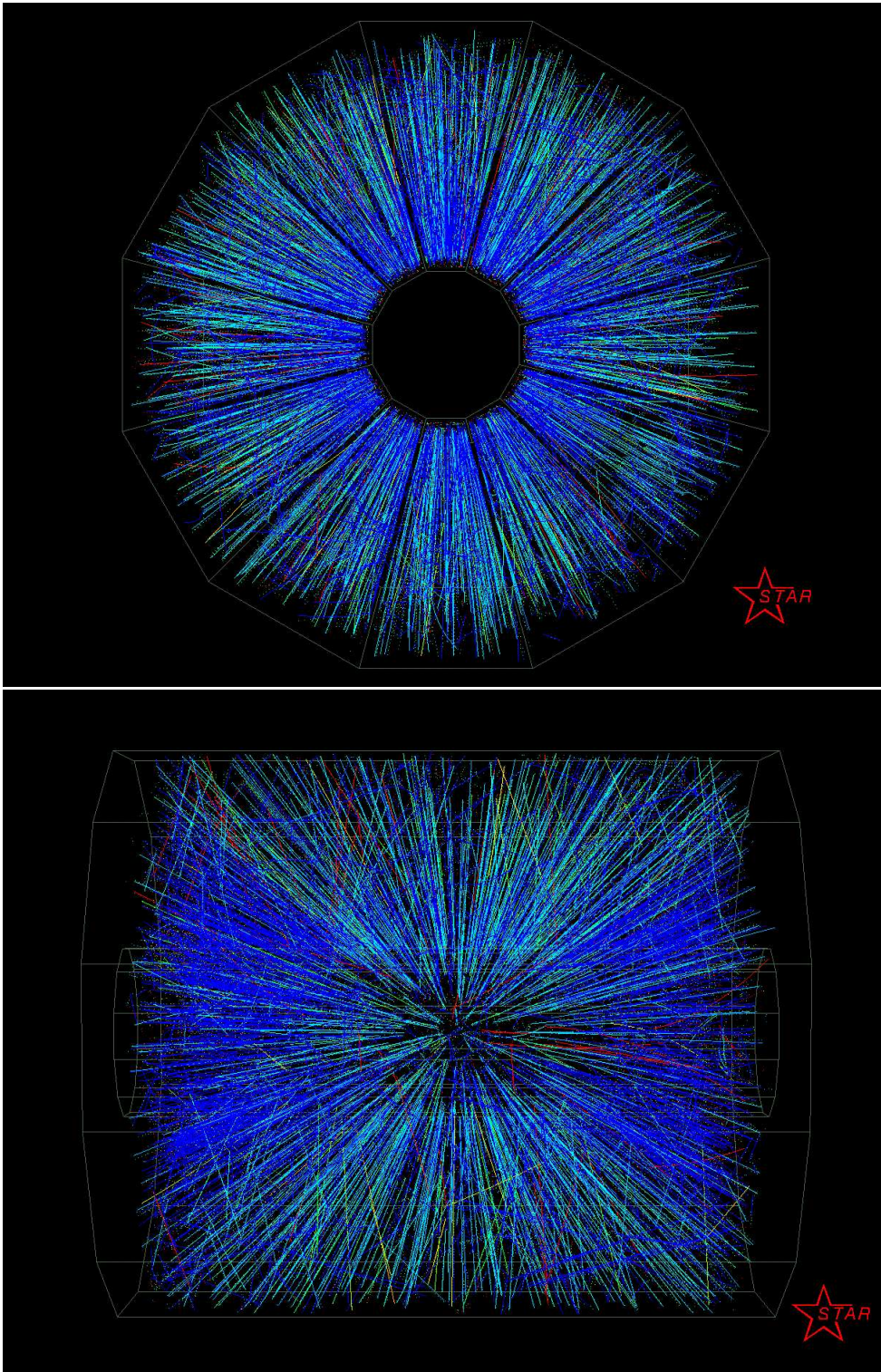


Figure 2.4.: Front (top) and side (bottom) view of the first collision of two gold nuclei at RHIC, observed by the STAR experiment on the on-line event display (9.12 p.m., 12th June 2000) [40].

2. The RHIC Collider

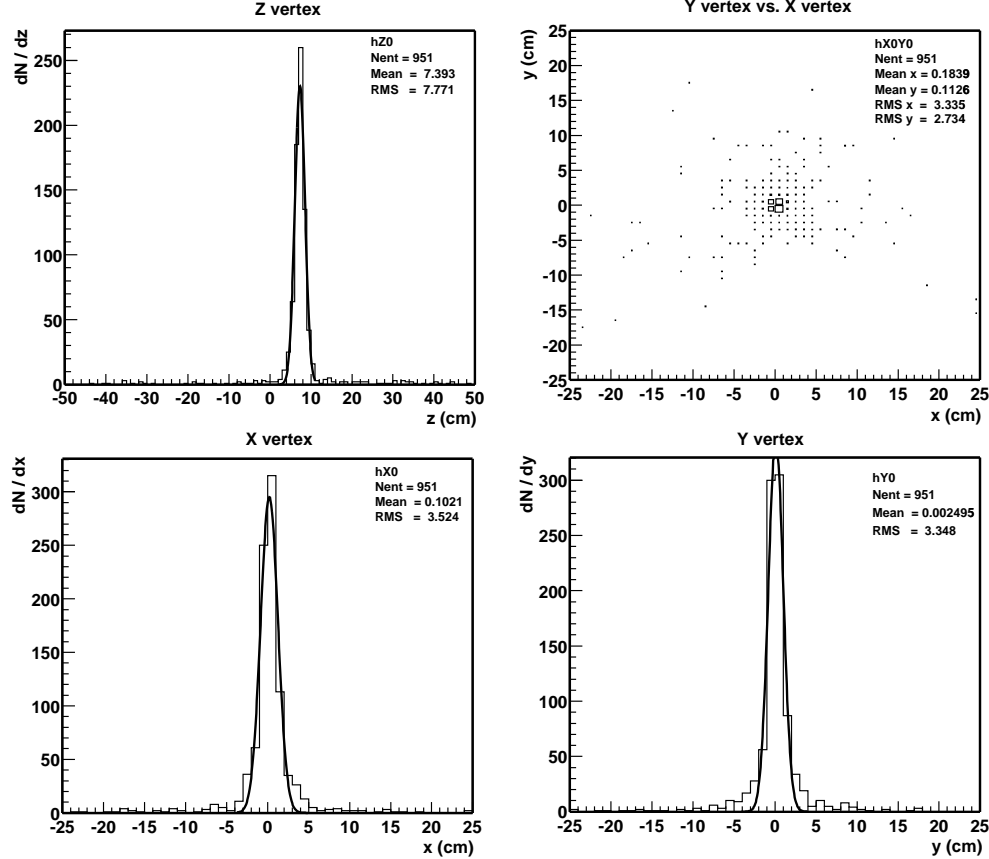


Figure 2.5.: Vertex determination for first collisions, using Level-3 trigger on-line reconstruction. 951 tracks were detected in the TPC with at least 23 hits per track and a $dca < 5$ cm to the event vertex. These tracks were considered as primaries and extrapolated back to their origin. The distribution in x , y , z and x versus y are shown. The distributions were fit by a Gaussian to determine the event vertex position: $x = 0.2 \pm 0.04$ cm, $y = 0.09 \pm 0.01$ cm, $z = 7.31 \pm 0.04$ cm.

resulted in long buckets with long bunches of gold ions. Although the beam loss at transition was moderate due to the low luminosity, the intensity of the stored bunches decreased dramatically during the store. This was caused by beam loss and beam-beam interactions [33]. Due to longer bunch length at a collider frequency of 28 MHz, the standard deviation of the collision vertex distribution was $\sigma \sim 100$ cm [41]. Due to displaced vertices, collisions with vertices at the outer boundaries of the experiment's acceptance occurred. These events were rejected, since only a fraction of the produced particles could be measured by the detectors in the different experiments.

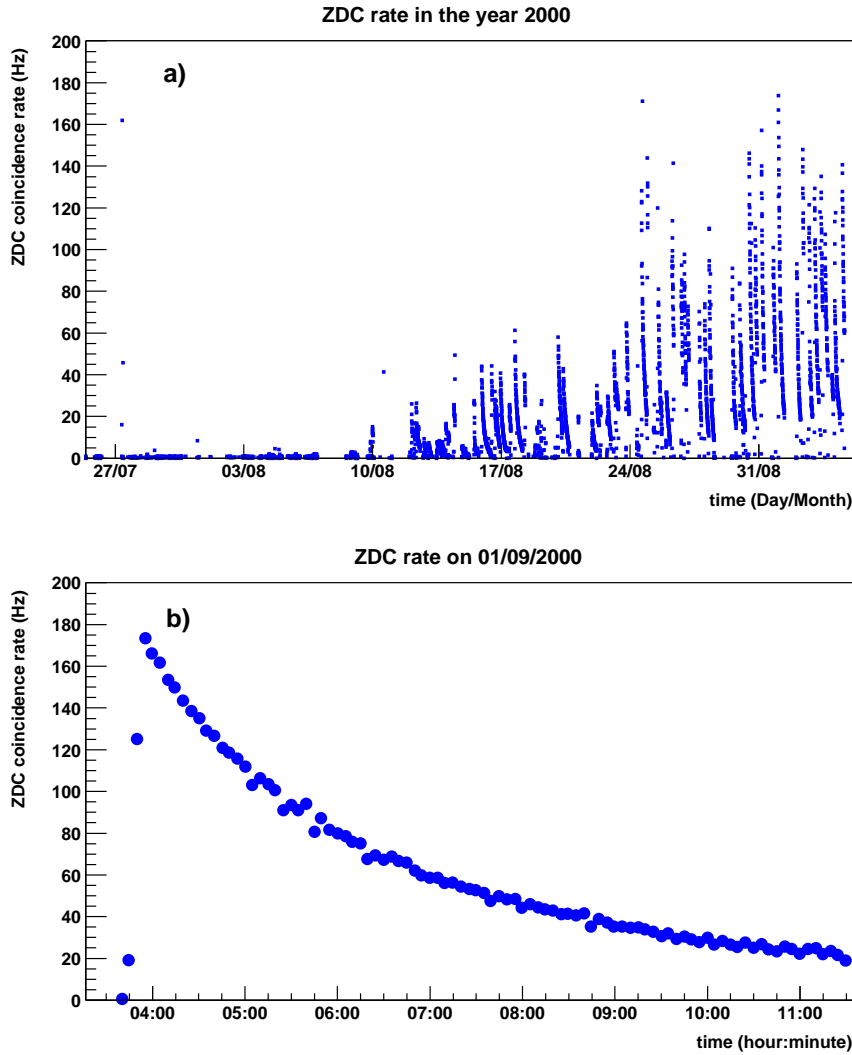


Figure 2.6.: a) ZDC coincidence rate (collision rate) at the STAR experiment during the 2000 run. b) Collision rate of a store at the end of the 2000 run.

2.5.2. Second Year of RHIC Operation

In August 2001, the second RHIC run started. Gold was accelerated in both rings to the maximum RHIC energy of 100 GeV/nucleon, resulting in collisions with a center of mass energy of $\sqrt{s_{NN}} = 200$ GeV. On August 12th at approximately 11 p.m., the first collisions at the full RHIC energy were seen by STAR (Fig. 2.7).

2. The RHIC Collider

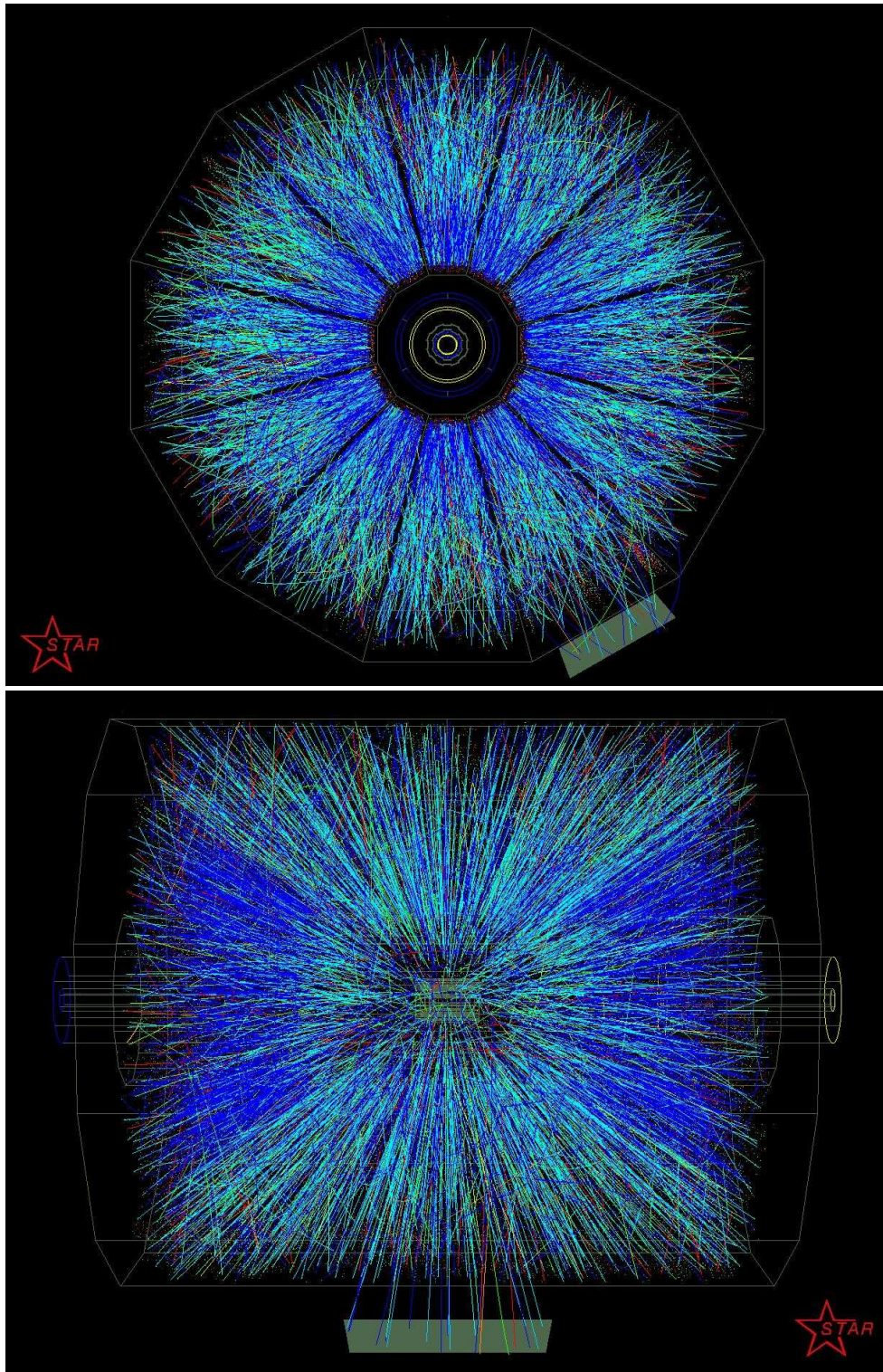


Figure 2.7.: Front (top) and side (bottom) view of the first 200 GeV $^{197}\text{Au} + ^{197}\text{Au}$ collision at RHIC. The grey rectangle which can be seen in both views is a schematic representation of the RICH detector (see Section 3.4.2) [40].

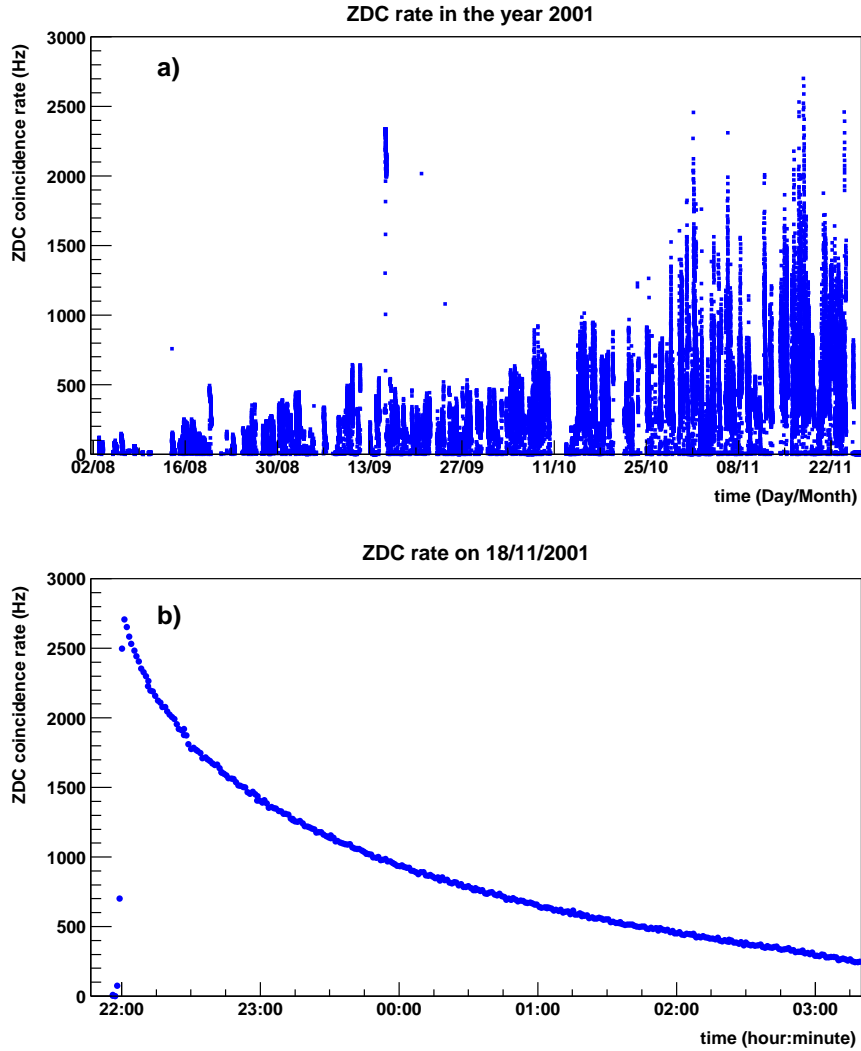


Figure 2.8.: a) ZDC coincidence rate (collision rate) at the STAR experiment during the 2001 $^{197}\text{Au} + ^{197}\text{Au}$ run and b) of a typical store at the end of the run.

From September 18th, the 200 MHz radio frequency was available and resulted in a narrower longitudinal collision vertex distribution and therefore an increased collision rate (Figure 2.8a) at the experiments. Figure 2.8b shows the decrease of the collision rate during the lapse of a store. During the first 15 minutes of the store the collision rate reached design luminosity, and subsequently decreased exponentially. Although the decrease was not as much as in the 2000 run, high collision rates could only be achieved at the very beginning of the stores. The gold operation mode ended on November 25th, and from then until February, 2003, RHIC was operated in proton mode. At the start, collisions of unpolarized

2. The RHIC Collider

proton beams with 100 GeV/nucleon ($\sqrt{s_{NN}} = 200$ GeV) were produced. Later, polarized proton beams were generated. Figure 2.9 shows a p+p collision in the STAR detector. The number of produced particles in a p+p collision is significantly lower compared to a $^{197}\text{Au} + ^{197}\text{Au}$ collision (Figure 2.7). The beam luminosity in p+p operation mode is much higher and exceeds a collision rate of 1.5 kHz [42]. This high collision rate can cause pile-up events in the TPC of the STAR experiment. This has repercussions for the track reconstruction procedure. In a pile-up event, the track of at least one other event, in addition to the triggered one, is recorded during read out of the TPC.

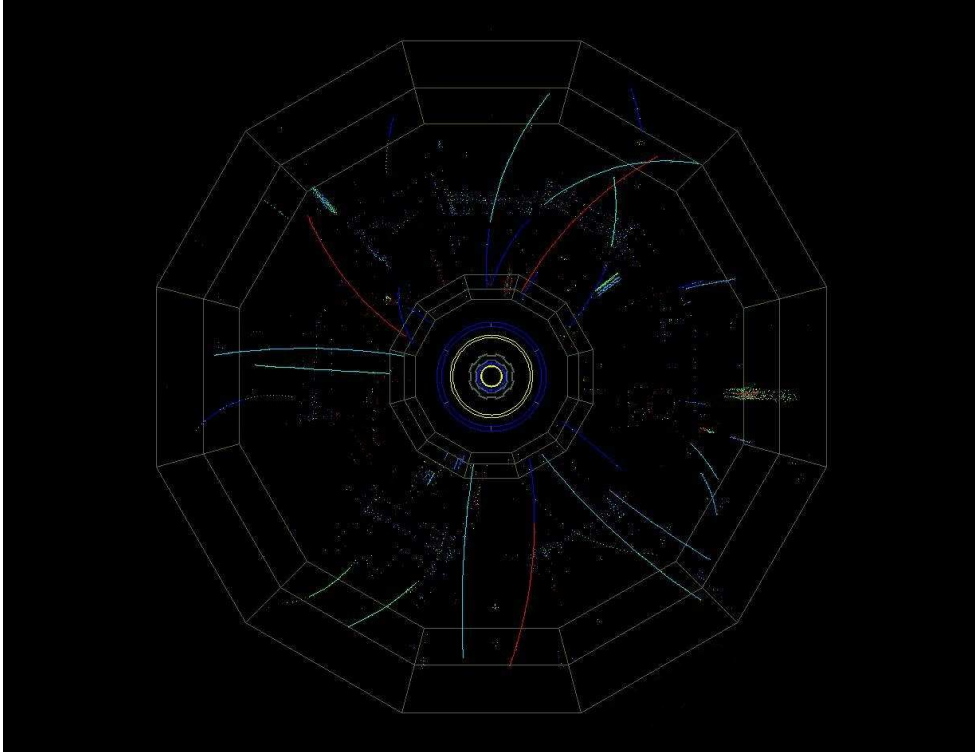


Figure 2.9.: Front view of a 200 GeV p+p collision

3. The STAR Experiment

The Solenoidal Tracker at RHIC (STAR) experiment is located at the 6 o'clock interaction region of the RHIC collider (see Figure 2.1). It consists of several detectors, covering different regions of rapidity, azimuth and momentum. Figure 3.1 shows a cross section of the main components of the experiment.

The experiment was designed with a view to measuring and identifying charged particles produced in heavy ion collisions. A huge number of charged particles are produced in central $^{197}\text{Au} + ^{197}\text{Au}$ collisions, especially around the mid-rapidity region. The STAR design specifications were such that the experiment would be capable of measuring central $^{197}\text{Au} + ^{197}\text{Au}$ collisions at the maximum RHIC energy. The measurement of smaller systems such as $^2\text{d} + ^{197}\text{Au}$ and p+p collisions can also be performed. Due to STAR's wide and continuous coverage, a large fraction of all hadrons produced in a heavy ion collision event can be detected.

3.1. STAR Instrumentation Overview

The detectors which were installed at the STAR experiment in 2001 are depicted in Figure 3.2. The main detector is a large volume TPC housed inside the STAR magnet, generating a solenoidal magnetic field, with a maximum field strength of $B = 0.5$ T. The direction of the magnetic field lines are parallel to the beam axis. The TPC is filled with a detector gas. Charged particles which are produced in collisions between nuclei leave clusters of secondary electrons along their helical trajectories in the TPC detector gas. In the reconstruction process, the track finder connects the clusters to reconstruct the particle trajectories, assuming a helical model. The particle momentum can then be determined by measuring the radius and dip angle (angle between the beam line and the trajectory in the z - y -plane, see Figure 3.1) of the reconstructed particle trajectories. Particle momenta from ~ 0.1 GeV/ c up to a few GeV/ c can be measured. Particles can be identified in the TPC within the momentum range of $0.3 < p < 1.0$ GeV/ c at $B = 0.5$ T, by measuring the specific ionization of the TPC gas by a charged particle (dE/dx). The x - y -plane is the azimuthal plane and the TPC covers all

3. The STAR Experiment

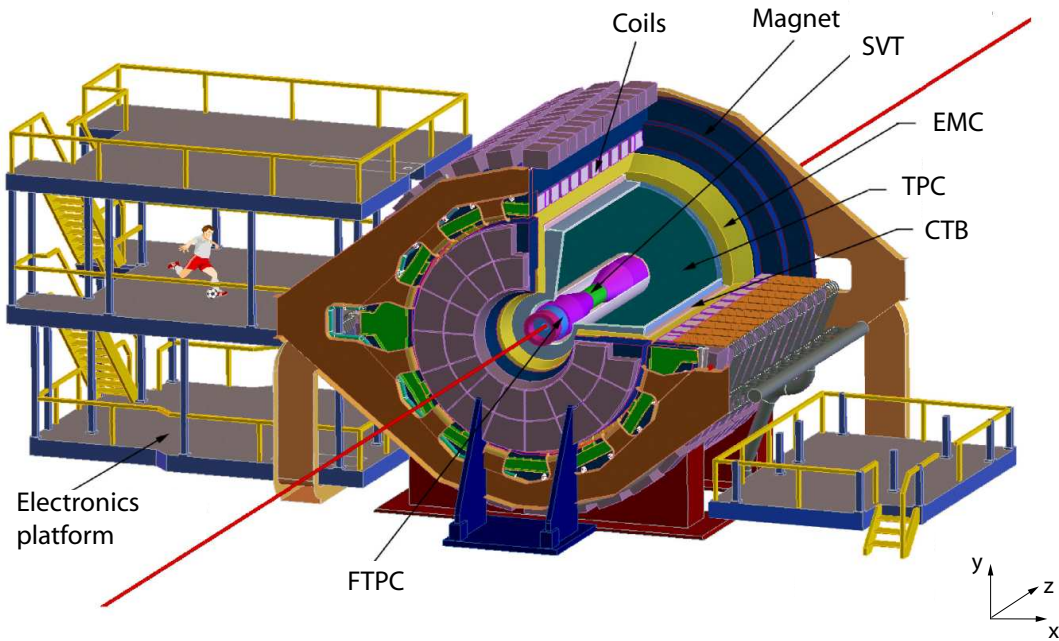


Figure 3.1.: The STAR experiment. The red line illustrates the RHIC beam line [37].

azimuthal angles, ϕ (i.e. $\Delta\phi = 360^\circ$). In terms of pseudorapidity, the range $-1.8 < \eta < 1.8$ is covered.

In the center of the experiment, the STAR silicon vertex tracker (SVT) is placed. The SVT is a silicon vertex detector which consists of 3 layers of silicon drift detectors. It has a radius $r = 14.5$ cm and spans the z axis in the range $-22.2 < z < 22.2$ cm. Making use of its high resolution and its proximity to the collision zone, the SVT is capable of identifying secondary vertices of short living particles which decay close to the event vertex. It provides particle identification through measurements of particle energy loss of particles upon passing through the silicon layers (dE/dx) in a process similar to that which takes place in the TPC detector gas. The SVT has full azimuthal coverage and covers the range $-1.0 < \eta < 1.0$ in pseudorapidity.

A ring imaging Čerenkov detector (RICH) is located just outside the TPC in the mid-rapidity region, at an angle $\phi = 60^\circ$ from the horizontal axis at 5 o'clock at a radius of 2.4 m from the beam line. The RICH detector has an azimuthal coverage of $\Delta\phi \sim 20^\circ$.

A forward time projection chamber (FTPC) can be found at either end of the TPC, within its inner diameter. The FTPCs are positioned at longitudinal dis-

tances of $z = \pm 1.5$ m from the center of the experiment. Each has a radius $r = 0.75$ m and a length $l = 1.2$ m. The FTPCs extend STAR coverage for charged particles in the forward pseudorapidity range ($2.5 < \eta < 4$).

The experiment is equipped with an electromagnetic calorimeter (EMC) which measures high transverse momentum photons, electrons and electromagnetically decaying particles. About 10% of the full-barrel electromagnetic calorimeter (BEMC) [43] was installed and commissioned successfully in 2001. The right half of the barrel was fully equipped with the EMC covering $0 < \eta < 1.0$ in pseudorapidity and $\Delta\phi = 360^\circ$, by the end of 2002. The EMC rapidity coverage will be extended by the addition of an end cap electromagnetic calorimeter (EEMC) which will cover the pseudorapidity range of $1 < \eta < 2$. The EEMC [44] will be installed, along with a complete BEMC, within the next 2 years.

A patch of a time of flight (ToF) detector was installed in 2001. The ToF detector partly overlaps the RICH detector. Its azimuthal coverage is $\Delta\phi = 7^\circ$, while its present pseudorapidity coverage is $-1 < \eta < 0$. The ToF detector extends particle identification for charged hadrons with a momentum in the range $0.2 < p < 3.0$ GeV/ c . It will be extended to full azimuthal coverage with a $-1.0 < \eta < 1.0$ pseudorapidity coverage by 2005.

STAR uses the central trigger barrel (CTB) and the zero degree calorimeters (ZDCs) as trigger detectors. These detectors are fast detectors that can be read out at a rate of higher than 10 MHz. The CTB consists of 240 scintillators placed around the outer shell of the TPC cylinder and covers $-1.0 < \eta < 1.0$ in pseudorapidity with full azimuthal coverage. The CTB signal is indicative of the number of particles created in a nucleus+nucleus collision. The ZDCs are located at a distance of 18.25 m from the center of the experiment along both beam directions. They detect spectator¹ neutrons emitted within a cone along both beam directions in heavy ion collisions. This quantity is indicative of the number of participants involved in a heavy ion collision. The trigger detector signals are used by the trigger system to issue a decision on a given event if it fulfills certain criteria. If the event passes the slower detectors are read out. The trigger system has different levels, distinguishable from each other by the time it takes to issue a trigger decision. At the highest trigger level (Level-3), a full event reconstruction is performed. This enables STAR to trigger on events with rare physics observables. The detectors are controlled and monitored by the slow control system [45].

After an event is selected, data from the detectors are sent via optical fiber to the data acquisition (DAQ) system. The data from the various detectors are collected there and sent by a gigabit ethernet connection to the RHIC computing facility (RCF), where they are stored on tape by digital tape drives.

¹Spectators are nucleons that do not participate in a collision.

3.2. The STAR Coordinate System

The STAR global Cartesian coordinate system in which particle trajectories and momenta are measured, is a right handed system. The origin of the coordinate system is the center of the STAR magnet (i.e. in the center of the TPC, see Figure 3.3). The longitudinal direction, z , is defined by the axis of the magnet and is parallel to the beam axis, with positive z pointing westwards. Positive x direction points to the south and positive y points upwards.

3.3. The STAR Magnet

Momentum measurements are done at STAR by measuring the helical trajectories produced by charged particles in a magnetic field. The STAR magnet (Figure 3.1, 3.2) is cylindrical, 6.85 m long, with inner and outer diameters, d_i and d_o of 10.52 and 14.64, respectively. The magnet generates a solenoidal magnetic field, with a maximum strength of $\vec{B} = (0, 0, 5)$ T. The direction of the magnetic field lines are parallel to the beam axis. When a particle with charge, e , mass, m , and velocity, \mathbf{v} , comes under the influence of a magnetic field, \mathbf{B} , perpendicular to its path, the particle will be deflected due to Lorentz force compensation, $F_L = e \mathbf{v} \times \mathbf{B}$, and the centrifugal force $F_c = \frac{m\mathbf{v}^2}{r}$, which results in a helical particle trajectory.

$$\frac{m\mathbf{v}^2}{r} = e \mathbf{v} \times \mathbf{B}. \quad (3.1)$$

Taking the transverse componets of the particle velocity and the longitudinal componet of the magnetic field only

$$\frac{m v_{\perp}^2}{r} = e v_{\perp} B_z. \quad (3.2)$$

Hence, the transverse momentum $p_{\perp} = m v_{\perp}$ of a charged particle traversing through a constant magnetic field $\vec{B} = (0, 0, B_z)$ can be determined by measuring the radius r of the trajectory in the transverse plane:

$$p_{\perp} = e B_z r \quad (3.3)$$

Where p_{\perp} is given in N s (i.e. V A s²/m) for e given in A s and B in T (i.e. V s/m²). To express the momentum in units of GeV/ c , one must multiply p_{\perp} by factor

$$f = \frac{1\text{GeV}/c}{1\text{Ns}} = \frac{10^9 e(\text{As})(Z)}{(\text{VAs}^2/\text{m})2.9979 \times 10^8(\text{m/s})} \approx \frac{10e}{3}. \quad (3.4)$$

to convert N s in GeV/ c [46]. For B in T and r in m this leads to

$$p_{\perp}(\text{GeV}/c) \approx 0.3 B_z r \quad (3.5)$$

The longitudinal momentum p_z is given by

$$p_z = p_{\perp} \tan \lambda \quad (3.6)$$

where λ is the dip angle. The total momentum (p) of the particle is then given by

$$p = \sqrt{p_{\perp}^2 + p_z^2}. \quad (3.7)$$

Thus in a constant, homogeneous magnetic field, the radius of a charged particle's trajectory depends on its momentum. For example, a singly charged particle with a momentum $p = 0.5$ (5.0) GeV/ c leaves a trajectory with a radius $r = 3.3$ (33) m in the full STAR magnetic field of $\vec{B} = (0, 0, 0.5)$ T.

3.4. Description of STAR Detectors

The following section gives a detailed description of the STAR detectors which were used in this analysis. For the anti-proton to proton ratio analysis (see Chapter 5) the TPC and the ring imaging Čerenkov detector (RICH) were employed. The emphasis will therefore be on these two detectors. A description of the FTPC and the SVT is also given, since they were integrated into the Level-3 trigger (see Section 3.8) system and into the online event display described in Section 4.3.5.

3.4.1. The Time Projection Chamber

The time projection chamber (TPC) [47] is the principal detector of the STAR experiment. The TPC is cylindrical in shape, and is 4.2 m long. The cylinder's inner diameter is $d_i = 1.0$ m and its outer diameter is $d_o = 4.0$ m. The TPC was designed to cover a large portion of phase space, and performs tracking of charged particles at full azimuthal coverage within a pseudorapidity interval of $-1.5 < \eta < 1.5$.

The TPC can be compared to a three dimensional digital camera which records spatial points (clusters of pixels) along charged particle trajectories which have a helical form due to the presence of the magnetic field.

TPC Operating Principle

In the TPC, a particle can be measured by measuring the particle specific ionization (dE/dx) along its trajectory in the detector gas. When a particle travels through a given medium (e.g. a gas), it causes ionization of the molecules due to

3. The STAR Experiment

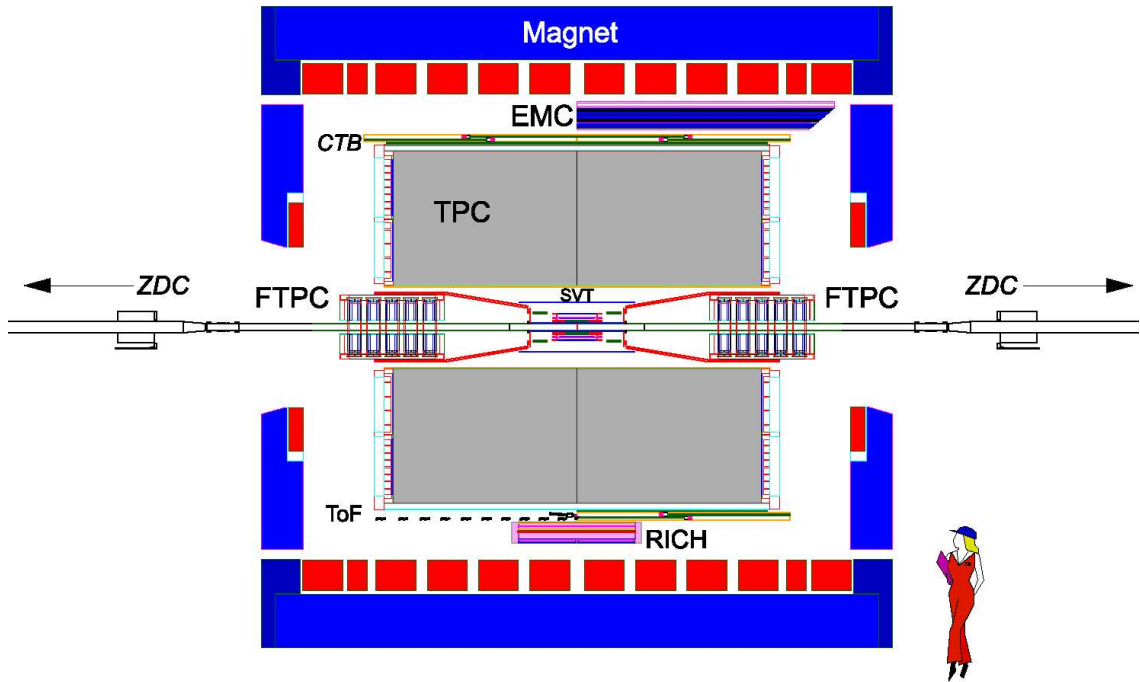


Figure 3.2.: Cutaway (z - y -plane) view of the STAR experiment with its detectors in 2001 [37].

collisions between the traversing particles and the gas molecules. This process is characterized by the Bethe-Bloch formula [48] [46]:

$$\frac{dE}{dx} = 4\pi N_o r_e^2 m_e c^2 \frac{Z}{A} \rho \frac{1}{\beta^2} z^2 \left(\ln \frac{2m_e c^2}{I} \beta^2 \gamma^2 - \beta^2 - \frac{\delta(\beta)}{2} \right) \quad (3.8)$$

where $m_e c^2$ is the rest energy of the electron, z is the particle charge, N_o is the Avogadro constant, r_e is the classical electron radius, ρ , A and Z are the density, mass number, and atomic number, respectively, of the medium being traversed, I is the ionization potential of the medium and $\delta(\beta)$ is a density correction which describes the ionization saturation at relativistic particle speeds.

Electrons which are produced in the ionization process along the particle trajectory knock other electrons out of the gas molecules, so that clouds of secondary electrons (clusters) emerge. Due to an electrical field in the longitudinal direction, these clusters drift toward the readout plane. To amplify the cluster charge, the readout plane is equipped with a thin multi-wire proportional chamber (MWPC). The drifting electrons must first pass through a gating grid which separates the TPC drift region from the amplification region of the MWPC. The readout plane is segmented into pads, so that two dimensional spatial information can be obtained from the individual pads. The longitudinal spatial information is obtained

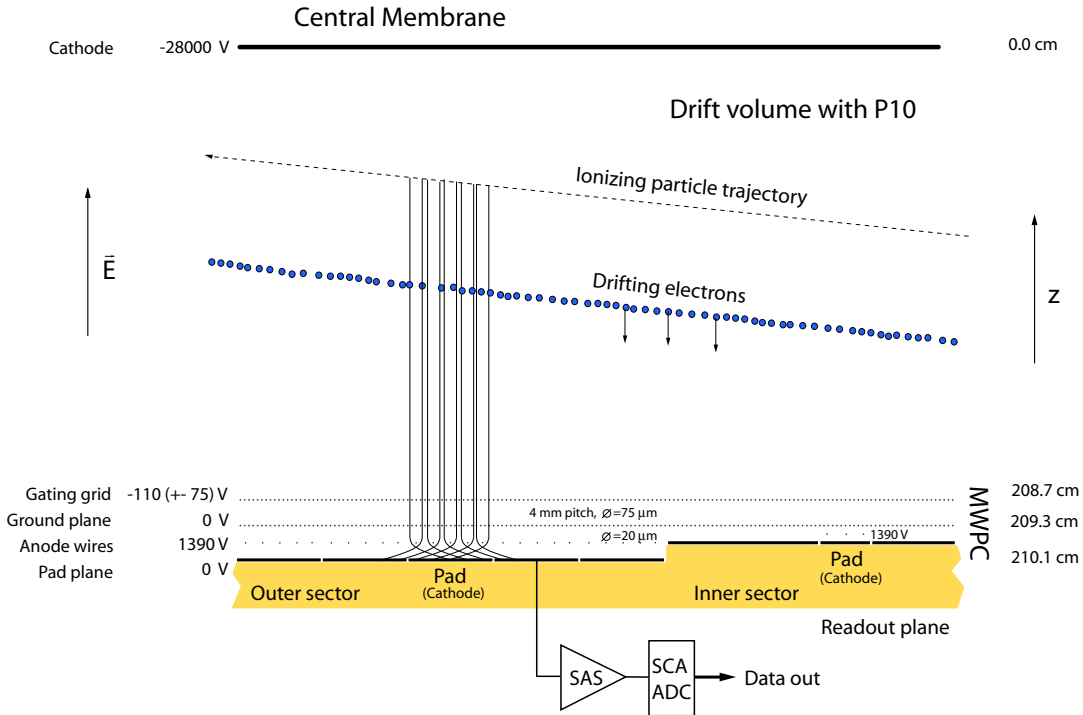


Figure 3.3.: Cut between inner and outer sector of the STAR TPC in the longitudinal direction. The central membrane, the detector gas volume and the MWPC, can be seen.

by measuring the electron drift time. In the case of a positive trigger decision, the TPC is read out by applying a voltage $U = -110$ V to the gating grid (“open state”), so that the drifting electron clusters pass through. The distance between ground plane and pad plane defines the effective volume of the MWPC (see Figure 3.3).

Anode wires which operate at a voltage $U = 1390$ V are placed above the pads. When drifting electrons enter the region of the anode wire, they are accelerated and multiplied by ionization avalanches in the gas. A high number of electron-ion pairs are created. The electrons are attracted by the anode wires, and the remaining positively charged ions induce an electric signal on the underlying pads of the readout plane. The spatial information (in the x - y -plane) is obtained by reading out the induced signal on the pads. The drift velocity is constant due to two factors - (a) the interaction of electrons with detector gas molecules and (b) the homogeneous electric field. Thus the longitudinal spatial information is obtained by measuring the drift time of electrons in the homogeneous electric field.

3. The STAR Experiment

During the closed period of the gating grid, the voltage alternates from wire to wire from $U = -110 \pm 75$ V. The positive ions are too slow to escape during the open state and are captured in the closed period.

TPC Detector Design Considerations

Figure 3.5 shows a view of the TPC main components. In the center of the cylinder is the central membrane. This membrane is made of carbon-coated polyamid foil (Kapton²) and acts as a cathode for the TPC electromagnetic drift field (~ 135 V/cm). The ground plane of the MWPC acts as an anode. The inner (IFC) and outer field cage (OFC) cylinders serve the dual purpose of gas containment and defining the electric drift field. The mechanical design was optimized to reduce mass so as to minimize track distortions from multiple Coulomb scattering and secondary particle production. The low mass, self-supporting field cage cylinders are a composite sandwich of two layers of Kapton with metal on both sides, separated by Nomex honeycomb (Figure 3.4).

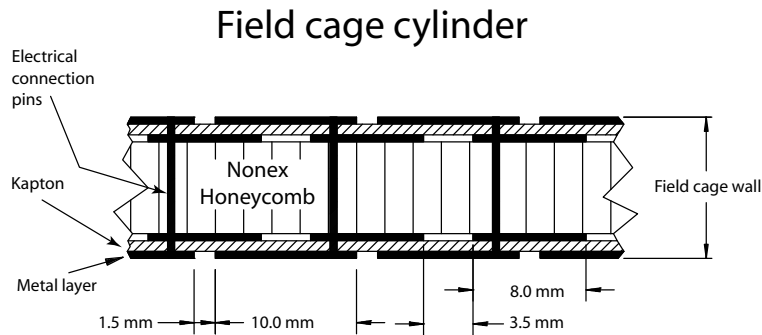


Figure 3.4.: Sandwich material used for the inner and outer TPC field cage [47].

The metal is etched to form electrically separated, 10mm wide strips, 1.5 mm apart. Punch-through pins are used to electrically connect the layers on either side of the sandwich. The metal strips are connected to a chain of resistors and are supplied with a voltage so that they act as equipotential rings of the electrical field. This helps to insure a homogeneous electrical drift field.

The OFC is isolated from the outermost shell of the TPC by a 5.7 cm thick layer of nitrogen. The outermost shell consists of a sandwich of two aluminum shells laminated onto an aluminum honeycomb and completely surrounded by aluminum support rails. The CTB and the ToF detector are mounted on these support rails. The TPC cylinder consists of the IFC, the OFC and the cylinder ends, which consist of support structures where the readout chambers are

²Kapton® , Nomex® by DuPont.

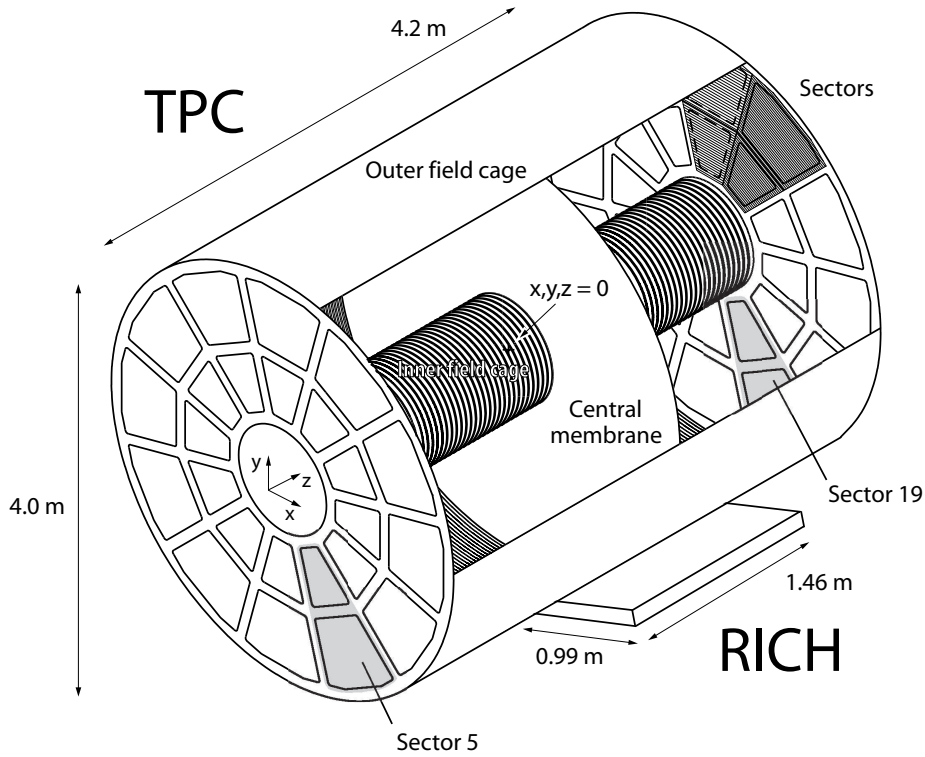


Figure 3.5.: TPC inner and outer field cage with the RICH detector.

mounted (12 sectors on each end). Each sector has an inner and an outer area as depicted in Figure 3.6. The pad arrangement is different in the inner and outer sector. In the inner sector, the pad size ($2.85 \times 11.5 \text{ mm}^2$) is approximately 1/4 the pad size of the outer sector ($6.2 \times 19.5 \text{ mm}^2$). The outer sector is optimized for energy loss measurement (dE/dx) and thus has an even distribution of pads across its surface. For the inner sector a compromise between a reasonable number of electronic channels, and a high two track resolution, due to the high track density close to the beam axis, was considered. This results in the small pad size and the padrows being aligned at a distance of 52 mm (cross spacing) from each other.

The anode wires are supplied with the same voltage in the inner and outer sector. In the inner sector, the distance from the wires to the readout plane is half, compared to the outer sector (see Figure 3.3). This yields 3 times higher amplification at the anode wires of an electron cluster in the inner, compared to the

3. The STAR Experiment

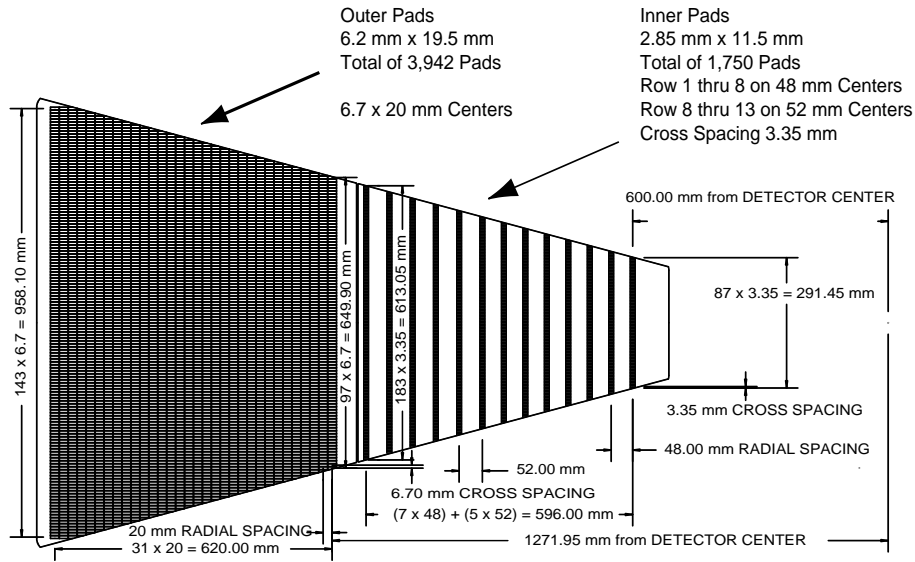


Figure 3.6.: TPC pad plane with rows of pads [47].

outer sector, yielding to the same signal to noise ratio (20:1) in the inner and outer sectors. A summary of parameters which differ between inner and outer readout sectors is given in Table A.2. The TPC detector gas is a mixture of 90% argon and 10% methane (P10). The choice of the gas determines the drift velocity, absorption and transverse and longitudinal diffusion of a drifting electron cluster. The drift time for an electron cluster drifting the maximum length in the TPC of $l = 210$ mm is typically $40 \mu\text{s}$. Thus the performance of the TPC, strongly depends on the magnetic field. For example, the transverse diffusion of electrons which drift through the gas is smaller at a higher magnetic field. The transverse diffusion for a cluster in P10 is $230 \mu\text{m}/\sqrt{\text{cm}}$ at the full magnetic field of $B = 0.5$ T. This corresponds to a maximum of $\sigma_T \sim 3.3$ mm after drifting the full length. In the longitudinal direction, the maximum diffusion of the electron cluster is $\sigma_L \sim 5.2$ mm. The read out rate of the TPC is mainly determined by the drift time, but digitizing time (10ms) and other dead times of the DAQ Trigger system must also taken into consideration. The TPC is designed to be read out at a maximum rate of 100 Hz.

For each event accepted by the STAR trigger, the signal of 32 pads are read out and collected by a front end card (FEE) [49]. The signals are amplified and shaped by a custom designed (SAS) chip. To obtain the electron cluster longitudinal information, the drift time is digitized into a maximum of 512 time-bins. For each time-bin, the pad signal is stored as a voltage in a switched capacitor array (SCA), which is a fast analog memory. For a typical drift time of $40 \mu\text{s}$, 380 time-bins are stored in the SCA. A 10 bit analog to digital converter

(ADC) subsequently digitizes the stored voltages. The readout boards combine up to 36 FEE cards and ship the ADC data to the data acquisition system (DAQ). The readout cards communicate with the trigger and the “slow control” system [45]. When the TPC is to be read out, the readout system receives a command from the trigger to read out the TPC. The total 136608 pads are read out by 4269 FEE cards.

To determine spatial distortions, as well as to calibrate and monitor the TPC, a laser calibration system is integrated into the detector. It produces ~ 500 thin laser beams simulating straight particle tracks in the TPC volume [50].

The main TPC parameters are summarized in Table A.1. The radiation length of the TPC materials can be found in A.3. Particle trajectory reconstruction and identification via dE/dx will be discussed in Chapter 4.

3.4.2. Ring Imaging Čerenkov Detector

During the first and second RHIC runs, the STAR experiment was equipped with a ring imaging Čerenkov (RICH) detector [51] [53], which was originally built as a prototype [52] [54] for ALICE at CERN. The RICH detector is located in the mid-rapidity region, at an angle $\phi = 60^\circ$ from the horizontal axis at 5 o’clock at a radius $r = 2.4$ m from the beam line. It covers the pseudorapidity range $|\eta| < 0.3$ and has a azimuthal coverage of $\Delta\phi \sim 20^\circ$ (see Figure 3.5). Although the detector covers only 2% of the TPC acceptance, it was included in the STAR experimental setup in order to extend the particle identification of the TPC to identify particles with transverse momenta in the range of $1.3 < p < 5.0$ GeV/ c . The RICH detector was used for anti-proton and proton identification in the present study (see Chapter 5). In the following sections, the underlying physics principles necessary to understand the functioning of the detector, its design, its role in track reconstruction (see Section 4.2) and data analysis will be discussed.

Operating Principle of the RICH Detector

When high-energy charged particles traverse dielectric media with relativistic velocities, part of the light emitted by excited atoms appears in the form of a coherent wavefront at a fixed angle with respect to the particle trajectory. This phenomenon is known as the Čerenkov effect, named after its discoverer³. Čerenkov radiation is produced whenever the velocity ($v = \beta c$) of a charged particle exceeds the phase velocity of light ($v_p = c/n$) in the medium traversed by the particle, where β is the particle velocity in units of the speed of light, c , and n is the refractive index of the medium. From the Huygens construction

³Discovered by P. A. Čerenkov in 1934 while studying the effects of gamma rays in liquids

3. The STAR Experiment

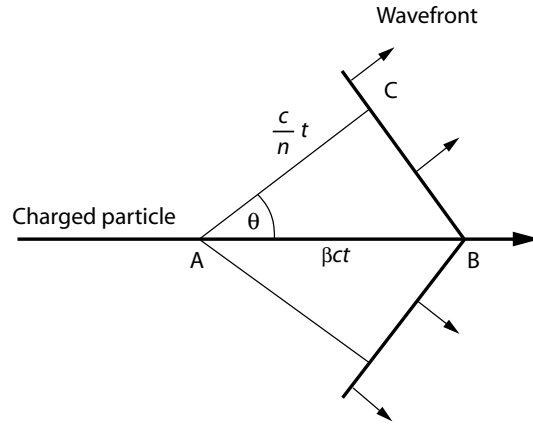


Figure 3.7.: Čerenkov light cone (explanation see text).

illustrated in Figure 3.7, one sees that the wavefront forms a conical surface about the trajectory axis, such that

$$\cos \theta = \frac{ct/n}{\beta ct} = \frac{1}{\beta n}, \quad \beta = \frac{v_{thres}}{c} \geq \frac{1}{n} \quad (3.9)$$

where $\beta = 1/n$ is the threshold velocity, t is time and θ is the Čerenkov angle. Čerenkov radiation appears as a continuous spectrum. In a dispersive medium, both n and θ depend on the wavelength, λ , of the radiation.

$$\theta = \arccos \frac{1}{n(\lambda) \beta} \quad (3.10)$$

The Čerenkov angle of a particle with momentum, p (GeV/ c), and mass, m , can be calculated, using the relationship between energy ($E = \sqrt{p^2 + m^2}$) and momentum $p = \beta/c E$

$$\theta = \arccos \frac{\sqrt{p^2 + m^2}}{n(\lambda) p} \quad (3.11)$$

The number of photons radiated per unit distance, x , in a dispersive medium is given by

$$\frac{dN}{dx} = k(\lambda) \int \frac{1}{1 - n^2(\lambda) \beta^2} \frac{d\lambda}{\lambda} \quad (3.12)$$

where k is a normalization factor which takes relevant detector characteristics into account [55]. The number of photons emitted per unit distance is inversely proportional to λ , so that the Čerenkov radiation spectrum shows a maximum at lower wavelengths (i.e. ultraviolet region).

In a Čerenkov detector, the correlation between particle speed and the angle between momentum direction and radiation emission is used to identify the particle mass.

RICH Detector Design

The RICH detector has dimensions $146 \times 99 \times 24 \text{ cm}^3$ and is located within the acceptance region of TPC sectors 5 and 19 (see Figure 3.5), between the magnet coils of the STAR magnet and the CTB. It is centered with respect to the TPC central membrane. Figures 2.7 and 4.12 pictorially represent the RICH detector as a rectangle sitting just outside the TPC barrel. Figure 3.2 illustrates a cutaway view of the STAR experiment and the position of the RICH detector in the z - y -plane.

For events having event vertex in the center of the experiment ($V_{event} = \{0, 0, 0\}$), the active area of the RICH detector extends an azimuthal angle of

$$\Delta\phi = \arctan \frac{\text{active detector width}}{\text{radial distance}} \approx \frac{84}{240} \approx 20^\circ. \quad (3.13)$$

The length of the active detector volume in the longitudinal direction ($\pm 65 \text{ cm}$) yields a minimum angle, θ , between the trajectory of a particle traversing the RICH detector and the beam axis in the y - z -plane of:

$$\theta = \frac{\pi}{2} - \arctan \frac{\text{active detector length}}{\text{radial distance}} \approx \frac{\pi}{2} - \arctan \frac{65}{240} \approx 75^\circ. \quad (3.14)$$

This leads to a pseudorapidity coverage, η , of

$$\eta = \ln[\tan(\theta/2)] \approx 0.27 \quad (3.15)$$

The detector is housed in a gas tight safety box, the contents of which are illustrated in Figure 3.8a. The entrance window at the top of the box is a 50 mm layer of Nomex honeycomb material, covered with a 1 mm layer of aluminum.

The RICH detector uses liquid perfluorohexane (C_6F_{14}) as a medium for the generation of Čerenkov radiation. Perfluorohexane has the advantage that it is chemically inert and has a transmission of $\sim 100\%$ for ultraviolet light of wavelength $\lambda > 180 \text{ nm}$ [56]. The circulating liquid is contained in a vessel which is 10 mm deep. The vessel must be sufficiently strongly, to withstand the perfluorohexane hydrostatic pressure. The depth of the radiator determines the number of photons generated (Equation 3.12), as well as influencing the width of the ring imaged onto the detection plane. The entrance window is a Neoceran⁴ plate, while the exit window is a quartz plate.

When a particle passes through the radiating medium, Čerenkov light is produced and is emitted in the form of a cone. The Čerenkov angle, θ , and the threshold velocity, β_{thres} , which a particle must have so that Čerenkov radiation is emitted, both depend on the index of refraction, n , of the radiator as does the number

⁴A heat resistant glass.

3. The STAR Experiment

of photons radiated in the cone. In a disperse medium, the index of refraction changes as a function of wavelength of the radiated light.

The refractive index of C_6F_{14} varies 3% in the wavelength range of $155 < \lambda < 225$ nm [56]. The dependence can be expressed as:

$$n = 1.177 + .0172hc/\lambda. \quad (3.16)$$

It is $n = 1.29$ at a wavelength of $\lambda = 180$ nm. Using this as a mean value $\langle n \rangle = 1.29$ and making the assumption that a particle traversing C_6F_{14} travels at a relativistic velocity of $\beta = 1$. The maximum Čerenkov angle which can be produced by a traversing particle is therefore given by Eq. 3.10

$$\theta_{max} = \arccos \frac{1}{\langle n \rangle \beta} \approx 39^\circ \quad (3.17)$$

The point at which this value is reached is determined by the particle mass and momentum. For pions, kaons and protons, this maximum Čerenkov angle is reached at momenta of $p \sim 2, 3$ and 5 GeV/ c , respectively (see Figure 4.8).

The mean index of refraction which determines the threshold velocity necessary for the emission of Čerenkov radiation for a charged particle with mass m is given by the following expression:

$$\beta_{thres} = \frac{v_{thres}}{c} \geq \frac{1}{\langle n \rangle} \quad (3.18)$$

In order to calculate the corresponding threshold particle momentum, p_{thres} , the relationship between β and γ is used. For $\beta = 1/1.29$, γ is given by

$$\gamma_{thres} = \frac{1}{\sqrt{1 - \beta_{thres}^2}} = 1.58 \quad (3.19)$$

The minimum particle energy necessary for the emission of Čerenkov light can thus be determined by the expression

$$E_{thres} = \gamma_{thres} m c^2. \quad (3.20)$$

The relationship between energy (E) and momentum $p = \beta/c E$ yields the threshold momentum to be

$$p_{thres} = \frac{\beta}{c} \gamma_{thres} m c^2 = (1/1.29) * 1.58 m c = 1.23 m c. \quad (3.21)$$

This gives threshold momenta $p_{thres} = 0.17, 0.61$ and 1.16 GeV/ c for pions, kaons and protons, respectively, as they traverse C_6F_{14} (see Figure 4.8).

The Čerenkov light which is generated by a relativistic charged particle traversing the radiator has to pass through the 5 mm thick quartz exit window. Quartz

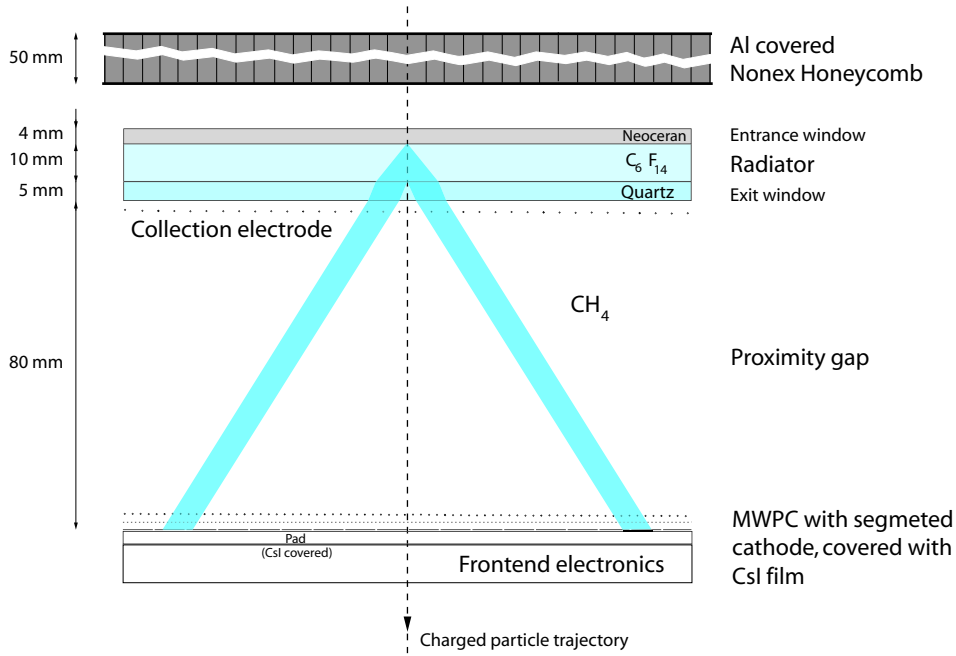


Figure 3.8.: Schematic drawing of the RICH detector.

($n = 1.59$) has a higher index of refraction than C_6F_{14} . Thus, due to Snell's law, light will be bent slightly towards the normal upon entering the quartz window. When exiting the quartz window, light will be radiated into the proximity gap and subsequently the MWPC, which is filled with methane. Methane has a lower index of refraction ($n=1.0$) than quartz, and so the light will be bent away from the normal when entering the gas volume of the MWPC. As an example of the angular changes involved, consider a particle travelling with a velocity $\beta \sim 1$, which emits a Čerenkov cone with $\theta \sim 39^\circ$ in the radiator. At the transition between C_6F_{14} and quartz, the angle will change to approximately 28° relative to the normal. This becomes $\sim 55^\circ$ as the light passes from quartz into the detector gas of the MWPC. Čerenkov light cone photons are converted to photoelectrons by a CsI layer coated onto the segmented detection plane. The photoelectrons are detected by a MWPC. The radiation length of the materials in front of the MWPC can be found in A.3.

The detection (pad) plane ($\sim 1m^2$) is divided into 4 quadrants, each having dimensions of $64.0 \times 39.2 \text{ cm}^2$. Each quadrant is further segmented into 3840 pads, each one measuring $8.0 \times 8.4 \text{ cm}^2$. The photoelectrons are accelerated along the field lines of the anode wires (sense wires) and are multiplied by ionization avalanches in the gas. A high number of electron-ion pairs are created. The electrons are attracted to the anode wires, while the charge of the remaining ions is measured by the segmented cathode pads. The pads enable a spatial

3. The STAR Experiment

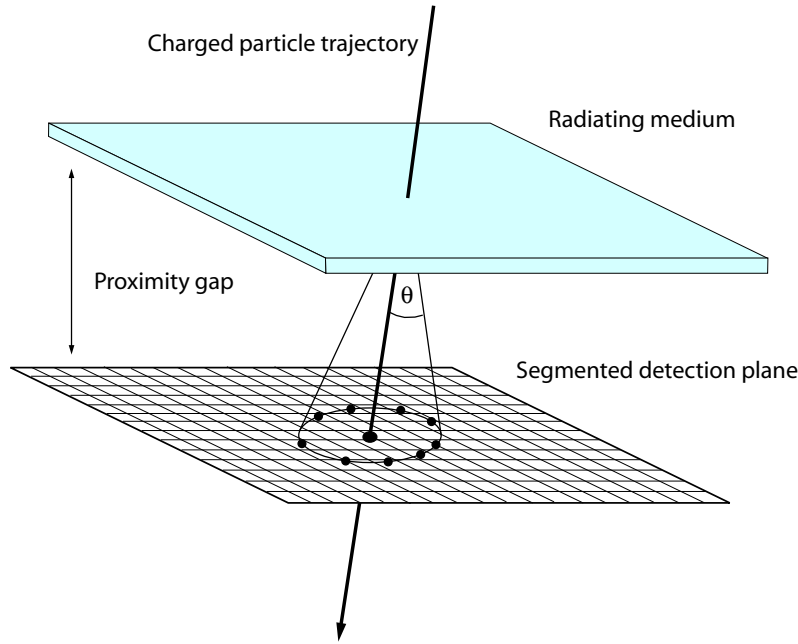


Figure 3.9.: Čerenkov ring formation in the RICH detection plane. The proximity gap serves to enlarge the ring diameter on the CsI coated, segmented detection plane. Dots: clusters, big dot: MIP (see Section 4.2)

measurement of the position of the Čerenkov ring photons (by now converted to electrons). The process is represented pictorially in Figure 3.9.

For each event, the pad signals of the MWPC segmented readout plane are read out, digitized and sent to the STAR DAQ. The pad signal is processed by a GASSIPLEX chip. Each quadrant requires 240 such chips. Each channel of the 16 channel GASSIPLEX chip has a charge sensitive amplifier, a filter shaper and a Track & Hold stage to store the signal in a capacitor.

Upon receipt of a fast pre-trigger created by the fast output of the CTB slats in front of the RICH detector, each channel is opened. When a positive trigger is generated by the STAR trigger system, the Hold stage is used to maintain the individual charge stored in the capacitor of each channel. In the case of a negative STAR trigger, the capacitor in the GASSIPLEX chip is reset.

The readout chips for all the quadrants are daisy-chained together, allowing the data to be sent over a set of 16 signal cables to a VME readout module. The digitization and zero suppression of the analogue data stream takes place there. The analogue signals are transformed into a 10-bit digital signal, before being sent to the RICH detector broker of the DAQ.

3.4.3. Forward Time Projection Chamber

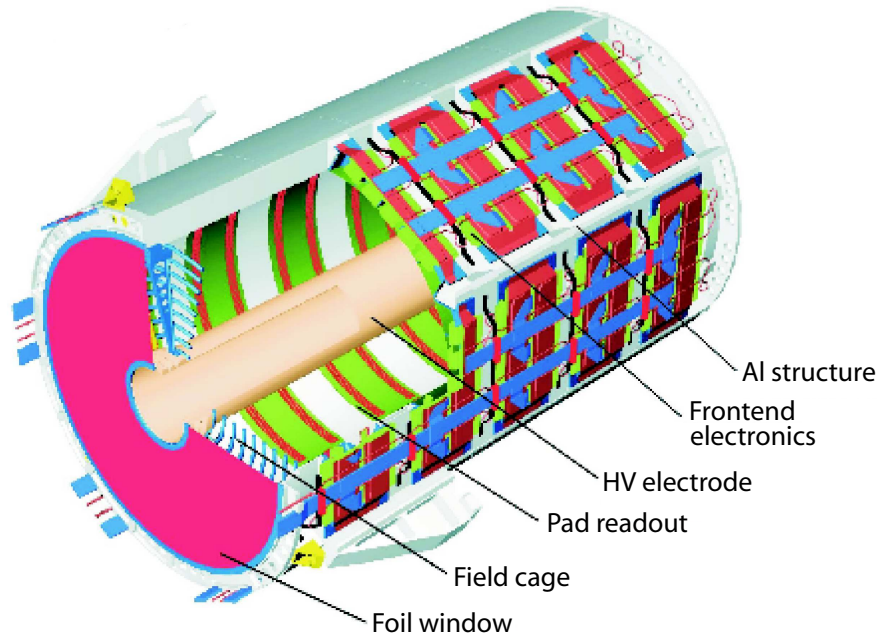


Figure 3.10.: A schematic diagram of the main components of the FTPC [57].

The two cylindrical forward time projection chambers (FTPC) [57] extend the coverage of the STAR experiment to the pseudorapidity range $2.5 < \eta < 4.0$ with full azimuthal coverage. The operation principle is similar to the TPC, with the speciality that the electrons in the FTPC drift in a radial drift field. Furthermore, the detector readout is installed on the outer cylinder of the FTPC. This design was chosen due to the high particle density at pseudorapidities near the beam. Up to 1000 trajectories are expected in the $\eta = 1.5$ wide rapidity interval covered by the FTPC. Although this design offers good two track separation (1-2 mm is expected), it also creates some difficulties. For instance, the strength of the electromagnetic drift field decreases with the radius of the detector, so that there is a non-constant drift velocity. In addition, the drift field lines and the magnetic field lines are perpendicular to each other, which causes electron clusters to be deflected towards the azimuthal direction due to the Lorentz force. Thus, a non trivial coordinate transformation is necessary in order to calculate the effective cluster coordinates from the recorded raw data.

An illustration of the detector is shown in Figure 3.10. The field cage consists of an inner high voltage (HV) electrode, a thin metalized plastic tube, and the outer cylinder wall which is connected to ground. The field region at both ends is closed by a planar structure of concentric rings, made of aluminum pipes. The

3. The STAR Experiment

detector gas is a mixture of 50% argon and 50% carbon dioxide, so as to achieve a (relatively slow) drift velocity of 0.3 to 2.0 cm/ μ s. The front end electronics (FEE), which amplifies, shapes and digitizes the signal, is mounted on the back of the readout chambers. The FTPCs can also be seen in Figure 2.7, on the left in blue (west) and on the right in yellow (east).

Each particle trajectory is sampled up to 10 times, which is not sufficient to separate particle species by a dE/dx measurement. Thus, the FTPC can only be used for particle multiplicity and momentum measurements. In each FTPC, the MWPC area is divided into 5 rings (shown in green in Figure 3.10). Each ring is divided into 6 modules for readout purposes. In one of these modules, there are 2 rows of pads, with 160 pads per row. This yields a total of 1920 pads per MWPC ring and 9600 per FTPC. The pads are read out by FEE cards similar to those used in the TPC, the difference being that in the FTPC case, only 265 time-bins are sampled.

3.4.4. Silicon Vertex Tracker

The SVT [58] is a silicon drift detector (SDD). A SDD may be envisioned as a solid state TPC, which has silicon, instead of gas, as the detector medium. The detector consists of several silicon wafers with different structures implanted on each layer. p^+ stripes (cathodes) are symmetrically implanted on the top and bottom of the wafer and symmetrically biased by applying a potential with a gradient in the drift direction. Segmented n^+ stripes (anodes) are located at the edge of the detector and run in a direction parallel to the p^+ stripes. A potential valley (as seen by a drifting electron) is formed by the p^+/n junctions on both sides of the wafer such that electrons generated by the passage of an energetic charged particle drift toward the middle (in depth) of the detector layer toward the segmented anodes.

The SVT consists of a total of 216 SDD wafers with a size of 63×63 mm². The SDD wafers have a cylindrical form and radii, r , of 6.9, 10.8, 14.5 cm with lengths l of 25.2, 37.9, 44.4 cm respectively. They are centered with respect to the origin of the experiment and around the beam pipe ($r = 4$ cm). A cross section through the SVT can be seen in Figure 2.7. The 3 SDD wafer layers can be seen as gray concentric circles arranged about the beam axis.

Each SDD consists of two half-detectors, separated by the dividing central cathode, which receives the maximum voltage bias of $U = -1500$ V. Electrons drift from the cathode to the segmented anodes at the sides of the wafer. Each of the anodes is divided into 240 segments. The drift time along the length of the wafer is segmented into 128 time-bins, yielding to 256×240 channels per wafer. The SDD has a spatial resolution of 20 μ m in both the anode and drift direction. In the radial direction, the resolution is given by the width of the wafer of 280 μ m.

The SVT provides particle identification by measuring the specific ionization, dE/dx , of the silicon by the charged particles (similar to the TPC). The dE/dx resolution was determined to be 7% in a test beam experiment. The total average radiation length of the SVT is slightly below $X_0 = 6\%$ for all three layers or $X_0 = 1.89\%$ per layer [58]. Twenty four readout electronic (RDO) boxes are mounted on the TPC wheel to read out the SVT. Each RDO box has interfaces to the trigger, DAQ and slow control. The SVT data are sent to the DAQ via an optical fiber. In 2001, the STAR experiment was fully equipped with the SVT. It is intended to install an additional layer of a silicon strip detector (SSD) [59] in the near future.

3.5. Trigger Detectors

The STAR experiment uses zero degree calorimeters (ZDCs) and the central trigger barrel (CTB) as trigger detectors to trigger on $^{197}\text{Au} + ^{197}\text{Au}$ collisions. These detectors differ from the detectors discussed in the previous sections, since they are fast detectors. The trigger detector signals are used by the STAR trigger system to assess whether or not to issue a trigger on quantities such as the collision impact parameter b and the z vertex position.

3.5.1. Zero Degree Calorimeters

The ZDCs [60] [62] are located at a distance of 18.25 m (Figure 3.2) from the center of the experiment, the position of the nominal interaction region, in each beam direction. They are located behind dipole magnets which are used to merge and separate the beam at the intersection regions. The dipole magnets deflect charged particles and fragments of nuclei. Only neutrons can reach the calorimeters.

Collisions of high energy nuclei lead to the emission of spectator neutrons from the colliding nuclei. Neutrons are created either in a reaction during a nucleus + nucleus collision or singly by dipole resonances of excited nuclei, with approximately the same cross sections [63]. The neutrons are emitted along the beam axis and diverge less than 2 milliradians. The STAR ZDCs detect these neutrons emitted within a cone along both beam directions, and measure their energy. The sum of the ZDC signal in ADC counts (named ZDC sum) along the two beam directions is indicative of the impact parameter b of the collision [61] and thus can be employed by the trigger system as a minimum bias selection criterion for heavy ion collisions [64].

The ZDCs are hadron calorimeters consisting of layers of tungsten absorbers together with plastic fibers. Relativistic electrons created in the hadronic shower

3. The STAR Experiment

of a neutron, produce Čerenkov radiation (Section 3.4.2) in the fibers. The fibers are fed to three photomultipliers in order to measure the Čerenkov light intensity. The energy resolution of the calorimeters for a 100 GeV neutron is $\sim 20\%$, which is sufficient to detect single neutrons. The ZDCs have a good time resolution of $t < 200$ ps. The timing information of the ZDCs was used in 2001 to determine the position of the collision vertex. The resolution achieved with this method is $\sigma = 7$ cm without slewing correction, and $\sigma = 3.5$ cm thereafter [64]. The frequency of the ZDC coincidence rate is a measure of the collision rate (or collider luminosity L) at the interaction region [63].

The ZDCs are read out by the CTB digitizer board (CDB) where the individual photomultipliers signals are read out, as well as the sum of all 3 modules.

3.5.2. Central Trigger Barrel

The central trigger barrel (CTB) [65] consists of 240 slats of plastic scintillators arranged in a cylindrical fashion around the outer shell of the TPC (Figure 3.2). The CTB has full azimuthal coverage ($\Delta\phi = 360^\circ$) and covers $-1.0 < \eta < 1.0$ in pseudorapidity. Each slat has one scintillator, one light guide and one photomultiplier. The slats are housed in aluminum trays, with two slats per tray. The trays are mounted onto rails on the outer shell of the TPC. Each tray has half the length of the TPC and therefore a coverage of $\eta = 0.5$ in pseudorapidity and $\Delta\phi = 6^\circ$ in azimuth. The total radiation length of a CTB tray is $X_0 \sim 20\%$ [66].

Each slat signal is sent to a digitizer board, each one having 16 inputs. Within each digitizer, the signal is integrated and digitized with an 8-bit ADC before being sent to a discriminator. The digital output of the discriminator is summarized and is then used as a trigger signal by the trigger system.

Each digitizer board has an external output for use by other detectors. The output from a single digitizer board can be obtained within 260 ns after an event has occurred. This output has been used for the slats in front of the RICH as a fast pre-trigger for the RICH detector (see Section 3.6).

The CTB is calibrated in such a way that a minimum ionizing charged particle gives an average of 5 ADC counts. The CTB ADC count sum (named CTB sum) is thus indicative of the number of particles created in the central pseudorapidity region in a heavy ion collision. In the case of a low multiplicity event (peripheral collision, large b), a small ADC count sum is measured in the CTB, whereas a large ADC count sum is indicative of a high multiplicity event (central collision, small b).

3.6. Trigger

The STAR trigger system [65] is subdivided into four levels, with each level having a different trigger processing time. Levels 0, 1 and 2 employ the CTB and ZDC trigger detectors, which can be read out faster than 100 ns. With information from these trigger detectors, it is possible to determine global event characteristics and subsequently to issue a decision to read out the tracking detectors (i.e. TPC, FTPC, SVT). The various trigger levels are:

Level-0: To trigger on collisions coming in with a collision rate (collider luminosity) of up to $R = 2.4$ kHz (design specification for $^{197}\text{Au} + ^{197}\text{Au}$ collisions, or even higher for proton-proton collisions), the trigger detectors are read out for every crossing bunch (every 107 ns) at the RHIC collider. Within $1.5 \mu\text{s}$, the trigger control unit (TCU) issues a decision on collision multiplicity and vertex position, thereby employing the ZDC and CTB signal, and the ZDC coincidence signal. To every event a trigger word is given, which depends on a combination of trigger detector signals. Each event is also given a token, which is only released when read out of all tracking detectors is completed. On the TCU, counters are implemented in order to determine the number of events taken with a certain trigger.

Level-1: Up to $100 \mu\text{s}$ are necessary to read out the tracking detectors. This is the processing time needed by the Level-1 trigger. The coarse pixel array (CPA) is used in conjunction with the Level-1 trigger. It is capable of processing CTB data, giving spatial information on event multiplicity distributions. Asymmetry in these distributions can thus be determined, and used for the decision.

Level-2: It takes about 10 ms to digitize the detector data. For this level, all trigger detector raw data are available and used to find a decision.

Level-3: The Level-3 trigger differs from previous trigger levels by the fact that it performs an on-line event reconstruction at up to 100 Hz from tracking detector data (e.g. TPC data) in real-time. Based on this on-line reconstruction, it can be determined whether or not an event fulfills certain criteria, and if it is stored or rejected. This trigger level is explained in Sections 3.8, 4.3 in greater detail.

For the analysis in this thesis, $^{197}\text{Au} + ^{197}\text{Au}$ event samples triggered by Level-0 and Level-3 were used.

3. The STAR Experiment

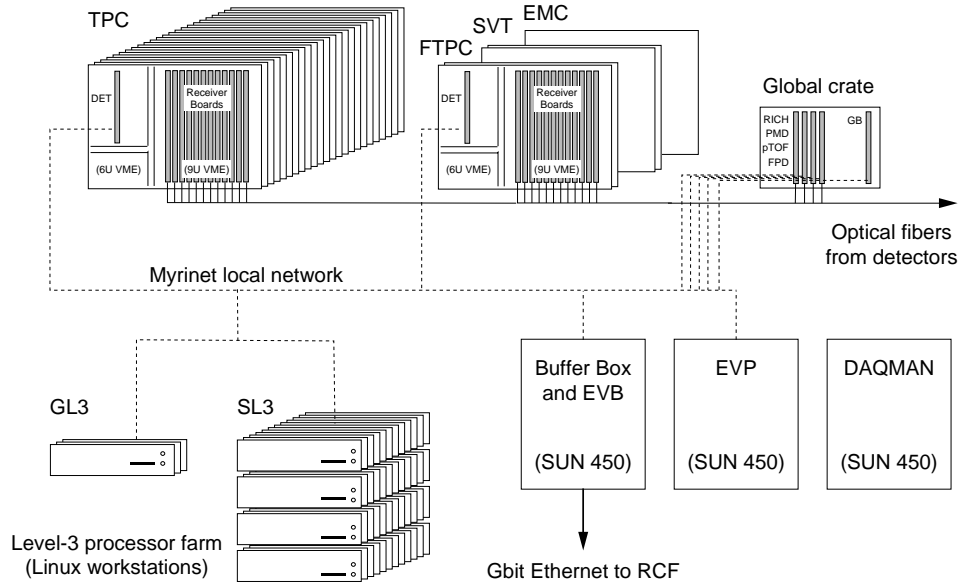


Figure 3.11.: Data acquisition (DAQ) of the STAR experiment [67].

3.7. Data Acquisition

The task of the STAR data acquisition (DAQ) system [67] is to collect the digitized data of the read-out electronics of each STAR detector and send the resulting event data to the RHIC computing facility (RCF), via a gigabit ethernet connection. At RCF, the event data are written to the high performance storage system (HPSS).

One event consists of over 100 MB of digital data, where the TPC contributes the largest fraction (~ 80 MB per event). At the maximum TPC read out rate of 100 Hz, the DAQ has to handle approximately 10 GB/s. To handle this rate the DAQ system is a parallel system consisting of a high speed network and processors. The Level-3 trigger is connected to the DAQ architecture.

The DAQ design is drawn in Figure 3.11. Raw data from the detector read out cards are sent, via optical fibers, to receiver boards. 144, 20 and 24 receiver boards are used to process the data for the TPC, FTPC and SVT, respectively. Each receiver board has 3 PCI slots equipped with *Mezzanine* cards. On these cards, a 10 to 8 bit data compression, as well as the zero suppression of the ADC signals is performed by a customized ASIC [68] chip. Each *Mezzanine* card is equipped with a i960 CPU (33 MHz) and a 4 MB dual ported memory, for buffering and pipelining raw data of up to 12 events. The i960 is used for data

formatting and on-line cluster finding of TPC, FTPC or SVT clusters (Section 3.8.1, 4.3.1). The high number of processors working in parallel ($144 \times 3 = 432$) allows TPC cluster finding to be performed in ~ 20 ms and reduces the event to ~ 2 MB of cluster data (see Section 4.3.1). These data are shipped via Myrinet to the Level-3 processor farm (SL3, GL3) as will be discussed in the next section.

The benefit of zero subtraction of raw data depends on the occupancy of a detector. A TPC occupancy of $< 10\%$ (typical for a central $^{197}\text{Au} + ^{197}\text{Au}$ collision) results in ~ 6 MB zero-suppressed TPC raw data (compared to ~ 80 MB without zero-suppression).

The receiver boards are held in sector crates, where each sector crate has 9 receiver boards. Each sector crate is controlled by a detector broker (DET) which controls the communication and data transfer between receiver boards and other components of the DAQ system. In the case of the RICH detector, data are sent via a point to point ethernet connection to the RICH detector broker. This is possible since the data volume of the RICH is small compared to that of the TPC.

The global broker (GB) is the central control unit of the DAQ. It receives information from the STAR trigger at the same time that the data are shipped from the detector read out cards to the receiver boards. The GB communicates with the DETs and insures that all detector data are collected for one event. It also keeps book of all incoming events. The event builder (EVB) collects DET data and transforms it into a format in which the complete event is saved. The EVB is implemented on a SUN Enterprise 450 Server with a 140 GB disk buffer (buffer box). From there, the data are sent via a Gbit ethernet (~ 30 MB/s) connection to HPSS at RCF. The event pool (EVP) enables a fraction of the events to be saved locally at the STAR experiment for monitoring purposes. DAQMAN is a server for the DAQ software. The interplay of the components of the DAQ system with the Level-3 trigger is described in the next section.

3.8. The Level-3 Trigger System

As shown in the previous section, the bandwidth at which event data can be stored at STAR, is limited by the HPSS bandwidth (~ 30 MB/sec in 2001). Although the TPC can be read out at a maximum rate of 100 Hz, only ~ 5 events/s of zero compressed raw data can be stored. Assuming a rate of 5 events/s, a few million events can be collected in a typical RHIC run (~ 3 months). The statistics of such a data sample are sufficient for the analysis of yields and correlations of identified particles. For studying rare particles such as Upsilon (Υ), anti-helium ($^4\overline{\text{He}}$) and high momentum particles traversing a detector having a small acceptance (e.g. the RICH detector in STAR), the statistics collected with the regular trigger

3. The STAR Experiment

might not be sufficient.

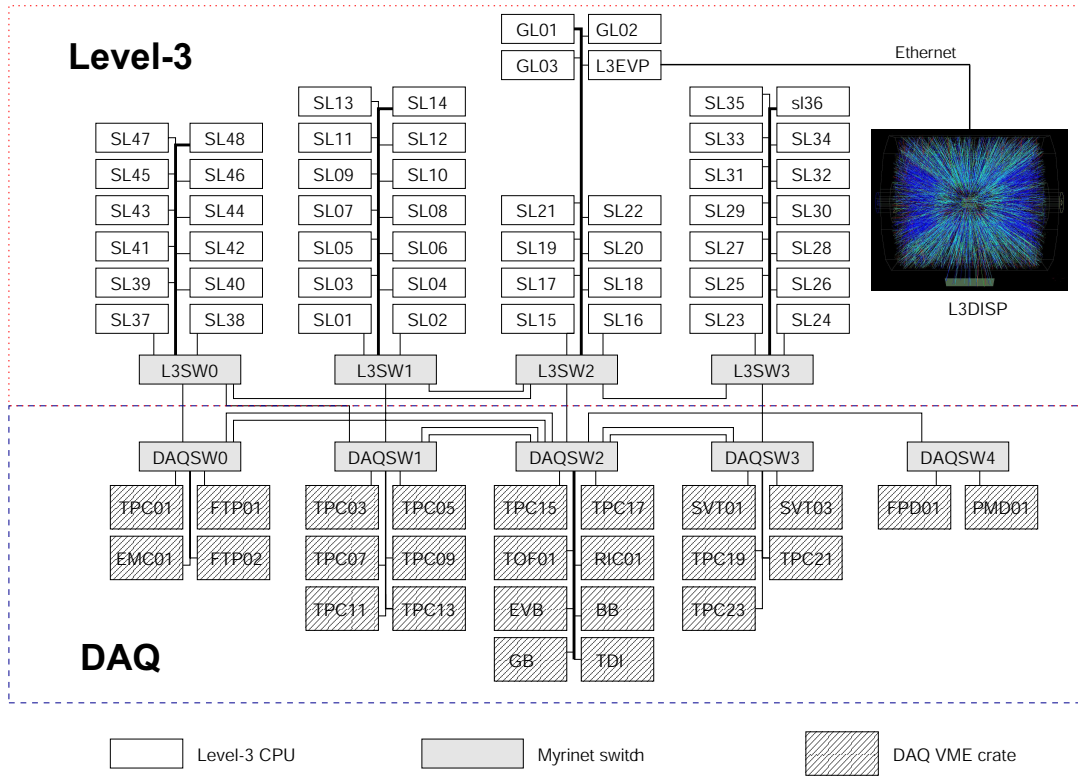


Figure 3.12.: DAQ and L3 Trigger [70] with L3DISP.

In order to enhance the number of events containing rare particles, on-line reconstruction of detector data and selecting events only with certain signatures is employed by the Level-3 trigger. Thus the event rate is no longer limited to the rate at which events can be stored, but to the TPC readout rate. The trigger's processing time per event (~ 100 ms) is given by the TPC readout time of ~ 10 ms times 12 which is the number of events that the DAQ event buffer stores. When the Level-3 trigger system was designed, the specification was to process events at a rate the same as the maximum TPC readout rate (100 Hz), assuming a HPSS bandwidth of 20 MB/sec and a much larger event size of 20 MB. Thus the Level-3 trigger would reconstruct and analyze a factor 100 more events than the number of events which could be written to HPSS. This enhancement was a strong motivation to build an on-line analysis trigger system [69].

In the following section, a brief description of the Level-3 Trigger will be given, to aid in the understanding of the Level-3 RICH algorithm (see Section 4.3.4), employed as a trigger for the dataset used in this analysis. Further description of the Level-3 trigger system can be found in [70] [71].

3.8.1. Architecture

In Figure 3.12 the Level-3 trigger architecture is illustrated. Raw data of two TPC sectors are collected by the 9 receiver boards of one sector crate (TPC0 to TPC23). The task of finding TPC clusters is performed by the Level-3 cluster finder software (see Section 4.3.1) which runs in parallel on 432 i960 processors located on the receiver boards. The cluster finder task takes ~ 20 ms per event. The Level-3 cluster data are sent via a Myrinet network to sector Level-3 processors (SL0 to SL47), where the track finder algorithm (see Section 4.3.2) is running. This processing farm consists of 48 Alpha 21264 CPU's where each node is dynamically assigned to one VME crate. Tracking of two TPC sectors is done on one node. Thus the set of 48 nodes allows four events to be processed in parallel. The track finding in two TPC sectors consumes ~ 70 ms CPU time. The analysis results in ~ 0.3 MB track data per event. The global Level-3 (GL3) nodes collect the tracking results from the SL3 nodes. The GL3 communicates with the GB and EVB of the DAQ and issues a yes-no-decision, based on the result of an Level-3 trigger algorithm. The Level-3 trigger system has been described here using only the TPC. However, the Level-3 trigger system was extended to include the FTPC and the SVT in 2001.

Trigger algorithms which issue trigger decisions are run on the GL3 processor nodes. In 2001, four algorithms were run:

$\Upsilon \rightarrow e^+e^-$: Calculates the invariant mass of pairs with a momentum of $p > 3$ GeV/ c . It selects an event if it contains a pair where the invariant mass is found to be within the region of the Υ particle [71] [84].

$\overline{^4He}$: Triggers on events containing anti-particles close to the $Z = -2$ band using the Bethe-Bloch parametrization in the dE/dx -momentum-plane [72].

RICH: Triggers on events containing particles with $p > 3$ GeV/ c in the acceptance of the RICH detector (see Section 4.3.4).

True: Triggers every event.

To derive absolute cross sections, it is necessary to differentiate between triggered (biased) events and randomly selected (unbiased) events. Therefore the "True" algorithm passes events through without introducing a bias to the saved event sample. Counters are provided on GL3 to get the number of events processed and triggered by each of the algorithms [72]. To optimize the enhancement of an algorithm and the HPSS bandwidth, it is possible to pre and post-scale every Level-3 trigger algorithm (pre-scaling reduces the number of events given to the algorithm, post-scaling reduces the number of events triggered by the algorithm [71]).

3. *The STAR Experiment*

In 2001, the whole reconstruction process of a central $^{197}\text{Au} + ^{197}\text{Au}$ event, including cluster finding, track finding and running the algorithms took less than 200 ms on the L3-Trigger processor farm, consisting of 48 SL3 nodes. A fraction of events reconstructed by Level-3 was stored onto disks of the Level-3 event pool (L3EVP). The fact that events reconstructed by Level-3 can be saved ~ 1 second later to the L3EVP disks allows for a fast analysis of global event characteristics. In 2001, the L3EVP disks were shared via an ethernet connection with other nodes such as the Level-3 display (L3DISP) located in the STAR control room. L3DISP is a graphics workstation equipped with high end graphics and an 42" wide SONY Plasma Screen. L3DISP runs the on-line event display (Section 4.3.5) which draws reconstructed events ~ 2 seconds after detector read out. This offers the shift crew a quick feedback about the performance of the experiment and its detectors.

4. Event Reconstruction

The task of the reconstruction software is to reconstruct particle trajectories measured by STAR detectors. In the following sections, the principle of the off-line reconstruction software will first be discussed, with an emphasis on the TPC and RICH detectors. Secondly the similar, but much faster, on-line reconstruction software for the TPC, which is run by the Level-3 trigger system will be discussed.

4.1. Event Reconstruction in the TPC

The offline event reconstruction procedure in the TPC uses the cluster/hit finder as a first step. Corrections to the hits are applied after the finding process. The reconstruction of trajectories is then performed on the basis of the coordinates of the found hits. The specific energy loss of the particle along its path, dE/dx , is calculated from the charges (ADC) of the accepted clusters on the track.

4.1.1. Cluster Reconstruction

A particle traversing the TPC ionizes molecules of the TPC gas. Electrons released in the ionization process along the particle trajectory knock other electrons out of the gas molecules, so that clouds of electrons (clusters) emerge. Due to a constant electric drift field, these clusters drift toward a segmented readout plane, where they induce a signal on the pads. The cluster coordinate is then derived from the x - y -position of the pads and through the clusters drift time, the longitudinal (z) position is obtained.

A pixel is the integer ADC value for a pad in a single time-bin. A cluster gives rise to a signal in consecutive pixels of adjacent pads. The task of the cluster finder (TCL) [73] [75] is to find groups of pixels and determine the center of gravity of the cluster with respect to the deposited charge.

The TPC zero suppressed raw data from the ASICs on the readout boards contain pixel information and are arranged in a format of potential clusters. The charge information of each pad is corrected for individual gain variations. To

4. Event Reconstruction

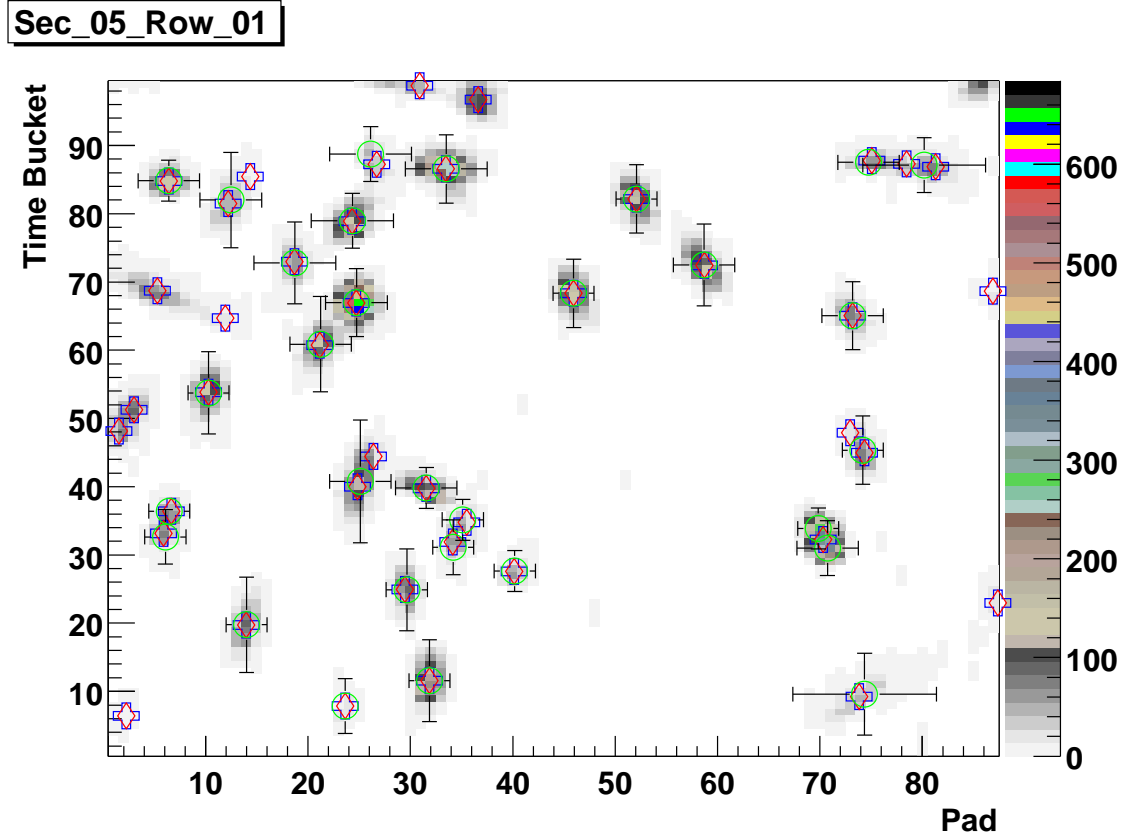


Figure 4.1.: TPC pixels in pad-time-space of padrow 1 in sector 5. Symbols show reconstructed clusters. Green circles with error bars: Off-line cluster finder (TCL, TPH). Red diamonds: On-line Level-3 trigger cluster finder run on the i960 CPUs during data-taking in 2000. Blue crosses: On-line cluster finder used with a different parameterization in the off-line reconstruction [74].

find clusters, the following procedure is performed: In a pixel sequence a center of gravities are determined. Then it is checked whether if in the sequence of a previous pad, center of gravities in the same time-bin range are found. If so, the according pixels are marked that they belong to clusters. This procedure is applied in each individual padrow, and results in a list of cluster centeroids in pad-time-space, where only clusters fulfilling certain quality criteria are accepted.

The hit finder (TPH) is applied to each cluster to reconstruct local peaks. In the case of merged clusters, this can happen if tracks are too close and clusters from these tracks merge into one, clusters are treated by a “multippeakfinder” algorithm [73]. In a central $^{197}\text{Au} + ^{197}\text{Au}$ event, typically 35 to 40% of the clusters have multiple hits [72]. Once a peak of a cluster is found, the hit position is extracted.

The hit position along the padrow is determined using a 3-point Gaussian fit. The position in time direction is determined by a weighted mean of the ADC values. The x - y -coordinates are then derived from the geometrical position of the padrow, and the z -coordinate is calculated by multiplying the time-bin position with the constant drift velocity. Figure 4.1 shows TPC pixels in pad-time-space. The uncertainties associated with each space point are estimated using hit residuals as a function of track crossing and dip angle.

At full magnetic field, the resolution of the cluster reconstruction reaches 0.5 (2.0) mm in padrow direction for small (large) padrow crossing angle and 1.0 (3.0) mm in the drift direction for small (large) dip angles [47].

4.1.2. Coordinate Transforms and Distortion Corrections

Before track reconstruction, the hit positions are translated from local sector coordinates (sector, row, pad, time) to global coordinates. The x and y coordinates can be calculated using geometrical transformations from the sector coordinates. However, the z coordinate requires knowledge of the drift velocity of the TPC gas mixture with a precision of 0.1%, as well as the offset of the first time-bin [47]. The drift velocity varies due to the dependence on atmospheric pressure and the gas mixture. To minimize this effect, the TPC is operated so that the electric field in the TPC corresponds to the peak in the drift velocity curve [47] [71]. Additionally, a laser calibration is performed before each run. Due to the known position of the laser beams inside the TPC, the drift velocity can be determined by measuring the drift time of clusters generated by the laser beam.

The offset of the first time-bin is constant over the full TPC volume and can be corrected by reconstructing the event vertex of a given event separately in the two halves of the TPC, and merging the resulting vertex positions.

At this level of the reconstruction procedure, differences between reconstructed hit positions and actual positions of the originating clusters caused by distortions are taken into account. Known effects which cause distortions are:

- $E \times B$ distortions are caused if field lines of the drift field (E-field) are not perpendicular to those of the magnetic field (B-field), due to field inhomogeneities.
- The crossing between the inner and outer sectors causes distortions which causes drifting electrons to be shifted towards the inner sectors, at padrow 13.
- The non-flat shape and tilt of the central membrane (cathode) and TPC endcaps causes an inhomogenous drift field.

4. Event Reconstruction

- The TPC is placed at a slight angular offset relative to the axis of the magnetic field.
- Misalignment between the inner and outer field cage causes a shift of hit coordinates.
- Space charge build up causes a shift of cluster coordinates in the area of high track density (effect is most dominant at the center of the TPC, when taking central $^{197}\text{Au} + ^{197}\text{Au}$ events).

The magnitude of the distortions are shown in Table 4.1. Although the distortions are all below 1 mm, they would have an impact on the momentum determination of tracks having high momentum and a large radius (e.g. $r = 33$ m at $p = 5$ GeV/ c). Distortions at the central membrane are most undesirable, since clusters from particle trajectories in this area have a long drift time.

In order to understand the distortions and correct for them, the magnetic field of the STAR magnet was mapped out with HALL and NMR probes before the TPC was installed, while the electric field was calculated taking the geometry of the TPC into account. Since the dependence of the field strength on the coordinates is known, the correct hit position along the padrows can be calculated as shown in [47]. The corrections to the hit coordinates are carried out before track reconstruction and reduce the relative error between a point and the track-model fit to 50 μm , while the absolute error for any point is about 500 μm [47].

Distortion	Magnitude of Imperfection	Magnitude of correction
Non-uniform B field	± 0.0040 T	0.10 cm
Geometrical effect between inner and outer sub-sectors	Exact calculation based on geometry	0.05 cm (near padrow 13)
Cathode - non-flat shape and tilt	0.1 cm	0.04 cm
Angular offset between E and B field	0.2 mr	0.03 cm
TPC endcaps - non-flat shape and tilt	0.1 cm	0.03 cm
Misalignment between IFC and OFC	0.1 cm	0.03 cm
Space charge build up in the TPC	0.001 C / ϵ_0	0.03 cm

Table 4.1.: Distortions, corrections applied to cluster coordinates, and distortion magnitudes [47].

4.1.3. Track Reconstruction

To reconstruct the trajectories along which charged particles traverse the TPC, the hit positions of reconstructed clusters are connected. The TPC tracking software (TPT) [75] uses the follow-your-nose algorithm, which has already been used in experiments such as NA49 at the SPS. It starts by connecting hits in the outermost padrows, where the track density is smallest, to form track seeds. Using the track seeds, a straight line parameterization is extrapolated inwards. Hits lying along this extrapolation are added to the original seeds and will define a track segment. Once a track segment has been defined, the associated hits are marked as used and a new seed is found to form another track segment. This process is continued until all track segments are found. Attempts are then made to add additional hits to the track segments that were not assigned to the track in the first place, starting with the largest segments. In contrast to the linear extrapolation used in the initial segment formation, a helix track model (Section 4.1.3) is used to predict the location of the next hit. Hits on the track are marked as used and added to the collection of points forming the track. The extension of the track segment continues inwards towards the interaction region in the centre of the TPC and then outwards, until no further hits can be assigned to the track. The last step in the tracking process is to merge split tracks.

Helix Parameterization

As already discussed in Section 3.3, the trajectory of a charged particle in a static uniform magnetic field with $\vec{B} = (0, 0, B_z)$ is a helix. To determine the helix parameters of a given track, a circle-line fit is performed in two independent procedures [46]: The transverse momentum associated with the track is obtained by fitting a circle to the collection of assigned hits projected onto the plane perpendicular (x - y) to the magnetic field vector (Figure 4.2a). A least squares fit of the track hits to a straight line in the bend (s - z) plane gives the longitudinal momentum along the beam axis, where s is the pathlength along the track (Figure 4.2b). The circle-line fits are performed within the errors of the reconstructed hits. The helix parameterization in STAR is given by the following [76]:

$$x(s) = x_0 + \frac{1}{\kappa} (\cos(\Phi_0 + h s \kappa \cos \lambda) - \cos \Phi_0) \quad (4.1)$$

$$y(s) = y_0 + \frac{1}{\kappa} (\sin(\Phi_0 + h s \kappa \cos \lambda) - \sin \Phi_0) \quad (4.2)$$

$$z(s) = z_0 + s \sin \lambda \quad (4.3)$$

where x, y, z are Cartesian coordinates expressed as functions of the pathlength s along the helix, (x_0, y_0, z_0) is the origin at $s = s_0 = 0$, λ is the dip angle, κ is the curvature ($\kappa = 1/r$), q is particle charge in units of positron charge, h is the

4. Event Reconstruction

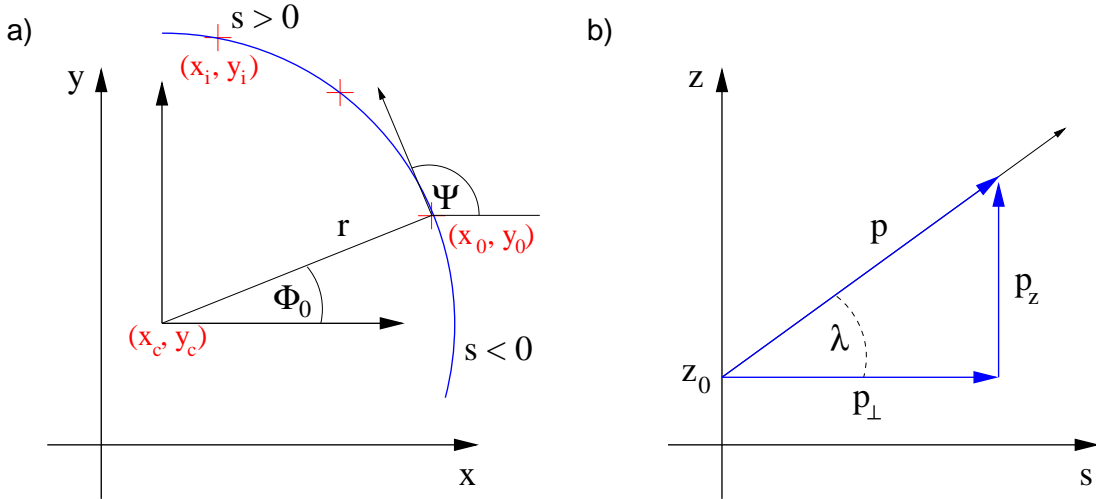


Figure 4.2.: a) Projection of a helix onto the transverse (x - y) plane. b) Projection onto the bend (s - z) plane.

direction of rotation of the projected helix in the x - y -plane ($h = -\text{sign}(qB) = \pm 1$), Φ_0 is the azimuth angle of the origin in cylindrical coordinates with respect to the helix axis ($\Phi_0 = \Psi - h\pi/2$), Ψ is the azimuthal angle of the track direction at the origin, i.e. $\arctan(dy/dx)_{s=0}$.

The parameters can be visualized with the aid of Figure 4.2, where in (a), a particle trajectory is projected onto the transverse (x - y) plane and appears as a circle. The projection onto the bend (s - z) plane illustrated in (b) shows a linear dependence of the longitudinal component z on the pathlength s , due to fact that the magnetic field lines are parallel to the particle trajectory in the longitudinal direction.

From these parameters, the transverse and longitudinal momentum (p_\perp , p_z) can be calculated using Equations 3.3 and 3.6. To calculate the momentum components of the particle trajectory (p_x, p_y, p_z), the helix has to be extrapolated to the origin, where the particle is produced (e.g. the main event vertex for a primary particle), in order to determine the azimuthal angle, Ψ , of the track direction at that point.

4.1.4. Particle Identification via dE/dx in the TPC

Particle identification in the TPC is performed by measuring a particle's specific ionization in the detector gas (dE/dx) and correlating it with the measured momentum as explained in Section 3.4.1. The ionization along the particle's trajectory is sampled by up to 45 clusters, measured in the padrows crossed by

the track. The ionization is measured by the summed cluster charge, taking the different amplification of pads from the inner and outer sectors into account, and dividing it by the track pathlength across the sensitive pad length. Due to the possibly large energy transfer between the traversing particle and the electrons of the gas molecules in hard collisions, the measured charge distribution follows a Landau distribution [79], with a long tail towards high cluster ionizations. The best estimate for the most probable value of the Landau distribution is the “truncated mean”, where the asymmetric tail is truncated (top 30% of the charge distribution) and the mean of the remaining almost Gaussian distributed sample is taken. The dE/dx versus momentum (p) is shown in Figure 4.3. The lines show the expected dE/dx for electrons (e), pions (π), kaons (K), protons (p) and deuterons (D), based on the Bethe-Bloch equation 3.8.

A high resolution dE/dx measurement is crucial for effective particle identification in the TPC. This requires calibration of the hardware and the TPC response, which depends on the physical properties of the TPC gas. The gain correction of each pad is applied before the clusters are found. The correction accounts for gain variations caused by the electronics and marks dead or noisy pads as unusable. The correction table is obtained from pulser data, where each channel is pulsed with an identical test signal during the beginning of each run.

The following corrections are applied after track reconstruction, where the measured ionization is compared with the expected Bethe-Bloch value for pions. The corrections account for local gas gain variations versus sector and row, and gas gain variations due to pressure and gas mixture [47] [78].

The best achievable dE/dx resolution in events of central $^{197}\text{Au} + ^{197}\text{Au}$ collisions used in the analysis in Section 5.1.1 was found to be 7.6% for tracks with 45 fit points on the track, while excluding merged clusters [72].

4.1.5. Global Track Model

A goal of the STAR experiment was to reconstruct the information of the several detector subsystems (e.g. SVT, TPC and EMC) as one global detector in a so-called “global event reconstruction” chain. This was still a work in progress in 2001. The data from the 2001 $^{197}\text{Au} + ^{197}\text{Au}$ run were reconstructed in the TPC first. In the case of the RICH detector, TPC tracks were then extrapolated and matched to the RICH detector information. However, the global tracking algorithm was applied to the TPC data only, after initial track finding with TPT. The global tracking algorithm is based on the Kalman Filter [80] approach, which allows simultaneous track reconstruction and fitting. The Kalman Filter refits the tracks found by TPT, taking multiple Coulomb scattering and energy loss in the beam pipe, IFC and TPC gas into account, assuming the particle is a pion. Multiple scattering is calculated [46], while the energy loss is modelled by

4. Event Reconstruction

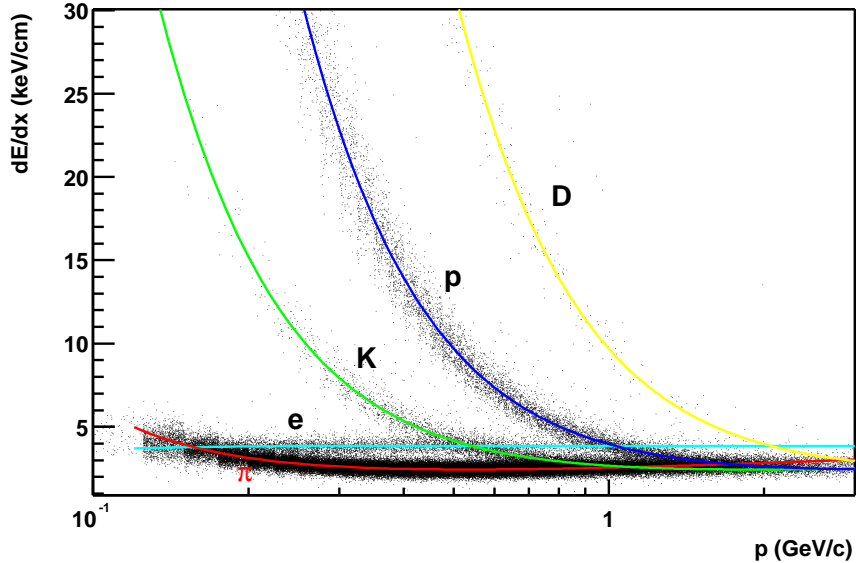


Figure 4.3.: Energy loss dE/dx as a function of reconstructed momentum (p). Lines show the values calculated using the Bethe-Bloch equation.

GEANT [82] using the STAR geometry. Incorrectly assigned and outlying hits are removed during the refit based on the hit errors provided by the clusterfinder (TCL/TPT). Reconstructed tracks passing the Kalman Filter are called global tracks. In the global track model, the number of hits that were used in the track fit, $N_{fit\ hits}$, are indicative of the track length (maximum is $N_{fit\ hits} = 45$).

The crosses in Figure 4.4 show the track finding efficiency dependency on the transverse momentum of global tracks. The efficiency was determined by embedding simulated pixels from tracks with a momentum of 0.5, 1, 2 and 5 GeV/ c into data of central $^{197}\text{Au} + ^{197}\text{Au}$ collisions taken at half magnetic field $B = 0.25$ T, using STAR's TPC response simulator (TRS) [77]. The events were then reconstructed and an analysis was carried out to determine if the embedded tracks could be found with $N_{fit\ hits} \geq 23$. The ratio of embedded to found tracks determines the reconstruction efficiency. The efficiency is found to be above 80% for momenta larger than 1 GeV/ c .

The open dots in Figure 4.5 show the transverse momentum resolution of global tracks determined with the same embedding technique as above. The momentum resolution ($\Delta p_{\perp}/p_{\perp}$) is determined from the fraction of momentum difference of the reconstructed embedded track and the momentum of the initial embedded track. Figures 4.4 and 4.5 also show the tracking efficiency and momentum resolution of the Level-3 trigger online reconstruction (to be discussed in Section 4.3).

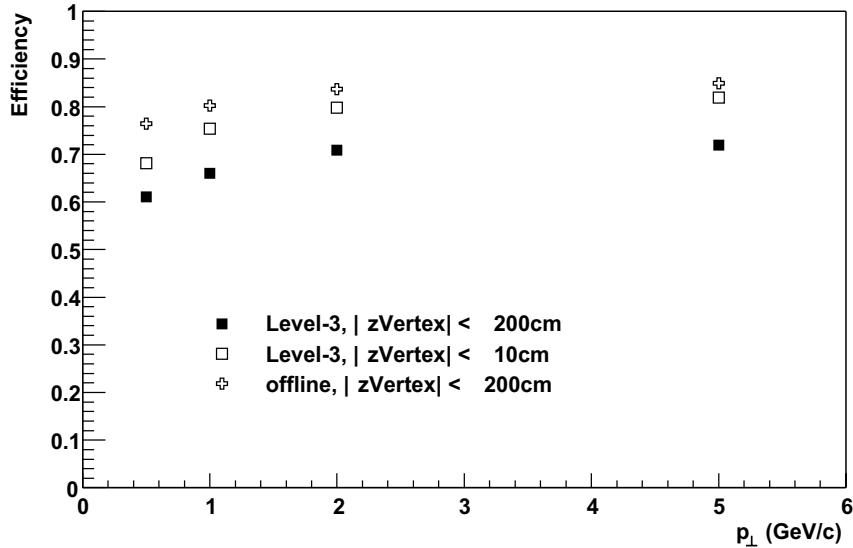


Figure 4.4.: Tracking efficiency of pions as a function of transverse momentum (p_{\perp}) in central $^{197}\text{Au} + ^{197}\text{Au}$ collisions.

4.1.6. Event Vertex Reconstruction

Knowledge of the event vertex position with a high accuracy is essential. With this knowledge, tracks originating from the event vertex (primary) can be distinguished from secondary (originating elsewhere) tracks.

The vertex is reconstructed by extrapolating the global tracks to a point (normally the beam position) on the x - y -plane, close to the estimated vertex. The global average is then taken, using a least-mean-square (LMS) method, where outliers are truncated. The process is repeated 3 or 4 times. The algorithm [81] achieves a vertex resolution of $350\ \mu\text{m}$ using the TPC data only. A 10 fold improvement in vertex resolution would be expected if SVT data were included.

4.1.7. Primary Track Model

In the primary track model, the primary vertex position is added to the track fit for tracks originating from the event vertex within a distance of closest approach $dca < 3.0\ \text{cm}$. The dca is the minimum distance between a particle trajectory extrapolated to the vertex and the event vertex position, as illustrated in Figure 4.6. Adding the primary vertex to the track fit can significantly improve the momentum resolution, since the primary vertex position is precisely measured and gives a long lever to a TPC track (distance from the event vertex of the first

4. Event Reconstruction

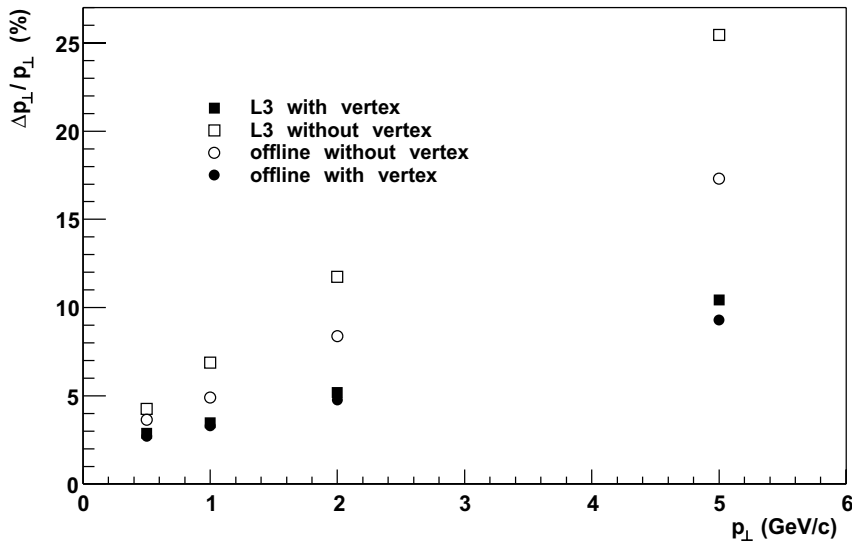


Figure 4.5.: p_{\perp} -Resolution (r.m.s.) of pions as a function of transverse momentum in central $^{197}\text{Au} + ^{197}\text{Au}$ collisions.

hit on the track in the TPC is $l > 55$ cm). When the trajectory is reconstructed from TPC hits effected by distortions, fitting the track with a primary track model does not necessarily improve the momentum resolution, since adding the primary vertex is a significant constraint. The solid dots in Figure 4.5 show the transverse momentum resolution of primary tracks using embedding as discussed in the previous section. The achieved momentum resolution is found to be better at high momentum when compared to the global track model (open dots).

4.2. RICH Event Reconstruction

The identification of particles in the RICH detector is done by detection of Čerenkov radiation produced by charged particles passing through the detector radiator. The Čerenkov radiation is emitted in a cone which has an opening angle, called the Čerenkov angle, determined by the velocity of the particle. Particles can be identified by correlating the Čerenkov angle with the momentum reconstructed in the TPC. As illustrated in Figure 3.9, the Čerenkov radiation is projected onto the CsI covered pads of the segmented pad plane. There, the Čerenkov photons are converted into photoelectrons by a CsI layer. The photoelectrons are amplified in the MWPC and thus ionization clusters are measured on the segmented pad plane. The charged particle itself produces a large charge cluster called a MIP (“MIP” stands for the energy loss/ionization of a “minimum

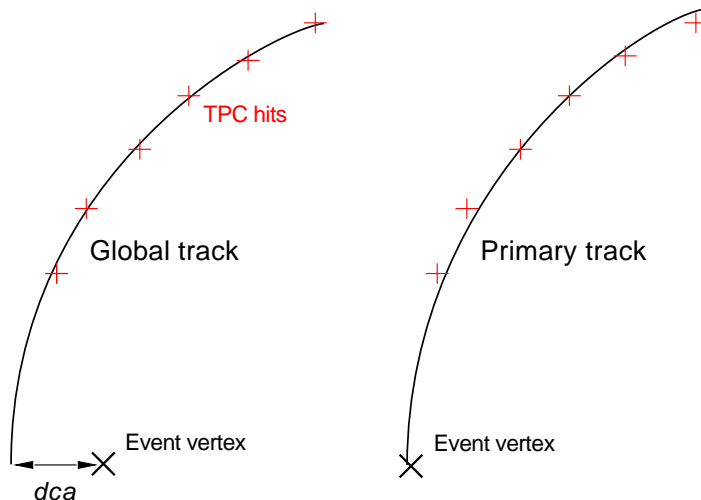


Figure 4.6.: Global and primary track model (see text).

ionizing particle”), marking its intersection point with the pad plane. A pad is characterized by its location and together with its ADC value, is referred to as a “pixel” (see Figure 4.7). A pedestal value is subtracted from each pad as a first step. The pedestal values are measured before each run. The mean ADC value of each pad is thus determined. The reconstruction of the charge clusters from Čerenkov photons or traversing tracks is then carried out. The impact point of a photon or track is referred to as a “hit” and is determined from the charge cluster information. A charge cluster is a collection of one or more pads associated with the charge avalanche produced by either a photoelectron or a single track ionization in the detector gas. The cluster finder algorithm begins by selecting an initial pixel from a set of pixels having ADC values above a certain threshold. Starting with this seed, any pixels adjacent to the initial pixel are added to the collection, thus defining the charge cluster. The hit position of the cluster is determined from the center of gravity of the cluster using the ADC value of each cluster pixel. Merging clusters and hits that are close together will undergo a refit [55].

The task of the pattern recognition software is to find a MIP and match its hit position with a primary TPC track which is extrapolated to the RICH pad plane [76]. The photon clusters around the MIP are correlated to a Čerenkov cone projection. When a particle is normally incident on the RICH detector, the projection of the cone produces a ring shape on the pad plane. In the case where the particle strikes the detector at non-normal angles, the produced patterns (Čerenkov fiducial area) on the pad plane are non-round. The extreme case is when particles are incident at angles of inclination of $\sim 25^\circ$ relative to the RICH radiator. In this case, Čerenkov light rays in the forward region suffer total

4. Event Reconstruction

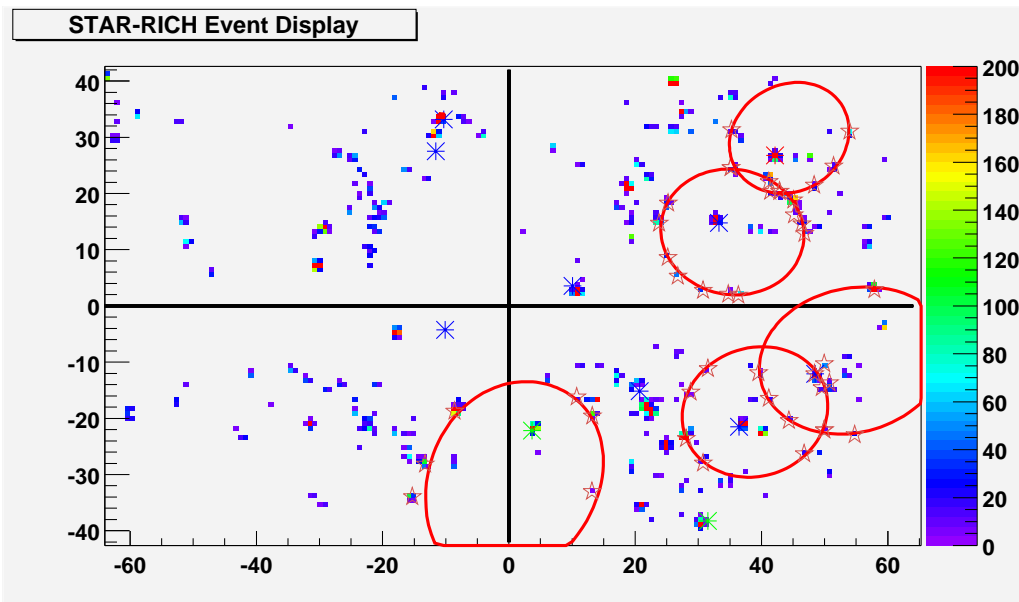


Figure 4.7.: Event display of the pad plane of the RICH detector. Dots indicate pixels with their corresponding ADC values (see color legend). Crosses indicate reconstructed hits from clusters from traversing particles (MIP) while stars indicate hit positions from photoelectron clusters. Red lines show projections of reconstructed Čerenkov cones.

internal reflection in the quartz exit window of the RICH detector, and only a part of the cone is projected onto the pad plane.

The frequency dependence of the Čerenkov light on the index of refraction (see Equation 3.10), and the depth of the radiator lead to a Čerenkov cone with a certain angular width. The Čerenkov spectrum ranges typically from $170 < \lambda < 220$ nm [55]. Using Eq. 3.16, 3.10 the angular width for the afore mentioned spectrum can be calculated to $\Delta\theta \sim 1.4^\circ$ for a particle traveling with $\beta = 1$.

The photon clusters around the MIP are correlated to a Čerenkov fiducial volume. For determining the ring diameter at a known momentum, hypothetical particle masses of pions, kaons and protons are assumed. The best fit of the cluster to the Čerenkov fiducial area is used, and the Čerenkov angle, θ is determined, by taking the refractive index of the materials, the light has to pass through, into consideration, [55].

Figure 4.8 shows the dependence of the reconstructed Čerenkov angle (θ) for pions (π), kaons (K) and protons (p) on their respective momenta (p). The solid lines show the expected Čerenkov angle using Equation 3.21 for a mean index of refraction of $\langle n \rangle = 1.29039$ (2001 run).

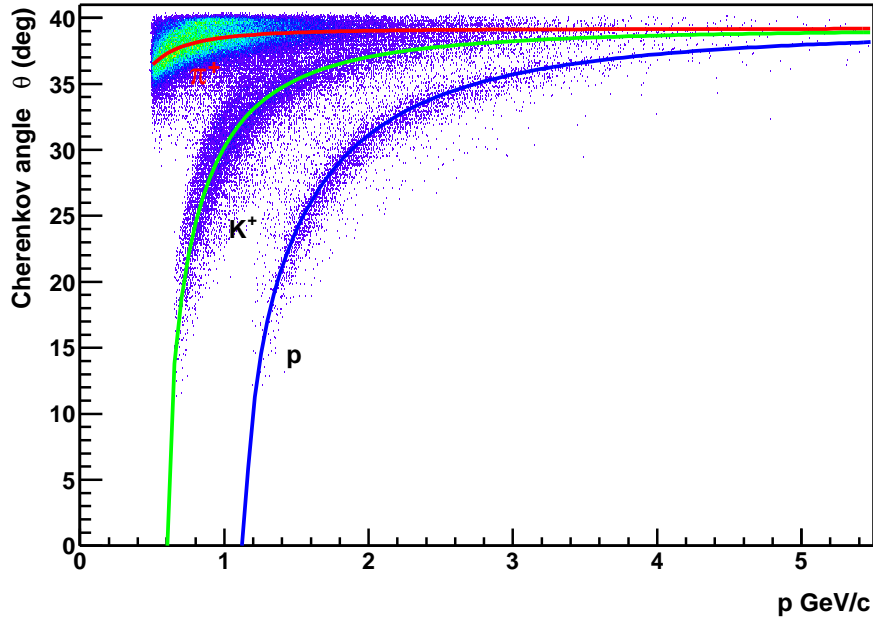


Figure 4.8.: Čerenkov angle versus momentum. The solid red, green and blue line indicate the calculated Čerenkov angle for pions (π), kaons (K) and protons (p).

4.3. On-line TPC Event Reconstruction

In this section, we give an overview of the TPC reconstruction software used on the Level-3 trigger processor farm. The fast Level-3 event reconstruction process is very similar to the off-line reconstruction described in Section 4.1. The fundamental difference is that the Level-3 trigger software is optimized for speed, to achieve short processing times and therefore compromises resolution and efficiency slightly. To illustrate this, consider that the off-line reconstruction of one event takes one minute on a single CPU, while it takes less the 200ms on the Level-3 processor farm, where 11 CPU nodes are reconstructing one event in parallel. The on-line cluster and track finder software will first be discussed and its efficiency and momentum resolution will be compared to the off-line software. We will then introduce the Level-3 RICH trigger algorithm and the online event display.

4.3.1. Cluster Reconstruction

The on-line cluster finder of the Level-3 trigger system performs fast cluster reconstruction on the 432 i960 processors of the TPC readout boards. The hit position is determined by the weighted mean of the pixel charge in pad and time-bin directions. The summed pixel charge (cluster charge) gives the ionization measurement which is used for the calculation of the specific energy loss of the particle, dE/dx , in the detector gas. An attempt is made to split merged clusters of tracks which are close together in both pad and time-bin direction using the cluster finder. The on-line cluster finder does not determine the uncertainties of the reconstructed cluster position. The red diamonds in Figure 4.1 show the reconstructed cluster position of TPC pixels in pad-time-space. The hit positions are very close to those reconstructed by the offline cluster finder (TCL/HTL). It is only in the case of merged clusters that the on-line cluster finder does not unfold the cluster as HTL does. The efficiency and resolution of the cluster finder was studied using embedding of pixels into data (see Section 4.1.5). The efficiency was found to be higher than 80% [70]. It was found that the efficiency of the on-line cluster finder is higher than the TCL in the region of sector boundaries, since TCL discards clusters that are cut by the sector borders [71]. Recent results have shown that keeping these clusters for tracking does not influence the quality of the tracking negatively. The on-line cluster finder has an average resolution that is only 3% worse than the off-line cluster finder [70]. The algorithm is optimized for efficient data formatting and uses the architecture of the i960 to an optimum [71]. The finding of ~ 140 k clusters of a central $^{197}\text{Au} + ^{197}\text{Au}$ event takes approximately 20 ms. The incoming zero suppressed raw data of ~ 6 MB/event are thereby reduced to ~ 2 MB/event containing the hit position, charge and flag.

4.3.2. Track Reconstruction

The on-line track finder associates reconstructed hits from the on-line cluster finder to tracks, and fits the corresponding hits with a helix track model. It runs on the 48 SLxx nodes of the Level-3 trigger, and was especially developed for online event reconstruction [83], where the main focus was on short processing times.

Before reconstruction, hit coordinates are translated from sector coordinates to global coordinates and corrections to the hit positions are performed using a look-up table [71].

The track finding algorithm uses the follow-your-nose method in conformal space and in s - z -space. As shown in Figure 4.2, a helix can be described as a circle in the x - y -plane and as a straight line in the s - z -plane. Using a circle as a model

for finding particle trajectories in x - y -space is not a favorable choice, since the radius is not known at the initial track finding. The hit coordinates (x, y) are therefore transformed into conformal space (x', y') according to

$$x' = \frac{x - x_t}{r^2}, \quad y' = \frac{y - y_t}{r^2} \quad \text{using} \quad r^2 = (x - x_t)^2 + (y - y_t)^2. \quad (4.4)$$

where (x_t, y_t) is a point on the trajectory. This can either be the origin of the track (vertex constraint) or the first point on the track (no vertex constraint). An example of this transformation can be found in [71]. Using this transformation, the track finding task is reduced to finding straight lines in conformal $(x'-y')$ and s - z -spaces.

The track parameter can be extracted from straight-line fits in conformal and s - z -spaces. The highest momentum resolution is achieved if a precisely known vertex position is used in the transformation. However, the track fit in conformal space then fails for secondary particle tracks. It is preferable to perform a helix-straight-line fit in Cartesian coordinates, after the initial track finding, where primary and secondary tracks can be fit simultaneously.

The event vertex position in the x - y -plane is well defined by the small beam size (1.0 mm) and the almost constant beam position during the 2001 run. However, the z vertex position distribution, restricted by the ZDC coincidence trigger to $|z \text{ vertex}| < 35$ cm (see Section 5.1.3) is much wider. Accordingly, in 2001, the algorithm reconstructed the tracks using the nominal beam position (x, y) as a starting point in conformal space, but refitted the tracks in Cartesian coordinates without including the vertex position in the fit. Thus, tracks reconstructed by the Level-3 trigger do not use the primary track model. In the on-line case, the number of hits that were assigned to the track during finding, N_{hits} , are indicative of the track length.

Figure 4.4 compares the tracking efficiency of on-line reconstruction with off-line reconstruction. At higher transverse momenta and for event z vertices close to the center of the TPC (mainly the case in 2001), the on-line tracking efficiency reaches the off-line efficiency for higher transverse momenta. When comparing the efficiency of the on-line reconstruction with the efficiency of the off-line reconstruction, it must be remembered that in the off-line case, the whole TPC is tracked at once. However, in the Level-3 trigger case, two TPC sectors are tracked by one SLxx node, and a GL3 node builds an event from all SL3 nodes which analyse the event in parallel. This results in splitting of tracks at sector boundaries, where the splitting is most dominant for low momentum tracks ($p_{\perp} \leq 0.5$ GeV/ c) with a small radius.

A comparison of the momentum resolution of the on- and off-line analyses is shown in Figure 4.5. For track fitting which do not include the vertex position, the momentum resolution is ~ 1.5 (2.5) times worse than that achieved with the

4. Event Reconstruction

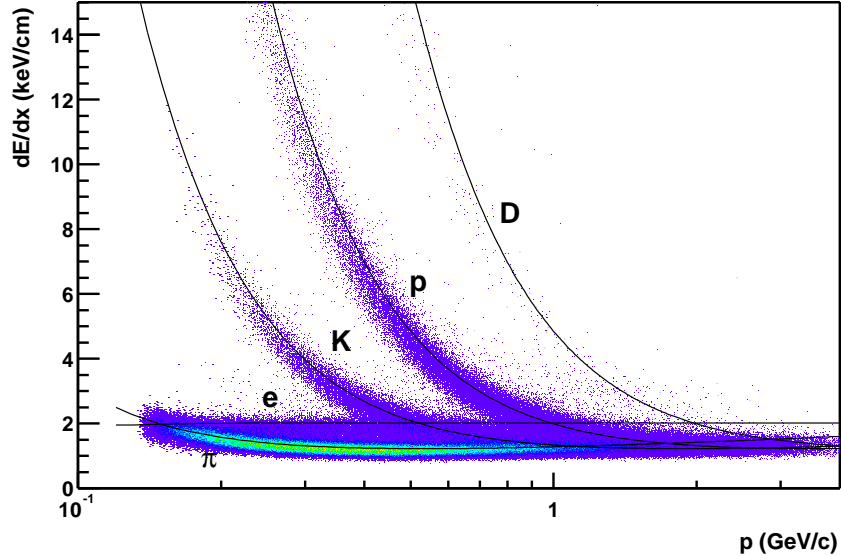


Figure 4.9.: Energy loss dE/dx as a function of reconstructed momentum (p) calculated on-line. Lines show the Bethe-Bloch predictions for electrons (e), pions (π), kaons (K), protons (p) and deuterons (D).

global (primary) track model in the off-line analysis. In 2001, track fits which did not include the vertex position was the default mode which also allowed reconstruction of secondary tracks. However, for tracks refit with the vertex position, the momentum resolution of on-line reconstructed tracks is very close to that for primary tracks reconstructed off-line.

As in the off-line reconstruction case, the specific energy loss dE/dx due to gas ionization of a particle when traversing the TPC is determined. The truncated mean is calculated from the summed cluster charges given by the on-line cluster finder, discarding the highest 30% of cluster charges and dividing by the pathlength along the padrows. Due to the processing time constraints, the pathlength across a padrow is approximated by a straight line. Only, for those tracks having $N_{hits} \geq 15$, the dE/dx is calculated. In contrast to the off-line case discussed in Section 4.1.4, second iteration corrections cannot be applied in on-line reconstruction, so that no further calibration of the dE/dx is carried out. For the on-line reconstruction case, Figure 4.9 shows the dependence of the energy loss dE/dx on the momentum. The bands for electrons, pions, kaons, protons and deuterons are similar to the values predicted by the Bethe-Bloch equation. Due to a smaller gain ($\sim 50\%$), used for the dE/dx calculation, the absolute dE/dx values are approximately half the amount compared the offline dE/dx (see Figure 4.3). From a Gaussian fit to the proton band at a momentum range of $0.5 < p_{\perp} < 0.6$ GeV/c

(see Section 5.1.11) measured with at least 23 ionization samples (clusters) in the TPC, a dE/dx resolution of 11.3% can be determined. The result is comparable to that achieved with the off-line analysis, where the resolution is found to be $\sim 9\%$ for pions, having the same number of ionization samples [72].

4.3.3. Vertex Determination

In the $^{197}\text{Au} + ^{197}\text{Au}$ run in 2001, the event vertex position was used as a cut criterion in the trigger algorithms and for the determination of track dca . The dca was used to determine if a given track could be considered as a primary or secondary track.

The calculation of the event vertex is performed within the framework of the GL3 software, and the event vertex position is then available for all algorithms. Considering the time available for vertex finding (a few ms), a fast algorithm which delivers a sufficiently high vertex resolution was employed. Since in 2001 no absolute beam position was available to the Level-3 trigger system, each track having more than $N_{hits} > 14$ and a momentum $p > 0.25 \text{ GeV}/c$ was extrapolated to the position of the nominal beam line in the x - y -plane (0.0,0.0), which was taken as track origin. The coordinates in x, y, z from this calculation were then sorted into histograms with a bin width of $\Delta x, \Delta y = 0.2 \text{ cm}$ in the x - y -plane and a bin width of $\Delta z = 0.5 \text{ cm}$ in longitudinal direction. For each histogram, the maximum was found and a weighted mean was calculated, taking the 3 nearest bins from the maximum into consideration. A second iteration was performed where the accepted tracks were extrapolated to the x and y vertex position determined in the first step.

Figure 4.10a shows the x and y vertex position of central $^{197}\text{Au} + ^{197}\text{Au}$ events calculated by the off-line vertex finder (see Section 4.1.6). The x and y vertex position of the same events determined by the L3 trigger on-line analysis is shown in Figure 4.10b. The difference between the mean vertex position is $\sim 1 \text{ mm}$, where the on-line method shows the tendency to introduce a bias towards the nominal beam line position. The difference in the z vertex position of the off-line and on-line z vertex position is shown in Figure 4.11. The well centered distribution has an r.m.s. width of 0.17 cm. The slight difference in the vertex determination had to be taken into account in the L3 trigger algorithms when applying cuts on the event vertex and dca .

4. Event Reconstruction

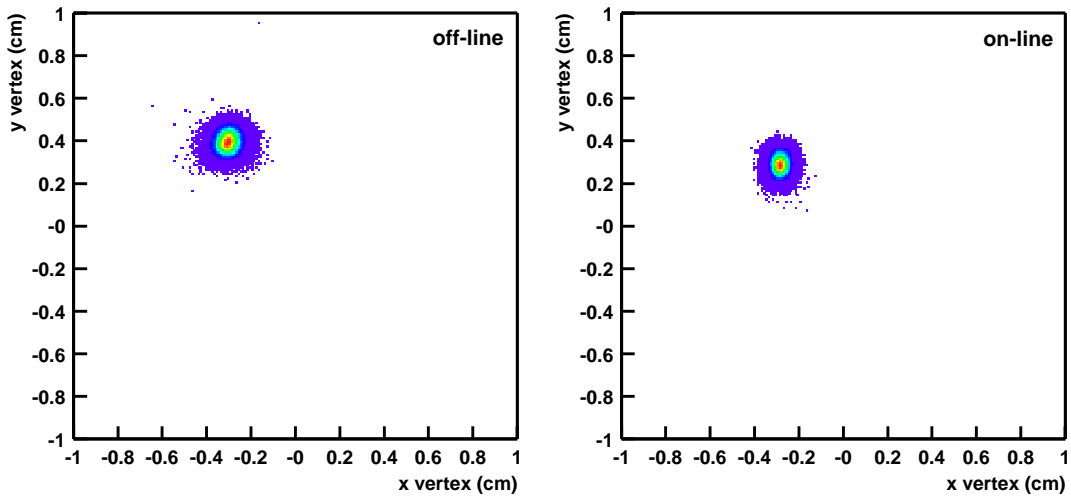


Figure 4.10.: Off and on-line reconstruction of the event x - y -vertex.

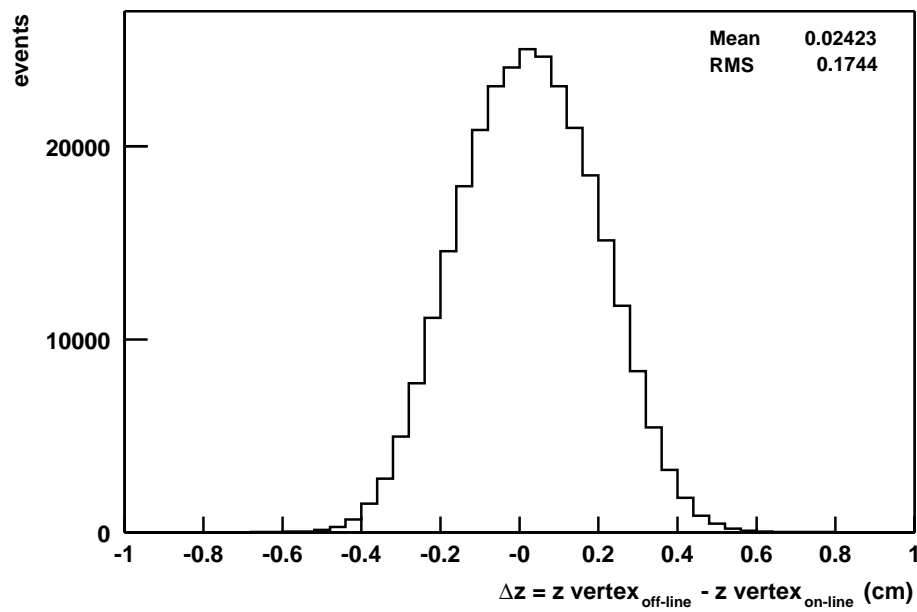


Figure 4.11.: Difference (Δz) of the off and on-line reconstructed event z vertex.

4.3.4. Level-3 RICH algorithm

The Level-3 RICH algorithm was one of the trigger algorithms (see Section 3.8.1) that was run on the global nodes (GLxx) of the Level-3 trigger. The task of the algorithm was to select events with a particle having a high momentum within the acceptance region of the RICH detector ($|\eta| < 0.3$, $\Delta = 20^\circ$).

For the 2001 $^{197}\text{Au} + ^{197}\text{Au}$ run, a collision rate of ~ 2.4 kHz (design luminosity) was expected at the STAR interaction region. The DAQ storage rate was expected to be 5 Hz. The number of charged hadrons with a momentum of $p > 1$ GeV/ c in the acceptance of the RICH detector ($|\eta| < 0.3$, $\Delta = 20^\circ$) has been measured to be approximately one per central $^{197}\text{Au} + ^{197}\text{Au}$ collision at $\sqrt{s_{NN}} = 130$ GeV. The number of charged hadrons decreases by approximately a magnitude per GeV/ c in momentum. Thus every ~ 100 event, a charged particle having a momentum $p > 3$ GeV was measured in the acceptance of the RICH detector. The goal for the 2001 run was to collect a sample of ~ 5 million events, yielding to a total of $\sim 50\text{k}$ (0.5k) hadrons with a momentum of $p = 3$ (5) GeV/ c , respectively.

From the previous run and the Level-3 trigger fully equipped with 48 SL3 nodes, a maximum processing rate of ~ 50 Hz for central $^{197}\text{Au} + ^{197}\text{Au}$ collisions at RHIC design luminosity was expected. Accordingly, the Level-3 trigger was employed to select events with a hadron having a momentum of $p > 3$ GeV/ c in the acceptance of the RICH detector (named RICH candidates). Using such a trigger, the event sample could be enhanced with high momentum ($p > 3$ GeV/ c) hadrons of up to factor 10, since the Level-3 trigger could process 10 times the number of events that could be written to HPSS by the DAQ. Therefore, 0.5 million RICH candidates were expected.

The trigger criterion for a Level-3 RICH algorithm had to be optimized (see Section 5.2.4), so that the cut would be loose enough to result in a good efficiency, but tight enough to keep the trigger rate at an acceptable level. The cuts were derived from the RICH analysis of 2000 run data [92] [55]. The event z vertex was restricted to $|z \text{ vertex}| < 25$ cm. Reconstructed tracks were required to have more than 20 TPC points, within a pseudorapidity range of $|\eta| < 0.3$, a momentum $p > 2.7$ GeV/ c , a $dca < 10$ cm and had to be extrapolated to the area covered by the RICH detector. Cuts were applied in this order to keep the number of tracks that had to be extrapolated to the RICH detector surface small, since the track extrapolation [76] was the most time consuming task. The algorithm consumed ~ 10 ms of CPU time on a GL3 node.

This set of cuts was tested on $^{197}\text{Au} + ^{197}\text{Au}$ events taken in 2000. Figure 4.12a shows a $^{197}\text{Au} + ^{197}\text{Au}$ event drawn with the on-line event display. All tracks within the acceptance of the RICH are extrapolated to the detector volume (the RICH is shown from the side). Figure 4.12b shows the same event, where only

4. Event Reconstruction

tracks with a momentum $p > 1.5 \text{ GeV}/c$ are drawn. One track with a momentum $p > 3 \text{ GeV}/c$ remains in the acceptance of the RICH detector. All other event and track criteria required by the algorithm are also fulfilled by this event/track. This event would thus be accepted by the L3 Trigger.

4.3.5. Online Event Visualization

The on-line event display (L3GViewer) [85] uses the on-line reconstruction of the Level-3 trigger to display reconstructed hit positions and trajectories. The event display serves two purposes. The first is to visualize a fraction of events, a few seconds after they were triggered, during data taking. The second purpose is to act as a tool to display cluster and track parameters for a visual control of detector performance and on-line reconstruction quality.

The display draws the outer detector geometry as a wire frame. Reconstructed clusters (hits) are drawn as dots and particle trajectories are represented as lines. Clusters and tracks are colored according to their gas ionization, where red (blue) is indicative of high (low) ionization. In 2000, only TPC data were drawn (see Figure 2.4). With the integration of the FTPC and the SVT into the Level-3 trigger, these detectors were added to the display as well (see Figure 2.7 and [70]). Additionally, TPC tracks within the acceptance of the RICH detector were extrapolated to the sensitive detector volume, which is drawn as a flat rectangle (see Figure 4.12). The extrapolation of TPC tracks to the RICH detector was used as a visual control of the Level-3 RICH trigger algorithm during data taking. Thereafter, it was used to optimize the efficiency of the algorithm on an event sample stored on L3EVP. It is possible to apply cuts on cluster (e.g. position, charge), track (e.g. N_{hits} , p_{\perp} , η) and event (e.g. z vertex, trigger word) variables to display events with certain characteristics only.

In a central $^{197}\text{Au} + ^{197}\text{Au}$ collision, $\sim 140\text{k}$ clusters and $\sim 2.8\text{k}$ tracks are drawn by the display. The L3GViewer uses the *OpenGL* graphics library, together with a 3D graphics card (NVidia GForce) on a Linux workstation, so that mouse-controlled operations like panning, rotating and zooming can be performed in real time without any significant delay. The program is based on the *Qt* library [85].

The event display was used in 2000 and 2001, together with an on-line monitor (L3Online) [70], which is a histogramming tool and displays distributions of event (e.g. z vertex, trigger word) and track parameters (e.g. N_{hits} , p_{\perp} and η) on an event-by-event or on a run-by-run basis.



Figure 4.12.: top) Event of a central $^{197}\text{Au} + ^{197}\text{Au}$ collision where on-line reconstructed TPC tracks are extrapolated to the RICH volume. bottom) Event accepted by RICH Level-3 algorithm: One high momentum track fulfills the trigger criteria.

4. *Event Reconstruction*

5. Analysis of Anti-Proton to Proton Ratio

An analysis of the anti-proton to proton ratio, \bar{p}/p , in $^{197}\text{Au} + ^{197}\text{Au}$ collisions at a center of mass energy of $\sqrt{s_{NN}} = 200$ GeV is presented in this chapter. All data for this analysis were collected during the second year of RHIC operation. Anti-protons and protons were identified by correlating their energy loss due to ionization of the TPC gas, dE/dx , with the measured momentum (see Section 4.1.4). This allows an identification of anti-protons and protons at mid-rapidity ($|y| < 0.5$) in the transverse momentum range of $0.4 < p_{\perp} < 1.0$ GeV/ c . The events were reconstructed using the STAR off-line analysis software. A similar analysis, using on-line reconstructed events from the Level-3 Trigger system was also employed. Both analysis methods are described in this chapter, and both results are compared. The analysis of the ratio from 10% central $^{197}\text{Au} + ^{197}\text{Au}$ collisions at high transverse momentum ($1.3 < p_{\perp} < 4.5$) GeV/ c is presented in Section 5.2. The ring imaging Čerenkov detector (RICH), covering $|\eta| < 0.3$, $\Delta\phi \sim 20^\circ$ at $\phi = 60^\circ$ (see Section 3.4.2), was employed for anti-proton and proton identification. Thus the measurement of the anti-proton to proton ratio at high transverse momentum is limited to a small but symmetric acceptance at mid-rapidity. Section 5.3 concludes with the combined result from the low and high transverse momentum analysis.

5.1. \bar{p}/p at Low Transverse Momentum

For the mid-rapidity \bar{p}/p analysis at low transverse momentum, the time projection chamber (TPC) in the magnetic field of the STAR magnet was employed to detect and identify anti-protons and protons. The ZDC provided a trigger for minimum bias, and the ZDC and CTB a trigger for central events of $^{197}\text{Au} + ^{197}\text{Au}$ collisions.

TPC data, which were reconstructed by the STAR off-line reconstruction software are analyzed. The various steps of the analysis are presented in this section. Firstly, the datasets used in the analysis are introduced. The method used to

5. Analysis of Anti-Proton to Proton Ratio

identify anti-protons and protons in the TPC is explained. The detector acceptance and the corrections to the identified anti-proton and proton raw yields are subsequently discussed. The corrections to the anti-proton to proton ratio include corrections for secondary protons generated in, and anti-protons absorbed by, the detector material. A momentum correction due to energy loss of anti-protons and protons passing through the detector has also been applied. The systematical error for the anti-proton to proton ratio measurement is estimated by varying the selection criteria applied to the data. Finally, the results of the STAR off-line event reconstruction are compared to the Level-3 Trigger on-line event reconstruction.

5.1.1. Dataset

$^{197}\text{Au} + ^{197}\text{Au}$ collisions at a center of mass energy of $\sqrt{s_{NN}} = 200$ GeV are analyzed. The data were collected during the second year of RHIC operation (see Section 2.5). Two datasets were used for the analysis:

1. One million events taken with the minimum bias trigger. This dataset includes the entire range from peripheral to central $^{197}\text{Au} + ^{197}\text{Au}$ collisions. Events were taken with the run type “productionMinBias”.
2. One million central events, taken with the Level-0 central trigger that selects the 10% most central $^{197}\text{Au} + ^{197}\text{Au}$ collisions. The run type for these central events was “productionCentral”.

For each dataset, part of the data was taken with the STAR magnet being operated with a full magnetic field of $B = 0.5$ T, while the remainder was taken with a reverse full magnetic field of $B = -0.5$ T. Data were reconstructed with the STAR off-line software (production library version P02gc+P02gd).

5.1.2. Trigger Operation

To trigger a $^{197}\text{Au} + ^{197}\text{Au}$ collision, STAR uses the ZDCs (east+west) and the CTB. Figure 5.1 shows the correlation of the ZDC sum to the CTB sum. These Events were triggered using the ZDC sum. Collisions between nuclei having a large impact parameter, b , due to a small geometric overlap, result in a small number of dissociation neutrons being detected in the ZDC, resulting in a low CTB sum. This class of events occupy the lower left corner of Figure 5.1.

For events taken with run type “productionMinBias” a CTB sum of at least 75 counts was required. This rejected ultra peripheral collisions [87]. A smaller impact parameter between the colliding nuclei results in a larger number of neutrons

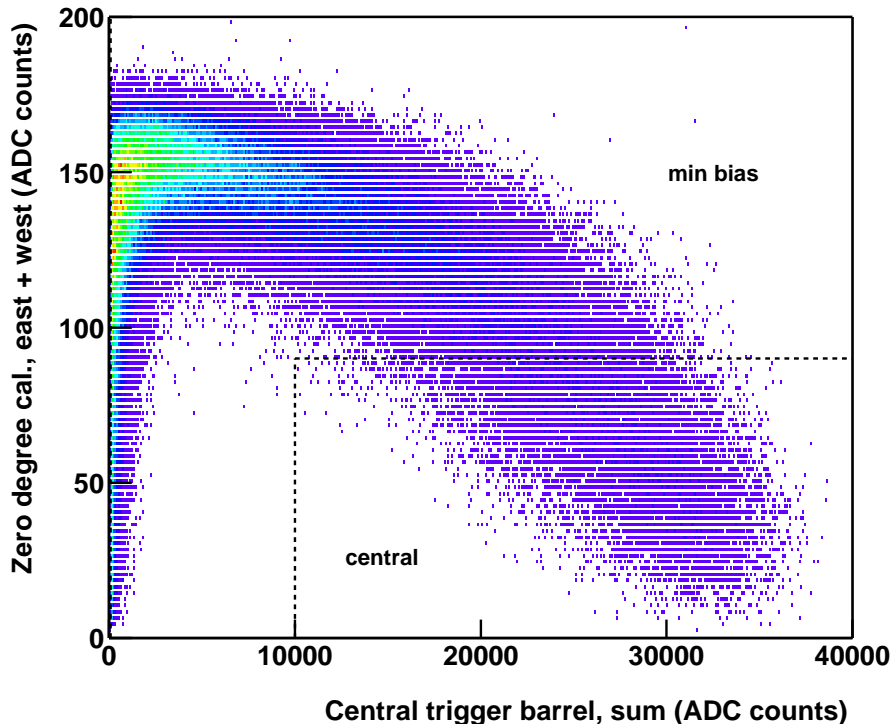


Figure 5.1.: The summed east+west ZDC signal versus the summed CTB signal from $^{197}\text{Au} + ^{197}\text{Au}$ collisions at $\sqrt{s_{NN}} = 200$ GeV taken in 2001. Central events are characterized by a high ADC count sum in the CTB and a small ADC count sum of the ZDC.

detected in the ZDCs, along with a larger CTB signal, indicating an increase in particle production at mid-rapidity. At high impact parameters a point is reached where the centrality is high enough such that most of the neutrons are in the reaction volume of the collision. This leaves fewer spectator neutrons to be emitted which leads to a small ZDC sum. Thus the particle multiplicity, along with the corresponding CTB signal, grows with the centrality of the collision while the ZDC signal decreases.

The lower right end of the “boomerang” in Figure 5.1 corresponds to the most central events, where the CTB sum is largest and the ZDC sum is very small. This characteristic distribution is used to trigger on central events. On Level-0 a trigger is implemented to take central events. It requires an CTB sum of at least 10000 ADC counts and a ZDC sum of less than 90 ADC counts. This requirement selects the 10% most central events, determined by the event multiplicity, based on a Glauber calculation (see Section 1.2.1). Figure 5.20a illustrates the correlation of the ZDC sum and the CTB sum given by the central trigger in a “productionCentral” run.

5.1.3. Vertex Position Determination

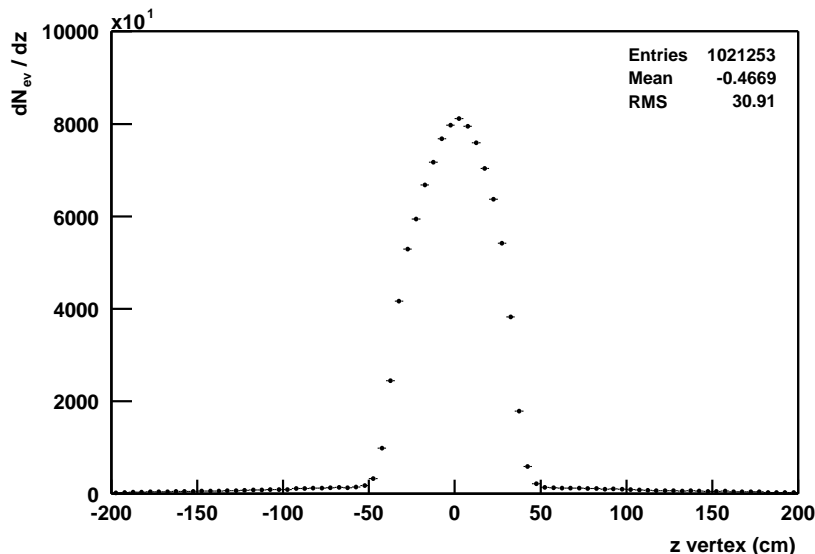


Figure 5.2.: Longitudinal event vertex (z vertex) distribution of minimum bias events from $^{197}\text{Au} + ^{197}\text{Au}$ collisions at $\sqrt{s_{NN}} = 200$ GeV.

In the 2001 $^{197}\text{Au} + ^{197}\text{Au}$ run, the r.m.s. width of the longitudinal collision vertex distribution was ~ 86 cm in the STAR intersection region [89]. To narrow the vertex distribution, a ZDC timing trigger at Level-0 was employed during data taking. This timing trigger is used to eliminate events with a $|z \text{ vertex}| > 35$ cm. Figure 5.2 shows the z vertex distribution of events taken with this ZDC timing trigger. In order to avoid a centrality bias, caused by the resolution of the z vertex trigger (see Section 3.5.1), an event vertex cut of $|z \text{ vertex}| < 25$ cm was chosen. About $\sim 72\%$ of the events taken with run type “productionMinBias” and 76% of the events taken with “productionCentral” pass the z vertex cut.

5.1.4. Centrality Considerations

The correlation between produced particles and impact parameter, b , in a given collision (see Section 1.2.1) is used to determine the collision centrality by measuring the event multiplicity. Events taken with the run type “productionMinBias”, consist of peripheral (large b) to central collisions (small b). Figure 5.3 shows the multiplicity distribution from accepted minimum bias events that pass a cut of the longitudinal vertex of $|z \text{ vertex}| < 25$ cm. Counterd is the number of tracks that are measured with $N_{fit \ hits} \geq 10$, $dca < 3$ cm and $|\eta| \leq 0.5$ in the TPC. The multiplicity distribution is not corrected for detector efficiencies and does

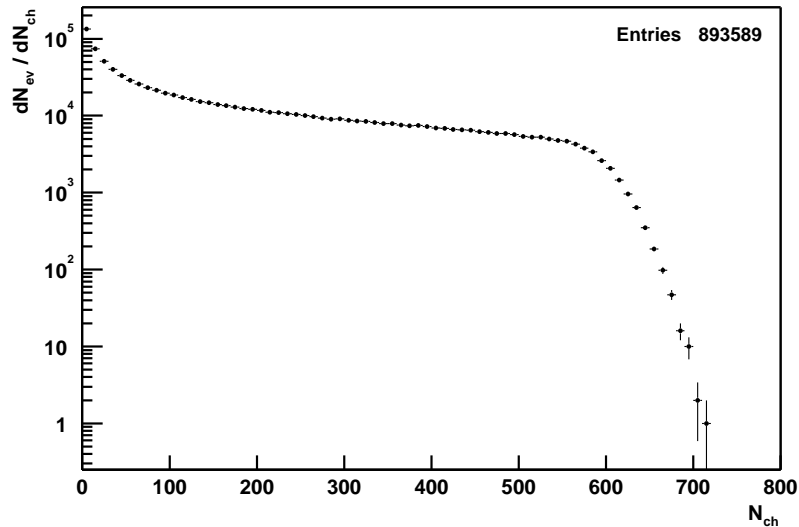


Figure 5.3.: Uncorrected distribution of charged particles (N_{ch}) per event of minimum bias events from $^{197}\text{Au} + ^{197}\text{Au}$ collisions at $\sqrt{s_{NN}} = 200$ GeV, divided into 9 centrality classes.

not, therefore, represent a precise measurement of the total event multiplicity. However, it can be used to estimate the centrality of the collision. The sample is divided into 9 centrality classes. The mapping between multiplicity of charged particles, N_{ch} , and centrality is shown in Table 5.1. This classification is used to study the production of the produced particles, depending on the centrality of the collision, i. e. b . Events taken under run type “productionCentral” with the central trigger on Level-0 correspond to centrality classes 8+9 of the “productionMinBias” run.

Class	Centrality (%)	N_{ch} cut (\geq)
1	80	14
2	70	30
3	60	56
4	50	94
5	40	146
6	30	217
7	20	312
8	10	431
9	5	510

Table 5.1.: Centrality classes for minimum bias events dN_{ev}/dN_{ch} distribution. Shown in Figure 5.3 [90].

5.1.5. Detector Acceptance

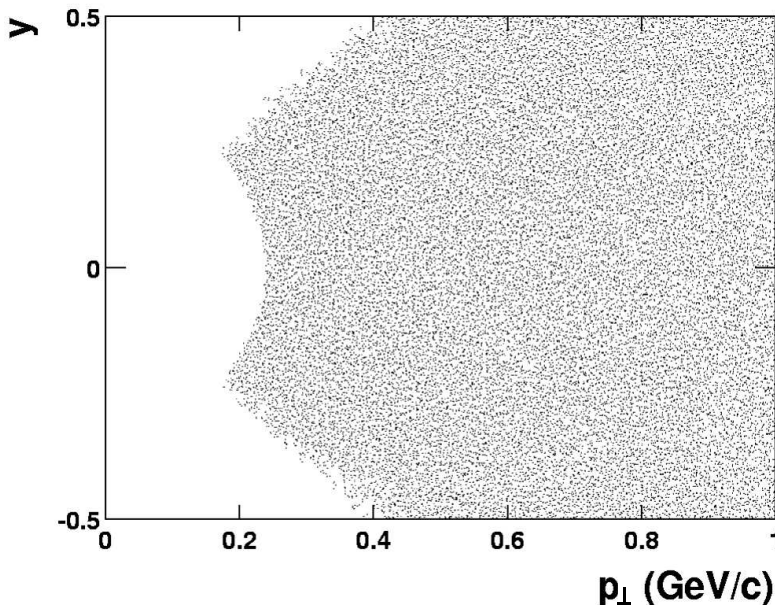


Figure 5.4.: Acceptance within $|\eta| \leq 0.5$ for anti-protons and protons in the TPC ($B = \pm 0.5$ T).

The STAR experiment has a wide and uniform acceptance around mid-rapidity. Figure 5.4 shows the acceptance within the pseudorapidity range of $|\eta| \leq 0.5$ for anti-protons and protons in the TPC, operated in the full magnetic field of $B = 0.5$ T. The rapidity, y , versus the transverse momentum, p_{\perp} , shows identified protons measured with $N_{fit\ hits} \geq 23$ in the TPC, a cut that is used throughout the present analysis.

At large rapidities, the dip angle of the track is so small that the protons leave either less than 23 hits in the TPC, or they miss the acceptance of the TPC completely. At much higher rapidities they would be seen in the forward time projection chamber (FTPC). However, the FTPC is not capable of providing particle identification (see Section 3.4.3).

At full magnetic field, low momentum tracks ($p_{\perp} < 0.2$ GeV/c) are either bent too much to reach the TPC volume, or do not create a sufficiently high number of hits in the detector volume. At half magnetic field of $B = 0.25$ T, the transverse momentum range extends down to $p_{\perp} = 0.1$ GeV/c, which means sacrificing momentum resolution. Mid-rapidity protons traversing the TPC with a transverse momentum, $p_{\perp} > 1.0$ GeV/c, are not limited by the acceptance of the TPC, but they can not be identified via their specific energy loss (dE/dx), discussed in the next section.

5.1.6. Proton Identification

In Section 4.1.4, the method of particle identification via the specific energy loss (dE/dx) in the TPC gas is introduced. Correlating dE/dx with the momentum yields the particle identity. Figure 4.3 illustrates the particle energy loss, dE/dx , versus momentum (p) for electrons, pions, kaons, protons and deuterons. Below a momentum of $p < 1$ GeV/ c the observed particle species are clearly separated. Figure 4.3 shows only positive particles, the correlation looks the same for negative particles. For TPC operation in the full magnetic field ($B = 0.5$ T), anti-protons and protons are well identified in the transverse momentum range from $0.28 < p_{\perp} < 1.0$ GeV/ c . At higher transverse momentum, the proton band merge with the bands of pions and kaons. It should also be noted that the proton band overlaps with the electron band for momenta in the range $0.8 < p_{\perp} < 1.0$ GeV/ c . This causes contamination of identified proton yields by electrons. For extraction of anti-proton and proton yields, a quantity known as the Z quantity was used, and it is defined as

$$Z(m, p) = \ln \left(\frac{dE/dx}{(dE/dx)_{BB}(m, p)} \right) \quad (5.1)$$

where dE/dx is the measured ionization of the detector gas, $(dE/dx)_{BB}$ is the expected ionization from the Bethe-Bloch equation (Eq.3.8) for the observed particle species with mass, m , and momentum, p . The Z quantity gives a Gaussian distribution of the particle species centered at zero.

Z -distribution from reconstructed global tracks were taken in $\Delta p_{\perp} = 0.05$ GeV/ c wide transverse momentum bins, in the transverse momentum range from $0.3 < p_{\perp} < 1.0$ GeV/ c . The accepted tracks within the rapidity region of $-0.5 < y < 0.5$ were required to have $N_{fit\ hits} \geq 23$ in the TPC. This hit cut removes split tracks and it insures a dE/dx resolution of $\sigma \leq 9\%$ [72]. In Figure 5.5, four characteristic Z -distribution are shown. The Gaussian yield of anti-protons and protons is centered at zero. The yields of lighter particles are situated at the left of the proton yield. Figure 5.5a shows the Z -distribution of particles with transverse momentum in the range $0.35 < p_{\perp} < 0.4$ GeV/ c . The proton yield is clearly separated from the kaon, electron and pion yields. The higher the transverse momentum (Figure 5.5b, c, d), the smaller the separation between the different particle species. The yields merge completely at $p_{\perp} > 1.0$ GeV/ c . The yields of pions, kaons and protons were fit by a 3 Gauss fit function

$$f(Z) = \frac{A_{\pi}}{\sigma_{\pi} \sqrt{2\pi}} e^{-\bar{Z}_{\pi}^2/2 \sigma_{\pi}^2} + \frac{A_K}{\sigma_K \sqrt{2\pi}} e^{-\bar{Z}_K^2/2 \sigma_K^2} + \frac{A_p}{\sigma_p \sqrt{2\pi}} e^{-\bar{Z}_p^2/2 \sigma_p^2} \quad (5.2)$$

where A_i is the area, σ_i is the width and \bar{Z}_i is the mean of each fit denoted by $i=\pi, K, p$ for pions, kaons and protons, respectively. Generally, the fit function

5. Analysis of Anti-Proton to Proton Ratio

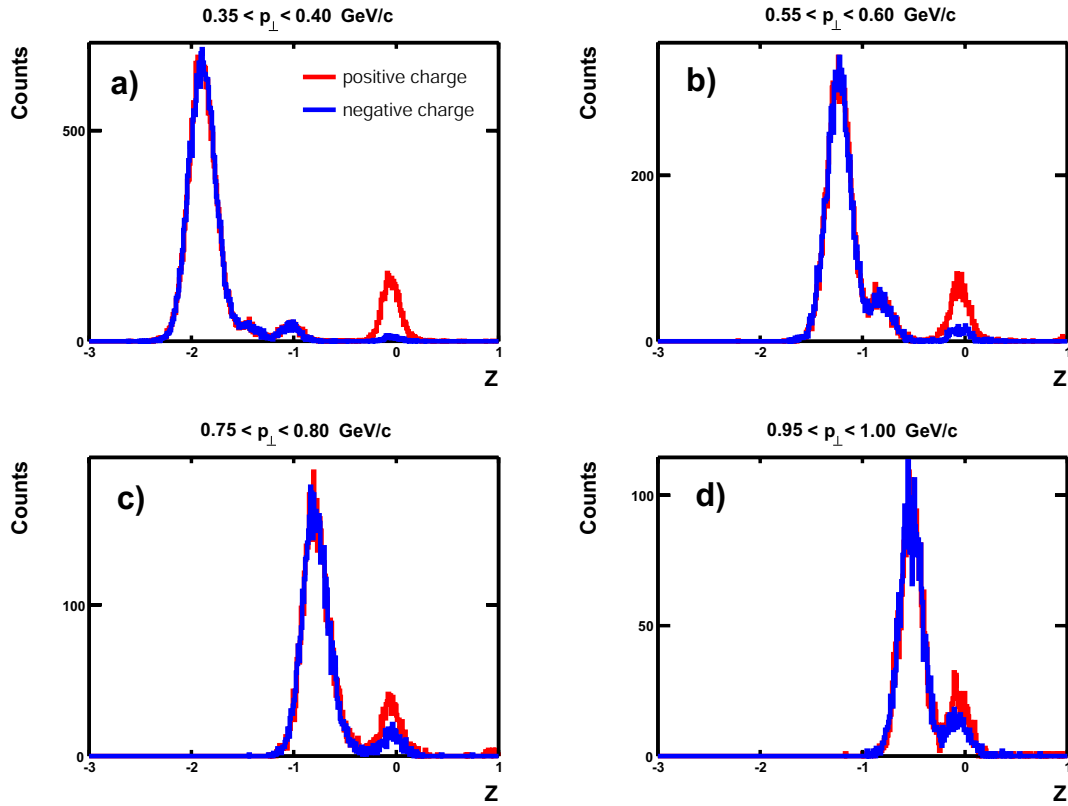


Figure 5.5.: Characteristic distributions of the Z -distribution, of minimum bias $^{197}\text{Au} + ^{197}\text{Au}$ collisions of centrality class 9 (5% central), in $0.05 \text{ GeV}/c$ wide transverse momentum (p_{\perp}) bins within a range of $0.35 < p_{\perp} < 1.0 \text{ GeV}/c$. At low transverse momenta the anti-protons and protons are widely separated from kaons, while at higher transverse momenta, they merge.

described the Z -distribution well, as shown in Figure 5.6. In the fitting procedure, the area of the Z -distribution was a fixed parameter. The electron yield is separated from other particle species in low transverse momentum bins, but was due to its low magnitude not considered in the fit function. The anti-proton and proton yields were extracted by making a cut on the width (σ) of the Gauss fit function within $1 < \sigma_p < 2$ from the mean of the proton fit (\overline{Z}_p). Additionally, a cut of $\sigma_{\pi} > 3$ from the mean of the pion fit (\overline{Z}_{π}) and $\sigma_K > 3$ from the mean of the kaon fit (\overline{Z}_K) was applied in order to exclude kaons and pions.

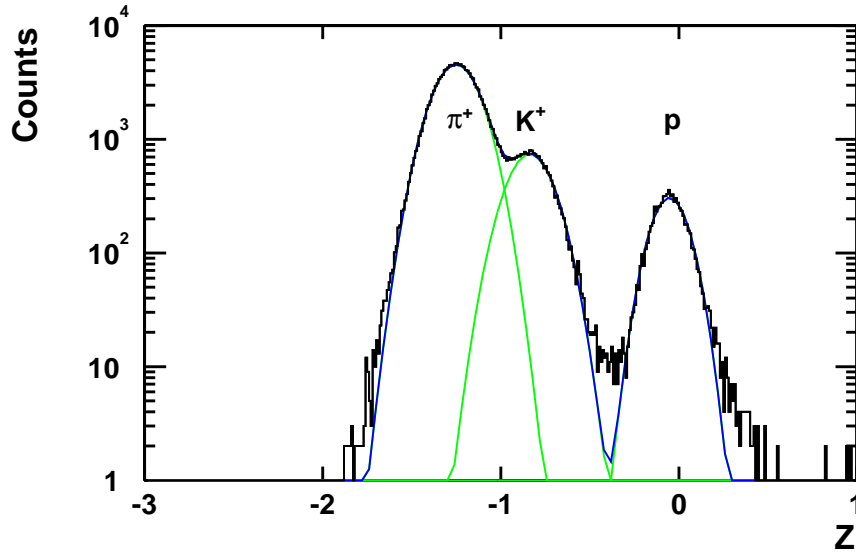


Figure 5.6.: Fit of the three Gauss function $f(Z)$ (Eq. 5.2) to the Z -distribution from particles with $0.65 < p_{\perp} < 0.7$ GeV/ c .

5.1.7. Corrections

Identified anti-proton and proton yields are altered by detector inefficiencies. In this section, the corrections that were applied to the raw yields of anti-protons and protons are discussed. The following issues were considered:

- Secondary interactions with detector material yield secondary particles (protons).
- Absorption of anti-protons in detector material.
- Energy loss correction of anti-proton and proton momentum, due to energy loss of anti-proton or proton traversing detector material.

The reconstruction efficiency is about the same for protons and anti-protons. A ratio measurement is, therefore, inherently less prone to systematic errors caused by detector inefficiencies than a measurement of absolute particle yields. Thus, detector inefficiency has not been considered in this analysis.

Operating the TPC in full magnetic field $B = 0.5$ causes an increase of factor 2-3 in momentum resolution [88], compared to half magnetic field $B = 0.25$ (Figure 4.5). Resulting in a momentum resolution of $\Delta p_{\perp}/p_{\perp} \leq 2\%$ for global tracks in the measured momentum range. Because of the finite momentum resolution,

5. Analysis of Anti-Proton to Proton Ratio

no correction for momentum resolution has been applied. However, this factor was taken into account when determining the systematic error of the analysis in Section 5.1.10. The resulting ratios in this analysis are not corrected for feed-down from the weak decay of heavier strange baryons, an estimate of the feed-down effects is given in Section 6.1.

Background Protons from Secondary Interactions

Before the particles produced in a collision are detected in the gas of the TPC, they must traverse detector material. The amount of material in the path of a charged particle can be expressed in terms of radiation length, X_0 , (see Table A.3). In the case of the 2001 setup, particles go through the beryllium beam pipe ($X_0 = 3.0\%$) of the RHIC accelerator. They subsequently pass through 3 layers of silicon from the SVT ($X_0 \sim 6.0\%$). Before entering the TPC, particles traverse the inner layers of the inner field cage of the TPC ($X_0 = 0.63\%$). Primary particles may interact with nuclei in the detector material, causing the production of secondary particles (protons).

Primary protons have a small dca (see Section 4.1.7). Since secondary protons arise from interactions with detector material, they are not produced at the main event vertex. They therefore give rise to a large dca , when the reconstructed particle trajectory is extrapolated to the event vertex. Figure 5.7 shows the dca -distribution in $\Delta p_\perp = 0.05$ GeV/ c wide transverse momentum bins of anti-protons (blue), protons (red) and the estimated proton background (green) within the measured transverse momentum range. The proton background is dependent on the transverse momentum and is highest at low transverse momenta. The proton dca -distribution shows long tails at wide dca s. The proton background distribution has been determined in each p_\perp -bin using the following procedure: The proton dca -distribution, dca_p , is the sum of the dca -distribution of protons produced in the collision ($dca_{p_{primary}}$), and the dca -distribution of background protons ($dca_{p_{background}}$) produced by secondary interactions

$$dca_p = dca_{p_{primary}} + dca_{p_{background}}. \quad (5.3)$$

In secondary interactions with detector material, no anti-protons are produced. Thus, assuming that the dca -distribution of primary protons ($dca_{p_{primary}}$) and the background free anti-proton dca -distribution ($dca_{\bar{p}}$) have a similar dca -distribution, except for a factor, C , due to the different yields, Equation 5.3 becomes

$$dca_p = C dca_{\bar{p}} + dca_{p_{background}} \quad (5.4)$$

5.1. \bar{p}/p at Low Transverse Momentum

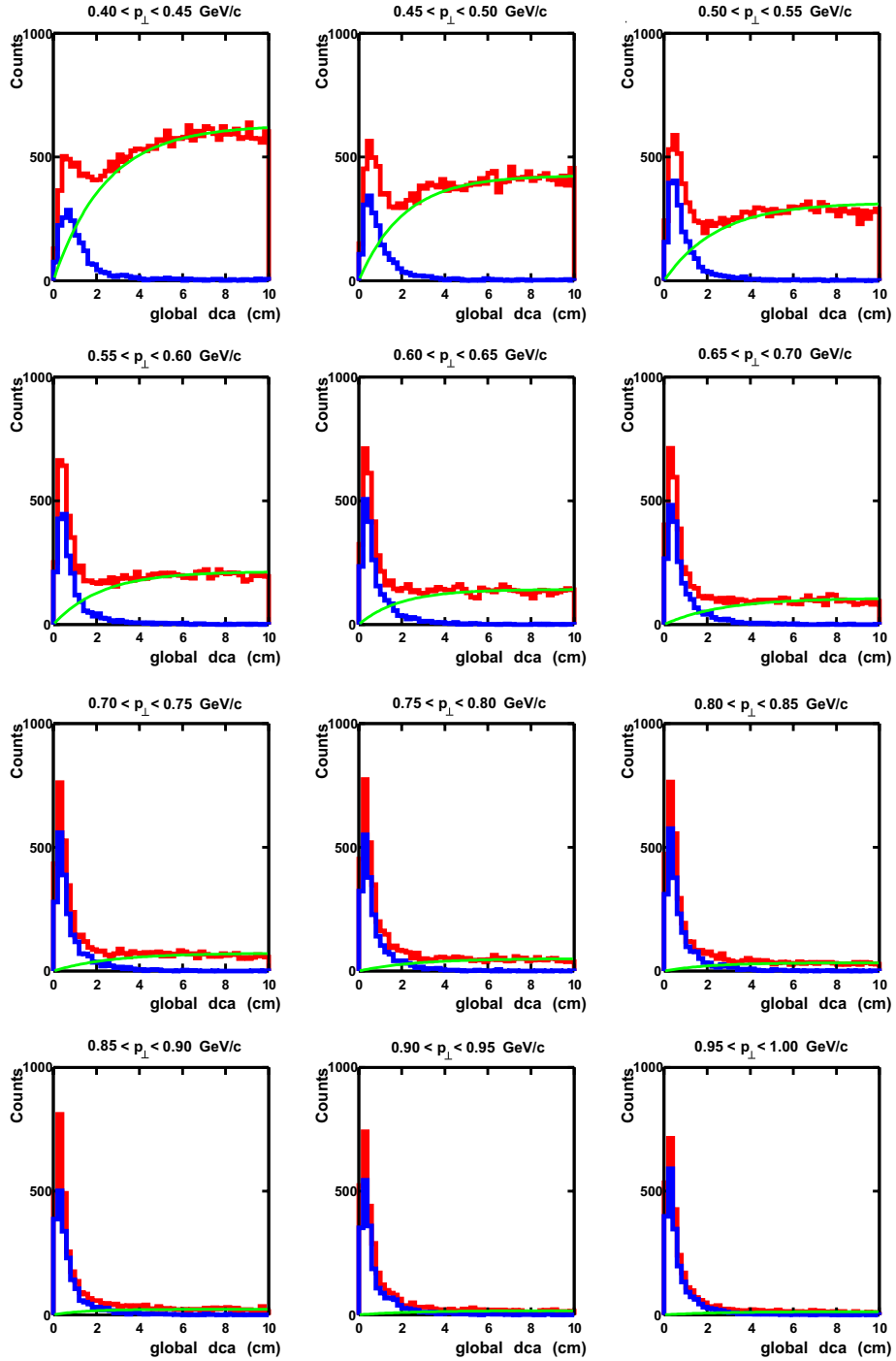


Figure 5.7.: dca -distributions of anti-protons (blue) and protons (red) in $\Delta p_{\perp} = 0.05$ GeV/ c wide bins. The secondary-proton background (green) is strongly dependent on the transverse momentum.

5. Analysis of Anti-Proton to Proton Ratio

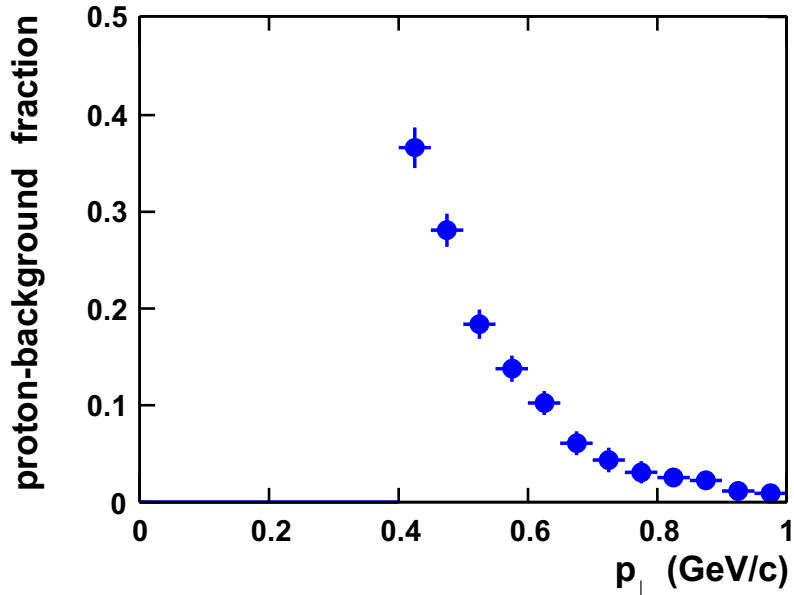


Figure 5.8.: Dependence of the secondary-proton background fraction on p_{\perp}

To study the dca -distribution of the background, GEANT [82] simulations have been performed [91]. The study has shown, that the dca -distribution of background protons, can be described by an exponential function:

$$f_{dca_{p_{background}}}(dca) = A(1 - e^{-dca/k}) \quad (5.5)$$

where A is the amplitude, and the rise of the function towards a constant value at high dca is described by k . The proton background, is large at low transverse momentum, but steeply decreases for higher values. Figure 5.8 shows the fraction of the proton background for different p_{\perp} bins.

To correct the identified proton yields, the background was subtracted in each p_{\perp} bin within the range of $0 < dca < 1.5$ cm. A dca of less than 1.5 cm was chosen to optimize the signal to background ratio for the extracted anti-proton and proton raw yields. Applying this cut, approximately 6% of the background free anti-protons are excluded.

Proton Background for Different Detector Geometries

The 2001 run saw, for the first time, the full installation of the silicon vertex tracker (SVT) detector at the STAR experiment. In 2000, the experiment was equipped with only a small part of the SVT, i.e. one test ladder. Unfortunately, the detector data were distorted by electronic noise during the data acquisition of the 2001 $^{197}\text{Au} + ^{197}\text{Au}$ run. It was subsequently discovered that the noise

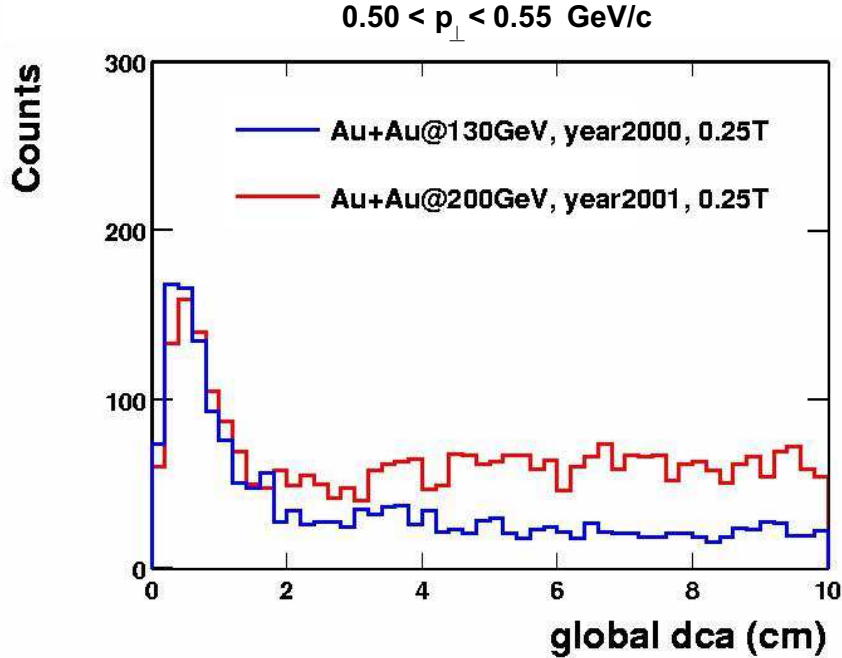


Figure 5.9.: *dca*-distributions of protons in 2000 and 2001 at $B = 0.25 \text{ T}$.

was caused by a grounding problem, which was later resolved. However, the SVT detector was not available as a tracking device in 2001 $^{197}\text{Au} + ^{197}\text{Au}$ run data.

A working SVT detector could have been used to match TPC tracks with the spatial information provided by the SVT. If a track was found in the first and all subsequent layers of the SVT, one could assume that it was not a background track. However, the missing tracking information meant that it was not possible to distinguish between tracks coming from the event vertex and from secondary interactions in the detector material. This gave rise to a large background signal in the identified proton distributions, as shown in the previous section. However, it was found that Equation 5.5 describes the background of both the 2000 and the 2001 detector geometries well, and was therefore applied.

Figure 5.9 illustrates the difference in the background for the different detector geometries. The distributions are both from data where the TPC was operated in half magnetic field ($B = 0.25 \text{ T}$) and are normalized to the number of entries at $dca = 1 \text{ cm}$. From the figure we conclude that the secondary-proton background between $0.5 < p_{\perp} < 0.55 \text{ GeV}/c$ in the 2001 $^{197}\text{Au} + ^{197}\text{Au}$ run is factor ~ 3 higher than that of the 2000 run, caused by the additional amount of material brought into the detector by the SVT in 2001 ($X_0 \sim 3.62, 9.62\%$ without, with SVT respectively. See Table A.3).

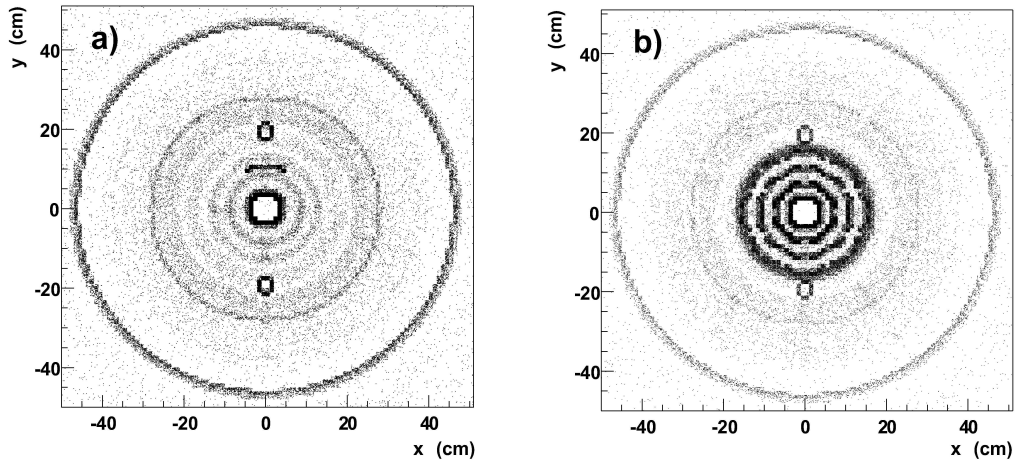
Anti-proton Absorption

Figure 5.10.: Absorption points of anti-protons in STAR's detector material for the detector geometry of a) 2000 and b) 2001, before entering the sensitive volume of the TPC. Results of a GEANT simulation.

Anti-protons pass through several detector materials, before reaching the sensitive gas volume of the TPC. Anti-protons can be absorbed by annihilation in the detector material. The effect is strongly dependent on the anti-proton momentum and the amount of material which must be traversed.

The effect of anti-proton absorption in various detectors of the STAR experiment, has been studied with a GEANT simulation. The simulation was done for the 2000 and the 2001 STAR detector geometry. For the simulation, anti-protons and protons, were generated within a transverse momentum range of 0.15^1 , $0.2^2 < p_{\perp} < 1.0$ GeV/ c . They were distributed evenly at mid-rapidity $|y| < 0.5$. The GEANT simulation yields two important pieces of information: 1) Where absorption takes place in the detector material. 2) The absolute amount of absorption.

Figure 5.10 shows where anti-protons are absorbed in the detector, before they reach the sensitive volume of the TPC. The plot shows a front view (x - y -plane) of the inner STAR detector. The absorption for the 2000 detector geometry is shown in Figure 5.10a. The plot shows absorption points of anti-protons in the detector materials. The beam pipe ($X_0 = 3.0\%$) can be seen at the center of the plot with a radius $r = 4$ cm. The support mounts of the SVT are visible at a radius $r < 20$ cm. The SVT test ladder is at $x = 0$, $y = 10$ cm, with a width of 10

¹2000 geometry: TPC operated in a magnetic field of $B = 0.25$ T.

²2001 geometry: TPC operated in a magnetic field of $B = 0.50$ T.

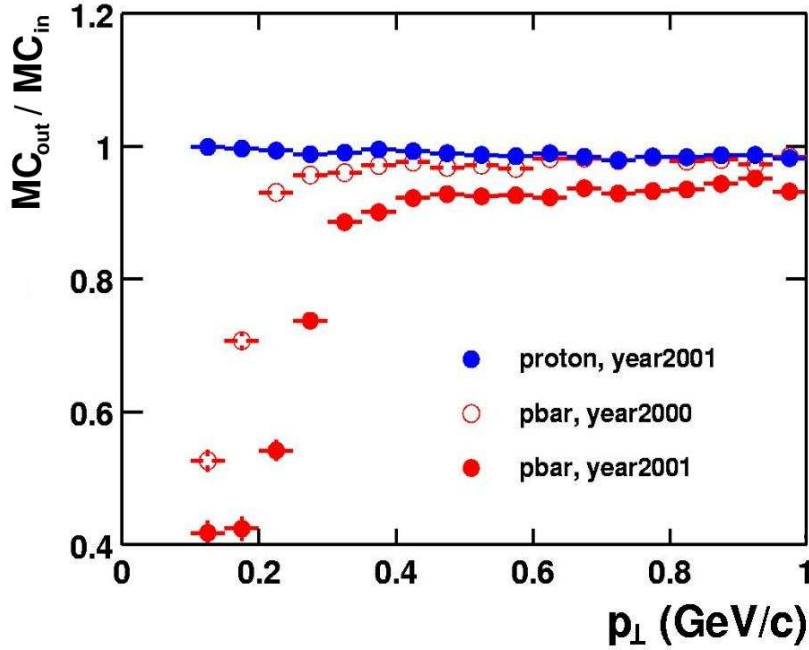


Figure 5.11.: Dependence of the anti-proton absorption MC_{out}/MC_{in} on the transverse momentum (p_{\perp}) determined in a GEANT simulation.

cm. The two objects with a diameter of 5 cm at $(x = 0, y \pm 20)$ are cable mounts for the SVT. The inner field cage ($X_0 = 0.62\%$) of the TPC is located at a radius of $r \sim 50$ cm. The same simulation was done for the 2001 detector geometry. Points of absorption of the 2001 detector geometry are plotted in Figure 5.10b. The anti-proton absorption is increased around the SVT ($X_0 \sim 6.0\%$, centered with a radius $r = 14.5$ cm), which was fully installed by this time. The intensity of the plot shows that the absorption has substantially increased, compared to the previous year.

Figure 5.11 shows the total absorption of anti-protons in detector materials before they reach the TPC gas volume, versus transverse momentum (p_{\perp}) in 2000 and 2001. MC_{out}/MC_{in} is the ratio of tracks which have traversed (*out*) the detector to simulated tracks (*in*). Protons (blue) which can only be absorbed by a hadronic interaction were simulated for comparison. The absorption is strongly dependent on the momentum of the produced anti-proton. The installation of the full SVT instrumentation increased the amount of material (see Table A.3) through which the particles must pass, thus bringing about a significant increase in absorption. The anti-proton absorption in the transverse momentum range $0.45 < p_{\perp} < 0.65$ GeV/c is increased by factor ≥ 2 from 2001 (3%) to 2000 (7.5%). The identified anti-proton yields were compensated for absorption according to Figure 5.11.

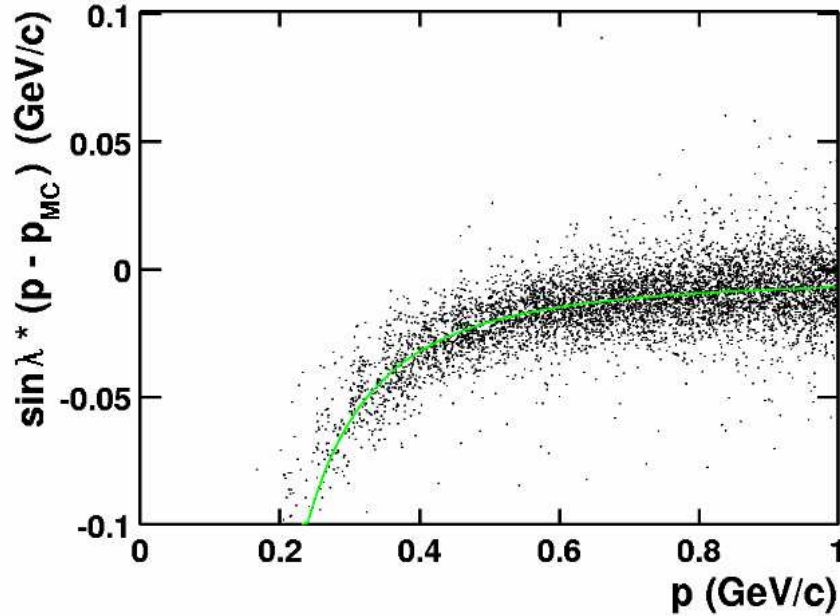
Energy Loss

Figure 5.12.: Difference (times sine of the dip angle λ) of the reconstructed momentum (p) and the initial momentum (p_{MC}) due to energy loss of protons in detector material, versus momentum (p). Determined using a GEANT simulation.

In the preceding sections, the anti-proton absorption and secondary-proton background caused by detector material were discussed. Another effect which must be considered is the energy loss of particles traversing the detector material. When a particle traverses a material, it loses energy due to multiple scattering interactions with same. It was shown that the energy loss correction applied in the global track model, assuming the particle is a pion (see Section 4.1.5), is not sufficient in the case of protons.

In order to study this effect, anti-protons and protons with a momentum of $0.2 < p < 1.0$ GeV/c were simulated with GEANT. The momentum difference (Δp) of the reconstructed momentum (p) and the initial momentum (p_{MC}) due to energy loss of protons is shown in Figure 5.12. The dependence of the momentum difference can be parametrized by

$$\Delta p = p - p_{MC} = a/\beta^n \frac{1}{\sin \lambda} \quad (5.6)$$

where $\beta = pc/E$ is the relativistic velocity of protons and anti-protons, λ is the

dip angle, The constant $a = -0.0032888$ and the exponent $n = 2.43938$ result from a fit to the distribution shown in Fig. 5.12. From the figure one can read that for example the mean momentum difference of an anti-proton or proton with a momentum of $p = 0.5$ GeV/ c is $\Delta p \sim 2\%$. The energy loss correction was applied to reconstructed global tracks, used in this analysis.

5.1.8. Corrected \bar{p}/p Ratio in Minimum Bias Events

The anti-proton to proton ratio in minimum bias events of $^{197}\text{Au} + ^{197}\text{Au}$ collisions at a center of mass energy of $\sqrt{s_{NN}} = 200$ GeV is illustrated in Figure 5.13. The mid-rapidity ($|y| < 0.5$) anti-proton to proton ratio versus transverse momentum for the 5% most central $^{197}\text{Au} + ^{197}\text{Au}$ collisions of centrality class 9 is shown in Figure 5.13a. The ratio does not depend on transverse momentum within the measured range of $0.4 < p_{\perp} < 1.0$ GeV/ c . The mean value of all $\Delta p_{\perp} = 0.05$ GeV/ c wide bins is $\langle \bar{p}/p \rangle|_{0.4 < p_{\perp} < 1.0 \text{ GeV}/c} = 0.81 \pm 0.002_{\text{stat.}} \pm 0.05_{\text{syst.}}$.

Figure 5.13b shows the anti-proton to proton ratio versus rapidity, within the transverse momentum range of $0.6 < p_{\perp} < 0.8$ GeV/ c for the 5% most central collisions. The ratio does not depend on rapidity within $|y| < 0.5$. The mean value of all $y = 0.1$ wide bins is $\langle \bar{p}/p \rangle|_{-0.5 < y < 0.5} = 0.82 \pm 0.002_{\text{stat.}} \pm 0.05_{\text{syst.}}$.

The dependence of the anti-proton to proton ratio on the number of hadrons produced per collision (N_{ch}) is shown in Figure 5.13c. The figure shows the anti-proton to proton ratio of the 9 centrality classes defined in Section 5.1.4. The ratio is slightly dependent on the centrality of the collision, it is $\bar{p}/p = 0.83 \pm 0.002_{\text{stat.}} \pm 0.05_{\text{syst.}}$ for the most peripheral collisions (less than 80% central, class 1) and decreases to $\bar{p}/p = 0.78 \pm 0.002_{\text{stat.}} \pm 0.05_{\text{syst.}}$ for the 5% most central collisions (class 9). The statistical error $\langle \bar{p}/p \rangle_{\text{stat.}} \leq \pm 0.002$ of the data points in Figure 5.13 is smaller than the symbol size. The systematic error been determined to $\langle \bar{p}/p \rangle_{\text{syst.}} \leq \pm 0.05 \sim 6\%$ and will be discussed in Section 5.1.10. The values of the anti-proton to proton ratio versus p_{\perp} , y and N_{ch} shown in Figure 5.13 are included in Table B.1.

5.1.9. Corrected \bar{p}/p Ratio in Central Events

The previous analysis is based on $^{197}\text{Au} + ^{197}\text{Au}$ events from 9 different centrality classes taken with run type “productionMinBias”. The same procedure will now be followed to analyze the 10% most central events triggered by the central Level-0 trigger in run type “productionCentral” (Dataset 2 mentioned in Section 5.1.1), to be compared with the results of the analysis at high transverse momentum in Section 5.2.

The cuts applied to the data are identical to those applied in the analysis of

5. Analysis of Anti-Proton to Proton Ratio

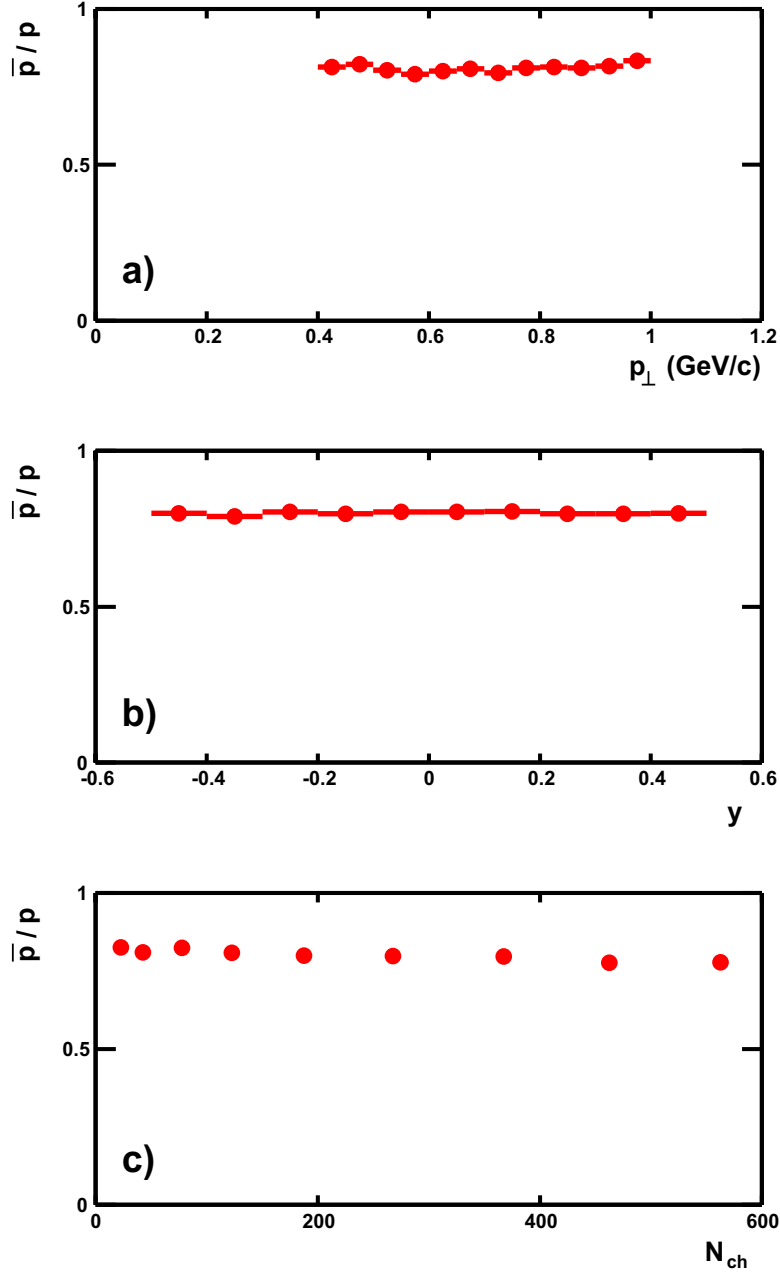


Figure 5.13.: Anti-proton to proton ratios in minimum bias events of $^{197}\text{Au} + ^{197}\text{Au}$ collisions at $\sqrt{s_{NN}} = 200$ GeV. a) \bar{p}/p versus p_{\perp} at mid-rapidity for 5% most central collisions, b) \bar{p}/p versus rapidity, y , within the transverse momentum range of $0.6 < p_{\perp} < 0.8$ GeV/c, for 5% most central collisions and c) \bar{p}/p versus N_{ch} at mid-rapidity.

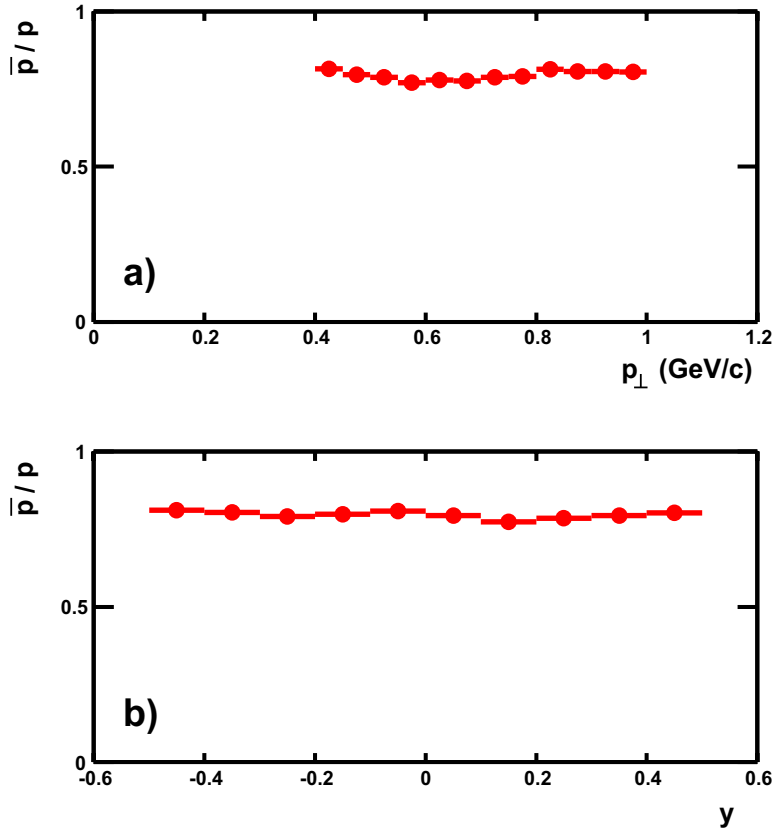


Figure 5.14.: Anti-proton to proton ratio in central events of $^{197}\text{Au} + ^{197}\text{Au}$ collisions at $\sqrt{s_{NN}} = 200$ GeV. a) \bar{p}/p versus transverse momentum p_{\perp} at mid-rapidity, b) \bar{p}/p versus rapidity y within the transverse momentum range of $0.6 < p_{\perp} < 0.8$ GeV/c.

the minimum bias events, as are the corrections to the anti-proton and proton yields. Figure 5.14a shows the resulting anti-proton to proton ratio versus transverse momentum at mid-rapidity $|y| < 0.5$. The ratio is comparable to the minimum bias result in the most central class. The mean value of all p_{\perp} -bins is $\langle \bar{p}/p \rangle|_{0.4 < p_{\perp} < 1.0 \text{ GeV}/c} = 0.80 \pm 0.002_{\text{stat.}} \pm 0.05_{\text{sys.}}$.

The mean value of all y -bins in Figure 5.14b, where the ratio versus rapidity is shown, is $\langle \bar{p}/p \rangle|_{-0.5 < y < 0.5} = 0.80 \pm 0.002_{\text{stat.}} \pm 0.05_{\text{sys.}}$. The numbers for the anti-proton to proton ratio versus p_{\perp} and y shown in Figure 5.13 can be found in Table B.2.

5.1.10. Systematic Errors

To determine the systematic uncertainties of this analysis, cuts on event and track characteristics were examined and uncertainties for each characteristic were determined. The effect of these uncertainties on the anti-proton to proton ratio was studied. The following event characteristics were considered:

1. Ratio dependence on runs taken on different days (different run number).
2. Difference of the mean $\langle \bar{p}/p \rangle$ in the 5% most central events taken with run type “productionMinBias” and “productionCentral”.

On the track level, the following quantities were considered:

1. Requiring a fit hit cut of $N_{fit\ hits} \geq 28$ fit hits on tracks from centrality class 9 in events from “productionMinBias”.
2. Accepting protons and anti-protons with a $dca < 2$ cm, thereby subtracting the background from a wider dca (compared to a $dca < 1.5$ cm) on tracks in events from “productionMinBias”.
3. Taking the momentum resolution of $\Delta p_{\perp}/p_{\perp} \sim 2\%$ into account.

The effects on the anti-proton to proton ratio are shown in Table 5.2. In order to determine the systematic error, the effects on the ratio due to uncertainties in track characteristics were summed up, resulting in a systematic error of $\langle \bar{p}/p \rangle_{\text{syst.}} \leq \pm 0.05$. The effect on the ratio due to run number dependence and from different trigger settings, were found to be well within the systematic error.

Event characteristics	Effect on \bar{p}/p
run number	$\pm < 0.010$
top 5% min bias \leftrightarrow cent.	$\pm < 0.020$
Track characteristics	
$N_{fit\ hits} \geq 28$	$\pm < 0.005$
$dca < 2$ cm	$\pm < 0.030$
$\Delta p_{\perp}/p_{\perp} \sim 2\%$	$\pm < 0.015$

Table 5.2.: Studies on event and track characteristics to determine the systematic error of the analysis.

5.1.11. Comparison to On-line Reconstructed Events

In this section, the results of the anti-proton to proton ratio in $^{197}\text{Au} + ^{197}\text{Au}$ collisions at $\sqrt{s_{NN}} = 200$ GeV determined using the on-line analysis of the STAR Level-3 trigger are presented. Events recorded at the beginning of the 2001 $^{197}\text{Au} + ^{197}\text{Au}$ run are analyzed. In the first instance, the events were written by the 'L3EVP' node in the GL3 data format for quality assurance of the Level-3 Trigger system. The recorded events also served the Level-3 on-line event display (L3GViewer) and the Level-3 on-line monitor (L3Online) (see Section 4.3.5). On the Level-3 Trigger system, on-line reconstructed events are available immediately during the data-taking. By analyzing the events a short time after data-taking, it is possible to get a quick first impression of the data quality. After on-line

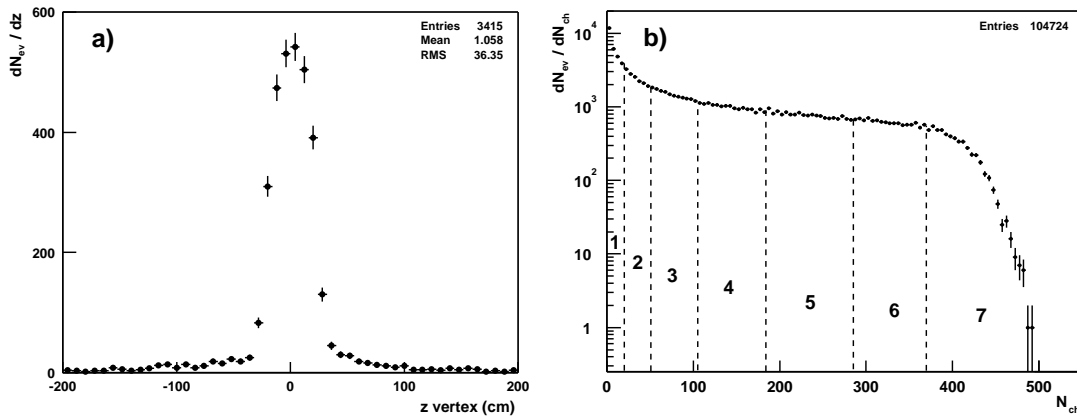


Figure 5.15.: a) Longitudinal event vertex (z vertex) Distribution of on-line reconstructed minimum bias events. b) Uncorrected charged particle (N_{ch}) distribution from on-line reconstructed minimum bias events, divided into 7 centrality classes.

reconstructed events were recorded early in the 2001 $^{197}\text{Au} + ^{197}\text{Au}$ production run, a similar analysis to that described in Section 5.1 was carried out. The first results of the analysis shown in this section were available a few weeks after the run had started. The information gained from the preliminary on-line analysis was very useful for the anti-proton to proton ratio off-line analysis. For instance, the comparison of the 2000, 2001 detector geometries was first studied with on-line reconstructed events. A sample of 137k on-line reconstructed events of $^{197}\text{Au} + ^{197}\text{Au}$ collisions at $\sqrt{s_{NN}} = 200$ GeV, taken with the minimum bias trigger were available within the first days of the data-taking run. This dataset is used for the present analysis.

Figure 5.15a shows the distribution of the longitudinal event vertex (z vertex) of a fraction of the event sample. The z vertex distribution peaks around zero due

5. Analysis of Anti-Proton to Proton Ratio

to the ZDC timing trigger at trigger Level-0. In the present analysis events with a longitudinal event vertex of $|z \text{ vertex}| < 30$ cm were used. A total of 104.7k of the initial 137k events (76%) pass this cut.

Figure 5.15b shows the uncorrected distribution of charged particles (N_{ch}) from on-line reconstructed minimum bias events of $^{197}\text{Au} + ^{197}\text{Au}$ collisions. Particles were counted if a track at mid-pseudorapidity ($|\eta| \leq 0.5$) with $N_{hits} \geq 23$ and a $dca < 3$ cm was reconstructed. The distribution shows a smaller absolute multiplicity compared to the distribution in the off-line analysis shown in Figure 5.3. This is due to the fact that on-line reconstructed tracks had to have a substantially higher number of points in order to be counted. This was chosen in order to avoid double counting of split tracks and to insure a good track quality.

In order to study the dependence of the anti-proton to proton ratio on the centrality of the collision, the distribution (Figure 5.15b) of charged particles (N_{ch}) was divided into centrality classes, as in the off-line analysis case. However, due to limited statistics, the charged particle distribution was divided into 7 centrality classes ranging from central (class 7) to peripheral (class 1) collisions. Table 5.3 shows the centrality classes, the centrality of the collision for each class and the lower limit of charged particles (N_{ch}) per event which an event has to have in order to be accepted into the corresponding centrality class.

Class	Centrality (%)	N_{ch} cut (\geq)
1	< 75	1
2	75	20
3	60	51
4	45	105
5	30	184
6	15	285
7	5	370

Table 5.3.: Centrality classes used for studying dependence on collision centrality for on-line reconstructed $^{197}\text{Au} + ^{197}\text{Au}$ collisions.

Particle Identification

Anti-protons and protons were identified, as in the off-line analysis case (see Section 5.1.6), by correlating their energy loss (dE/dx) due to ionization in the TPC gas, with the reconstructed momentum. At mid-rapidity ($|y| < 0.3$), on-line reconstructed tracks were accepted if they were reconstructed with $N_{hits} \geq 23$. The particle dE/dx was calculated on-line by the Level-3 Trigger system

5.1. \bar{p}/p at Low Transverse Momentum

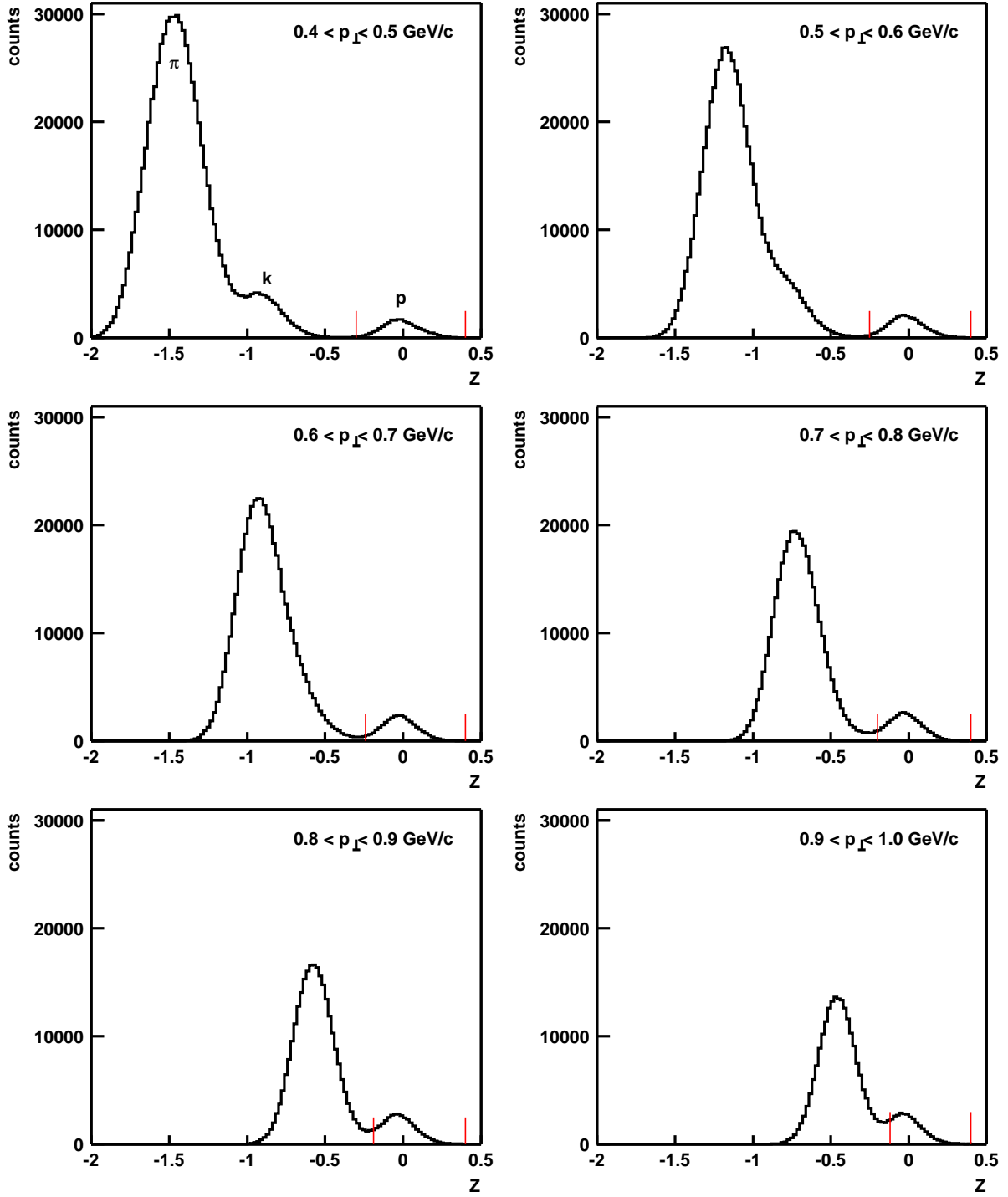


Figure 5.16.: Distributions of Z -distribution of on-line reconstructed 5% most central $^{197}\text{Au} + ^{197}\text{Au}$ collisions, in $0.1 \text{ GeV}/c$ wide p_{\perp} bins within the range of $0.4 < p_{\perp} < 1.0 \text{ GeV}/c$. At low p_{\perp} , the anti-protons and protons are widely separated from kaons, while at higher p_{\perp} , the proton and kaon Gauss distributions merge.

5. Analysis of Anti-Proton to Proton Ratio

during event reconstruction (see Section 4.3.2). For the extraction of anti-proton and proton yields from the produced particles of the recorded $^{197}\text{Au} + ^{197}\text{Au}$ collisions, the Z variable introduced in Section 5.1.6 was used. As depicted in Figure 5.16, spectra of the Z variable were taken in $\Delta p_{\perp} = 0.1$ GeV wide transverse momentum bins from $0.4 < p_{\perp} < 1.0$ GeV/ c . For this preliminary analysis at the beginning of the data-taking run, the anti-protons and protons, which are well separated from other hadrons up to a momentum of ~ 1.0 GeV/ c , were fit by a Gaussian function. The mean of the anti-proton and proton Gaussian function was found to be $\overline{Z}_p \sim -0.02$. This indicates that the measured dE/dx does not exactly match the dE/dx calculated using the Bethe-Bloch equation. However, since this is the on-line reconstructed dE/dx and no final calibrations are included, a shift of the mean of $\sigma = 0.2$ is acceptable. Yields of anti-protons and protons were extracted by a cut around the mean of the Gauss distribution of the Z variable. For each transverse momentum bin an upper and lower limit was chosen to optimize the anti-proton and proton yields and to minimize contamination by other hadrons. Table 5.4 shows the ranges in width (σ) from the Gauss function fit, within which protons and anti-protons, were accepted. The merging of the proton Gauss with the kaon Gauss at higher transverse momenta can be seen in Figure 5.16, where distributions of the Z variables in 0.1 GeV/ c wide transverse momentum bins are shown. The Z range of the cut, as shown in Table 5.4, is marked with red lines.

min. p_{\perp}	max. p_{\perp}	cut in σ_Z	min. Z	max. Z
0.4	0.5	$-2.75 < \sigma < 3.70$	-0.30	0.40
0.5	0.6	$-2.28 < \sigma < 3.70$	-0.25	0.40
0.6	0.7	$-2.19 < \sigma < 3.70$	-0.24	0.40
0.7	0.8	$-1.82 < \sigma < 3.70$	-0.20	0.40
0.8	0.9	$-1.73 < \sigma < 3.70$	-0.19	0.40
0.9	1.0	$-1.09 < \sigma < 3.70$	-0.12	0.40

Table 5.4.: Correlation of the width (σ) cut of the Z -distribution and transverse momentum (p_{\perp}) to identify anti-protons and protons from on-line reconstructed $^{197}\text{Au} + ^{197}\text{Au}$ collisions.

Proton Background Subtraction

Secondary protons are produced due to interactions of primary particles with nuclei in the STAR detector material. Secondary protons typically have a wide dca (see Section 5.1.7 and Figure 4.6). This causes long tails in the proton dca -distribution. Figure 5.17 shows the distribution of (a) protons and (b) anti-protons with the measured transverse momentum range of $0.4 < p_{\perp} < 1.0$ GeV/ c .

5.1. \bar{p}/p at Low Transverse Momentum

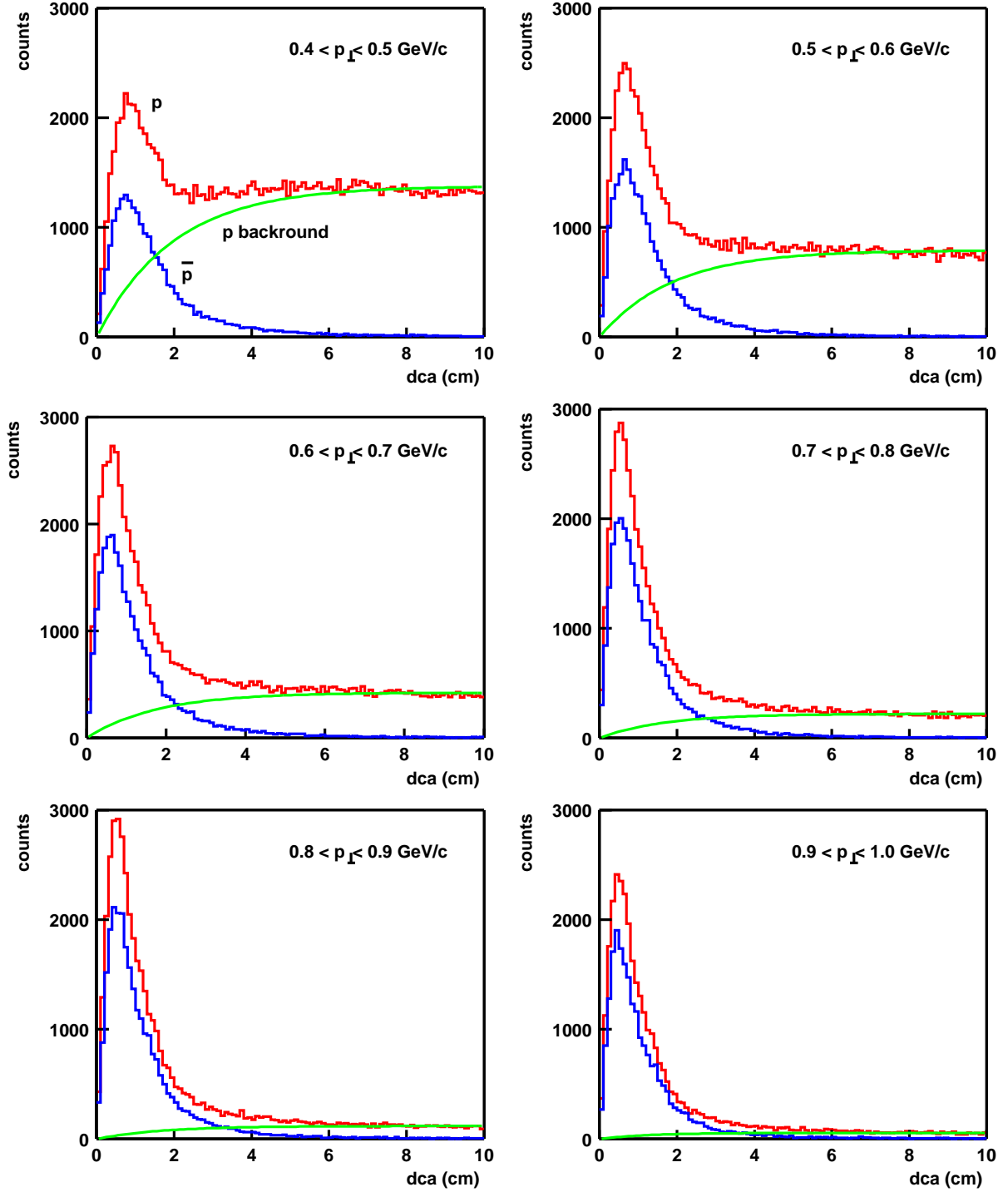


Figure 5.17.: Spectra of proton (red) and anti-proton (blue) dca for on-line reconstructed 5% central $^{197}\text{Au} + ^{197}\text{Au}$ collisions, in 0.1 GeV/c wide p_{\perp} bins within a transverse momentum range of $0.4 < p_{\perp} < 1.0$ GeV/c. At low p_{\perp} , the background fraction is about 25%.

5. Analysis of Anti-Proton to Proton Ratio

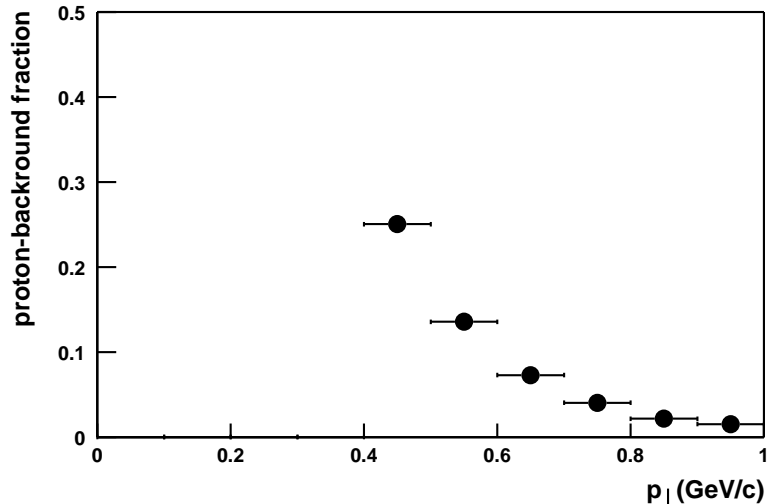


Figure 5.18.: Dependency of the secondary-proton background fraction with p_{\perp} for on-line reconstructed 5% most central minimum bias events from $^{197}\text{Au} + ^{197}\text{Au}$ collisions.

The shapes of the dca -distributions are similar to the dca -distributions in the off-line analysis. However, in the on-line analysis, the peak in the dca -distributions at less than 2 cm is found to be considerably wider than in the off-line analysis case (compare with Figure 5.7). 90% of the anti-protons reconstructed with the off-line analysis, have a dca of less than 1 cm, while 97% have a $dca < 2$ cm. In the on-line analysis 52% of the anti-protons are found to be within a $dca < 1$ cm, and 82% are found to have a $dca < 2$ cm. Factors responsible for this effect are the factor *sim*1.5 worse momentum resolution (see Section 4.1.5) of the Level-3 trigger compared to the off-line reconstruction and the lack of distortion correction of the cluster data. However, for secondary-proton background subtraction, the same method described in the off-line analysis has been applied (see Section 5.1.7). This procedure was done for every dca -distribution from the six transverse momentum bins, in which anti-proton and proton yields were identified. The dca -distributions of protons (red), secondary-proton background after subtraction (green) and anti-protons (blue) are shown in Figure 5.17.

The same trend as in the off-line analysis can be seen. The secondary-proton background is high at low p_{\perp} , and falls steeply with increasing p_{\perp} . The dependency of the secondary-proton background fraction on p_{\perp} , for a $dca < 1.5$ cm, is summarized in Figure 5.18. When comparing the secondary-proton background fraction found in this on-line analysis with the off-line case (Figure 5.8), one finds good agreement in amplitude and general behavior of the curve versus p_{\perp} . This confirms that for anti-proton to proton ratio analysis, the faster on-line reconstruction is capable of reproducing the result of the off-line analysis well.

Anti-proton absorption is dealt with in the same way as in the off-line analysis (see Section 5.1.7).

Anti-Proton to Proton Ratio from On-line Reconstructed Events

In order to determine the anti-proton to proton ratio from the on-line reconstructed events, secondary background protons were subtracted from the identified proton yield. The anti-proton yield was corrected for anti-proton absorption. To optimize the signal to background ratio, the reconstructed tracks of identified protons and anti-protons were required to have a $dca < 1.5$ cm. In order illustrate how the corrections effect the raw yields, consider the following example: At mid-rapidity ($|y| < 0.3$), the yield of identified anti-protons and protons in the $0.6 < p_{\perp} < 0.7$ bin for 5% most central on-line reconstructed events is $Y_{\bar{p}} = 19222$ and $Y_p = 28461$, respectively. The anti-proton yield was corrected for anti-proton absorption of 7.02% which increases the yield to

$$Y_{\bar{p}_{corrected}} = 19222 * 1/(1 - 0.0702) = 20673 \quad (5.7)$$

The secondary-proton background was determined to be 7.3% after fitting, which results in a corrected proton yield of

$$Y_{p_{corrected}} = 28461 - 28461 * 0.07285 = 26388 \quad (5.8)$$

This yields an anti-proton to proton ratio of

$$\bar{p}/p = Y_{\bar{p}_{corrected}}/Y_{p_{corrected}} = 0.7834 \pm 0.0096 \quad (5.9)$$

In this case, the anti-proton absorption is quite low at 7.02%. At lower momentum, where the proton yield is widely separated from the kaon yield, the absorption is found to be significantly higher.

The dependence of the anti-proton to proton ratio on transverse momentum at mid-rapidity ($|y| < 0.3$) for the 5% most central on-line reconstructed events is shown in Figure 5.19a. The ratio does not show a dependence on p_{\perp} , although the value for the first p_{\perp} bin is slightly raised with respect to the higher bins. However, both the secondary-proton background fraction ($\sim 25\%$) and the anti-proton absorption ($\sim 11\%$) are highest in this bin, which results in a high systematical error. The mean value of the ratio over the measured range of $0.4 < p_{\perp} < 1.0$ GeV/c is found to be p_{\perp} -bins is $\langle \bar{p}/p \rangle_{0.4 < p_{\perp} < 1.0 \text{ GeV}/c} = 0.80 \pm 0.004_{\text{stat.}} \pm 0.05_{\text{syst.}}$

Figure 5.19b shows the anti-proton to proton ratio versus rapidity ($-0.3 < y < 0.3$) within the transverse momentum range of $0.6 < p_{\perp} < 0.8$ GeV/c. There is no dependence with respect to rapidity. The mean value over the six rapidity bins between $-0.3 < y < 0.3$ is found to be $\langle \bar{p}/p \rangle_{-0.5 < y < 0.5} = 0.81 \pm 0.066_{\text{stat.}} \pm 0.05_{\text{syst.}}$

5. Analysis of Anti-Proton to Proton Ratio

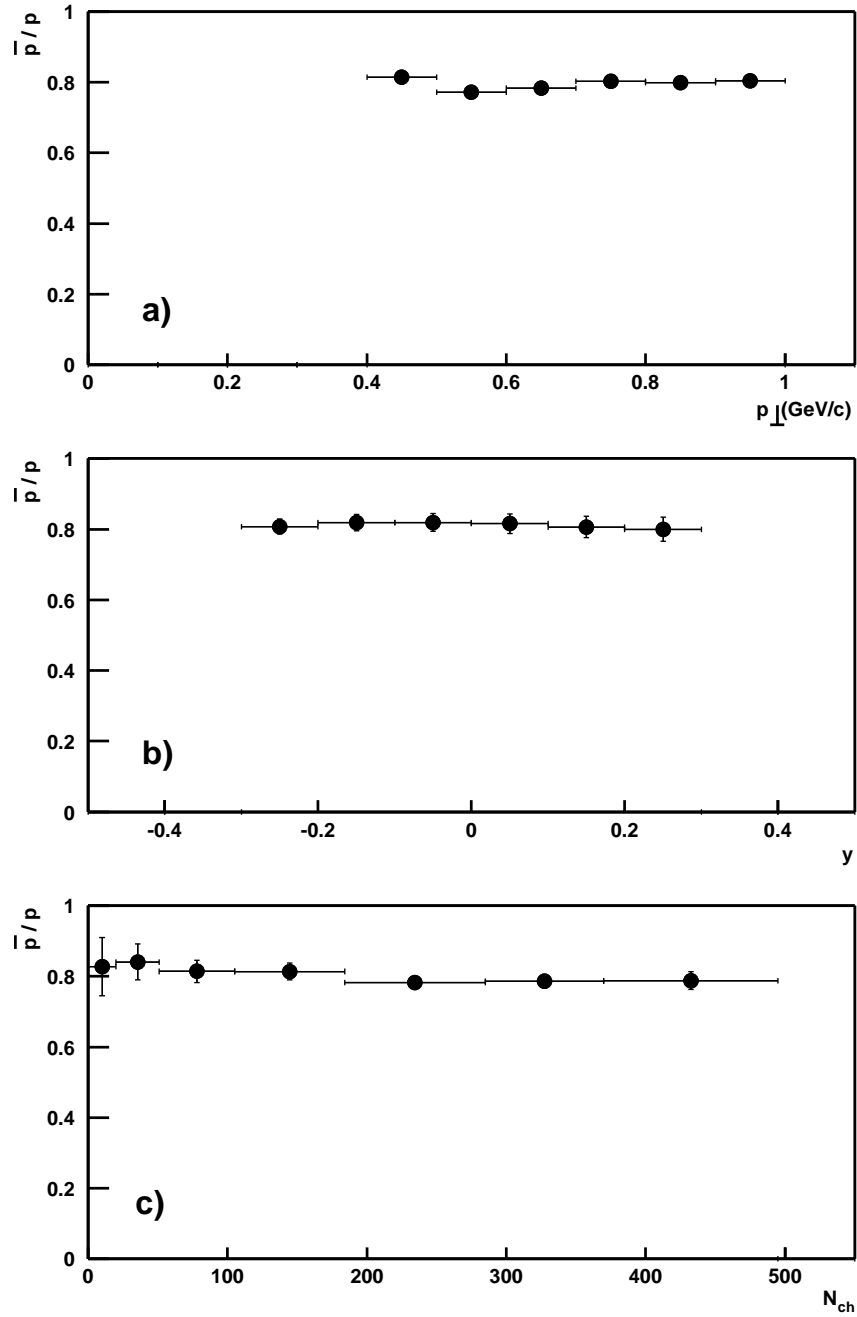


Figure 5.19.: Anti-proton to proton ratio in $^{197}\text{Au} + ^{197}\text{Au}$ collisions at $\sqrt{s_{NN}} = 200$ GeV from minimum bias events, on-line reconstructed with the STAR Level-3 trigger. a) \bar{p}/p versus p_{\perp} at mid-rapidity ($|y| < 0.3$) for 5% most central collisions. b) \bar{p}/p versus rapidity (y) within $0.6 < p_{\perp} < 0.8$ GeV/c, for 5% most central collisions. c) \bar{p}/p versus number of charged hadrons (N_{ch}) at mid-rapidity, $0.6 < p_{\perp} < 0.8$ GeV/c. The systematic uncertainties for this analysis were determined to be $\langle \bar{p}/p \rangle_{\text{sys.}} = \pm 0.05$.

5.1. \bar{p}/p at Low Transverse Momentum

The anti-proton to proton ratio versus centrality of $^{197}\text{Au} + ^{197}\text{Au}$ collisions is shown in Figure 5.19c. The correlation between particles produced and collision centrality was shown in Figure 5.15a. Depicted in Figure 5.19c is the ratio versus number of charged particles produced per collision, in bins of centrality class 1 (left - least central collisions) to centrality class 7 (right). No dependence of the ratio on centrality is seen, although the value in class 1 is slightly higher than that in class 7. The systematic uncertainties for this analysis have been estimated to be in the order of $\sim 6.5\%$, which gives a systematic error of $\langle \bar{p}/p \rangle_{\text{sys.}} = \pm 0.05$. The systematic uncertainties have been determined by varying the dca and N_{hits} cut and rejecting tracks crossing the central membrane.

The numerical values of the anti-proton to proton ratio from on-line reconstructed events versus, p_{\perp} , y and N_{ch} are included in Appendix B (Table B.3).

The results of this analysis compare well with the results of the off-line analysis. Bearing in mind the limited statistics of the on-line analysis system, the values of the data agree within a few percent and are within the errors of the off-line analysis. This confirms the high quality of the on-line analysis. This result might support the idea to use the Level-3 trigger to trigger on events with a high number of reconstructed Lambdas ($\Lambda \rightarrow p\pi^{-}$). In such a trigger algorithm a good proton identification would be necessary to reduce combinatorics in the invariant mass calculation of proton and pion $^{-}$ pairs.

5. *Analysis of Anti-Proton to Proton Ratio*

5.2. \bar{p}/p Analysis at High Transverse Momentum

In this section, the analysis of the anti-proton to proton ratio at high transverse momentum ($1.3 < p_{\perp} < 4.5$ GeV/ c) in central $^{197}\text{Au} + ^{197}\text{Au}$ collisions at a center of mass energy of $\sqrt{s_{NN}} = 200$ GeV is presented. The ring imaging Čerenkov (RICH) detector was employed for the identification of anti-protons and protons. The coverage of the RICH detector is $|\eta| < 0.3$ in pseudorapidity. Its coverage in azimuth is $\Delta\phi = 20^{\circ}$ at an angle of $\phi = 60^{\circ}$ from the horizontal axis at 5 o'clock (see Figure 2.7). Thus the measurement of \bar{p}/p at high p_{\perp} is limited to a small but symmetric acceptance at mid-rapidity.

The RICH detector relies on tracking provided by the TPC to determine the particle momentum as described in Section 3.4.2. The identification is carried out by detecting Čerenkov radiation produced by charged particles going through a radiating medium. The Čerenkov radiation is emitted in a cone, the opening angle of which is determined by the velocity of the particle. Thus the momentum is known, and particles can be identified by the correlation of the reconstructed Čerenkov angle and the reconstructed momentum (see Figure 4.8).

The RICH detector was included in STAR in the first run (2000) when $\sim 800k$ central events of $^{197}\text{Au} + ^{197}\text{Au}$ collisions at a center of mass energy of $\sqrt{s_{NN}} = 130$ GeV were recorded. An average of one charged hadron with $p > \sim 1$ GeV/ c was measured by the RICH detector in a central $^{197}\text{Au} + ^{197}\text{Au}$ collision per accepted event. The number of charged hadrons decreases by approximately a magnitude per GeV/ c . Thus in every 100 events, a charged particle having a momentum above $p > 3$ GeV/ c was detected by the RICH. In spite of limited statistics at high momentum, the anti-proton to proton ratio within a transverse momentum from $1.3 < p_{\perp} < 3.0$ GeV/ c was extracted out of this dataset [92] [55].

The main goal for the second year of STAR operation with the RICH detector was to extend the measurement of anti-protons and protons in central $^{197}\text{Au} + ^{197}\text{Au}$ collisions to the transverse momentum of $1.3 < p_{\perp} < 5$ GeV/ c . It became obvious that even if 5 million events were taken, one yielded only ~ 500 hadrons at $p_{\perp} \sim 5$ GeV/ c . Taking the reconstruction efficiency to be 80% and an identification efficiency of $\sim 80\%$, the expected yield would be in the order of ~ 300 charged hadrons.

This makes the RICH detector a perfect candidate to use the Level-3 trigger to select events with high momentum hadrons in the detector's acceptance. A Level-3 trigger algorithm was therefore developed which could enrich the event sample by up to ~ 10 times, by triggering on high momentum tracks in the RICH acceptance.

In the following sections, we will give an overview of the dataset used for the

5. Analysis of Anti-Proton to Proton Ratio

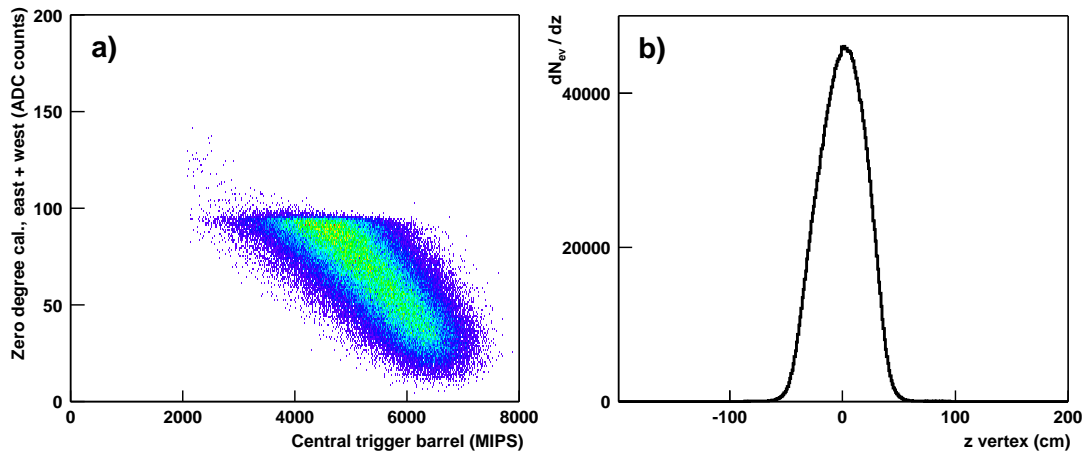


Figure 5.20.: a) Correlation of the summed ZDC signal versus the summed CTB signal of 10% most central events taken with the central Level-0 trigger. b) Longitudinal event (z) vertex distribution of the events in the dataset.

analysis and show the effect of the Level-3 trigger on the dataset. Then we will introduce the particle identification with the RICH detector, present the corrections applied and conclude with the resulting anti-proton to proton ratio.

5.2.1. Central Dataset Details

A dataset of 2.52 million central events of $^{197}\text{Au} + ^{197}\text{Au}$ collisions at a center of mass energy of $\sqrt{s_{NN}} = 200$ GeV was available for physics analysis. As in the previous analysis, the data were taken between August and November, 2001. Events were taken employing run types “productionCentral”, “productionCentral600” and “productionCentral1200”. Approximately half of the dataset is taken with the STAR magnet operating with full magnetic field, and the other half with reversed full magnetic field. The track reconstruction in the TPC was performed with software production library version P02gc+P02gd+P02ge. The ring reconstruction in the RICH detector was performed with the reconstruction software of production library version P02gf.

5.2.2. Event Centrality and Vertex Distribution

The data were taken with the central Level-0 trigger (see Section 5.1.2). The ZDC sum combined with the CTB sum were used to trigger on central events. Required was a ZDC ADC count sum of less than 90 ADC counts and a CTB

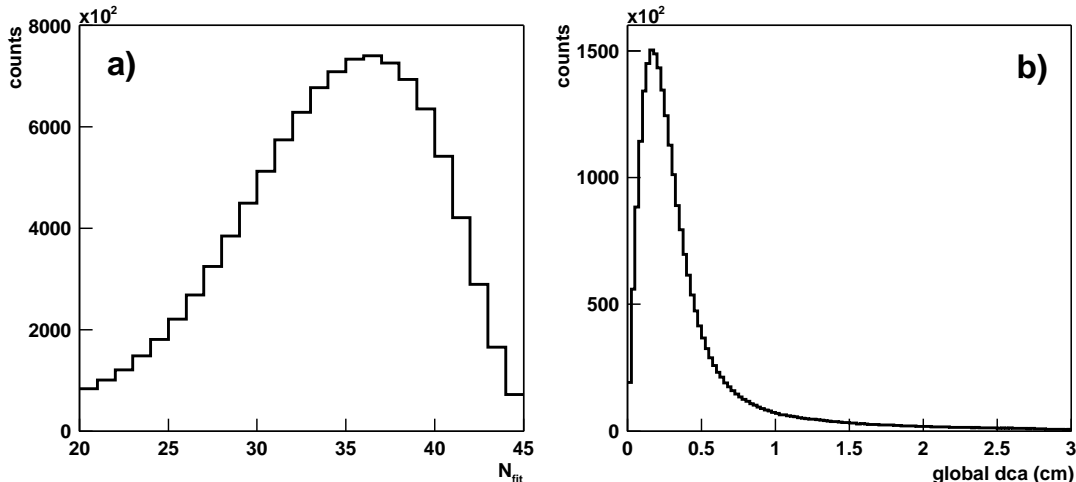


Figure 5.21.: Number of fit hits ($N_{fit\ hits}$) in the TPC (a) and dca -distribution of tracks with $N_{fit\ hits} \geq 22$ in the TPC and $p_{\perp} > 1.0$ GeV/ c (b), within the acceptance of the RICH detector.

sum³ of more than 2000 MIPS (1 MIP = 5 ADC counts) (Figure 5.20a) to trigger on 10% most central events from $^{197}\text{Au} + ^{197}\text{Au}$ collisions at $\sqrt{s_{NN}} = 200$ GeV.

The vertex distribution of the 2.52 million events is shown in Figure 5.20b. The events were taken with the Level-0 ZDC timing trigger to restrict the longitudinal vertex of the recorded events (see Sections 3.6 and 5.1.3). Due to the characteristics of the Level-0 ZDC timing trigger, an additional restriction of the longitudinal event vertex of $|z\ \text{vertex}| < 25$ cm was necessary. 77% of the events remain after this cut. This criterion also insures that the events are well within the acceptance range of the RICH detector. The RICH detector is located at mid-rapidity and extends ± 65 cm along the longitudinal axis of the experiment.

5.2.3. Track Quality Criteria

The RICH relies on the momentum measurement of the particles in the TPC for particle identification. The momentum resolution for a primary track is approximately $\Delta p_{\perp}/p_{\perp} \sim 1\%$ per one GeV/ c in transverse momentum [88], for a track with $N_{fit\ hits} \geq 22$. Figure 5.21a shows the distribution of the number of fit hits ($N_{fit\ hits}$) on tracks that were extrapolated to the RICH detector. Only tracks within the detector acceptance with $N_{fit\ hits} \geq 20$ were accepted for extrapolation.

³expressed as MIPS, “MIP” stands for the energy loss/ionization of a “minimum ionizing particle”,

5. Analysis of Anti-Proton to Proton Ratio

Particles having a small dca are considered as primaries. Secondary particles give rise to wide dca s and can be produced either by Lambda ($\Lambda \rightarrow p\pi^-$), or by interactions of primary particles (π , K , p etc.) with nuclei of the detector material. The ring reconstruction in the RICH detector employs only particles that can be reconstructed using the primary track model, only primary tracks having a $dca < 1$ cm, were used (see Figure 5.21b). This dca criterion insures a high track quality and gives sufficient statistics for the analysis. It also suppresses tracks originating from secondary decays [93] or primary particle interactions with the detector material. 92% of all tracks which can be extrapolated to the RICH detector pass the $dca < 1$ cm cut.

5.2.4. Level-3 Trigger Enhancement

Due to the small coverage ($|\eta| < 0.3$, $\Delta\phi = 20^\circ$) of the RICH detector only a small fraction of the particles produced in a central $^{197}\text{Au} + ^{197}\text{Au}$ collision at mid-rapidity traverse the detector. The distribution of the number of hadrons produced in these collisions falls steeply with increasing momentum. The number of charged hadrons with a momentum of $p > 1$ GeV/ c in the acceptance range of the RICH detector has been measured to be approximately one per central $^{197}\text{Au} + ^{197}\text{Au}$ collision. In the dataset of 10% central events roughly every ~ 100 rd event, has a charged particle having a momentum $p > 3$ GeV/ c in the acceptance of the RICH detector.

To enrich the recorded dataset of central Au+Au collisions with a track having a momentum $p > 3$ GeV/ c in the detector acceptance the RICH detector (i.e. RICH candidates) a Level-3 RICH algorithm running on the GL3s of the Level-3 trigger system was developed (Section 4.3.4). It was calculated that if RHIC would reach the promised design luminosity of $R = 2.4$ kHz, the L3-Trigger system would run with a rate of $r = 50$ Hz. Assuming that 5 events/s could be written to HPSS, the L3 RICH algorithm would enhance the sample of RICH candidates by a factor of 10, yielding up to 500k RICH candidates instead of 50k in a unbiased event sample.

Unfortunately during the 2001 $^{197}\text{Au} + ^{197}\text{Au}$ run, the luminosity of RHIC was low and increased from a small collision rate of a few hundred collisions per second in early August up to ~ 1000 collisions/s at end of Oktober. Figure 2.8a shows the ZDC rate during this run. When running the 10% central Level-0 trigger, the STAR accepted ~ 7 central events per second at a ZDC coincidence rate of 700 Hz. Where the DAQ was capable of writing ~ 7 central $^{197}\text{Au} + ^{197}\text{Au}$ collisions per second to HPSS at RCF. In early November the collision rate finally increased to over 1000 Hz in the beginning of a RHIC store and the STAR Level-3 trigger was used in the beginning of those stores to trigger on rare events, thereby enhancing the taken event sample with Υ , ^4He and RICH candidates

(see Section 3.8.1).

For coincidence rates between 600 and 1200 Hz, the run type “productionCentral600” was used to record an event sample which was enriched (biased) by RICH candidates and other Level-3 triggers. In “productionCentral600” the default unbiased Level-3 trigger “True” algorithm was prescaled by a factor of two. Thus, every second event was passed through unbiased, and remaining events were available for the other Level-3 algorithms (see Section 3.8.1). The Level-3 trigger system would thereby reconstruct twice the number of events. It triggered on RICH candidates, and increased the number of RICH candidates in the saved event sample by a factor two. In run type “productionCentral1200” used for coincidence rates higher than 1200 Hz, the unbiased Level-3 trigger true algorithm was prescaled by 5, so that every fifth event was passed through unbiased. The trigger would ideally reconstruct 4 times the number of events that could be written to tape and thus would increase the number of RICH candidates in the saved event sample by a factor of four. The L3 Trigger actually ran at a rate of ~ 14 Hz and ~ 28 Hz in “productionCentral600” and “productionCentral1200” respectively. In the run type “productionCentral1200” $\sim 14\%$ of the events saved were triggered by the Level-3 RICH algorithm.

Figure 2.8b shows the coincidence rate for a RHIC store, at the end of the run, where a high luminosity was achieved. For such a store, central events would be taken under the run type “productionCentral1200” for ~ 1.5 hours. Thereafter, one would switch to “productionCentral600” for another ~ 1.5 hours until the coincidence rate decreases to below 600 Hz. Thereafter, one would subsequently switch to take unbiased events with “productionCentral”. The various run types of the dataset are shown in Table 5.5. Owing to the low luminosity of the collider, only a small fraction of the central event dataset was triggered by the Level-3 trigger.

Run type	Prescale	# Events	# Events accepted	#RICH candidates	RICH cand. (%)
productionCentral	1	2.092M	1.603M	21.2k	1.30
productionCentral600	2	0.349M	0.275M	5.9k	2.15
productionCentral1200	5	0.080M	0.065M	2.9k	4.38

Table 5.5.: Run types employed to record the central event dataset with corresponding prescale referred to the Level-3 True algorithm (prescale 1 \Rightarrow unbiased events), number of events for each run type, number of accepted events, number of RICH candidates and fraction of RICH candidates.

5. Analysis of Anti-Proton to Proton Ratio

Figure 5.22a shows the uncorrected momentum spectra of charged particles that traverse the active volume of the RICH detector for the various run types.

In order to compare the momentum spectra of “productionCentral600” and “productionCentral1200” triggered (biased) by the Level-3 RICH algorithm and the unbiased “productionCentral” run, the biased spectra were normalized to one in the first bin to the number of entries of the “productionCentral” spectra and divided by the “productionCentral” spectra (5.22b,c) In Figure 5.22b, it can be seen that the event sample is enriched with tracks having a momentum larger than 3 GeV/ c by a factor of ~ 1.7 . This falls short of the prescale factor 2, due to the Level-3 trigger efficiency of $\sim 80\%$ (see below). The increase of tracks having a momentum lower than 3 GeV/ c is due to the lower momentum cut used for triggering by the Level-3 RICH algorithm. This lower momentum cut ($p_{\perp} > 2.7$ GeV/ c) was necessary to reach an efficiency of the Level-3 RICH algorithm of $\sim 80\%$ with a momentum resolution of the on-line reconstruction which is, in the mode the Level-3 trackfinder was operated, a factor ~ 2.5 worse compared to off-line reconstruction (see Section 4.3.2). Figure 5.22c shows that an enhancement of ~ 3.5 times the number of tracks having $p > 3$ GeV/ c was achieved in “productionCentral1200”.

Taking the momentum resolution and the efficiency of the Level-3 trigger system into consideration, it was expected that the Level-3 RICH algorithm should have an efficiency of 80% compared to the off-line analysis. This is supported by Figure 5.23 which shows the efficiency of the Level-3 RICH algorithm on the 2001 dataset. In the off-line analysis, a track was considered to be a RICH candidate if it possessed the following features: $p > 3.0$ GeV/ c , $dca < 1$ cm, $N_{fit\ hits} \geq 23$ and $|\eta| < 0.3$. The tail in the momentum region $2.5 < p < 3.0$ GeV/ c is caused by the slightly looser momentum cut used in the Level-3 RICH algorithm (see Section 4.3.4).

For the analysis of corrected hadron yields, identified with the RICH, in central events of Au+Au collisions taken in 2001, two factors have to be taken into consideration: 1) To determine absolute cross sections, it is necessary to normalize the hadron yields in the “productionCentral600” and “productionCentral1200” runs with the number of events triggered by the Level-3 RICH algorithm, employing the Level-3 counters (see Section 3.8.1). 2) The efficiency of the Level-3 RICH algorithm has to be taken into consideration.

However, in the analysis of the anti-proton to proton ratio described here, the correction and extrapolation factors should be the same and are expected to cancel out.

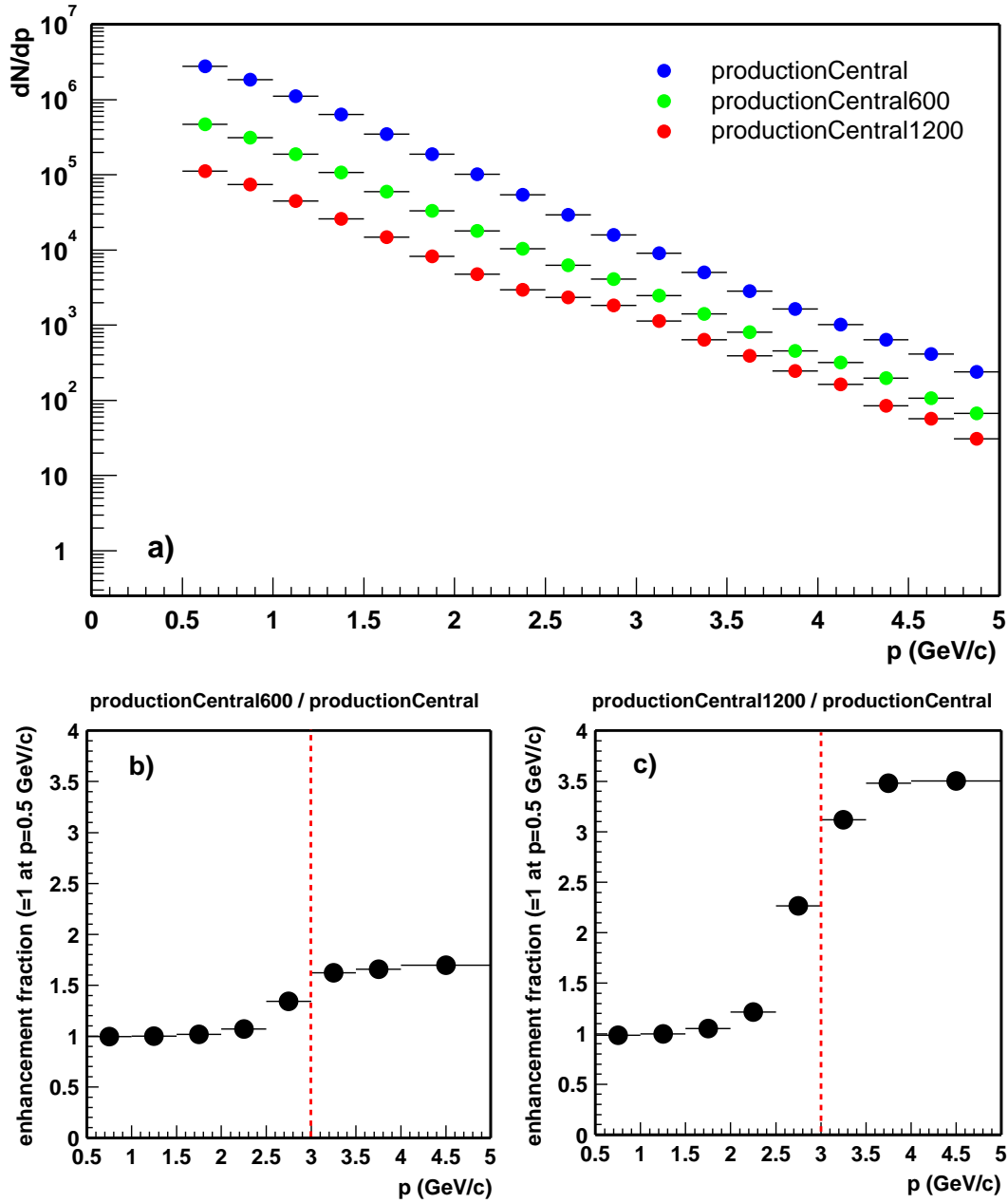


Figure 5.22.: a) Uncorrected transverse momentum distribution of charged particles within the acceptance of the RICH detector from “productionCentral”, “productionCentral600” (triggered, prescale=2) and “productionCentral1200” (triggered, prescale=5). Enhancement of tracks with a momentum of $p > 3$ GeV/c in the RICH detector in b) “productionCentral600” and c) “productionCentral1200” runs.

5. Analysis of Anti-Proton to Proton Ratio

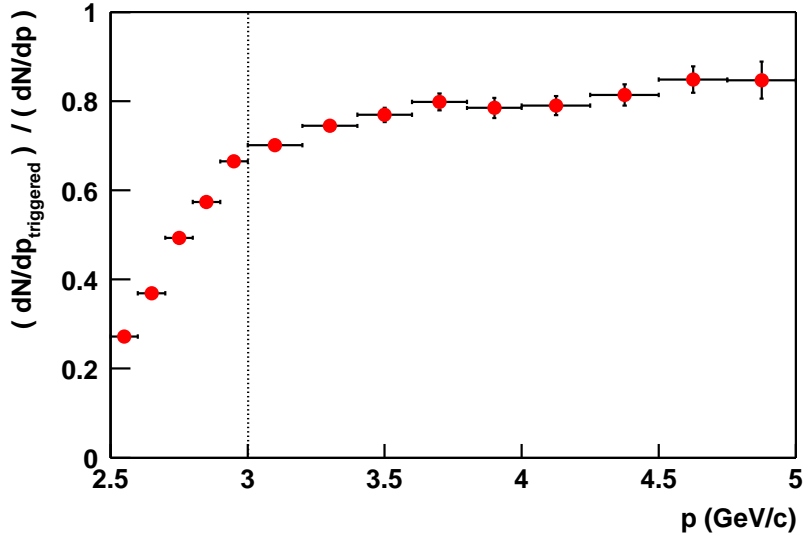


Figure 5.23.: Trigger efficiency of the Level-3 RICH algorithm, compared to the off-line analysis.

Expected Level-3 Trigger Enhancement During 2001

The enhancement of high transverse momentum particles in the RICH detector acceptance, using the Level-3 RICH algorithm has been discussed in this section. It is worth mentioning that, due to the low luminosity of the RHIC collider in 2001, the desired data sample of 5 million events was not taken. The full potential of the Level-3 trigger could therefore not be exploited. The rate of storage to HPSS was, however, higher than expected, at ~ 7 Hz. An enhancement of RICH candidates of ~ 7 could have been expected if RHIC had been running at design luminosity. If that luminosity had been reached, the Level-3 trigger would have processed events at a rate of 50 Hz. In such a scenario, the Level-3 RICH algorithm would have yielded ~ 350 k RICH candidates (compared to 30k under the conditions given here) for the desired event sample. This would have increased the statistics by an order of a magnitude.

5.2.5. Pseudorapidity Distribution of Particles in the Acceptance of the RICH Detector

Figure 5.24a shows the raw pseudorapidity distribution of charged particles within the acceptance range of the RICH detector. These were required to be reconstructed with $N_{\text{fits}} \geq 23$, $p_{\perp} > 1.0$ GeV/c and a $dca < 3$ cm from events of central $^{197}\text{Au} + ^{197}\text{Au}$ collisions having a $|z \text{ vertex}| < 25$ cm. For a symmet-

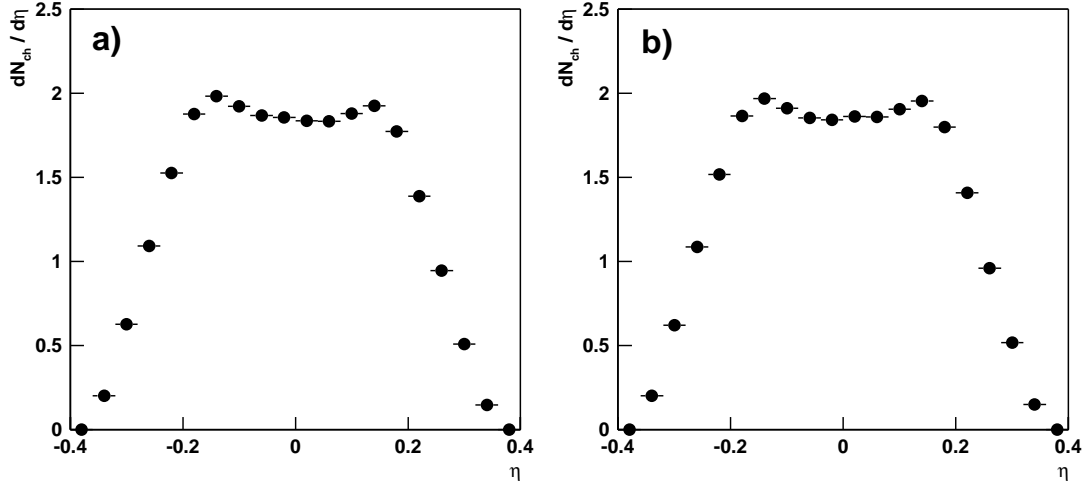


Figure 5.24.: Uncorrected pseudorapidity distribution from central events of charged particles for events with a hadron with $p_{\perp} > 1.0$ GeV/ c within the acceptance range of the RICH detector (a) from tracks with $N_{fit\ hits} \geq 23$ in the TPC (b) from tracks with $N_{fit\ hits} \geq 20$ in the west side and $N_{fit\ hits} \geq 23$ in the east side of the TPC.

ric collision system such as $^{197}\text{Au} + ^{197}\text{Au}$, a symmetric distribution of particles about zero pseudorapidity would be expected. However, the raw pseudorapidity distribution in this case was found to be slightly asymmetric. The asymmetry of the pseudorapidity distribution (Figure 5.24a) can be corrected by applying a different point cut for the east(positive η) and west (negative η) TPC regions. A point cut of $N_{fit\ hits} \geq 23$ in the west side and $N_{fit\ hits} \geq 20$ in the east side produces a more symmetric pseudorapidity distribution 5.24b. The TPC shows different efficiencies at small pseudorapidities around the central membrane for the east and west sides. This effect has already been seen in the central data from the 2000 run [94]. From Figure 5.24b, the average number of charged hadrons with $p_{\perp} > 1.0$ GeV/ c and $|\eta| \leq 0.2$ is found to be $\langle N_{ch} \rangle \geq 1.88$ per central $^{197}\text{Au} + ^{197}\text{Au}$ collision. The track criterion of $N_{fit\ hits} \geq 23$ in the west side and $N_{fit\ hits} \geq 20$ in the east side was then used for further analysis.

5.2.6. Particle Identification using the RICH Detector

The identification of particles in the RICH detector is done by correlating the opening angle of the emitted Čerenkov radiation cone with the particle momentum measured in the TPC (Figure 4.8). See Section 4.2 for details about the reconstruction process.

RICH Detector Residuals

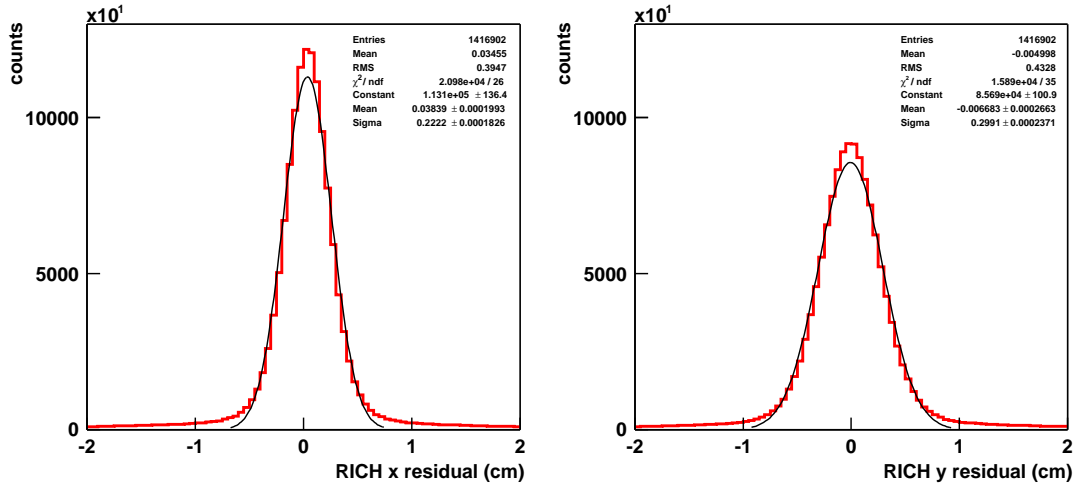


Figure 5.25.: Residuals of extrapolated tracks and MIP in the RICH detector in drift (x in local RICH coordinates) and bending plane (y in local RICH coordinates) directions.

The difference between the predicted intersection point, given by the extrapolation of the track from the TPC reconstruction, and the actual intersection point, given by a MIP in the RICH radiator, can be used as a quality parameter and is commonly referred to as a residual. A small residual at the pad plane implies a small difference between the predicted and actual intersection point at the RICH radiator. Thus it is desirable to select tracks having a small residual, since this implies a well-defined intersection at the RICH radiator, where the Čerenkov light originates.

The residual between the predicted track and actual intersection point (MIP) is measured in the TPC drift direction⁴, (x in RICH local coordinates) and TPC's bend plane (y in RICH local coordinates). Figure 5.25 shows the residuals in both directions. The distributions are fit by a Gaussian function, fit results are

⁴ z direction in global STAR coordinates

given in the figure. For the identification of the anti-protons and protons, tracks with a residual less than $\sigma = 1.6$ ($|x| = |y| < 0.5$ cm) from the mean of the residual distribution were accepted for the further analysis.

Photon Multiplicities

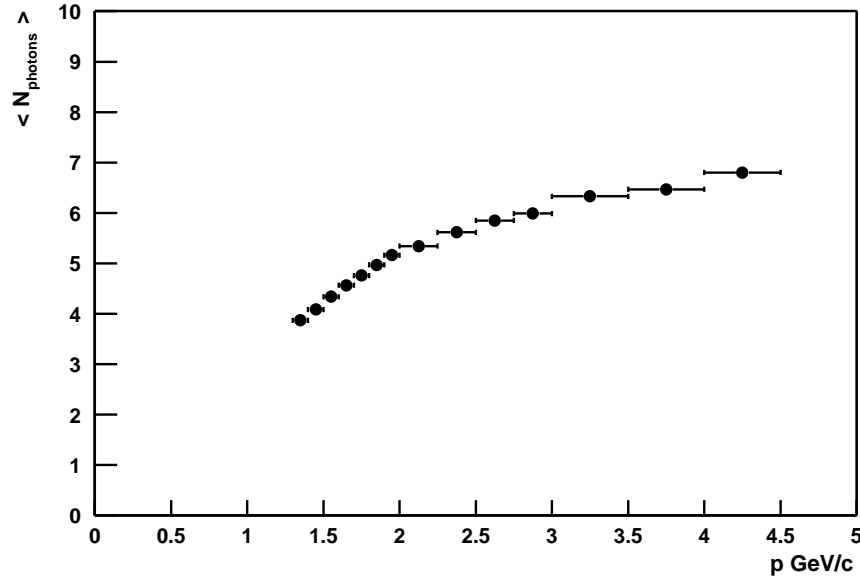


Figure 5.26.: Mean number of photons ($\langle N_{photons} \rangle$) versus momentum (p) produced by protons traversing the radiator.

The number of photons (N_{photon}) in the Čerenkov cone for a given detector is depending on the velocity of the particle (Equation 3.12). Accordingly, at high momentum more photons are produced for a given particle species, or a faster pion gives rise to a higher number of photons than a slower proton with the same momentum. The dependence of the mean number of photons ($\langle N_{photons} \rangle$) on the momentum is shown in Figure 5.26. In order to achieve a reasonable efficiency combined with a low background of the Čerenkov spectra, a minimum of $N_{photons} \geq 4$ was required in this analysis. This cut determines the lower momentum cut of ($p > 1.3$ GeV/c) at which protons can be identified with the RICH detector.

Čerenkov Spectra

The reconstructed Čerenkov angle as a function of momentum is shown in Figure 4.8. Bands with low background centered around the predicted curves for pions,

5. Analysis of Anti-Proton to Proton Ratio

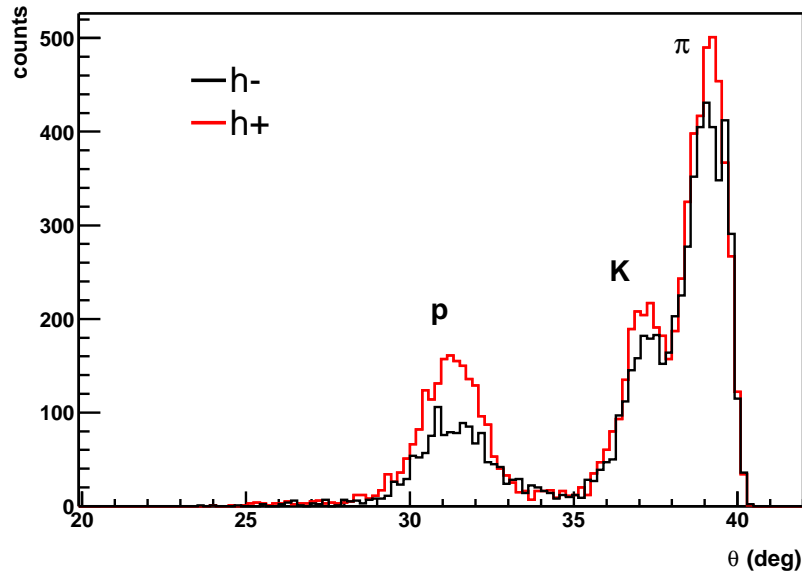


Figure 5.27.: Čerenkov angle spectra for positive (red) and negative (black) hadrons within the momentum range $2.0 < p < 2.1$ GeV/ c

kaons and protons can be seen. In Figure 5.27, the Čerenkov angle spectra for positive and negative hadrons within the momentum range $2.0 < p < 2.1$ GeV/ c are shown. It is clearly visible that for particles having the same momentum, the mean of the Gaussian distributions of the slower protons (p) can be found at smaller angles than the Gaussian distributions of kaons (K) and pions (π). Within this momentum range, the proton and kaon distributions are clearly separated, while the kaon and pion distributions merge.

We define the variable $\Delta\theta = \theta_{exp} - \theta_{m_p}$, which gives the difference between the theoretical Čerenkov angle, θ_{m_p} , for a proton with a given momentum and the experimentally measured Čerenkov angle, θ_{exp} . If the measured particle is a proton, $\Delta\theta$ is small, and is Gaussian distributed about zero. If the measured particle is a kaon or a pion $\Delta\theta$ is greater. The theoretical Čerenkov angle, θ_{m_p} , for a proton with the mass, m_p , having the momentum, p (GeV/ c), is calculated using Equation 3.11:

$$\theta_{m_p} = \arccos \frac{\sqrt{p^2 + m_p^2}}{\langle n \rangle p} \quad (5.10)$$

Using an average value $\langle n \rangle = 1.29039$ as the refractive index of the radiator (2001 run).

The advantage of using the $\Delta\theta$ variable is that it shows the difference between the theoretically and experimentally determined Čerenkov angles (similar to the

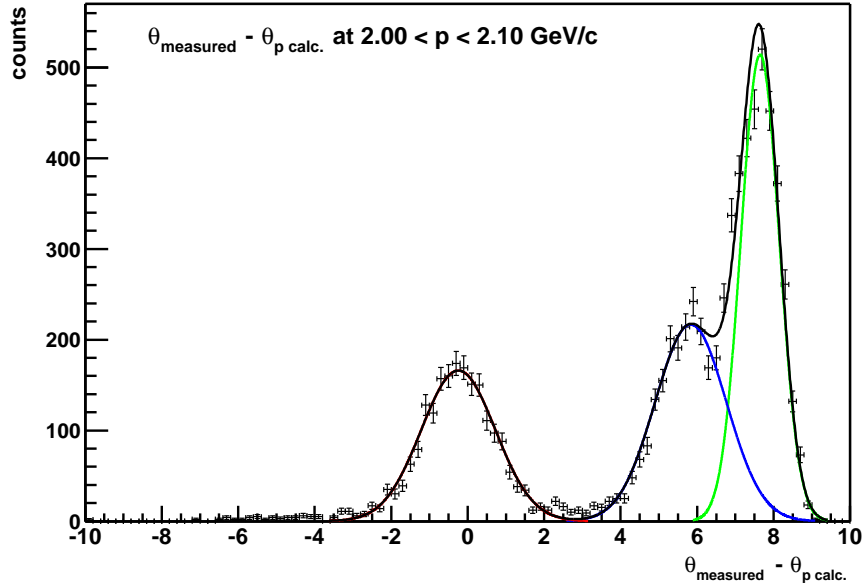


Figure 5.28.: $\Delta\theta = \theta_{exp} - \theta_{m_p}$ spectra for positive hadrons within the momentum range of $2.0 < p < 2.1$ GeV/c. Spectra are fit with function $f(\Delta\theta)$ given in Equation 5.11.

Z variable used for the dE/dx identification in Section 5.1.6). $\Delta\theta$ is shown in Figure 5.28 for the same momentum region as in Figure 5.27. The proton Gaussian distribution is centered around zero. The distribution is fit with a 3 Gauss fit function

$$f(\Delta\theta) = \frac{A_\pi}{\sigma_\pi \sqrt{2\pi}} e^{-\overline{\Delta\theta}_\pi^2 / 2 \sigma_\pi^2} + \frac{A_K}{\sigma_K \sqrt{2\pi}} e^{-\overline{\Delta\theta}_K^2 / 2 \sigma_K^2} + \frac{A_p}{\sigma_p \sqrt{2\pi}} e^{-\overline{\Delta\theta}_p^2 / 2 \sigma_p^2} \quad (5.11)$$

where A_i is the area, σ_i the width and $\overline{\Delta\theta}_i$ the mean of each fit for pions, kaons and protons denoted by $i = \pi, K, p$ respectively. Generally, the fit described the Čerenkov spectra well, and therefore no attempt was made to include background in the fit function. Studies of the dependence of background on the residual, η and number of photons have shown that for a residual of $x = y < 0.5$, $\eta < 0.2$ and $N_{photons} > 4$, the background can be reduced to the order of $\sim 4\%$ in this momentum region. The background will be taken into consideration in the determination of the systematic error. Spectra of $\Delta\theta$ were taken in $\Delta p_\perp = 0.1$ GeV/c wide momentum bins within the momentum range between $1.4 < p < 2.5$ GeV/c. Due to the limited statistics at higher momenta, bins were widened to $\Delta p_\perp = 0.25$ GeV/c from $2.5 < p < 4.5$ GeV/c. The results of the fit with the function $f(\Delta\theta)$ are summarized in Figure 5.29. The solid lines are the theoretical prediction for pions, kaons and protons using Equation 3.11. Points indicate the

5. Analysis of Anti-Proton to Proton Ratio

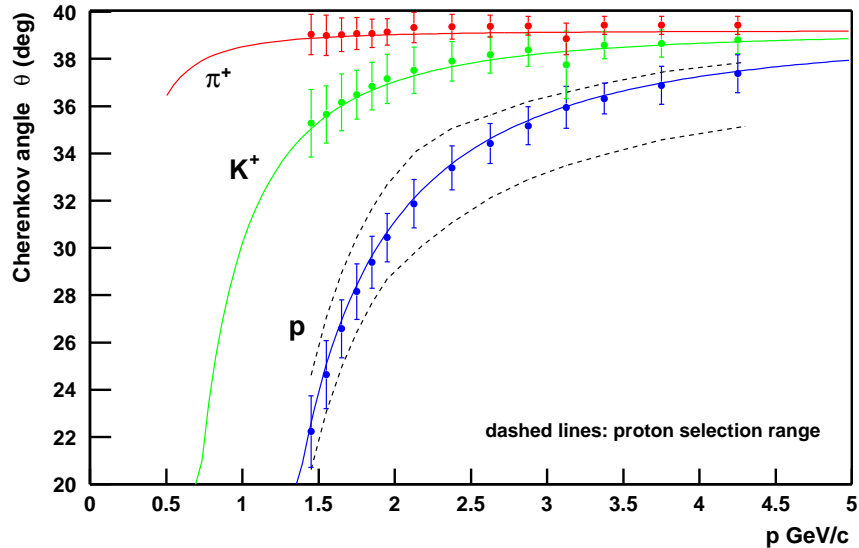


Figure 5.29.: The solid lines represent the theoretical prediction of the Čerenkov angle, θ , versus momentum, p , for pions (red), kaons (green) and protons (blue). The dots represent the mean, the error bars the sigma from the Gaussian fit on the $\Delta\theta$ spectra. The dashed lines show the selection range used for proton identification.

mean and the error bar represents the sigma of the Gaussian fit. Due to limited statistics at momentum $p > 3.5$ GeV/ c , the $\Delta\theta$ spectra could not be fit here. The black dashed line gives the selection ranges in θ where anti-protons and protons are taken as identified. In the momentum range $2.0 < p < 2.25$ GeV/ c , a lower cut of $\sigma = -2$, and a upper cut of $\sigma = 2$ was applied around θ_{m_p} to select anti-protons and protons. The upper cut was tightened to $\sigma = 0.13$ at momenta in the range $4.00 < p < 4.50$ GeV/ c , in order to reduce contamination from kaons and pions.

5.2.7. Raw \bar{p}/p Ratio from RICH Detector Data

The uncorrected transverse momentum distributions for anti-protons and protons, identified by the RICH detector using the aforementioned cuts, is shown in Figure 5.30. Anti-protons and protons from all the events which were accepted from the 2.5 million event dataset are shown as solid dots. The increase of the spectra in the transverse momentum range between $1.3 < p_{\perp} < 2.0$ GeV/ c is caused by the low number of photons detected in the Čerenkov rings in that momentum range (see Figure 5.26). The uncorrected transverse momentum spectra

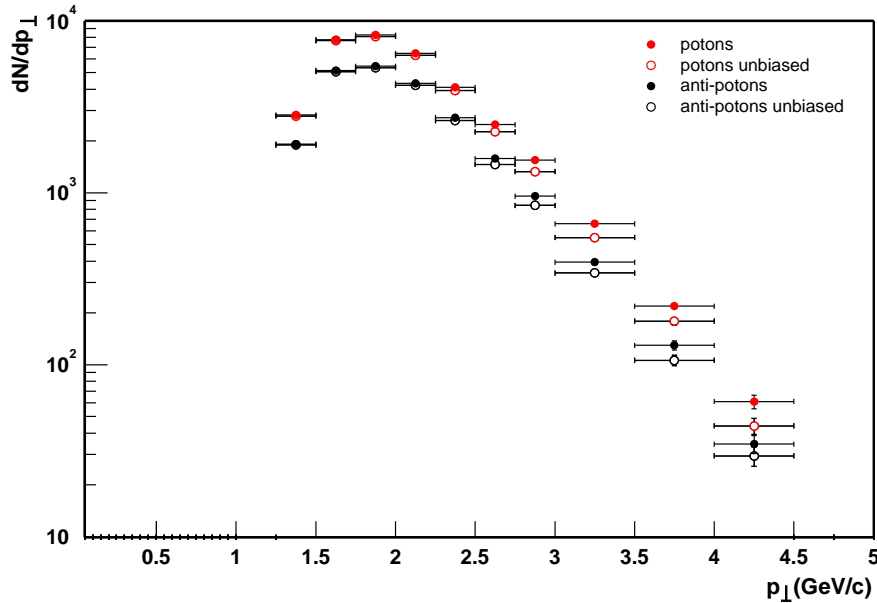


Figure 5.30.: Raw transverse momentum (p_{\perp}) spectra of anti-protons (black) and protons (red) identified by the RICH detector. p_{\perp} spectra from events that are not enriched (i.e. unbiased) by the Level-3 RICH trigger are represented by open circles.

of anti-protons and protons of events which are unbiased by the Level-3 trigger (prescale 1) are shown as open circles⁵. This allows comparison of the enhancement of the yield of anti-protons and protons brought about by using the Level-3 RICH algorithm in the events taken with the “productionCentral600” and “productionCentral1200” run types. The integrated raw yield of protons within the acceptance of the RICH in the momentum range $3.0 < p_{\perp} < 4.5$ GeV/ c is $N_{biased} = 941 \pm 5$ for the whole set of events and $N_{unbiased} = 771 \pm 5$ for the unbiased events only. This comparison shows that the proton yield could be enhanced by 22% with the use of the Level-3 trigger in the 428k events of “productionCentral600” and “productionCentral1200” run types. The uncorrected ratio of anti-protons and protons from anti-proton and proton yields of Figure 5.30 is shown in Figure 5.31. Events from the whole dataset, including events enhanced by the Level-3 trigger were used. The ratio decreases slightly at higher transverse momenta ($p_{\perp} > 2.5$ GeV/ c). However, a high systematic error is expected at momentum $p_{\perp} > 3.5$ GeV/ c (see Section 5.3).

⁵Events which were triggered by the Level-3 RICH algorithm of the Level-3 trigger in the “productionCentral600” and “productionCentral1200” runs are not included.

5. Analysis of Anti-Proton to Proton Ratio

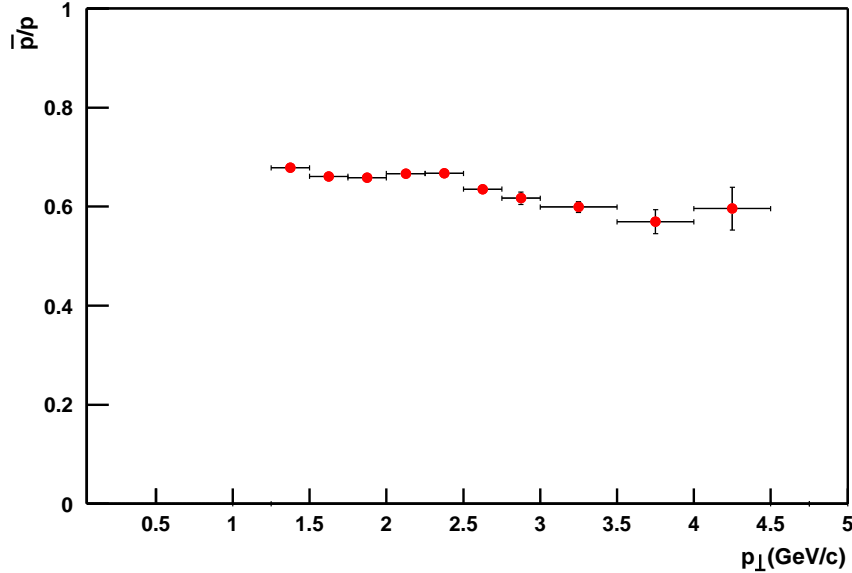


Figure 5.31.: Uncorrected anti-proton to proton ratio, \bar{p}/p , versus transverse momentum, p_{\perp} , for (anti-)protons identified with the RICH detector.

5.2.8. Corrections to Raw RICH Detector \bar{p}/p Ratio

The secondary background was found to be less than 1% for protons with a momentum of $p \sim 1.0$ GeV/ c and a $dca < 1.5$ cm, identified in the TPC (see Section 5.1.7). In the case of the RICH detector, there is approximately twice the detector material (see Table A.3) which particles can interact with, before being detected. The tight $dca < 1$ cm combined with the residual cut of less than 0.5 cm, suppresses the secondary protons to an estimated fraction of $\sim 2\%$.

To determine the absorption correction for anti-protons in detector material in front of the RICH detector, a full GEANT simulation was performed. In the simulation, the absorption of anti-protons and protons along the path through the STAR detector was studied. Figure 5.32 shows where anti-protons are absorbed. Regions of high density indicate a high anti-proton absorption. The SVT can be seen at $r = 14.5$, as well as the inner field cage at $r = 50$ cm. These sources of absorption are already known from a similar study for anti-protons detected in the TPC alone (see Section 5.1.7). Within the TPC, anti-proton absorption can be seen in the gas ($X_0 = 1.17\%$). At the end of the TPC at a radius of $r = 200$ cm, the outer field cage ($X_0 = 14.8\%$) can be identified as a source of anti-proton absorption. Some absorption points are visible in the region of the RICH detector. The radiation length of the RICH detector materials in front of the MWPC is ($X_0 = 15\%$).

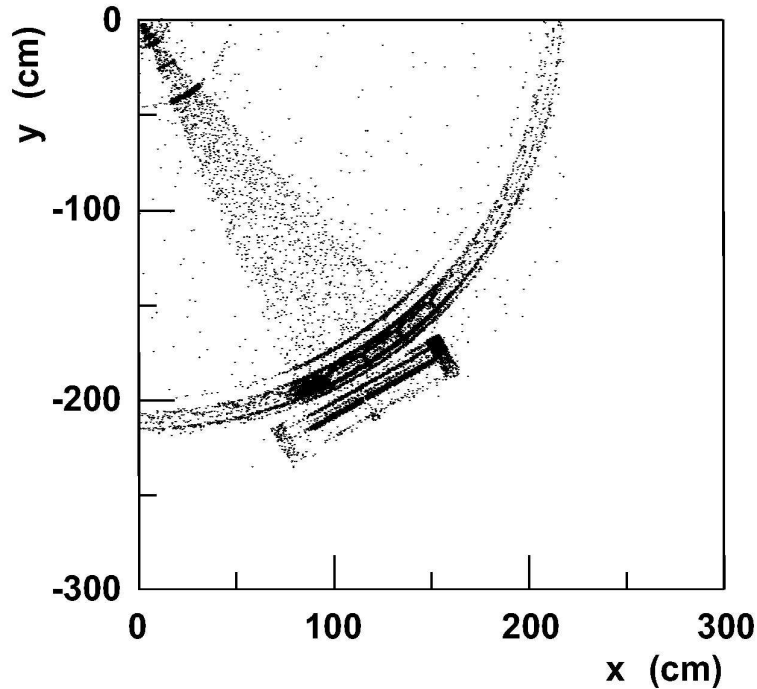


Figure 5.32.: Points of absorption of anti-protons in the x - y -plane, within the acceptance of the RICH detector in the STAR experiment (2001 geometry).

For a transverse momentum of $p_{\perp} = 2.0$ GeV/ c a rate of anti-proton absorption of 19% was found. Protons involved in hadronic interactions with the detector material were found to be absorbed at a rate of 9.3% at the same momentum. At a higher transverse momentum of $p_{\perp} = 4.0$ GeV/ c , the absorption for anti-protons is still high at 17% and at 8.7% for protons. The dependence of the anti-proton and proton absorption on the transverse momentum is shown in Figure 5.33. The increase of absorption compared to the absorption of anti-protons in the TPC is consistent with the additional Material that particles have to traverse to be detected in the RICH detector (see Table A.3).

5.3. \bar{p}/p for Low & High Transverse Momentum

The corrected \bar{p}/p versus transverse momentum p_{\perp} from 10% central events of $^{197}\text{Au} + ^{197}\text{Au}$ collisions at a center of mass energy of $\sqrt{s_{NN}} = 200$ GeV is shown in Figure 5.34. Within the transverse momentum range of $0.4 < p_{\perp} < 1.0$ GeV/ c the anti-proton and proton yields were identified by correlating the specific ionization of particles in the detector gas of the TPC (dE/dx) with the momentum of

5. Analysis of Anti-Proton to Proton Ratio

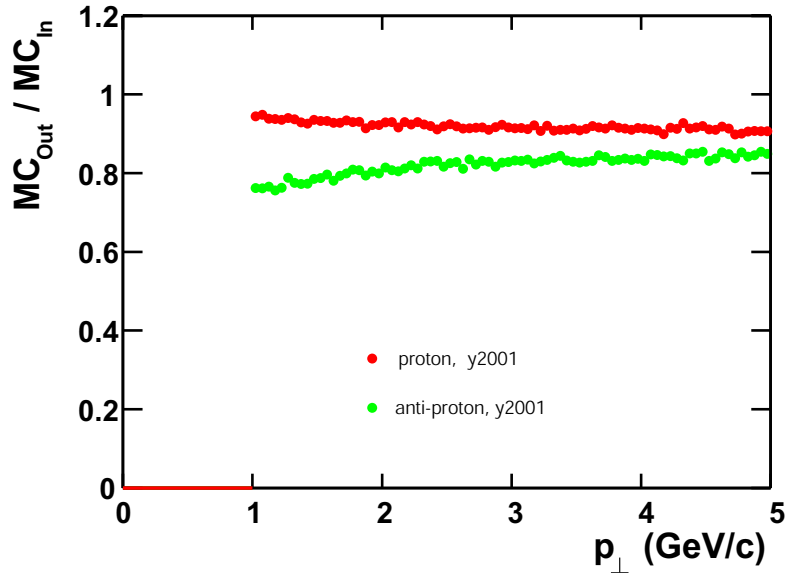


Figure 5.33.: Fraction of anti-protons (green points) and protons (red points) that reach the active volume of the RICH detector and are not absorbed in matter in front of the RICH detector, versus p_{\perp} (2001 geometry).

the particles. The measurement was performed in the rapidity range of $|y| < 0.5$ with full azimuthal coverage. The \bar{p}/p within this momentum range was corrected for secondary-background protons and anti-proton absorption. The anti-proton and proton momentum was corrected for energy loss in the detector material.

The ring imaging Čerenkov detector was used for to identify anti-proton and proton yields at higher transverse momentum within $1.3 < p_{\perp} < 4.5$ GeV/ c . The coverage of the RICH detector is $|\eta| < 0.3$ in pseudorapidity and $\Delta\phi = 20^{\circ}$ at $\phi = 60^{\circ}$ in azimuth.

The comparison of TPC data with RICH data is reasonable, since events of central $^{197}\text{Au} + ^{197}\text{Au}$ collisions at an energy of $\sqrt{s_{NN}} = 200$ GeV are highly symmetric around mid-rapidity. Thus, the particle yields measured in a limited angular space can be extrapolated to the full angular range.

At low transverse momentum of $0.4 < p_{\perp} < 1.0$ GeV/ c the ratio does not show a dependence on the transverse momentum, taking the systematic errors in account. Comparing the TPC data with the ratio determined using the RICH detector, one finds good agreement below $p_{\perp} < 2.5$ GeV/ c . From the average of $\langle \bar{p}/p \rangle|_{0.4 < p_{\perp} < 1.0 \text{ GeV}/c} = 0.80 \pm 0.002_{\text{stat.}} \pm 0.05_{\text{syst.}}$ from the TPC data, the ratio decreases to $\bar{p}/p = 0.645 \pm 0.005_{\text{stat.}} \pm 0.10_{\text{syst.}}$ at $p_{\perp} = 4.25$ GeV/ c . However, the systematic errors at higher transverse momentum increase as well.

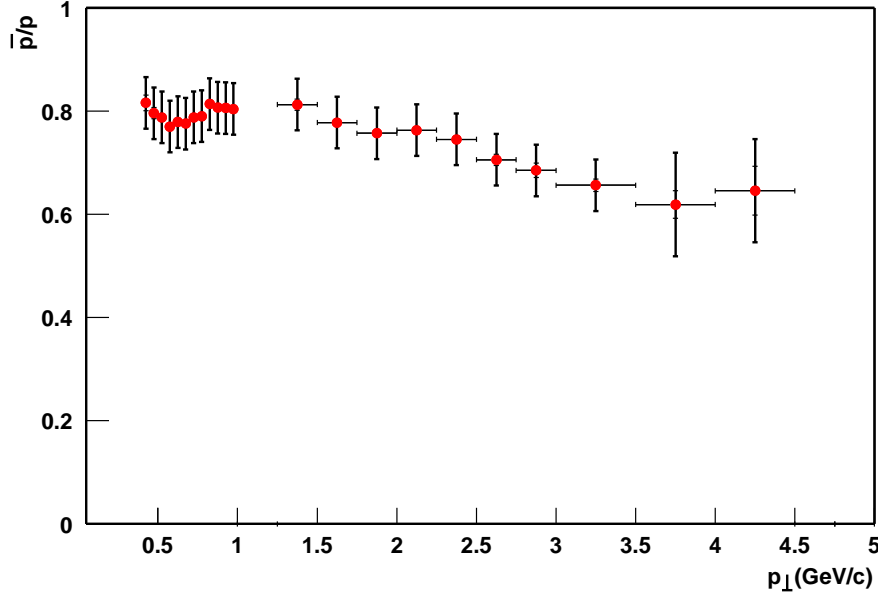


Figure 5.34.: Corrected \bar{p}/p versus p_{\perp} from 10% central $^{197}\text{Au} + ^{197}\text{Au}$ collisions at $\sqrt{s_{NN}} = 200$ GeV. Protons(anti-protons) were identified with dE/dx in the TPC within the momentum range of $0.4 < p_{\perp} < 1.0$ GeV/ c and with the RICH from $1.3 < p_{\perp} < 4.5$ GeV/ c . Statistical uncertainties are drawn as thin lines, systematical uncertainties as thick bars.

The systematic error of the RICH analysis was determined by comparing the global track model with the primary track model, taking the background in the Čerenkov spectra (see Section 11) into consideration and rejecting tracks crossing the central membrane. Within the lower transverse momentum ($1.3 < p_{\perp} < 3.5$ GeV/ c) range a systematic error of $\langle \bar{p}/p \rangle_{\text{syst.}} \leq \pm 0.05$ was determined. For the higher momentum $p_{\perp} > 3.5$ GeV/ c region the systematic error increases to an estimated $\langle \bar{p}/p \rangle_{\text{syst.}} \leq \pm 0.10$, because due to the limited statistics proton yields could not be fit in this momentum range and the selection criteria had to be extrapolated. Additionally the r.m.s angular deflection of ~ 0.5 [55] suffered by a particle traversing the detector material in front of the RICH detector becomes an issue in a momentum range $p = 4.25$ GeV/ c where the angular difference between a proton and a kaon is $\Delta\theta = 1.32^{\circ}$.

5. *Analysis of Anti-Proton to Proton Ratio*

6. Results and Discussion

In the previous chapter, an analysis of the anti-proton to proton ratio (\bar{p}/p) in $^{197}\text{Au} + ^{197}\text{Au}$ collisions at a center of mass energy of $\sqrt{s_{NN}} = 200$ GeV was presented, in the momentum range $0.4 < p_{\perp} < 1.0$ GeV at mid-rapidity $|y| < 0.5$. The ratio was found to be independent of transverse momentum and rapidity (Figure 5.13, 5.14) with a mean value of $\langle \bar{p}/p \rangle|_{0.4 < p_{\perp} < 1.0 \text{ GeV}/c} = 0.80 \pm 0.002_{\text{stat.}} \pm 0.05_{\text{syst.}}$ and $\langle \bar{p}/p \rangle|_{-0.5 < y < 0.5} = 0.80 \pm 0.002_{\text{stat.}} \pm 0.05_{\text{syst.}}$ from events taken with the 10% central trigger. For the 5% most central events taken with the minimum bias trigger a mean ratio of $\langle \bar{p}/p \rangle|_{0.4 < p_{\perp} < 1.0 \text{ GeV}/c} = 0.81 \pm 0.002_{\text{stat.}} \pm 0.05_{\text{syst.}}$ and $\langle \bar{p}/p \rangle|_{-0.5 < y < 0.5} = 0.82 \pm 0.002_{\text{stat.}} \pm 0.05_{\text{syst.}}$ was found. From this analysis, a slight dependence of the ratio on the centrality of the collisions was seen. It decreases from $\bar{p}/p = 0.83 \pm 0.002_{\text{stat.}} \pm 0.05_{\text{syst.}}$ for the most peripheral collisions (less than 80% central) to $\bar{p}/p = 0.78 \pm 0.002_{\text{stat.}} \pm 0.05_{\text{syst.}}$ for the 5% most central collisions. However, the effect is well within the systematical error of the measurement.

In the higher transverse momentum region at mid-rapidity, a decrease of the anti-proton to proton ratio was measured. It was found to be $\bar{p}/p = 0.645 \pm 0.005_{\text{stat.}} \pm 0.10_{\text{syst.}}$ at $p_{\perp} = 4.25 \text{ GeV}/c$. However, the systematic error of the measurement is large. In the following sections we will discuss these results and compare them to models.

6.1. Feed-down of \bar{p} and p from Heavier Baryons

The measured anti-proton and proton yields contain contributions from the decay of heavier strange baryons (feed-down), Lambda ($\Lambda \rightarrow p\pi^{-}$), Xi ($\Xi^{-} \rightarrow \Lambda\pi^{-}$), Omega ($\Omega^{-} \rightarrow \Lambda K^{-}$) and their anti-particles. The decay of $\Lambda \rightarrow p\pi^{-}$ and $\bar{\Lambda} \rightarrow \bar{p}\pi^{+}$ are expected to be the most prominent contributions to the anti-proton and proton yields.

In order to estimate the contribution of feed-down of (anti-)protons from (anti-)Lambda decays to the (anti-)proton yield, the data given here were used. The preliminary proton and anti-proton yield in central $^{197}\text{Au} + ^{197}\text{Au}$ collisions at $\sqrt{s_{NN}} = 200$ GeV were taken to be $dN_p/dy|_{y < 1} = 32.96 \pm 5.2$, $dN_{\bar{p}}/dy|_{y < 1} =$

6. Results and Discussion

26.70 ± 4.0 [95]. Due to the lack of published results of Lambda yields at $\sqrt{s_{NN}} = 200$ GeV, the anti-Lambda yield in central $^{197}\text{Au} + ^{197}\text{Au}$ collisions at $\sqrt{s_{NN}} = 130$ GeV, $dN_{\bar{\Lambda}}/dy|_{|y|<1} = 12.3 \pm 0.3$ [99], is multiplied by the increase in hadron multiplicity, $R_{\frac{200}{130}} = 1.15$ [97]. The preliminary anti-Lambda to Lambda ratio $\Lambda/\bar{\Lambda} = 0.83 \pm 0.02$ [98] from central 200 GeV $^{197}\text{Au} + ^{197}\text{Au}$ collisions was then used to calculate the Lambda yield. The feed-down corrected anti-proton to proton ratio, $\bar{p}_{\text{cor}}/p_{\text{cor}}$, from the measured ratio is therefore given by

$$\frac{\bar{p}_{\text{cor}}}{p_{\text{cor}}} = \frac{\bar{p} - \bar{p}_{\bar{\Lambda}}}{p - p_{\Lambda}} = \frac{(dN_{\bar{p}}/dy) - (dN_{\bar{\Lambda}}/dy)}{(dN_p/dy) - (dN_{\Lambda}/dy)} \approx 0.77 \pm 0.05 \quad (6.1)$$

The decrease in value of the feed-down corrected ratio, is still within the systematic error of this analysis. At higher transverse momentum the feed-down effect is expected to be smaller.

The anti-Lambda to Lambda ratio for $^{197}\text{Au} + ^{197}\text{Au}$ collisions at $\sqrt{s_{NN}} = 130$ GeV reported in [96] shows a slight increase from central to peripheral events (see Table 6.1). The larger the anti-Lambda to Lambda ratio, the more symmetric is the feed-down in anti-proton and proton yields. The asymmetry of the $\Lambda/\bar{\Lambda}$ might contribute to the slight centrality dependence in the anti-proton to proton ratio versus number of charged particles (N_{ch}) shown in Figure 5.19c.

Centrality	$\Lambda/\bar{\Lambda}$
0%-5%	0.71
5%-10%	0.74
10%-20%	0.73
20%-35%	0.77
35%-75%	0.78

Table 6.1.: Anti-Lambda to Lambda ratio in minimum bias events of $^{197}\text{Au} + ^{197}\text{Au}$ collisions at $\sqrt{s_{NN}} = 130$ GeV [96].

6.2. Energy Dependence of \bar{p}/p

In the introductory section to this thesis, Figure 1.7 illustrated the behavior of \bar{p}/p with respect to collision energy. In Figure 6.1, two further points from RHIC experiments are added to the aforementioned graph. A mean value of $\bar{p}/p = 0.71 \pm 0.002_{\text{stat.}} \pm 0.05_{\text{syst.}}$ from central $^{197}\text{Au} + ^{197}\text{Au}$, at $\sqrt{s_{NN}} = 130$ GeV [99] and $\bar{p}/p = 0.81 \pm 0.002_{\text{stat.}} \pm 0.05_{\text{syst.}}$ for central $^{197}\text{Au} + ^{197}\text{Au}$ at $\sqrt{s_{NN}} = 200$ GeV, as well as the \bar{p}/p ratios at SPS energies are plotted. The \bar{p}/p ratio increases by a factor of ~ 11 as the energy increases from the top SPS

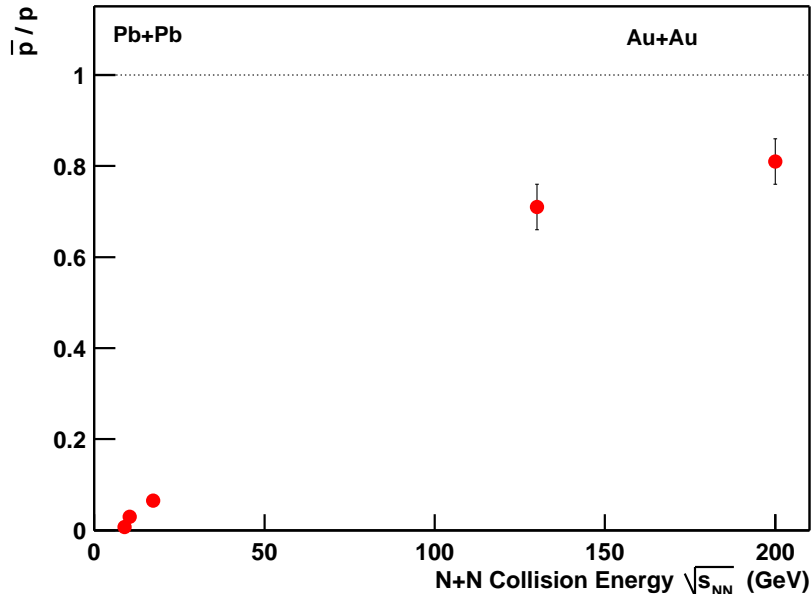


Figure 6.1.: Anti-proton to proton ratio at SPS and RHIC energies.

energy of $\sqrt{s_{NN}} = 17.3$ GeV to $\sqrt{s_{NN}} = 130$ GeV, and by a factor of ~ 1.14 from $\sqrt{s_{NN}} = 130$ GeV to 200 GeV at RHIC.

As already mentioned in Section 1.5, the production of anti-proton and proton yields at mid-rapidity are customarily described by two processes: 1) production of an anti-proton and a proton (Y_c) during the hadronization stage of the fireball. 2) Transport of incident protons (Y_{tr}) from beam rapidity towards mid-rapidity. This results in

$$\frac{\bar{p}}{p} = \frac{Y_c}{Y_c + Y_{tr}}. \quad (6.2)$$

Using this equation, the ratio Y_c/Y_{tr} of produced anti-protons and protons (Y_c) and the yield of transported protons (Y_{tr}) can be calculated for the SPS and RHIC energies ($\sqrt{s_{NN}} = 17.3, 130, 200$ GeV). The measured ratios $\bar{p}/p = 0.065 \pm 0.0055$, 0.71 ± 0.05 and 0.81 ± 0.05 give $Y_c/Y_{tr} = 0.07 \pm 0.007$, 2.45 ± 0.7 and 4.26 ± 1.88 , respectively. Thus, while transport processes dominate proton production at SPS energies, the production of anti-protons and protons at RHIC are dominated by particle production. This is equivalent to saying that the number of net protons ($p_{net} = p - \bar{p}$) is significantly smaller at RHIC energies. This is referred to as an “almost net-baryon free” region, at mid-rapidity. From [95] the number of net baryons around mid-rapidity can be calculated to be $dN_{p_{net}}/dy|_{y<1} = dN_p/dy|_{y<1} - dN_{\bar{p}}/dy|_{y<1} = 34.7 \pm 6.2 - 26.7 \pm 4.2 = 8.0 \pm 2.2$.

An analysis of central $^{197}\text{Au} + ^{197}\text{Au}$ collisions at $\sqrt{s_{NN}} = 130$ GeV has been presented within the framework of the statistical model [5]. The best fit to 5

6. Results and Discussion

identical and 4 non-identical particle ratios is described by a temperature $T = 174 \pm 7$ MeV and a baryon chemical potential of $\mu_B = 46 \pm 5$ MeV. The anti-proton to proton ratio given by this model is $\bar{p}/p = 0.629$. A recent analysis [99] resulted in $\bar{p}/p = 0.71 \pm 0.002_{\text{stat.}} \pm 0.05_{\text{sys.}}$ for central $^{197}\text{Au} + ^{197}\text{Au}$ collisions at $\sqrt{s_{NN}} = 130$ GeV. The difference between the ratio derived in the statistical model and the measurement may be due to the lack of feed-down correction.

In order to predict hadron ratios in $^{197}\text{Au} + ^{197}\text{Au}$ collisions at a center of mass energy of $\sqrt{s_{NN}} = 200$ GeV, the baryon chemical potential is parametrized phenomenologically as $\mu_B \sim 1.3 \text{ GeV} (1 + \sqrt{s}/4.5 \text{ GeV})^{-1}$ [5]. Assuming a unified freeze-out condition giving a fixed energy per particle of ~ 1.1 GeV, results in a temperature of $T = 177 \pm 7$ MeV and a baryon chemical potential of $\mu_B = 29 \pm 8$ MeV. For these parameters, the calculated anti-proton to proton ratio is $\bar{p}/p = 0.752$. This is in good agreement with the low momentum analysis of the anti-proton to proton ratio presented here, especially in the case when the feed-down of heavier baryons is considered.

6.3. Transverse Momentum Dependence of \bar{p}/p

In Section 5.3, the transverse momentum dependence of the \bar{p}/p ratio for $^{197}\text{Au} + ^{197}\text{Au}$ collisions at a center of mass energy of $\sqrt{s_{NN}} = 200$ GeV was presented. The predictions of a pQCD calculation and a non-perturbative quenched and baryon junction scenario, i.e. the so-called *Soft+Quench* model, for the transverse momentum dependence of the anti-baryon to baryon ratios in $^{197}\text{Au} + ^{197}\text{Au}$ collisions at $\sqrt{s_{NN}} = 130$ GeV are discussed in [100]. Although these calculations are for $\sqrt{s_{NN}} = 130$ GeV, they can be compared to the $\sqrt{s_{NN}} = 200$ GeV results, since it is expected that although the total value of the ratios will change, the qualitative behavior will not.

Figure 6.2 plots the two models, as well as the resulting \bar{p}/p ratio versus p_{\perp} from this analysis, as shown in Section 5.3. The application of pQCD theory predicts that protons at high transverse momentum with small longitudinal momentum, originate predominantly from valence quarks. This results in a decrease of the anti-proton to proton ratio towards high transverse momentum. In Figure 6.2, the pQCD calculation is compared to a non-perturbative *Soft+Quench* scenario. In the latter, baryon transport is described by topological, non-perturbative baryon production and a transport mechanism based on the Regge trajectory. Baryon creation is enhanced by baryon junctions. In the baryon junction scenario, the incident baryons are described in a Y-string configuration. While the 3 strings of valence quarks fragment into hadrons, the baryon consisting of sea quarks remains. The \bar{p}/p value from the *Soft+Quench* model for intermediate transverse momentum ($0.5 < p_{\perp} < 5.0$ GeV/c) are higher than those predicted by pQCD

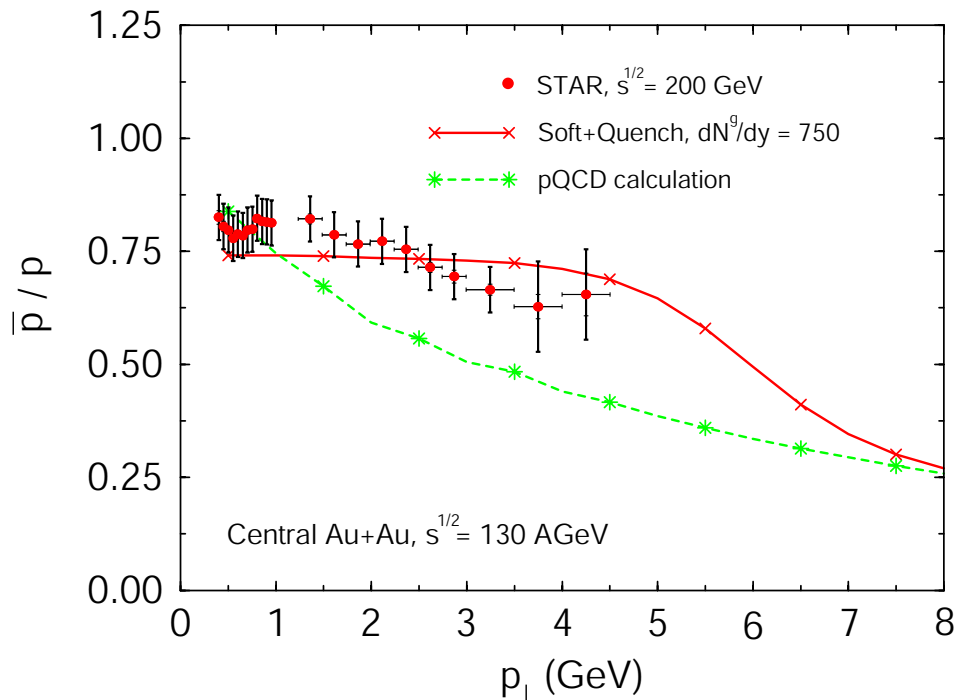


Figure 6.2.: Red dots: anti-proton to proton ratio versus transverse momentum (p_{\perp}) in central $^{197}\text{Au} + ^{197}\text{Au}$ collisions at $\sqrt{s_{NN}} = 200$ GeV. Green line: pQCD calculation. Red line: *Soft+Quench* model [100].

calculations.

The \bar{p}/p ratio analysis presented in this thesis shows no strong dependence of the ratio on transverse momentum, as predicted by the pQCD calculation. The results are better described by the non-perturbative quenched+baryon junction scenario. In conclusion, it would seem that the maximum transverse momentum available in these measurements ($p_{\perp} = 4.5$ GeV/ c) is not high enough to enter the range where the creation of anti-protons and protons and their ratios are well described by pQCD calculations.

6.4. Fragmentation versus Recombination Picture

The measurements of \bar{p}/p reveal that the central rapidity region of $^{197}\text{Au} + ^{197}\text{Au}$ collisions at $\sqrt{s_{NN}} = 200$ GeV is close to, but not totally, net-baryon free, since the ratio is smaller than unity. It must therefore be considered if mechanisms such as baryon stopping and transport from beam rapidity to mid-rapidity can explain the data presented here. However, constituents of the beam nuclei (i.e.

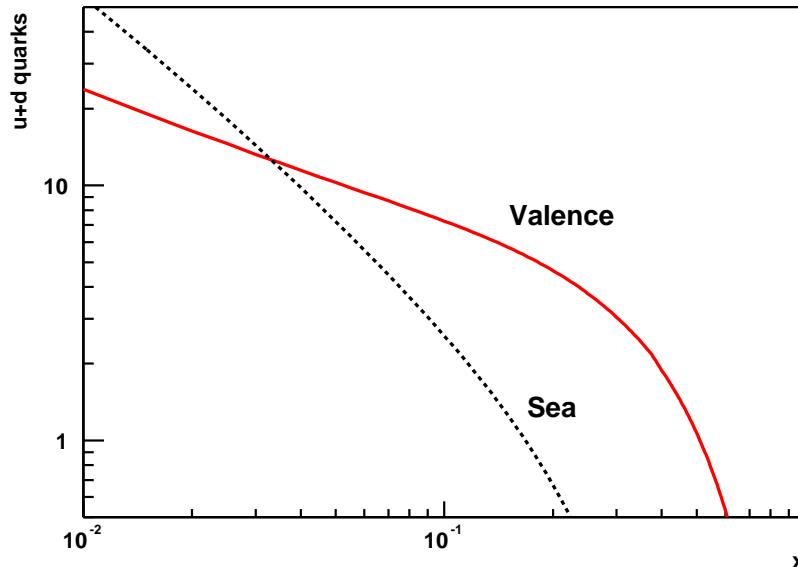


Figure 6.3.: Parton distribution function of valence (red line) and sea $u+d$ quarks (black, dashed line), depending on their longitudinal momentum fraction x .

their valence and sea quarks and gluons), are distributed over the entire rapidity range. This is shown in Figure 6.3 which depicts the valence and sea $u+d$ quark distribution in a proton, calculated with the GRV-98 parton distribution function [102]. The break-up of the initial state nucleons would already lead to a baryon anti-baryon asymmetry, due to the valence quarks. This has been recently pointed out in [103] and for the forward region of proton+nucleus collisions in [104].

A nucleus+nucleus collision can be considered in a simple breakup picture without “stopping”. It is assumed that quarks and anti-quarks from the incoming nucleons are resolved at a scale $Q \sim p_{\perp} = 1$ GeV, which is a typical hadronic scale. Their rapidity distribution is obtained from the GRV-98 parton distribution functions by translating the rapidity y of the quark into the longitudinal momentum fraction $x = \frac{p_{quark}}{p_{beam}}$ using [103]:

$$x = \frac{Q}{m_p} e^{y-y_b}, \quad (6.3)$$

where m_p is the proton mass and $y_b = 5.36$ is the beam rapidity of a nucleon with an energy of $E_N = 100$ GeV resulting in $\sqrt{s_{NN}} = 200$ GeV at RHIC (Eq. 1.10).

Assuming that these resolved quarks and anti-quarks fragment into hadrons,

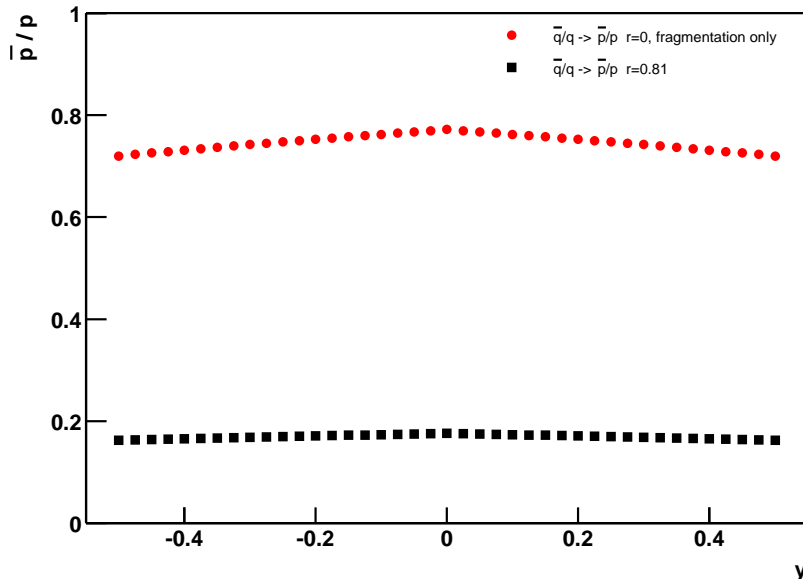


Figure 6.4.: \bar{p}/p ratio versus rapidity. Fragmentation of quarks directly into protons (red points). Recombination scenario (black squares).

some fraction will be protons and anti-protons. The ratio then equals the ratio of anti-quarks to quarks. If so, the result shown in Figure 6.4 (red points) is obtained. Both the absolute and the weak rapidity dependence appear to agree surprisingly well with the data shown in Figure 5.13. In this simple scenario, the measured \bar{p}/p ratio is reproduced without additional need for stopping or transport of quarks.

On the other hand, a recombination mechanism of liberated quarks and anti-quarks could be considered to form the final state hadrons [105]. In this scenario, a fraction r of the total number of anti-quarks will be “lost” to form mesons, leaving $N_{\bar{q}}(1-r)$ anti-quarks to produce anti-protons. At the same time, $N_q - rN_{\bar{q}}$ will remain to form protons. Hence,

$$\frac{N_{\bar{p}}}{N_p} = \frac{1-r}{N_q/N_{\bar{q}} - r}, \quad (6.4)$$

For $r \rightarrow 1$, \bar{p}/p approaches zero. To estimate r it is assumed that $rN_{\bar{q}}$ anti-quarks form pions, neglecting other hadron species for simplicity. This leads to

$$\frac{N_{\bar{p}}}{N_{\pi^-}} = \frac{1-r}{3r}, \quad (6.5)$$

The factor of 3 in the denominator accounts for the three pion states (π^+ , π^- , π^0). STAR measured an anti-proton to pion $^-$ ratio of $\bar{p}/\pi^- = 0.079 \pm 0.015$ [106],

6. Results and Discussion

leading to $r = 1/(3N_{\bar{p}}/N_{\pi^-} + 1) = 0.81 \pm 0.03$. Using this value of r in Eq. 6.4, results in the curve depicted by black squares in Figure 6.4. Evidently, \bar{p}/p is well below the data in this scenario. Thus, to achieve the measured ratio of $\langle \bar{p}/p \rangle|_{-0.5 < y < 0.5} = 0.80 \pm 0.002_{\text{stat.}} \pm 0.05_{\text{syst.}}$ in central $^{197}\text{Au} + ^{197}\text{Au}$ collisions, the recombination scenario requires additional production of quarks and anti-quarks by gluon-gluon interactions, which would be expected. Nevertheless, it should be noted that the additional production or transport of q, \bar{q} -pairs must exactly compensate for the loss due to meson production in order to be consistent with the data. In conclusion, the anti-proton to proton ratio measured in $^{197}\text{Au} + ^{197}\text{Au}$ collisions can be reproduced assuming quark fragmentation into anti-protons and protons. Alternatively, assuming a recombination scenario with a realistic fraction of produced mesons requires substantial quark pair production, possibly by gluon fusion.

It should be noted that apart from the two scenarios given here as an attempt to explain the absolute value and the rapidity dependence of the anti-proton to proton ratio, other approaches have also been discussed [107].

7. Conclusion

In this thesis the anti-proton to proton ratio in $^{197}\text{Au} + ^{197}\text{Au}$ collisions, measured at mid-rapidity, at a center of mass energy of $\sqrt{s_{NN}} = 200$ GeV is reported. The value was measured to be $\bar{p}/p = 0.81 \pm 0.002_{\text{stat.}} \pm 0.05_{\text{syst.}}$ in the 5% most central collisions. The ratio shows no dependence on rapidity in the range $|y| < 0.5$. Furthermore, a dependence on transverse momentum within $0.4 < p_{\perp} < 1.0$ GeV/ c is not observed. At higher p_{\perp} , a slight drop in the ratio is observed. In the present analysis, the highest momentum considered is $p_{\perp} = 4.5$ GeV/ c yielding $\bar{p}/p = 0.645 \pm 0.005_{\text{stat.}} \pm 0.10_{\text{syst.}}$. However, the systematic error is higher in this momentum range. A slight centrality dependence was observed, where a decrease from $\bar{p}/p = 0.83 \pm 0.002_{\text{stat.}} \pm 0.05_{\text{syst.}}$ for most peripheral collisions (less than 80% central) to $\bar{p}/p = 0.78 \pm 0.002_{\text{stat.}} \pm 0.05_{\text{syst.}}$ for the 5% most central collisions was measured. An estimate of the feed-down contributions from the decay of heavier strange baryons results in $\bar{p}/p = 0.77 \pm 0.05_{\text{syst.}}$.

The measured ratio indicates a ~ 12.5 times higher value compared to the highest SPS energy of $\sqrt{s_{NN}} = 17.3$ and an “almost net-baryon free” region, at mid-rapidity. The asymmetry of protons and anti-protons may be explained by the contribution of valence quarks in a nucleus break-up picture. In such a scenario, the absolute value of the ratio and the fact that the ratio does not depend on rapidity (at mid-rapidity) is well reproduced. Fragmentation of quarks and anti-quarks into protons and anti-protons is assumed.

An estimate of the ratio, when feed-down correction is taken into consideration, agrees well with the prediction of a statistical model analysis at a temperature of $T = 177 \pm 7$ MeV and a baryon chemical potential of $\mu_B = 29 \pm 8$ MeV. The temperature achieved is only slightly higher when compared to the top SPS energy, while the baryochemical potential is factor ~ 10 lower. As in the case of the SPS results, these parameters are close to the phase boundary of Figure 1.6.

The measurement of the ratio at high transverse momentum was of special interest in this analysis, since at RHIC energies, the cross section for hadrons at high transverse momentum is increased with respect to SPS energies. The weak dependence of the ratio on the transverse momentum is well described by the non-perturbative quenched and baryon junction scenario (i.e. *Soft+Quench* model), where baryon creation is enhanced by baryon junctions. In comparison the ratio

7. Conclusion

does not decrease within the considered momentum range as predicted by pQCD.

7.1. Outlook

As documented in this work, two new techniques were applied in the field of heavy ion physics: 1) To identify protons at high transverse momentum, a Ring Imaging Čerenkov detector was used. 2) The Level-3 trigger was used to enrich events with rare signals such as particles with a momentum $p > 3$ GeV/ c , in a small acceptance window.

Corrected hadron spectra from the STAR experiment, using the RICH detector, are a work in progress at present. In this analysis a correction for energy loss of the traversing particle in detector material should increase the resolution of the Čerenkov spectra. The consequence would be a higher separation of the particle yields in the Čerenkov spectra.

RHIC operation energies brought about an increase in cross section of high momentum particles with respect to SPS energies, so that these high momentum particles became measurable. These capabilities will again be improved when the LHC (Large Hadron Collider) at CERN is up and running. A center of mass energy of up to $\sqrt{s_{NN}} = 5,5$ TeV will be available in relativistic nucleus+nucleus collisions at LHC. A shortcoming of the STAR RICH detector prototype was the small number of clusters that defined the projection of the Čerenkov cones onto the detection plane. ALICE (A Large Ion Collider Experiment) [108] at the LHC will be covered with 7 RICH detector modules. The aforementioned shortcoming is expected to be eliminated due to the presence of a thicker radiator layer and an increased photon efficiency of the CsI layer [52].

Rare events containing particles such as Upsilon (Υ), anti-helium (${}^4\overline{He}$) and high momentum particles traversing the small acceptance RICH detector, were present with low cross sections at RHIC. The Level-3 trigger at STAR was successfully used to enhance the signal of these rare particles. In 2003, the EMC information was integrated into the Level-3 System. Right now it is under consideration to use a combination the Level-2 and Level-3 triggers in the 2004 ${}^{197}\text{Au} + {}^{197}\text{Au}$ run to trigger on events containing Upsilon ($\Upsilon \rightarrow e^+e^-$) candidates.

A high level trigger [109] [111] (HLT, comparable to the STAR Level-3 trigger) will be applied in ALICE, where cross sections for rare events are likely to increase, due to the higher center of mass energy. ALICE is again using a TPC as the principal detector of the Experiment. The HLT system will run at a higher frequency than in the STAR case, and the trigger system will have the capability to process information from more detectors. This means that additional particle identification information will be available at that trigger level, such as electron identification via the transition radiation detector [111].

A. Tables with Detector Attributes

A. Tables with Detector Attributes

Item	Dimension	Comment
Length of the TPC	420 cm	Two halves, 210 cm long
Outer diameter drift volume	400 cm	200 cm radius
Inner diameter drift volume	100 cm	50 cm radius
Distance cathode ground plane	209.3 cm	Each side
Cathode	400 cm diameter	At the center of the TPC
Cathode potential	28 kV	Typical
Drift gas	P10	10% methane, 90% argon
Pressure	atmospheric + 2 mbar	Regulated at 2 mbar
Drift velocity	5.45 cm/ μ s	Typical
Transverse diffusion (σ)	230 μ m/ $\sqrt{\text{cm}}$	At 140 V/cm and 0.5 T
Longitudinal Diffusion (σ)	360 μ m/ $\sqrt{\text{cm}}$	At 140 V/cm
Number of anode Sectors	24	12 on each end
Number of pads	136608	
Signal to noise ratio	20 : 1	
Electronics shaping time	180 ns	
Signal dynamics range	10 bits	
Sampling rate	9.4 MHz	
Sampling depth	512 time buckets	380 time buckets typical
Magnetic field	0, ± 0.25 , ± 0.5 Tesla	Solenoidal

Table A.1.: Summary of the TPC parameters TPCNIM:02.

Item	Inner Sector	Outer Sector
Pad size	$2.85 \times 11.5 \text{ mm}^2$	$6.2 \times 19,5 \text{ mm}^2$
Pad rows	13 (#1 to #13)	32 (#14 to #45)
Pad radial spacing	48 mm	20 mm
Pad cross spacing	3.35 mm	6.7 mm
Number of pads	1750	3942
Dist. anode wires to pad plane	2 mm	4 mm
Anode voltage	1170 V	1390 V
Anode amplification	3770	1230

Table A.2.: Comparison of the Inner and outer sector attributes and geometry of the readout sectors of the MWPC of the TPC [47].

Structure	Material	x (cm)	ρ (g/cm ³)	X_0 (cm)	x/X_0 (%)
Beam pipe total	Be	0.1	1.848	35.30	3.0
1 SVT layer	Si (mostly)	–	–	–	1.8
SVT total=3 layers		–	–	–	~6.0
Insulating gas	N ₂	30	0.001	37.99	0.10
TPC IFC	Al	0.004	2.700	24.01	0.04
TPC IFC	Kapton	0.015	1.420	40.30	0.05
TPC IFC	Nomex	1.27	0.064	40	0.20
TPC IFC	Adhesive	0.08	1.20	40	0.23
IFC Total (with gas)					0.62
TPC gas	P10	150.00	1.56E-03	20.04	1.17
TPC OFC	Cu	0.013	8.96	12.86	0.91
TPC OFC	Kapton	0.015	1.420	40.30	0.05
TPC OFC	Nomex	0.953	0.064	40	0.15
OFC	Adhesive	0.05	1.20	40	0.15
OFC Total (with gas)					2.43
Insulating gas	N ₂	5.7	0.001	37.99	0.02
Outmost shell	Al	0.5	2.700	24.01	4.31
Outmost shell	Honeycomb	2.0	0.037	–	0.09
Outmost shell	Adhesive	0.16	1.20	40	0.47
Support rail	Al	~ 0.8	2.700	24.01	6.85
Outmost shell total (w/ gas)					11.74
TPC total					14.8
CTB slat total	Scintillator	1.0			~0.20
Aluminium	Al	0.1	2.70	24.01	1.0
Honeycomb front panel	Rohacell 51	5.0	0.0513	–	2.0
Neoceran entrance window	Glass	0.4	–	~28.3	3.0
Radiator	C ₆ F ₁₄	1.0	–	–	5.0
Quartz exit window	SiO ₂	0.5	2.2	27.05	4.0
RICH total					15.0

Table A.3.: Material Properties in terms of radiation length, X_0 , of the materials used in the STAR experiment [112] [58] [47] [66] [55] [52] [113].

A. *Tables with Detector Attributes*

B. Tables with Results

B. Tables with Results

p_{\perp}	\bar{p}/p (\pm stat.) (\pm syst.)
0.425	$0.822 \pm 0.008 \pm 0.05$
0.475	$0.808 \pm 0.006 \pm 0.05$
0.525	$0.800 \pm 0.005 \pm 0.05$
0.575	$0.792 \pm 0.005 \pm 0.05$
0.625	$0.803 \pm 0.005 \pm 0.05$
0.675	$0.808 \pm 0.005 \pm 0.05$
0.725	$0.793 \pm 0.004 \pm 0.05$
0.775	$0.816 \pm 0.005 \pm 0.05$
0.825	$0.824 \pm 0.005 \pm 0.05$
0.875	$0.819 \pm 0.005 \pm 0.05$
0.925	$0.828 \pm 0.005 \pm 0.05$
0.975	$0.821 \pm 0.005 \pm 0.05$

y	\bar{p}/p (\pm stat.) (\pm syst.)
-0.450	$0.824 \pm 0.004 \pm 0.05$
-0.350	$0.817 \pm 0.004 \pm 0.05$
-0.250	$0.816 \pm 0.005 \pm 0.05$
-0.150	$0.810 \pm 0.005 \pm 0.05$
-0.050	$0.813 \pm 0.005 \pm 0.05$
0.050	$0.809 \pm 0.005 \pm 0.05$
0.150	$0.804 \pm 0.005 \pm 0.05$
0.250	$0.811 \pm 0.005 \pm 0.05$
0.350	$0.815 \pm 0.005 \pm 0.05$
0.450	$0.821 \pm 0.004 \pm 0.05$

class	$\langle N_{ch} \rangle$	\bar{p}/p (\pm stat.) (\pm syst.)
1	22.5	$0.835 \pm 0.010 \pm 0.05$
2	42.5	$0.837 \pm 0.007 \pm 0.05$
3	77.5	$0.829 \pm 0.006 \pm 0.05$
4	122.5	$0.821 \pm 0.005 \pm 0.05$
5	187.5	$0.810 \pm 0.004 \pm 0.05$
6	267.5	$0.806 \pm 0.003 \pm 0.05$
7	367.5	$0.801 \pm 0.003 \pm 0.05$
8	462.5	$0.789 \pm 0.003 \pm 0.05$
9	562.5	$0.789 \pm 0.003 \pm 0.05$

Table B.1.: \bar{p}/p with statistical and systematic uncertainties in minimum bias $^{197}\text{Au} + ^{197}\text{Au}$ collisions at $\sqrt{s_{NN}} = 200$ GeV, versus transverse momentum p_{\perp} , rapidity y and centrality classes $\langle N_{ch} \rangle$.

p_{\perp}	\bar{p}/p (\pm stat.) (\pm syst.)
0.425	$0.816 \pm 0.015 \pm 0.05$
0.475	$0.796 \pm 0.011 \pm 0.05$
0.525	$0.788 \pm 0.009 \pm 0.05$
0.575	$0.770 \pm 0.008 \pm 0.05$
0.625	$0.779 \pm 0.007 \pm 0.05$
0.675	$0.776 \pm 0.006 \pm 0.05$
0.725	$0.788 \pm 0.006 \pm 0.05$
0.775	$0.790 \pm 0.006 \pm 0.05$
0.825	$0.814 \pm 0.006 \pm 0.05$
0.875	$0.807 \pm 0.006 \pm 0.05$
0.925	$0.806 \pm 0.005 \pm 0.05$
0.975	$0.804 \pm 0.006 \pm 0.05$

y	\bar{p}/p (\pm stat.) (\pm syst.)
-0.450	$0.824 \pm 0.004 \pm 0.05$
-0.350	$0.817 \pm 0.004 \pm 0.05$
-0.250	$0.816 \pm 0.005 \pm 0.05$
-0.150	$0.810 \pm 0.005 \pm 0.05$
-0.050	$0.813 \pm 0.005 \pm 0.05$
0.050	$0.809 \pm 0.005 \pm 0.05$
0.150	$0.804 \pm 0.005 \pm 0.05$
0.250	$0.811 \pm 0.005 \pm 0.05$
0.350	$0.815 \pm 0.005 \pm 0.05$
0.450	$0.821 \pm 0.004 \pm 0.05$

Table B.2.: \bar{p}/p with statistical (stat.) and systematic uncertainties from 10% central $^{197}\text{Au} + ^{197}\text{Au}$ collisions at $\sqrt{s_{NN}} = 200$ GeV, versus transverse momentum p_{\perp} and rapidity y .

B. Tables with Results

p_{\perp}	\bar{p}/p (\pm stat.) (\pm syst.)
0.45	$0.814 \pm 0.012 \pm 0.1$
0.55	$0.771 \pm 0.010 \pm 0.1$
0.65	$0.783 \pm 0.010 \pm 0.1$
0.75	$0.802 \pm 0.010 \pm 0.1$
0.85	$0.799 \pm 0.010 \pm 0.1$
0.95	$0.804 \pm 0.011 \pm 0.1$

y	\bar{p}/p (\pm stat.) (\pm syst.)
-0.25	$0.808 \pm 0.021 \pm 0.1$
-0.15	$0.819 \pm 0.023 \pm 0.1$
-0.05	$0.819 \pm 0.025 \pm 0.1$
0.05	$0.816 \pm 0.027 \pm 0.1$
0.15	$0.806 \pm 0.030 \pm 0.1$
0.25	$0.800 \pm 0.034 \pm 0.1$

class	$\langle N_{ch} \rangle$	\bar{p}/p (\pm stat.) (\pm syst.)
1	10.0	$0.828 \pm 0.083 \pm 0.1$
2	35.5	$0.841 \pm 0.051 \pm 0.1$
3	78.0	$0.814 \pm 0.032 \pm 0.1$
4	144.5	$0.814 \pm 0.024 \pm 0.1$
5	234.5	$0.783 \pm 0.019 \pm 0.1$
6	327.5	$0.786 \pm 0.020 \pm 0.1$
7	432.5	$0.788 \pm 0.025 \pm 0.1$

Table B.3.: \bar{p}/p with statistical and systematic uncertainties from minimum bias $^{197}\text{Au} + ^{197}\text{Au}$ collisions at $\sqrt{s_{NN}} = 200$ GeV reconstructed with the online analysis, versus transverse momentum p_{\perp} , rapidity y and centrality classes, $\langle N_{ch} \rangle$.

p_{\perp}	\bar{p}/p (\pm stat.) (\pm syst.)
0.425	$0.816 \pm 0.015 \pm 0.05$
0.475	$0.796 \pm 0.011 \pm 0.05$
0.525	$0.788 \pm 0.009 \pm 0.05$
0.575	$0.770 \pm 0.008 \pm 0.05$
0.625	$0.779 \pm 0.007 \pm 0.05$
0.675	$0.776 \pm 0.006 \pm 0.05$
0.725	$0.788 \pm 0.006 \pm 0.05$
0.775	$0.790 \pm 0.006 \pm 0.05$
0.825	$0.814 \pm 0.006 \pm 0.05$
0.875	$0.807 \pm 0.006 \pm 0.05$
0.925	$0.806 \pm 0.005 \pm 0.05$
0.975	$0.804 \pm 0.006 \pm 0.05$
1.375	$0.813 \pm 0.011 \pm 0.05$
1.625	$0.778 \pm 0.007 \pm 0.05$
1.875	$0.757 \pm 0.007 \pm 0.05$
2.125	$0.763 \pm 0.007 \pm 0.05$
2.375	$0.745 \pm 0.009 \pm 0.05$
2.625	$0.706 \pm 0.011 \pm 0.05$
2.875	$0.685 \pm 0.014 \pm 0.05$
3.25	$0.656 \pm 0.012 \pm 0.05$
3.75	$0.619 \pm 0.026 \pm 0.10$
4.25	$0.645 \pm 0.047 \pm 0.10$

Table B.4.: \bar{p}/p with statistical and systematic uncertainties from 10% central $^{197}\text{Au} + ^{197}\text{Au}$ collisions at $\sqrt{s_{NN}} = 200$ GeV. Protons(anti-protons) were identified with dE/dx in the TPC within the momentum range of $0.4 < p_{\perp} < 1.0$ and with the RICH from $1.3 < p_{\perp} < 4.5$.

B. Tables with Results

Bibliography

- [1] J. W. Harris and B. Müller,
“The search for the quark-gluon plasma”,
Ann. Rev. Nucl. Part. Sci. **46**, 71 (1996)
- [2] S. A. Bass, M. Gyulassy, H. Stöcker and W. Greiner,
“Signatures of Quark-Gluon-Plasma formation in high energy heavy-ion collisions: A critical review”,
J. Phys. G **25**, R1 (1999).
- [3] S. A. Bass *et al.*,
“Last Call for RHIC Predictions”,
Nucl. Phys. A **661**, 205 (1999).
- [4] H. Stöcker, J. Berger, U. Eichmann, S. Salur, S. Scherer and D. Zschesche,
“Critical Review Of Quark Gluon Plasma Signatures”,
AIP Conf. Proc. **631**, 553 (2003).
- [5] P. Braun-Munzinger, D. Magestro, K. Redlich and J. Stachel,
“Hadron production in Au Au collisions at RHIC”,
Phys. Lett. B **518**, 41 (2001)
- [6] P. Braun-Munzinger, K. Redlich and J. Stachel,
“Particle production in heavy ion collisions”,
To appear in Quark Gluon Plasma 3,
eds. R.C. Hwa and Xin-Nian Wang,
World Scientific Publishing. arXiv:nucl-th/0304013.
- [7] C. Alt *et al.* (NA49 Collaboration),
“Observation of an Exotic $S = -2$, $Q = -2$ Baryon Resonance in Proton Proton Collisions at the CERN SPS”,
arXiv:hep-ex/0310014.
- [8] P. Schmüser
“Feynman-Graphen und Eichtheorien für Experimentalphysiker”,
Springer-Verlag, 2. Auflage (1995).

Bibliography

- [9] D. J. Gross and F. Wilczek,
“Ultraviolet Behavior Of Non-Abelian Gauge Theories”,
Phys. Rev. Lett. **30**, 1343 (1973).
- [10] J. Letessier, J. Rafelski,
“Hadrons and Quark-Gluon Plasma”,
Cambridge University Press (2002).
- [11] F. Karsch,
“Lattice QCD at high temperature and density”,
Lect. Notes Phys. **583**, 209 (2002).
- [12] E. Kolb, M. S. Turner,
“The Early Universe”,
Addison-Wesley, Redwood City (1990).
- [13] S. L. Shapiro, S. A. Teukolsky,
“Black Holes, White Dwarfs and Neutron Stars”,
Wiley, New York (1983).
- [14] R. u. H. Sexl,
“Weiße Zwerge - Schwarze Löcher”,
Vieweg Verlag, 2., erweiterte Auflage (1990).
- [15] R. Stock,
“Hadron production in relativistic nuclear collisions”,
Varenna Summer School 2002
arXiv:hep-ph/0212287.
- [16] C.-Y. Wong,
“Introduction to High-Energy Heavy-Ion Collisions”,
World Scientific Publishing (1994).
- [17] J. D. Bjorken, “Highly relativistic nucleus-nucleus collisions: The
central rapidity region”, Phys. Rev. D **27**, 140 (1983).
- [18] H. J. Specht,
“Experimental conference summary”,
Nucl. Phys. A **698**, 341 (2002).
- [19] P. Braun-Munzinger, “Chemical Equilibration and the Hadron-QGP
Phase Transition”, Nucl. Phys. A **681**, 119 (2001)

- [20] S. A. Bass, A. Dumitru, M. Bleicher, L. Bravina, E. Zabrodin, H. Stoecker and W. Greiner,
“Hadronic freeze-out following a first order hadronization phase transition in ultrarelativistic heavy-ion collisions”,
Phys. Rev. C **60**, 021902 (1999).
- [21] S. A. Bass and A. Dumitru,
“Dynamics of hot bulk QCD matter: From the quark-gluon plasma to hadronic freeze-out”,
Phys. Rev. C **61**, 064909 (2000).
- [22] B. B. Back *et al.* (PHOBOS Collaboration),
“Charged-particle pseudorapidity density distributions from Au+Au collisions at $\sqrt{s_{NN}}=130$ GeV”,
Phys. Rev. Lett. **87**, 102303 (2001).
- [23] T. Alber *et al.* (NA49 Collaboration),
“Transverse Energy Production in Pb+Pb Collisions at 158 GeV per Nucleon”,
Phys. Rev. Lett. **75**, 3814 (1995).
- [24] R. Hagedorn,
“Remarks On The Thermodynamical Model Of Strong Interactions”,
Nucl. Phys. B **24**, 93 (1970).
- [25] T. Anticic *et al.* (NA49 Collaboration),
“Energy and Centrality Dependence of Deuteron and Proton Production in Pb+Pb Collisions at CERN-SPS”,
manuscript in preparation.
- [26] F. Becatini *et al.*, manuscript in preparation
F. Becatini, M. Gazdzicki and J. Sollfrank,
“On Chemical Equilibrium in Nuclear Collisions”,
Eur. Phys. J. C **5**, 143 (1998).
- [27] S. V. Afanasiev *et al.* (NA49 Collaboration),
“Recent results on spectra and yields from NA49”,
Nucl. Phys. A **715**, 161 (2003).
- [28] “A New State of Matter created at CERN”,
CERN press release (2000),
<http://cern.web.cern.ch/CERN/Announcements/2000/NewStateMatter>
- [29] RHIC Design Manual (1990-2000),
<http://www.agrhichome.bnl.gov/AGS/Accel/Reports>

Bibliography

- [30] Relativistic Heavy Ion Collider,
<http://www.bnl.gov/RHIC>
- [31] D. Adams *et al.* (Spin Muon Collaboration),
“Spin Structure of the Proton from polarizes inclusive deep-inelastic Muon-Proton scatterin”,
Phys. Rev. D **56**, 5330 (1997).
- [32] S. Vigdor,
“The RHIC Spin Program: Snapshots of Progress”,
Proceedings of the 13th International Symposium on High Energy Spin Physics, World Scientific Pub. Comp. (1999).
- [33] T. Roser,
“RHIC Performance”,
Nucl. Phys. A **698**, 23 (2002).
- [34] J. Benjamin, C. Carlson, I. Feigenbaum, M. Manni, D. B. Steski and P. Thieberger, “Injecting RHIC from the Brookhaven Tandem Van de Graaff”,
IEEE Particle Accelerator Conference (PAC 99) Proceedings, A. U. Luccio, W. W. MacKay (eds.), 2277, New York, (1999).
- [35] F. Vidbæk,
“The BRAHMS Experiment at RHIC”,
Nucl. Phys. A **566**, 299 (1994).
- [36] J. M. Katzy *et al.*,
“The PHOBOS experiment at the RHIC collider”,
Nucl. Phys. A **661** 690c (1999).
- [37] K. H. Ackermann *et al.* (STAR Collaboration), “STAR Detector Overview”,
Nucl. Instrum. Meth. A **499**, 624 (2003).
- [38] K. Adcox *et al.* (PHENIX Collaboration),
“Phenix Detector Overview”,
Nucl. Instrum. Meth. A **499**, 469 (2003).
- [39] J. Chwastowski,
“The PP2PP experiment at RHIC”,
<http://www.rhic.bnl.gov/pp2pp/>
- [40] STAR Collaboration,
“STAR Even Pictures from the Level-3 Display”,
http://www.star.bnl.gov/protected/l3/L3_PICTURES/

- [41] M. Calderon de la Barca Sanchez,
“Charged Hadron Spectra in Au+Au Collisions at $\sqrt{s_{NN}} = 130$ GeV”,
Ph.D. Thesis, Yale University, December 2001.
- [42] T. Roser,
“RHIC Status and Plans”,
Talk presented at: RHIC Retreat, March 5-7, 2002
- [43] M. Beddo *et al.*,
“The STAR Barrel Electromagnetic Calorimeter”,
Nucl. Instrum. Meth. A **499**, 725 (2003).
- [44] C. Allgower *et al.*,
“The STAR Endcap Electromagnetic Calorimeter”,
Nucl. Instrum. Meth. A **499**, 740 (2003).
- [45] D. Reichhold *et al.* (STAR Collaboration),
“Hardware Controls For The Star Experiment At RHIC”,
Nucl. Instrum. Meth. A **499**, 792 (2003).
- [46] W. Blum, L. Rolandi,
“Particle Detection with Drift Chambers”,
Springer-Verlag, (1993).
- [47] M. Anderson *et al.*,
“The STAR Time Projection Chamber: A Unique Tool for Studying
High Multiplicity Events at RHIC”,
Nucl. Instrum. Meth. A **499**, 659 (2003).
- [48] H. A. Bethe,
Analen der Physik **5** (1930) 325.
F. Bloch,
Z. Physik **81** (1933) 363.
E. Fermi,
Phys. Rev. **57** (1940) 445.
- [49] M. Anderson *et al.*,
“A readout system for the STAR time projection chamber”,
Nucl. Instrum. Meth. A **499**, 679 (2003).
- [50] J. Abele *et al.* (STAR Collaboration),
“The Laser System For The Star Time Projection Chamber”,
Nucl. Instrum. Meth. A **499**, 692 (2003).
- [51] B. Lasiuk *et al.* (STAR-RICH Collaboration),
“The STAR-RICH Detector”,
Nucl. Phys. A **698**, 452 (2002).

- [52] ALICE Collaboration,
 “Detector for High Momentum PID”,
 Technical Design Report of the ALICE HMPID detector,
 CERN/LHCC 98-19, ALICE TDR 1, (14 August 1998).

- [53] A. Braem *et al.*,
 “Identification of High $p \perp$ Particles with the STAR-RICH Detector”,
 Nucl. Instrum. Meth. A **499**, 720 (2003).

- [54] Y. Andres *et al.*,
 “R&D in ALICE: The CsI-based RICH high momentum particle identification detector”,
 EPJdirect C **4**(S1), 25 (2002).

- [55] M. Horsley,
 “A measurement of the Charged Particle Ratios $\frac{\pi^-}{\pi^+}$, $\frac{K^-}{K^+}$, $\frac{\bar{P}}{P}$ at High Transverse Momentum in an Ultra-Relativistic Heavy Ion Collision”,
 Ph.D. Thesis, Yale University, June 2002.

- [56] Y. Andres *et al.* (STAR-RICH Collaboration),
 “Cleaning And recirculation of perfluorohexane (C_6F_{14}) in the STAR-RICH detector”,
 Nucl. Instrum. Meth. A **486**, 590 (2002).

- [57] K. H. Ackermann *et al.*, “The Forward Time Projection Chamber (FTPC) in STAR”,
 Nucl. Instrum. Meth. A **499**, 713 (2003).

- [58] R. Bellwied *et al.*,
 “The STAR Silicon Vertex Tracker: A Large Area Silicon Drift Detector”,
 Nucl. Instrum. Meth. A **499**, 640 (2003).

- [59] L. Arnold *et al.*,
 “The STAR Silicon Strip Detector (SSD)”,
 Nucl. Instrum. Meth. A **499**, 652 (2003).

- [60] C. Adler,
 “Bau und Test einer Null Grad Kalorimeters für RHIC”,
 Diplomarbeit, Institut für Kernphysik der Johann-Wolfgang-Goethe Universität, Frankfurt am Main (1998).

- [61] H. Appelshäuser *et al.*,
 „Spectator Nucleons in Pb+Pb Collisions at 158 AGeV“,
 Eur. Phys. J. A **2**, 383 (1998).

- [62] C. Adler, A. Denisov, E. Garcia, M. Murray, H. Strobele and S. White, “The RHIC Zero Degree Calorimeters”, Nucl. Instrum. Meth. A **470**, 488 (2001).
- [63] A. J. Baltz, C. Chasman and S. N. White, “Correlated forward-backward dissociation and neutron spectra as a luminosity monitor in heavy ion colliders”, Nucl. Instrum. Meth. A **417**, 1 (1998).
- [64] J. E. Gonzales, “Calibration of STAR Zero Degree Calorimeters”, Internal Report: STAR-Note 437 (2001).
- [65] F. S. Bieser *et al.*, “The STAR Trigger”, Nucl. Instrum. Meth. A **499**, 766 (2003).
- [66] P. Nevski, “GEANT description of the STAR Experiment”, <http://www.star.bnl.gov/STAR/comp/simu/gstar/GEOM/btof/btomat.html>
- [67] J. M. Landgraf *et al.*, “An Overview of the STAR DAQ System”, Nucl. Instrum. Meth. A **499**, 762 (2003).
- [68] M. Botlo, M. J. LeVine, R. A. Scheetz, M. W. Schulz, P. Short, J. Woods and D. Crosetto, “The Star Cluster-Finder ASIC”, IEEE Trans. Nucl. Sci. **45**, 1809 (1998).
- [69] J. Berger *et al.*, “Level-3 Trigger System Proposal”, Internal Report, Institut für Kernphysik der Johann-Wolfgang-Goethe Universität, Frankfurt am Main (1998).
- [70] C. Adler *et al.*, “The STAR Level-3 trigger system”, Nucl. Instrum. Meth. A **499**, 778 (2003).
- [71] C. Adler, “Der STAR Level-3 Trigger”, Doktorarbeit, Institut für Kernphysik der Johann-Wolfgang-Goethe Universität, Frankfurt am Main (2002).

Bibliography

- [72] C. Struck,
“Antinuclei Production in Central Au-Au Collisions at RHIC”,
Ph.D. Thesis, Institut für Kernphysik der Johann-Wolfgang-Goethe
Universität, Frankfurt am Main (2002).
- [73] M. A. Lisa,
“The STAR-TPC Clusterfinder/Hitfinder”,
Internal Report: STAR-Note 238 (1996).
- [74] D. Flierl,
“L3 Efficiencies“,
Internal Report, STAR Level-3 trigger group (2001).
- [75] R. Bossingham,
“STAR Offline Simulations and Analysis Software Design”,
Internal Report: STAR-Note 281 (1997).
- [76] B. Lasiuk, Th. Ullrich,
“STAR C++ Class Library, User Guide and Reference Manual”,
Internal STAR Documentation (1999).
- [77] B. Lasiuk *et al.*,
“TPC Respose Simulator, User Guide and Reference Manual”,
Internal STAR Documentation, Rev. 1.4 (2000).
- [78] J. Fisiak,
Internal Presentation (2002).
- [79] L. Landau,
Journal of Physics U.S.S.R. **8** 201 (1944).
- [80] D. Liko,
“Track Fitting in the STAR Detector using the Kalman Filter
Method”,
Internal Report: STAR-Note 87 (1992).
- [81] S. Margetis and D. Cebra,
“Main Vertex Reconstruction in STAR”,
Internal Report: STAR-Note 89 (1992).
- [82] CERN Computing and Networks Division,
Geant 3 (1984-1997),
<http://wwwinfo.cern.ch/asdoc/geantold/GEANTMAIN.html>

- [83] P. Yepes,
“A Fast Track Pattern Recognition”,
Nucl. Instrum. Meth. A **380**, 582 (1996) .
- [84] J. S. Lange (STAR Collaboration),
“B physics at STAR”,
arXiv:nucl-ex/0306005.
- [85] J. Berger,
“L3GIViewer”,
<http://www.star.bnl.gov/protected/l3/eventdisplay>
- [86] Trolltech,
“Qt”,
<http://www.trolltech.com>
- [87] C. Adler *et al.* (STAR Collaboration),
“Coherent ρ^0 Production in Ultra-Peripheral Heavy Ion Collisions”,
Phys. Rev. Lett. **89**, 272302 (2002).
- [88] J. Adams *et al.* (STAR Collaboration),
“Transverse momentum and collision energy dependence of high p_T hadron suppression in Au + Au collisions at ultrarelativistic energies”,
arXiv:nucl-ex/0305015.
- [89] Z. Xu,
“Vertex Cut using ZDC Timing”,
Internal Report.
- [90] Z. Xu,
“Common centrality cuts in year 2001”,
Internal Report (June 5, 2002).
- [91] C. Adler *et al.* (STAR Collaboration),
“Measurement of inclusive Antiprotons from Au + Au collisions at $\sqrt{s_{NN}} = 130$ GeV”,
Phys. Rev. Lett. **87**, 262302 (2001).
- [92] J. C. Dunlop for the STAR Collaboration and the STAR-RICH Collaboration,
“High p_{\perp} Spectra from Au+Au Collisions at $\sqrt{s_{NN}} = 130$ GeV”,
Nucl. Phys. A **698**, 515 (2002).
- [93] J. C. Dunlop,
“Effects of secondary protons from Λ decays in the RICH”,
Private communication (2002).

- [94] B. Lasiuk,
“P01hi Production Analysis”,
Internal Report (March 4, 2002).
- [95] STAR Collaboration,
“Identified particle distributions in pp and Au+Au Collisions at
 $\sqrt{s_{NN}}=200$ GeV”,
submitted to Phys. Rev. Lett. (October 6, 2003),
arXiv:nucl-ex/0310004.
- [96] C. Adler *et al.* (STAR Collaboration),
“Midrapidity Λ and $\bar{\Lambda}$ production in Au + Au collisions at
 $\sqrt{s_{NN}}=130$ GeV”,
Phys. Rev. Lett. **89**, 092301 (2002).
- [97] B. B. Back *et al.* (PHOBOS Collaboration), “Centrality Dependence
of the Charged Particle Multiplicity near Mid-Rapidity in Au+Au
Collisions at $\sqrt{s_{NN}} = 130$ and 200 GeV”, Phys. Rev. C **65**, 061901
(2002).
- [98] A. Billmeier (STAR Collaboration),
“Strange and Multi-strange Particle Ratios in p+p reactions at
 $\sqrt{s_{NN}}=200$ GeV at RHIC”,
Talk given at “7th International Conference on Strange Quarks in
Matter” (2003).
- [99] C. Adler *et al.* (STAR Collaboration),
“Midrapidity Antiproton-to-Proton Ratio from Au+Au collisions at
 $\sqrt{s_{NN}}=130$ GeV”,
Phys. Rev. Lett. **86**, 4778 (2001) [Erratum-ibid. **90**, 119903 (2003)].
- [100] I. Vitev,
“High- p_{\perp} Pion Quenching versus anti+Baryon Enhancement in
Nucleus-Nucleus Collisions”,
Nucl. Phys. A **715**, 779 (2002).
- [101] S. S. Adler *et al.* (PHENIX Collaboration),
“Identified charged particle spectra and yields in Au + Au collisions
at $\sqrt{s_{NN}}=200$ GeV”,
arXiv:nucl-ex/0307022.
- [102] M. Glück, E. Reya and A. Vogt,
“Dynamical Parton Distributions Revisited”,
Eur. Phys. J. C **5**, 461 (1998).

- [103] S. A. Bass, B. Müller and D. K. Srivastava,
“Net baryon density in $Au + Au$ collisions at the Relativistic Heavy Ion Collider”,
Phys. Rev. Lett. **91**, 052302 (2003).
- [104] A. Dumitru, L. Gerland and M. Strikman,
“Proton breakup in high-energy pA collisions from perturbative QCD”,
Phys. Rev. Lett. **90**, 092301 (2003).
- [105] R. J. Fries, B. Müller, C. Nonaka and S. A. Bass,
“Hadron production in heavy ion collisions: Fragmentation and recombination from a dense parton phase”,
arXiv:nucl-th/0306027.
- [106] T. S. Ullrich,
“Experimental summary on global observables, hadron spectra and ratios”,
Nucl. Phys. A **715**, 399 (2003).
- [107] “QUARK MATTER 2002”,
Proceedings of the 16th international conference on ultra-relativistic nucleus-nucleus collisions,
Nucl. Phys. A **715** (2003).
- [108] ALICE Collaboration,
“A Large Ion Collider Experiment at CERN LHC”,
<http://alice.web.cern.ch/Alice/>
- [109] ALICE Collaboration,
“ALICE High-Level Trigger Conceptual Design”,
ALICE HLT (L3) Conceptual design report, (December 09, 2002).
<http://www.kip.uni-heidelberg.de/ti/L3/>
- [110] V. Lindenstruth *et al.*,
“Online Pattern Recognition for the ALICE High Level Trigger”,
arXiv:physics/0310052.
- [111] ALICE Collaboration,
“ALICE TRD Technical Design Report”,
CERN/LHCC 2001-021, ALICE TDR 9, (3 October 2001).
- [112] L. Kot, D. Fritz
“STAR Beam Pipe Study”,
Internal Report: STAR-Note 220 (1995).

Bibliography

- [113] K. Hagiwara *et al.* (Particle Data Group Collaboration), “Review Of Particle Physics”, *Phys. Rev. D* **66**, 010001 (2002).

Acknowledgements

I want to express my gratitude to Dr. Reinhard Stock and Dr. Ströbele to trust a group of four PhD students, under the supervision of Dr. Sören Lange, to set up the Level-3 trigger project from scratch at the STAR experiment. Dr. Dieter Röhrich was the original driving force of this project at IKF. At BNL, strong supervision was provided by Dr. Mike Levine and Dr. Tonko Ljubicic of the DAQ group. I therefore wish to acknowledge Dieter, Sören, and the DAQ Group. I want to thank Dr. John Harris, Dr. Timothy Hallman, Dr. Jim Thomas and Dr. Bill Christie for the continuous support they gave the Level-3 group at BNL. Credit goes to Dirk Schmischke and Dr. Pablo Yepes for proving that the Level-3 trigger might work in the first place! I especially remember Dr. Clemens Adler for the good atmosphere during many long hours in the STAR control room, Dr. Dominik Flierl for being the thinker when it came to physics questions and Dr. Christof Struck for implementing such a good dE/dx calculation into the Level-3 trigger system. Sincere thanks to Thomas Dietel for his support (even remote!) when the first events triggered by Level-3 were recorded. Dr. Adrian Dumitriu provided many stimulating discussions, one of which led to the nucleus+nucleus comparison included in the discussion of the results of this thesis. I want to express my gratitude to Dr. Kai Schweda for his help with the low momentum analysis of the anti-proton to proton ratio and with absorption calculations for the high momentum anti-proton to proton ratio analysis in the RICH detector. Dr. James Dunlop's help with the RICH detector analysis was also invaluable. I thank Dr. Nu Xu for interesting discussions about statistical models. Dr. Frank Laue was instrumental in finding the right data format for the RICH detector analysis. Werner Amend's technical support during the thesis write-up at IKF was much appreciated, as were suggestions for improvement to detector descriptions from Dr. Rainer Renford. I owe a debt of gratitude to Dr. Orla Feeney for editing this work many times and Dr. Dominik Flierl for his effort in editing and improving the comprehension of the text.

Lebenslauf

Persönliche Informationen	Name:	Jens Berger
	Familienstand	ledig
	Staatsangehörigkeit:	deutsch
	Geburtsdatum:	30.09.1969
	Geburtsort:	Frankfurt am Main
Schulbildung	1976-1980	Grundschule, Kronberg-Oberhöchstadt
	1980-1982	Altkönigschule, Kronberg
	1982-1986	Integrierte Gesamtschule, Oberursel-Stierstadt
	1986-1989	Technisches Gymnasium, Bad Homburg
		Abschluss: Abitur
Zivildienst	1989 -1990	Alfred Delp Haus, Oberursel Gruppenbetreuung von geistig Schwerstbehinderten
Studium	10/1989 -	Technische Universität Darmstadt
	10/1992	Studium der Physik
	10/1992	Johann-Wolfgang-Goethe Universität Frankfurt Studium der Physik
	12/1994	Vordiplom im Fach Physik
	3/1996 -	Diplomarbeit am Institut für Kernphysik
	5/1998	Titel: „Messung von Lepton-Paaren aus Meson-Zerfällen in den Hadronexperimenten Na49 und STAR” Betreuer: Prof. Dr. Reinhard Stock, Prof. Dr. Dieter Röhrich
	7/1998	Diplom im Fach Physik
	12/1998	Beginn der Promotion am Institut für Kernphysik Betreuer: Prof. Dr. Reinhard Stock
	4/1999-	Aufenthalt am Brookhaven National Laboratory, USA, zum Aufbau und Inbetriebnahme des Level-3 Trigger Systems
	02/2003	am STAR Experiment